UNIVERSITAT DE BARCELONA

Exploring Signatures of New Physics in Cosmology

Nicola Bellomo

EXPLORING SIGNATURES OF NEW PHYSICS IN COSMOLOGY

NICOLA BELLOMO

DIRECTOR:
Prof. Licia Verde

UNIVERSITAT DE BARCELONA

Departament de Física Quàntica i Astrofísica
Facultat de Física
Universitat de Barcelona

Nicola Bellomo, *Exploring Signatures of New Physics in Cosmology*,
PhD Thesis
Barcelona, 30 September 2019

Cover Image: ???? (Credit: ????. Composition and copyright: ????)

UNIVERSITAT DE BARCELONA
DEPARTAMENT DE FÍSICA QUÀNTICA I ASTROFÍSICA
Programa de doctorat en física
Línia de recerca en astronomia i astrofísica

Exploring Signatures of New Physics in Cosmology

Memòria presentada per
Nicola Bellomo
per optar al grau de
Doctor en física per la Universitat de Barcelona

Directora de la tesi:
Prof. Licia Verde
Tutor de la tesi:
Dr. Alberto Manrique Oliva

Barcelona, 30 September 2019

DECLARATION

This thesis is presented following the regulations of the University of Barcelona (Aprovada pel CdG en sessió del 16 de març de 2012 i modificada pel CdG de data 9 de maig i 19 de juliol de 2012, 29 de maig i 3 d'octubre de 2013, 17 de juliol de 2014, 16 de juliol de 2015, 15 de juny i 21 de novembre de 2016, 5 de desembre de 2017 i 4 de maig de 2018). The listed regulations allow for the presentation of a PhD thesis as a "compendia of published articles". According to the regulations, the thesis must contain a minimum of four published or accepted articles. This thesis contains the published version of four articles, which is sufficient to allow its presentation. It also contains one additional article, submitted but not yet accepted for publication at the moment of thesis presentation.

Barcelona, 30 September 2019

Nicola Bellomo

There is only one god, and his name is *Set of Initial Conditions Of The Universe And Physical Laws That Have Given Rise To My Particular Circumstances*. And what do we say to *Set of Initial Conditions Of The Universe And Physical Laws That Have Given Rise To My Particular Circumstances*? Yeah, I guess it might be today, depending on the initial conditions of the universe and physical laws that have given rise to my particular circumstances.

— H. G. M. Silverwood

ABSTRACT

Cosmology is the study of the origin and evolution of our Universe as a whole. Despite the great advance in the last decades, culminating into the definition of a standard model of Cosmology, the ΛCDM, there are still several open problems that we need to address to provide a comprehensive description of this Universe from its first moments to the present-day. The goal of this thesis is to explore how several of these open problems in Cosmology can be addressed in novel ways, with particular attention to the observational consequences and possibility of experimental confirmation.

The work is divided in five parts. The first one is an introductory chapter in which I present the main ingredients of the ΛCDM, namely General Relativity, the different components existing in our Universe and Inflation.

The second part is focused on the possible degeneracy between the effects of massive neutrinos and modified gravity theories. In particular I investigate how Horndeski theory has enough freedom to reproduce a ΛCDM-like expansion and, at the same time, to boost the growth of structures at small scales, hiding the effects that massive neutrinos have on the clustering of matter.

In the third part we discuss about one of the most popular dark matter candidate, primordial black holes. I show how it is possible to obtain upper limits on the abundance of primordial black holes with an extended mass distribution starting from upper limits obtained assuming a monochromatic one. I also prove that for popular mass distributions the constraints on primordial black holes abundance in the 10 $M_\odot$ window are tighter with respect to the monochromatic case. Moreover I also explain how, cross-correlating gravitational waves and galaxies maps, we can establish if the origin of black holes in merging binaries is stellar or primordial.

The fourth part describes how we can obtain new probes of the inflationary physics. I present a novel way to determine the energy scale of inflation through the measurement of a specific primordial non-Gaussianity signal, called "graviton exchange", in the clustering properties of dark matter halos. Moreover I present how primordial black holes can be used to put constraints on the maximum amplitude of the primordial curvature power spectrum.

The fifth part includes the summary of the results, discussion and conclusion reached in each work. Future perspectives and possible extension are also discussed in this section.

ACKNOWLEDGMENTS

First of all I would like to thank the three persons that inspired me in starting and moving on in my scientific career. It is very hard to find the correct words to thank my PhD advisor Licia Verde. Thank you for all the teachings, the patience, the guidance but also the freedom to develop my projects you gave me. I wouldn't have reached this point without your mentorship. Then I would like to thank Alvise Raccanelli for motivating me to work on so many different things and the numerous good tips and opportunities you gave me, they that will certainly help me in the future. Finally I thank Silvia Losso, my Physics teacher during high school, for transmitting me this passion.

I deeply thank all the past and present members of this fantastic group for teaching me so many things and for all the good moments we had together. Therefore thank you Raúl, Emilio, Antonio, Fergus, Benedict, Ilia, Héctor, Davide B., Davide G., David, Katie, Ali and Samuel. A special thank to my fellow José who shared with me the past four years of scientific life. I would like to thank also the master students I co-advise: Giulio, Alba, David and Lorenzo. I have learnt a lot from this experience and I really hope I have taught you something valuable. I wouldn't have achieved so much without the many external collaborators I had, therefore thank you Carlos, Sabino, Nicola, Daniele, Angelo, Donghui, Valentí, Christian and Sam. A special thank to Donghui Jeong for hosting me at Penn State University and for teaching me so much about large scale structure.

These years would not have been so joyful without the "Chupi Pandi": thank you Dani, Lluís and Núria for all you have done for me during the past four years, my staying in Barcelona would not have been the same without you. I thank also the other PhDs of the "7th Floor Oasis": Ignasi, Laia, Victor, Roger, Alfred, Pau, Juan, Edgar and Hamish for all the good moments we had in the day-to-day life of the department.

Special thanks to all the personnel of the department and of the ICC for always solving my problems and for helping me so much in this eternal fight against bureaucracy and technology. Thank you JR, Ariadna, Esther, Miriam, Kayla, Marta, Surinye, Gabi, Jordi and Joan.

I really thank all my flatmates, Isa, Marta, Clara, Toni, Ari and Chris, for these years we have lived together, first in Sants 91 and then in Valencia 15, and for the artistic cover of this work.

Finally I thank my friends in Italy, Alessia, Marco, Monica and Nicolò for all the brief moments we had together every time I went back.

RESUMEN EN ESPAÑOL

La Cosmología es el estudio de las orígenes y la evolución de nuestro Universo como un todo. Aunque desde el punto de vista teórico la Cosmología nació hace un siglo, con la formulación de la teoría de la Relatividad General por Albert Einstein, ha sido únicamente en las últimas décadas que ha habido un avance experimental tan importante que la ha transformado desde una ciencia "pobre de datos" a una ciencia "guiada por los datos". Estamos viviendo la que se dice la "Edad del Oro" en Cosmología: no sólo tenemos suficiente evidencias experimentales para medir parámetros cosmológicos con una precision alrededor del uno por ciento, sino que también podremos ir mas allá de esa precisión con los experimentos planeados en las próximas décadas, que probarán por primera vez épocas de nuestro Universo nunca observadas directamente hasta ahora. Además, los avances tecnológicos conseguido en los últimos años serán fundamentales para darnos una visión alternativa de nuestro Universo, no sólo mediante la radiación electromagnética, sino también mediante las ondas gravitatorias, detectadas por primera vez hace cuatro años.

Esta tesis está dividida en cinco partes. La primera está constituida por un capítulo introductorio que describe el modelo estándar que se utiliza hoy en Cosmología, el modelo ΛCDM. Los ingredientes principales de este modelo son una teoría de la gravedad que describe como nuestro Universo evoluciona, en este caso la Relatividad General; las diferentes componentes que existen en nuestro Universo, es decir fotones, neutrinos, bariones, materia oscura fría (en inglés CDM) y energía oscura, descrita por una constante cosmológica Λ; y una teoría que explique las condiciones iniciales del Universo, que asumimos ser la teoría de la Inflación. Aunque décadas de investigación nos han permitido describir muchos de esto aspectos en gran detalle, hay varios problemas en los tres ámbitos (teoría de la gravedad, componentes del Universo y teoría de las condiciones iniciales). El objetivo de esta tesis es de explorar cómo estos problemas abiertos pueden encontrar una posible solución; en particular se discute cómo nuevas muestras experimentales y nuevos avances teóricos puedan jugar un papel en responder a estas preguntas abiertas.

La segunda parte se centra en la posible degeneración entre los efectos que neutrinos y teorías de gravedad modificada tienen en los observables cosmológicos. En el trabajo "Hiding neutrino masses in modified gravity cosmology" se investigó como la teoría de Horndeski, que es la teoría más general que incluye un campo escalar que tiene ecuaciones del movimiento del segundo orden y que obedece al principio de equivalencia débil, tenga suficiente libertad para reproducir

una expansión como la que predice el ΛCDM y, al mismo tiempo, pueda incrementar el crecimiento de las estructura a grandes escalas. Dicho crecimiento, si se produjera a escalas del orden de 100 Mpc, podría esconder los efectos que los neutrinos masivos tienen en el espectro de potencia de la materia.

En la tercera parte se debate de uno de los candidatos a ser materia oscura, es decir de agujeros negros primordiales, es decir, aquellos que se formaron en las primeras fracciones de segundos de nuestro Universo. En "Primordial black holes as dark matter: converting constraints from monochromatic to extended mass distributions" se muestra cómo, empezando desde los límites superiores que ya existen para agujeros negros primordiales que tienen una distribución de masa monocromática, es posible obtener límites superiores en la abundancia de agujeros negros primordiales que tengan una distribución de masa extendida. Además, se establece cómo validar si todas las asunciones hechas en la parte de modelización teórica se cumplen en el caso de distribuciones de masa extendidas. Por último, se enseña cómo para distribuciones log-normal y de ley potencial los límites en la abundancia de agujeros negros primordiales en la ventana de 10 masas solares son más estrictos que respeto al caso monocromático. En "GW$\times$LSS: chasing the progenitors of merging binary black holes" se explica cómo, relacionando mapas de galaxias y mapas de ondas gravitatorias generadas respectivamente por los survey de galaxias y los observatorios de ondas gravitatorias, se puede llegar a entender cuál es la origen de los agujeros negros que forman las binarias detectadas. Resulta que con experimentos ya en funcionamento, como DESI para galaxias y ALIGO para las ondas gravitatorias, se puede tener una primera indicación sobre la origen estelar o primordial, aunque se necesitarán los experimentos de la siguiente generación para obtener una confirmación definitiva.

La cuarta parte describe cómo se puede obtener nuevas pruebas sobre las primeras fracciones de segundos de nuestro Universo, y en particular sobre la teoría de la Inflación. En "Measuring the energy scale of inflation using large scale structure" enseñamos cómo se podría medir la escala energética de la Inflación mediante la medida de una señal específica de no-gaussianidades primordiales, llamada "graviton exchange". Esta no-gaussianidad está generada por la interacción de dos campos escalares con un gravitón y depende directamente del parámetro tensor-to-scalar ratio r, lo cual, a cambio, está directamente relacionado con la energía de la Inflación en los modelos de campo escalar cuya energía cinética es muy pequeña en comparación con su energía potencial. En el trabajo se enseña cómo esta señal primordial resulta ser del mismo orden de magnitud que la función a tres puntos estándar a escalas grandes, incrementando la posibilidad de una detección. En "From primordial black holes abundance to primordial curvature power spectrum (and back)" se utilizan los agujeros

negros primordiales para poner límites en la máxima amplitud que puede tener el espectro de potencia de la curvatura primordial. Más específicamente, se ha desarrollado un procedimiento que conecta las simulaciones numéricas de formación de agujeros negros primordiales a una correcta interpretación cosmológica de dichas simulaciones hasta el cálculo de la abundancia de estos agujeros negros primordiales utilizando la teoría de picos. Este desarrollo teórico permitió obtener limites significativamente más robustos respecto a la literatura anterior.

La quinta parte incluye el resumen de los resultados encontrados y una discusión de los mismos. Además, se debate sobre cuáles son las perspectivas futuras y sobre cómo extender estos trabajos para siguientes proyectos científicos. Aunque parezca que los diferentes problemas explorados en esta tesis vayan uno separado del otro, la explicación final de cuál es la origen, la evolución y también el futuro de nuestro Universo tiene que incluir respuestas a todos estas instancias.

PUBLICATIONS

Complete list of publications at the moment of thesis deposit.

Published articles in this thesis

[1] **Nicola Bellomo**, Nicola Bartolo, Raul Jimenez, Sabino Matarrese, and Licia Verde. "Measuring the energy scale of inflation with large scale structures." In: *Journal of Cosmology and Astroparticle Physics* 2018.11 (Nov. 2018), p. 043. DOI: 10.1088/1475-7516/2018/11/043. arXiv: 1809.07113.

[2] Giulio Scelfo, **Nicola Bellomo**, Alvise Raccanelli, Sabino Matarrese, and Licia Verde. "GW×LSS: chasing the progenitors of merging binary black holes." In: *Journal of Cosmology and Astroparticle Physics* 2018.9 (Sept. 2018), p. 039. DOI: 10.1088/1475-7516/2018/09/039. arXiv: 1809.03528.

[3] **Nicola Bellomo**, José Luis Bernal, Alvise Raccanelli, and Licia Verde. "Primordial black holes as dark matter: converting constraints from monochromatic to extended mass distributions." In: *Journal of Cosmology and Astroparticle Physics* 2018.1 (Jan. 2018), p. 004. DOI: 10.1088/1475-7516/2018/01/004. arXiv: 1709.07467.

[4] **Nicola Bellomo**, Emilio Bellini, Bin Hu, Raul Jimenez, Carlos Pena-Garay, and Licia Verde. "Hiding neutrino mass in modified gravity cosmologies." In: *Journal of Cosmology and Astroparticle Physics* 2017.2 (Feb. 2017), p. 043. DOI: 10.1088/1475-7516/2017/02/043. arXiv: 1612.02598.

Other published articles

[1] José Luis Bernal, **Nicola Bellomo**, Alvise Raccanelli, and Licia Verde. "Cosmological implications of primordial black holes." In: *Journal of Cosmology and Astroparticle Physics* 2017.10 (Oct. 2017), p. 052. DOI: 10.1088/1475-7516/2017/10/052. arXiv: 1709.07465.

Other articles submitted

[1] Daniele Bertacca, Angelo Ricciardone, **Nicola Bellomo**, Alexander C. Jenkins, Sabino Matarrese, Alvise Raccanelli, Tania Regimbau, and Mairi Sakellariadou. "Projection effects on the observed angular spectrum of the astrophysical stochastic gravitational wave background." In: (Sept. 2019). arXiv: 1909.11627.

[2] Alba Kalaja, **Nicola Bellomo**, Nicola Bartolo, Daniele Bertacca, Sabino Matarrese, Ilia Musco, Alvise Raccanelli, and Licia Verde. "From Primordial Black Holes Abundance to Primordial Curvature Power Spectrum (and back)." In: (Aug. 2019). arXiv: 1908.03596.

[3] Ali Rida Khalifeh, **Nicola Bellomo**, José Luis Bernal, and Raul Jimenez. "Can Dark Matter be Geometry? A Case Study with Mimetic Dark Matter." In: (July 2019). arXiv: 1907.03660.

White papers

[1] Yacine Ali-Haimoud et al. "Electromagnetic probes of primordial black holes as dark matter." In: (Mar. 2019). arXiv: 1903.04424.

Conference proceedings

[1] **Nicola Bellomo**, Giulio Scelfo, Alvise Raccanelli, Sabino Matarrese, and Licia Verde. "The origin of progenitors in merging black hole binaries." In: *Highlights on Spanish Astrophysics X*. Ed. by B. Montesinos, A. Asensio Ramos, F. Buitrago, R. Schödel, E. Villaver, S. Pérez-Hoyos, and I. Ordóñez-Etxeberria. Mar. 2019, pp. 88–97.

CONTENTS

1 INTRODUCTION

The desire to understand our Cosmos has deep roots in every human civilization. While ancient cultures used to explain its very existence through mythology, since the 20th century we have developed the mathematical tools and the technology to approach the problem using the scientific method.

Cosmology (from the Ancient Greek *κόσμος*, kósmos, "world, universe, order" and *-λογία*, -logía, "treating of") is in fact the study of the origin and evolution of our Universe from its first moments to the present and possibly also to its future.

In this chapter we will review the basic concepts which are necessary to understand the original works presented in chapters 2, 3 and 4. The content is freely inspired by several classical books of Cosmology, as the Dodelson [1], the Coles&Lucchin [2], the Kolb&Turner [3] or the Weinberg [4].

1.1 NOTATION AND CONVENTIONS

In the following, we define the conventions and the notation we use in the rest of this chapter, in the introductory part of sections 2, 3 and 4, and in chapter 5. These conventions might change in the published works in chapters 2, 3 and 4, however any eventual change in the notation is specified directly in the articles.

Greek indices indicate spacetime coordinates and range from 0 to 4. Repeated indices are summed over, according to Einstein notation. We use the $(-,+,+,+)$ signature. Covariant derivatives are indicated by D_μ, while ∂_μ indicates standard derivatives with respect to temporal and spatial coordinates, in particular " $\dot{}$ " will indicate derivatives with respect to cosmic time t. We choose natural units, in which $c = \hbar = k_B = 1$, where c is the speed of light, $\hbar$ is the reduced Planck constant and k_B is the Boltzmann constant. The scale factor today is taken to be $a_0 = 1$.

1.2 GENERAL RELATIVITY

In 1915 Albert Einstein presented his theory of General Relativity, able to describe gravitational effects ranging from laboratory experiments to the entire Universe using geometry. He introduced the concept of spacetime, a mathematical model that joins the three spatial and one temporal dimensions into a four dimensional continuum. This entity is not immutable, in fact all the different components that exists in

our Universe define its evolution. At the same time, the motion of these components is determined by the form of spacetime itself. In this novel description of our Universe, the container and the content are intertwined, in fact the theory of General Relativity can be summarized as

> *Matter curves spacetime while, at the same time, the curved spacetime controls how matter moves in it.*

The geometry of spacetime is described by the metric $g_{\mu\nu}$ or, equivalently, by the invariant interval $ds^2 = g_{\mu\nu}dx^\mu dx^\nu$, where x^μ are spacetime coordinates. The equations of motion for the metric are derived using a variational principle from the Einstein-Hilbert action:

$$S_{\text{EH}} = \int d^4x\sqrt{-g}\left[\frac{M_p^2}{2}R + \mathcal{L}_m\right], \tag{1.1}$$

where g is the determinant of the metric, $M_p = (8\pi G)^{-1/2}$ is the reduced Planck mass, G is Newton gravitational constant, R is the Ricci scalar and $\mathcal{L}_m$ is the Lagrangian density of all the matter fields[1]. These equations of motion are called Einstein equations and they read as

$$G_{\mu\nu} = R_{\mu\nu} - \frac{1}{2}g_{\mu\nu}R = \frac{T_{\mu\nu}}{M_p^2} \tag{1.2}$$

where $G_{\mu\nu}$ is called Einstein tensor, $R_{\mu\nu}$ is the Ricci tensor and $T_{\mu\nu} = -(2/\sqrt{-g})\delta\left(\sqrt{-g}\mathcal{L}_m\right)/\delta g^{\mu\nu}$ is the matter stress-energy tensor.

The covariant formulation of the theory guarantees that the form of the equations does not change in different reference frames, therefore the choice of any observer is completely equivalent.

1.2.1 *The Metric of the Universe*

According to the Hot Big Bang cosmological model, we live in an Universe which has been expanding since its first moments. Nowadays we also have an overwhelming evidence from multiple sources that this prediction is true. In chronological order, the first piece of evidence came from the Hubble diagram, i.e., from the measurement that galaxies are, on average, receding from us; later on we had confirmation of such expansion also from the abundance of light elements (mostly Hydrogen and Helium) predicted by Big Bang Nucleosynthesis and from the detection of a relic radiation in the microwave range of wavelengths, i.e., the Cosmic Microwave Background (CMB). Due to the expansion, physical distances between different objects increase even

1 In this case we use the term "matter" to indicate every component of the Universe, not only non-relativistic species. Therefore also the Lagragian density for photons is included in $\mathcal{L}_m$.

if objects do not move from their initial position, hence to describe this effect it is useful to introduce the scale factor a.

A second pillar of the modern Cosmology is the Cosmological Principle:

> *Viewed on a sufficiently large scale, the properties of the universe are the same for all observers,*

which is equivalent to state that on large scales the Universe is homogeneous and isotropic. The Cosmological Principle, combined with the observed cosmological expansion, suggest that the correct metric for an observer comoving with the expansion is the Friedmann-Robertson-Walker-Lemaitre (FRWL) one:

$$ds^2 = -dt^2 + a^2(t)\left[\frac{dr^2}{1-kr^2} + r^2 d\Omega^2\right], \tag{1.3}$$

where t is the cosmic time, the scale factor a depends only on time because of homogeneity and isotropy, r is a comoving radial coordinate, $d\Omega$ is the solid angle measure and k is the spatial curvature. Since the geometry of the Universe is consistent with being flat and error bars on this constarints are so small that essentially only negligible deviations from flatness are allowed [5–9], in the following we consider only the case in which $k = 0$.

Once the metric has been specified, we can compute the LHS of equation (1.2) by evaluating first the Christoffel symbols

$$\Gamma^{\mu}_{\alpha\beta} = \frac{1}{2} g^{\mu\nu}\left(\partial_\beta g_{\alpha\nu} + \partial_\alpha g_{\beta\nu} - \partial_\nu g_{\alpha\beta}\right), \tag{1.4}$$

then the Riemann tensor

$$R^{\rho}{}_{\sigma\mu\nu} = \partial_\mu \Gamma^{\rho}{}_{\sigma\nu} - \partial_\nu \Gamma^{\rho}{}_{\sigma\mu} + \Gamma^{\rho}{}_{\mu\lambda}\Gamma^{\lambda}{}_{\sigma\nu} - \Gamma^{\rho}{}_{\nu\lambda}\Gamma^{\lambda}{}_{\sigma\mu}, \tag{1.5}$$

and finally both the Ricci tensor $R_{\sigma\nu} = R^{\mu}{}_{\sigma\mu\nu}$ and the Ricci scalar $R = R^{\nu}{}_{\nu}$.

The content of the Universe is typically assumed to be described as perfect isotropic fluid, to be consistent with homogeneity and isotropy. Notice that the perfect fluid assumption is realistic in the cosmological context, where the mean free-path between particle collisions is much smaller than the physical scales of interest. The stress-energy tensor of a perfect fluid reads as

$$T^{\mu}{}_{\nu} = p g^{\mu}{}_{\nu} + (\rho + p) u^{\mu} u_{\nu}, \tag{1.6}$$

where ρ and p are the energy density and pressure of the fluid and $u^{\mu} = dx^{\mu}/\sqrt{-ds^2}$ is its four-velocity normalised as $u^{\mu}u_{\mu} = -1$. Moreover, we also have to specificy the relation between pressure and energy density, i.e., the equation of state parameter $w = p/\rho$. The reader should keep in mind the two particular cases of fluid

made of relativistic or non-relativistic particle, which have equation of state parameter $w = 1/3$ or $w = 0$, respectively. Moreover, it can be proven that standard matter has equation of state parameter in the range $[0, 1/3]$.

Combining these facts together, we have that in the case of a spatially flat FRWL metric, Einstein equations reduce to the two Friedmann equations

$$\begin{aligned} \left(\frac{\dot{a}}{a}\right)^2 &= \frac{\rho}{3M_p^2}, \\ \frac{\ddot{a}}{a} &= -\frac{\rho + 3p}{6M_p^2} = -\frac{(1+3w)\rho}{6M_p^2}, \end{aligned} \tag{1.7}$$

where $H = \dot{a}/a$ is also known as the Hubble expansion parameter.

Friedmann equations explicitly show that the energy content of the Universe (the RHS) determines its evolution (the LHS). From equation (1.7) we see that a Universe dominated by any form of standard matter, i.e., with equation of state parameter $w \in [0, 1/3]$, undergoes a decelerated expansion $\ddot{a} < 0$. However, it is useful to notice that more exotic components with equation of state parameter $w < -1/3$ induce an accelerated expansion of the Universe.

We conclude by remarking that the assumption of isotropy has been supported experimentally by different CMB experiments [10–12] and possible deviations are so small that we consider them negligible. Moreover new ways to probe homogeneity has been recently proposed [13], hence what has been for many decades an assumption is currently becoming an experimental fact.

1.3 THE CONTENT OF THE UNIVERSE

As shown in equation (1.7), the knowledge of the Universe content determines the evolution in time of the scale factor and ultimately, of the entire Universe itself. Motivated by this fact, we review in this section which are the main components of our Cosmos and to which level we understand their origin, nature and behaviour in a cosmological context.

The first piece of information we need is the abundance of every component, typically characterised by its fractional abundance parameter at present time $\Omega_{j0} = \rho_{j0}/\rho_{c0}$, where $\rho_{j0} = \rho_j(t_0)$ is the present-day energy density of the desired species, $\rho_{c0} := 3M_p^2 H_0^2$ is present-day critical density and $t_0 = 13.8$ Gyr is the age of our Universe according to the latest observational results [9].

The second piece of information we need is how each component evolves in time. The contracted Bianchi identity ($D_\mu G^\mu_{\ \nu} \equiv 0$) applied to Einstein equations (1.2) guarantees that the stress-energy tensor of matter is covariantly conserved, i.e., that $D_\mu T^\mu_{\ \nu} \equiv 0$. Therefore, assuming a species living in an Universe characterised by a FRWL

metric and that can be described as a perfect fluid, we have that its energy density evolves according to the continuity equation

$$D_\mu T^\mu_{\ 0} = \dot{\rho} + 3H(\rho + p) = \dot{\rho} + 3H(1 + w)\rho = 0. \tag{1.8}$$

1.3.1 *Photons*

Photons are the mediators of the electromagnetic force. Even if today they represent the most abundant species in terms of number density density, with approximately $n_\gamma \simeq 410$ photons/cm^3, in terms of energy density the are completely subdominant, with $\Omega_{\gamma 0} \simeq 5 \times 10^{-5}$. Since they are a relativistic species, their equation of state parameter is $w_\gamma = 1/3$, hence according to equation (1.8) their energy density scales as $\rho_\gamma = \Omega_{\gamma 0}\rho_{0c}a^{-4}$ as the Universe expands.

Even if they do not contribute significantly to the present-day energy budget of the Universe, in the past they did. These photons, that constitute the CMB radiation, are in fact the relic of a primordial thermal bath that filled the entire Universe during the so called radiation-dominated era, in agreement with the Hot Big Bang model. There are, of course, other photons generated by stars but the CMB radiation is by far the dominant component. Across the past 50 years, starting with the first discovery of CMB radiation by Penzias and Wilson, we have repeatedly measured the properties of these photons. Today we know that their temperature is $T_{\rm CMB} = 2.726$ K and they have an almost perfect black body spectrum with small anisotropies.

1.3.2 *Neutrinos*

Neutrinos are particles that interact only through weak force with other particles. In cosmological context, they decoupled from the photon thermal bath before Big Bang Nucleosynthesis, when the temperature dropped below $\mathcal{O}(1)$ MeV, and weak interactions stopped being effective in coupling neutrinos to electrons and positrons. After that moment they free-streamed, interacting with the rest of the Universe only through gravitational force.

Despite the success of the Standard Model, many of their properties remain unclear. For instance, it is not clear yet if they are Dirac or Majorana particles, i.e., if they are their own antiparticle or not. However, we know that there are three different neutrinos and thanks to the observation of neutrino oscillation, we have measured the difference in mass between different mass eigenstates, even if their absolute mass has not been measured yet.

Existing cosmological data are able to provide upper bounds on the sum of the three neutrinos masses $\sum_{j=1}^{3} m_j \lesssim 0.1 - 0.2$ eV [14–17], which are competitive or even stronger than those coming from ongoing laboratory experiments, as KATRIN [18, 19]. Moreover, future

galaxy survey as DESI [20] will provide even tighter constraints on the sum of neutrino masses. A detection of neutrino masses may also clarify the neutrino mass hierarchy, namely whether there two light and one heavy neutrinos (normal hierarchy) or one light and two heavy neutrinos (inverted hierarchy).

1.3.3 *Baryons*

Baryons are mainly composed by Hydrogen and Helium atoms, both created during the Big Bang Nucleosynthesis, along with a small fraction of all the other heavier elements created later as a result of stellar evolution and merger of stars. For cosmological purposes, baryons can be described as a non-relativistic form of matter, hence they have equation of state parameter is $w_b = 0$ and their energy density scales as $\rho_b = \Omega_{b0}\rho_{0c}a^{-3}$, with $\Omega_{b0} \simeq 0.05$.

Before Recombination, i.e., the moment where neutral atoms form, the Universe was opaque because of the continuous interaction between photons and charged nuclei and electrons: we can see the trace of that epoch interaction in the Baryon Acoustic Oscillations we observe both in the CMB and in large scale structure of the Universe.

Despite baryonic physics being well described in a very broad range of energies by the Standard Model, the origin of baryons themselves remains unexplained as well as the origin of the matter-antimatter asymmetry.

1.3.4 *Dark Matter*

Along the past century a great amount of observational evidence piled up in support of the existence of dark matter, a type of matter that does not interact electromagnetically. Dark matter drives structure formation by providing the potential wells in which baryons fall and form complex structures as galaxies and cluster of galaxies. It is also responsible of strong and weak gravitational lensing phenomena, in fact its gravitational interaction is of the same kind of that of baryons.

Even if it does not interact with baryons and it does not emit or absorb light, we know that dark matter is cold, i.e., non-relativistic. As baryons, it has equation of state parameter $w_{cdm} = 0$ and its energy density scales as $\rho_{cdm} = \Omega_{cdm0}\rho_{0c}a^{-3}$, with $\Omega_{cdm0} \simeq 0.26$. Moreover, thanks to CMB data, we also have proven that dark matter was already non-relativistic long before the epoch of Recombination.

Despite the huge amount of information on this component of the Universe, we know very little about its nature, namely whether it is composed of particles, compact objects or it is a mere effect of gravity, assuming GR, as we know it up to Solar System scales, is not a full description of gravity at large cosmological scales.

1.3.5 *Dark Energy*

The last component to be discovered, and surprisingly the most abundant one today, is dark energy. Dark energy, as dark matter, does not have any electromagnetic interaction, however its peculiarity resides in having negative pressure and in sourcing an accelerated expansion of the Universe.

In its simplest version, it is described by a cosmological constant Λ (already used by Einstein to motivate a the static Universe model), with constant energy density $\rho_\Lambda = \Omega_{\Lambda 0}\rho_{0c}$, where according to latest observations the present-day density parameter is $\Omega_{\Lambda 0} \simeq 0.69$, and equation of state parameter $w_\Lambda = -1$.

In General Relativity all forms of energy gravitate. It is therefore thought that also the energy of the vacuum should do it and indeed the energy of the vacuum has the right properties to describe dark energy. However, if we compute the expectation value of the vacuum state we find an estimate for ρ_Λ which is wrong at least by 60 orders of magnitude [21]. Different explanations have also been proposed for dark energy, the most popular one being a slow-rolling scalar field. Unfortunately, the nature of dark energy remains still unknown.

1.4 THE INITIAL CONDITIONS OF THE UNIVERSE

The final state of our Universe is determined not only by its content but also by its initial conditions. Despite its success, the Hot Big Bang model cannot justify some observed properties of our Universe, as the observed spatial flatness (flatness problem) or the fact that region that in principle were never in causal contact show the same properties (horizon problem), without invoking an extremely high level of fine-tuning. Moreover, it cannot provide an explanation for the existence of small perturbations on super-horizon scales, which provide the very first seeds of the large scale structure of the Universe we observe today.

Several classes of solutions to these problems have been proposed across the past decades, including inflationary models [22], cyclic universe models [23] and string gas cosmology [24]. In the following we will consider only the former, which has been establish itself as the reference model of Early Universe because of the numerous tests it has passed.

Nevertheless, it is important to keep in mind that the other alternatives have not been ruled out and that the inflationary model has not been confirmed beyond any doubt. For this reason it is important to find novel ways to discriminate between different models thanks to accurate theoretical predictions and new observational evidence.

1.4.1 *The Inflationary Model*

Many of the problems the Hot Big Bang model seems to have can be solved by a stage of accelerated expansion, called Inflation, previous to the radiation-dominated era. There are several mechanisms that can generate this stage, however the simplest one which we review in the following is that inflation has been generated by a scalar field, called inflaton, slowly rolling down a potential.

We consider a scalar field ϕ minimally coupled with gravity and moving in a potential V with Lagrangian density

$$\mathcal{L}_\phi = -\frac{1}{2}\partial_\mu\phi\partial^\mu\phi - V(\phi). \tag{1.9}$$

The scalar field energy density and pressure can be computed as the diagonal components of the stress-energy tensor $T_{\mu\nu} = -(2/\sqrt{-g})\delta\left(\sqrt{-g}\mathcal{L}_\phi\right)/\delta g^{\mu\nu}$, as done for the perfect fluid case. In the case where the potential is almost flat and the field is slowly rolling down the potential, namely when $\dot{\phi}^2 \ll V$, the equation of state of the scalar field reads as

$$w_\phi = \frac{p_\phi}{\rho_\phi} = \frac{\dot{\phi}^2/2 - V}{\dot{\phi}^2/2 + V} \simeq -1, \tag{1.10}$$

therefore, according to equation (1.7), in an Universe dominated by such scalar field the scale factor expands exponentially as $a(t) = e^{H_{\rm inf}t}$, where $H_{\rm inf} = V/(3M_p^2)$ is the Hubble expansion rate during inflation and can be considered approximately constant since the field is moving slowly along the potential.

Once the exponential expansion starts, a small patch of the Universe, that at that time was in causal contact, is stretched at least to the size of the Universe we observe today. At the same time, inhomogeneities are rapidly washed out since spatial curvature energy density scales as $\rho_k \propto a^{-2} = e^{-2H_{\rm inf}t}$. The duration of inflation is quantified in terms of number of e-folds $\mathcal{N} = \log(a_f/a_i)$, where a_f and a_i are the scale factors at the end and at the beginning of the inflation, respectively. If $\mathcal{N} \gg 60$ both horizon and flatness problem are solved.

In this standard picture, quantum fluctuations in the scalar field are responsible for the generation of curvature perturbations and will seed structure formation when reentering the horizon, during radiation- and matter-domination eras. In this sense, the presence of perturbations on super-horizon scales is a natural prediction of standard inflationary models. Moreover, since perturbations in fields, as the photons or matter density fields, in the Late Universe are effectively sourced by Early Universe physical mechanism, by studying the statistical properties of these fields we can reconstruct the dynamics of the Early Universe.

Finally, even if inflation solve some of the problems the Hot Big Bang model has, it does not solve all of them. Because of the accelerated exponential expansion, Inflation will dilute any other component that

previously existed, cancelling any trace of how the Universe was before it started. Hence at the end of inflation we need an additional stage, called Reheating, in which the Universe is warmed up again and all the species which exist today are recreated.

1.5 OVERVIEW OF THE THESIS

General Relativity, the different components of the Universe and Inflation are the ingredients of the Cosmological Standard Model, the ΛCDM. The model can describe incredibly well a vast range of cosmological observables with only six parameters: the reduced Hubble expansion rate today $h = H_0/(100\ \mathrm{km/s/Mpc})$, the baryon physical density $\omega_b = \Omega_{b0}h^2$, the cold dark matter physical density $\omega_{cdm} = \Omega_{cdm0}h^2$, the scalar fluctuations amplitude A_s, the scalar fluctuations tilt n_s and the optical depth to Reionization τ.

Despite its success, the ΛCDM remains a phenomenological model, which does not provide any description of the nature of its parts. General Relativity describes a wide range of phenomena both in the weak and strong field regime, however it has never thoroughly tested at scales comparable to the cosmological horizon today. The origin of many of the components, such as dark matter and dark energy, still escape understanding. Even some properties of less exotic components, as neutrinos, are still not understood. The physics of first fractions of seconds remains unexplained and very hard to test.

The goal of this thesis is to explore how several of these open problems in Cosmology can be addressed in novel ways, with particular attention to the observational consequences and possibility of experimental confirmation. In fact, since we are entering the golden era of Cosmology, in which the field is going to move from a data-scarce to a data-driven science, theoretical predictions and observations need to be as accurate as possible.

The thesis is organised as follows. In chapter 2 we investigate the possibility to actually measure neutrino mass in the sky, along with the intrinsic limitations that this kind of measurement come with. In chapter 3 we characterise one dark matter candidate, Primordial Black Holes, improving constraints on their abundance and novel ways to prove the constitute part of the dark matter sector. In chapter 4 we study novel avenues to extract information on the physics of the very first moments of our Universe using probes characteristic of the late Universe. Each chapter will contain a short introduction to the problem discussed in the papers, to help the reader in connecting the basic picture described in this introduction to state-of-the-art works. Finally, in chapter 5 we summarise the main findings of the different works thesis and we discuss future prospects.

Part I

NEUTRINO PHYSICS

2

NEUTRINO MASS MEASUREMENT

As stated in the Introduction, neutrinos are a component of the Standard Model, despite some of their properties currently unknown. Their existence and interaction with other particles have been studied during decades, however there are better prospect to measure some of neutrino properties in Cosmology than in traditional laboratory experiments.

Neutrino physics in Cosmology is well understood, see, e.g., Ref. [25]. Due to their small mass, were relativistic particle for a large fraction of the expansion of the Universe. They started to free-stream, i.e., they started travelling across the Universe without interacting with other species (with the sole exception of gravitational interaction) since when they decoupled from photons, before Big Bang Nucleosynthesis. The averaged distance covered by neutrinos before becoming non-relativistic particles is called free-streaming length. Since they tend to escape from potential wells because of their large momentum, they contribute in smoothing out gravitational potentials, hence neutrino free-streaming effectively suppress the growth of perturbation on scales smaller than the free-streaming length. Once they become non-relativistic, they behave as standard matter, e.g., as baryons and cold dark matter, falling into potential wells and contributing to the growth of the large scale structures of our Universe.

We can observe this suppression in the growth of perturbations as a damping in the clustering of matter at small scales, below the free-streaming length, with respect to large scales, above free-streaming length. Therefore the same kind of suppression will be present in the clustering of biased tracers of matter distribution, as galaxies. The magnitude of this suppression and the free-streaming length depend on neutrinos mass, hence by measuring this feature we can constraint this unknown parameter of the Standard Model.

However, in Cosmology we are performing a simultaneous measurement of the effects of neutrinos and gravity. Disentangling one from the other represents a challenge, since we have not tested gravity at cosmological scales as well as we have tested it in our Solar System. Even small changes in the strength of gravitational force at cosmological scales might partially hide this feature created by neutrinos and bias the measurement of their mass.

Moreover, many of the models proposed to explain dark energy physics produce change in the gravitational force, hence in the growth of structures, because of the existence of another long-range force acting at large scales. In the following, we focus on Horndeski theory

of gravity [26, 27], the most general scalar-tensor theory with one extra scalar field (playing the role of dark energy and mediating the extra long-range force) that have second order equations of motions on any background and that satisfy the weak equivalence principle. Horndeski theory includes many popular models of modified gravity, as quintessence [28, 29], $f(R)$ theories [30] and galileons [31], along with many others, therefore it provides a general framework that can be applied to a variety of theoretical models.

In this theory, the action for gravity and the scalar field ϕ reads as

$$S = \int d^4x\sqrt{-g}\Big[\mathcal{L}_2(\phi, X) + \mathcal{L}_3(\phi, X) + \mathcal{L}_4(\phi, X) + \mathcal{L}_5(\phi, X)\Big], \quad (2.1)$$

where the four Lagrangian densities $\mathcal{L}_{j=2,\cdots,5}$ are functions of the scalar field ϕ and its canonical kinetic term $2X = -D^\mu\phi D_\mu\phi$ and are given by

$$\begin{aligned}
\mathcal{L}_2 &= K(\phi, X), \\
\mathcal{L}_3 &= -G_3(\phi, X)\Box\phi, \\
\mathcal{L}_4 &= G_4(\phi, X)R + \frac{\partial G_4}{\partial X}\left[(\Box\phi)^2 - \left(D_\mu D_\nu\phi\right)\left(D^\mu D^\nu\phi\right)\right], \\
\mathcal{L}_5 &= G_5(\phi, X)G_{\mu\nu}D^\mu D^\nu\phi - \frac{1}{6}\frac{\partial G_5}{\partial X}\times \\
&\quad\times\left[(\Box\phi)^3 + 2\left(D_\mu D^\nu\phi\right)\left(D_\nu D^\rho\phi\right)\left(D_\rho D^\mu\phi\right) - 3\left(D_\mu D_\nu\phi\right)\left(D^\mu D^\nu\phi\right)\Box\phi\right],
\end{aligned} \quad (2.2)$$

where $\Box$ is the covariant d'Alembertian operator and $\{K, G_3, G_4, G_5\}$ are four arbitrary functions. These functions represent the freedom of Horndeski theory of gravity, i.e., different scalar-tensor theories of gravity are characterised by a different choice of this set of free functions, in particular General Relativity is recover for $K = G_3 = G_5 \equiv 0$ and $G_4 = 1/2$.

In the following I present the paper I have written, "Hiding neutrino masses in modified gravity cosmologies" [32], in which I discuss the potential degeneracy between neutrino and Horndeski gravity effects.

Journal of Cosmology and Astroparticle Physics
An IOP and SISSA journal

Hiding neutrino mass in modified gravity cosmologies

Nicola Bellomo,[a,b] **Emilio Bellini,**[a,c] **Bin Hu,**[a,d] **Raul Jimenez,**[a,e] **Carlos Pena-Garay**[f,g] **and Licia Verde**[a,e]

[a]ICC, University of Barcelona (UB-IEEC),
Marti i Franques 1, 08028, Barcelona, Spain
[b]Departament de Fisica Quantica i Astrofisica, Universitat de Barcelona,
Marti i Franques 1, E08028 Barcelona, Spain
[c]University of Oxford,
Denys Wilkinson Building, Keble Road, Oxford, OX1 3RH, U.K.
[d]Department of Astronomy, Beijing Normal University,
Beijing, 100875, China
[e]ICREA,
Pg. Lluis Companys 23, 08010 Barcelona, Spain
[f]Instituto de Fisica Corpuscular,
CSIC-UVEG, P.O. 22085, Valencia, 46071, Spain
[g]Laboratorio Subterráneo de Canfranc,
Estación de Canfranc, 22880, Spain
E-mail: nicola.bellomo@icc.ub.edu, emilio.bellini@physics.ox.ac.uk,
binhu@icc.ub.edu, raul.jimenez@icc.ub.edu, penya@ific.uv.es,
liciaverde@icc.ub.edu

Received December 9, 2016
Revised February 8, 2017
Accepted February 9, 2017
Published February 23, 2017

Abstract. Cosmological observables show a dependence with the neutrino mass, which is partially degenerate with parameters of extended models of gravity. We study and explore this degeneracy in Horndeski generalized scalar-tensor theories of gravity. Using forecasted cosmic microwave background and galaxy power spectrum datasets, we find that a single parameter in the linear regime of the effective theory dominates the correlation with the total neutrino mass. For any given mass, a particular value of this parameter approximately cancels the power suppression due to the neutrino mass at a given redshift. The extent of the cancellation of this degeneracy depends on the cosmological large-scale structure data used at different redshifts. We constrain the parameters and functions of the effective gravity theory and determine the influence of gravity on the determination of the neutrino mass from present and future surveys.

Keywords: cosmological neutrinos, modified gravity, neutrino astronomy, neutrino masses from cosmology

ArXiv ePrint: 1612.02598

doi:10.1088/1475-7516/2017/02/043

JCAP02(2017)043

Contents

JCAP02(2017)043

1 Introduction

Recent cosmological observations have brought upon us the era of precision cosmology. To challenge the current standard cosmological model seems to require very precise cosmological parameters determinations, as all current available observations are consistent with the simplest ΛCDM model [1]. However, the current model is just a convenient phenomenological description of the Universe as it gives no insight on the nature of the individual energy components like dark matter and dark energy. Most likely before major breakthroughs in our understanding of the Universe come through, precision cosmology should verify yet undetected, small effects, corresponding to standard expectations. Among them, the effect of neutrino masses on large-scale structure is the most promising candidate to verify cosmology at the sub-percent level. Is there any chance for surprise? This has been addressed in a series of works which involve a plethora of modified cosmological models (for a review, see [2, 3]) where some specific piece of the extended model mimics the impact of neutrino masses. Modified gravity models stand as the most promising alternative to the current paradigm (see e.g., [4–6]).

The impact of deviations of Einstein gravity on the determination of neutrino masses has been studied and analysed both in the linear and nonlinear regime [7–9]. Most often, the extended gravity models are specific and simplified scenarios which avoid the exploration of large parameter spaces in time-consuming simulations and/or analysis. The outcome of these studies typically shows a qualitative understanding of the influence of the modified model's parameters in the adopted neutrino mass bound.

In this paper, we make a more general characterization of the influence of modified gravity models on the determination of the neutrino mass. We characterize and analyse fully general massive neutrino scalar-tensor (Horndeski) cosmologies, for the first time, working with the effective theory and observations in the linear regime [10]. The modified gravity models are very generally characterized by a minimal number of given functions, set by a limited number of parameters. The redshift dependence of these functions is driven by searching for the largest impact on the neutrino mass constraints. In this framework, we can address the questions: "where is the degeneracy between neutrino mass and a modified gravity model hidden?" and "how could it be partially resolved?". Moreover, we can quantitatively characterize the knowledge of neutrino mass in the general models under scrutiny. Our results

can be directly applied to theoretically motivated tensor-scalar gravity theories by matching the functions of the effective theory to those used here (see section 2).

2 Models

The idea that DE/MG models could hide the effects of the mass of neutrinos on cosmological scales is intriguing and deserves investigation. However, one has to choose carefully the framework to work with. A simple DE/MG model has not enough freedom to be used both to drive the expansion history and to affect the formation of cosmic structure as massive neutrinos do. The reason is that neutrinos become non-relativistic at typical times ($z \simeq 100$) far before the usual on-set of DE created to drive the late-time cosmic acceleration ($z \simeq 1$). Then, the models we look at should have at least two different time scales, one for the background and one for the perturbations. Our focus is on a broad class of scalar-tensor theories, namely the Horndeski class of models [10–12]. Horndeski is the most general theory with one extra scalar propagating degree of freedom that have second-order equations of motion on any background and that satisfies the weak equivalence principle, i.e. all matter species are coupled minimally and universally to the same metric $g_{\mu\nu}$. This class of models has the freedom to choose four arbitrary functions of two variables, i.e. the extra propagating degree of freedom ϕ and its canonical kinetic term $X = -\phi^{,\mu}\phi_{;\mu}/2$. Any choice of these free functions affects simultaneously both the expansion history and the evolution of the perturbations.

A different approach, still encoding all the freedom of the Horndeski class of models, is the so called Effective Field Theory (EFT) for Dark Energy [13–16]. In [17] it was noticed that all the amount of cosmological information up to linear order in perturbation theory in Horndeski, can be compressed into one function of time driving the expansion history of the universe (the Hubble parameter $H(t)$), plus four functions of time and one constant acting just at the level of the perturbations. The constant can be identified as the fractional density of matter today (Ω_{m0}) and the other functions of time have been dubbed: *kineticity* $\alpha_K(t)$, *braiding* $\alpha_B(t)$, *Planck mass run-rate* $\alpha_M(t)$ or equivalently the *Planck mass* $M_*(t)$, where $\alpha_M \equiv \frac{d\ln M_*^2}{d\ln a}$, and *tensor speed excess* $\alpha_T(t)$. The advantage of using this approach instead of the original Horndeski function is twofold: (i) since all the cosmological information is compressed into a minimal set of functions, it is easier to understand the phenomenology of the models we are studying, and (ii) we can separate the contributions to the background from the contributions to the perturbations. In other words, we can directly modify the evolution of the perturbations keeping the expansion history fixed and compatible with data.

The price one has to pay for using this approach is that, since it is not possible with current data (and probably also with future ones) to constrain the α_i functions non-parametrically, any parametrization we choose can not be considered as representative of the full parameter space of the Horndeski theories, but it refers to specific and possibly fine-tuned class of models. In particular, it is not trivial to link this phenomenological description with classes of action-based theories [18]. Nevertheless, our approach is still useful since our purpose is to give a proof of principle that, under particular circumstances, the effects on the observables of the mass of neutrinos can be hidden into the gravity sector.

As stated before, the class of models we should look at, must have two time scales, one related to the on-set of DE at the background level, and one that can mimic the transition of neutrinos from the relativistic regime to the non-relativistic one. Then, we fix the expansion history to be the one predicted by the standard ΛCDM in a flat universe. On the other

JCAP02(2017)043

hand, the α_i functions are parametrized as follow: $\alpha_K(z) = c_K$, $\alpha_B(z) = c_B \times \texttt{mod}(z)$, $\alpha_M(z) = c_M \times \texttt{mod}(z)$ and $\alpha_T(z) = c_T \times \texttt{mod}(z)$, where c_j are constants. The choice of a constant α_K is due to the fact that its effect is subdominant on the growth of structures w.r.t. the other alphas and it is poorly constrained by present data [19] but also the next generation of surveys will not bring its uncertainty down to the level of the other alphas [20]. The function mod(z), is defined ad-hoc to switch on modifications to Einstein gravity at a given redshift $z_{\rm th}$ with a transition given by Δz. Then, a convenient formulation can be

$$\texttt{mod}(z) = \frac{1 + \tanh\left(\frac{z_{\rm th} - z}{\Delta z}\right)}{1 + \tanh\left(\frac{z_{\rm th}}{\Delta z}\right)}. \tag{2.1}$$

For our purposes, we choose $z_{\rm th}$ close to the redshift of neutrinos becoming non-relativistic and Δz comparable to $z_{\rm th}$ (see other scenarios in [21]).

In addition, Horndeski theories introduce a new scale dependence, the braiding scale k_B, that can be useful to separate the effects on small and on large scales. Indeed, k_B signals the transition between two different gravity regimes, imprinting a characteristic scale-dependence in the Power Spectrum. In a ΛCDM background, it reads

$$\frac{k_B^2}{a^2 H^2} = \frac{9}{2}\Omega_m + 2\left(\frac{3}{2} + \frac{\alpha_K}{\alpha_B^2}\right)(\alpha_M - \alpha_T)\,. \tag{2.2}$$

While the braiding scale is related to the scale where the shape-dependent modification of the growth manifests itself, in the ΛCDM model this scale is undefined. For this reason we cannot report a k_B value or limit where one univocally recovers the standard gravity regime.

3 Mock data and Likelihoods

We analyse our modified gravity models against the CMB temperature, E-mode polarization and deflection angle power spectra, as well as their cross correlation, simulated with the fiducial cosmological model using *Planck* results [22] and *Planck* blue book beam and noise specifications [23]. We use the cosmological parameters listed in table 1 along with the CAMB code [24] to produce the fiducial CMB temperature and E-mode polarization power spectra. We feed these to the FuturCMB package [25] to compute the noise power spectra for T, E-modes and the lensing deflection angle based on the Hu-Okamoto [26] quadratic estimator. For further details about the FuturCMB code we refer the reader to [25] while for the construction of the spectrum likelihood we refer to [25, 27].

We also consider an Euclid-like survey [28], with 14 redshift bin in the range $[0.7, 2.0]$ and scales in the range $[0.001, 0.12]$ Mpc^{-1} (or $k < 0.2h$/Mpc), in order to stay within the linear regime at every redshift. The number of galaxies per square degree is given by the Euclid 2016 settings, as well as the observed fraction of the sky. Our basic likelihood was constructed following [29] and includes a scale independent bias, a Kaiser term for redshift space distortions and errors in determining galaxies line of sight positions, which contains spectroscopic/photometric errors and Fingers of God effects. This basic setting will be indicated as *P(k)* dataset. We have then extended it to the *Full P(k)* dataset, where we added information due to geometrical distortions (i.e. BAO and Alcock-Paczynski) related to different expansion histories. In both cases we can choose to include just an observational error $\sigma_{\rm obs}$, given by shot noise and cosmic variance, or also a theoretical error $\sigma_{\rm the}$, as explained in appendix A of [29], which should account for all possible effects not considered

JCAP02(2017)043

	fiducial	MCMC run	MCMC run
Parameter	$\mathtt{GR}_{\rm fid}$+M0	$\mathtt{MG}_1$+M500	$\mathtt{MG}_2$+M500
$100\omega_b$	2.218	[2.23,2.28]	[2.26,2.30]
$\omega_{\rm cdm}$	0.1205	[0.113,0.115]	[0.112,0.114]
h	0.6693	[0.650,0.659]	[0.656,0.665]
$10^9 A_s$	2.124	[2.08,2.15]	[2.52,2.63]
n_s	0.9619	[0.969,0.979]	[0.965,0.975]
$z_{\rm reio}$	8.24	[7.7,9.3]	[15.3,17.0]
c_K		10	1000
$10^2 c_B$		[3.7,5.7]	[3.7,5.7]
$10^3 c_M$		[3.1,7.9]	[2.8,7.4]
$10^2 c_T$		[-0.8,-0.4]	[-15.5,-10.1]
$z_{\rm th}$		100	100
Δz		20	20

Table 1. Cosmological parameters of the fiducial model and the 95 % CL intervals of the modified gravity model parameters for two particular cases that have different values of c_K. These results were derived by analysing *CMB + Full P(k)*($\sigma_{\rm obs}$) dataset. The apparent detection of a non-zero MG parameter is due to the fact that cosmological parameters alone can not compensate for the presence of significantly heavy neutrinos.

in our likelihood. To calculate cosmological observables in our analysis we have used the `hi_class` [30] public code, an extension of the `CLASS` [31–33] code that allows us to include an additional scalar degree of freedom in the gravitational sector and to model its effects on gravity and matter, while the Monte Carlo Markov Chain (MCMC) forecast has been done with the `MONTEPYTHON` [34] code. Chains were considered converged when the Gelman and Rubin parameter was $R-1<0.01$.

In this work we used the following neutrino models: a) three massless neutrinos (model `M0`), b) three massive neutrinos in the normal ordering with $\sum m_\nu = 150\ meV$ (model `M150`) and c) three quasi-degenerate neutrinos in the normal ordering with $\sum m_\nu = 500\ meV$ (model `M500`). The first and second model were used to create the fiducial mock data, while the third was used along with modified gravity models.

4 Hiding neutrino masses

We have run several MCMC using the *CMB+Full P(k)*($\sigma_{\rm obs}$) dataset (see table 2). The fiducial model was calculated assuming General Relativity plus three massless neutrinos, using fiducial values reported in table 1. This fiducial will be indicated in what follows by $\mathtt{GR}_{\rm fid}$+M0. Every MCMC run was characterised by a different choice of the values of the kineticity function α_K and of the modulation function parameters $(z_{\rm th}, \Delta z)$, which were taken as fixed parameters. We explored the parameter space given by the cosmological and MG parameters $\{\omega_b, \omega_{\rm cdm}, h, A_s, n_s, z_{\rm reio}, c_B, c_M, c_T\}$, assuming a flat prior for each of them. In every run the neutrino mass scheme was given by the M500 model. The results for the particular case $\mathtt{MG}_1$+M500, where $\alpha_K = 10$, $z_{\rm th} = 100$ and $\Delta z = 20$, are shown in table 1.

JCAP02(2017)043

MCMC described in section	Fixed parameters	Varying parameters
Hiding neutrino masses	$c_K, \Sigma m_\nu, z_{\rm th}, \Delta z$	$\omega_b, \omega_{\rm cdm}, h, A_s, n_s, z_{\rm reio}, c_B, c_M, c_T$
Removing degeneracies	$c_K, c_T, z_{\rm th}, \Delta z$	$\omega_b, \omega_{\rm cdm}, h, A_s, n_s, z_{\rm reio}, c_B, c_M, \Sigma m_\nu$

Table 2. List of fixed and varying parameters in MCMC runs described in sections "Hiding neutrino mass" and "Removing degeneracy". We assumed a flat prior for each varying parameter.

Comparing the $\texttt{MG}_1\texttt{+M500}$ model results with the fiducial model, we find a lower value of h, required in order to preserve the acoustic peak scale, as well as a higher value of n_s, as expected since it helps to compensate the neutrino power suppression at small scales. The value of $\omega_{\rm cdm}$ decreases significantly in order to keep the global ω_m similar to the fiducial one, since also neutrinos contribute to the physical matter density with $\omega_\nu = 0.0054$. We found compatibility between cosmological parameters confidence regions for different sets of the modulation function parameters. The main changes between the models due to the choice of $(z_{\rm th}, \Delta z)$ is the allowed range of MG parameters, in particular α_B, since we have checked that it is responsible for the enhanced structure growth at small scales. Any deviation from GR that appears earlier requires a smaller global amplitude, since the modifications of gravity will be at work for a longer period of time; on the other hand, modifications that become significant slowly (or later) will require a bigger overall magnitude. The parameter α_M is highly correlated with α_B because they have opposite effects on the matter power spectrum. Notice that we have imposed stability conditions on the positiveness of the scalar field sound speed which partially induces such correlation.

The potential of modified gravity to hide neutrino mass is shown in figure 1. Using the $\texttt{MG}_1\texttt{+M500}$ result, we plot the relative matter power spectrum (to the $\rm GR_{fid}$) at representative redshift $z = 1.4$ (at other redshift such as 0.5 or 2 the plot is virtually indistinguishable) for three different models: the fiducial model with massive neutrinos ($\texttt{GR}_{\rm fid}\texttt{+M500}$), the modified gravity best fit model with massless neutrinos ($\texttt{MG}_{\rm bf}\texttt{+M0}$) and the modified gravity best fit model with massive neutrinos ($\texttt{MG}_{\rm bf}\texttt{+M500}$). Massive neutrinos imprint a power suppression at small scales in the GR cosmology, while the modified gravity model with massless neutrinos leads to an increased power at small scales. Both effects, massive neutrinos and modified gravity, can be approximately cancelled as shown by the model $\texttt{MG}_{\rm bf}\texttt{+M500}$, where the relative differences are below the error bars. We stress here the generality of this result, which we have verified for several modulation function parameters and redshifts.

Contrary to naive expectations, the value of α_K is not unconstrained. In the *CMB* only analysis, α_K changes the overall width of the MG parameters posteriors, but does not modify cosmological parameters. Once we include the *Full P(k)*$(\sigma_{\rm obs})$ dataset, cosmological parameters posteriors also change. Comparing the $\texttt{MG}_1\texttt{+M500}$ to the $\texttt{MG}_2\texttt{+M500}$ model results reported in table 1, we note that the value of $\alpha_K = 10$ is preferred with respect to higher values, due to a substantial shift in the confidence interval of A_s and, consequentially, of $z_{\rm reio}$.

This shift can be attributed to the interplay between the two relevant scales, the neutrino free-streaming scale at the non-relativistic transition k_{nr} and the MG braiding scale k_B. In order to hide the typical step-like feature in the power spectrum due to massive neutrinos, our MG model should introduce small deviations from GR for scales $k \lesssim k_{nr}$ and a considerable enhancement for $k \gtrsim k_{nr}$. This constraint already introduces a preferred value for the braiding scale k_B, which has to be similar to k_{nr}. In general one could tune the ratio α_K/α_B^2 in order to place the transition between the two gravity regimes at the desired scale, but in this case the amplitude of α_B is already fixed by the neutrino mass, since it is the only

JCAP02(2017)043

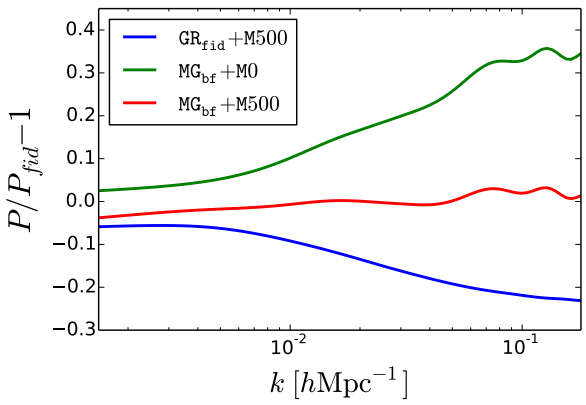

Figure 1. Relative difference in the matter power spectrum of three models with respect to the fiducial model $\mathrm{GR_{fid}}$ at redshift $z = 1.4$. The blue line shows the suppression due to massive neutrinos `M500` model vs `M0`. The green line corresponds to the MCMC best fit cosmological and MG parameters with the `M0` neutrino model, showing the MG enhancement in the matter power spectrum at small scales. The red line represents the MCMC best fit of the MG model with massive neutrinos, which mimics the GR model with massless neutrinos.

parameter that can enhance the power spectrum at large k. Therefore the only possible way to match the two scales is to change the value of α_K. Note however that, *at linear level*, different values of α_K do not change matter power spectrum features but just the range of modes where these features appear. For bigger kineticity values the braiding scale is translated to larger k as well as the desired MG step-like feature, however as soon as $k_B > k_{nr}$ there is a range of scales where we start to observe the neutrino-induced suppression but not the MG-induced enhancement. As a result the fit favours a larger primordial fluctuations amplitude (see right column of table 1).

Given this particular signature due to the kineticity, we have done additional runs where also α_K was allowed to vary (assuming a uniform prior) while keeping fixed the modulation function parameters to $(z_{\rm th}, \Delta z) = (100, 20)$ and the neutrino model to `M500`, finding for the first time constraints on this parameter: α_K is peaked around $\alpha_K^{\rm peak} = 6.5$ and is bounded to be in the interval $[1.9, 20.4]$ at the 95% CL.

Naively this is unexpected, since in the quasi-static (QS) limit — i.e. for modes such that $k/k_{c_s} \gg 1$, where $k_{c_s} = \frac{aH}{c_s}$ is the dark-energy sound horizon [35] — the kineticity α_K disappears from the perturbed equations. However, an Euclid-like survey will probe considerably large scales where the QS approximation may not hold. In fact,

$$\frac{k}{k_{c_s}} \geq \frac{k_{\rm survey,min}}{k_{c_s}(z=2)} \sim 0.3, \tag{4.1}$$

indicating that the QS limit condition is not fulfilled for every mode and redshift.

5 Removing degeneracies

In order to explore the degeneracy between modified gravity parameters and neutrino mass, we performed additional MCMC runs with different datasets and two different fiducial models (see table 2). We used the `GR+M0` fiducial described in the previous section and a new

JCAP02(2017)043

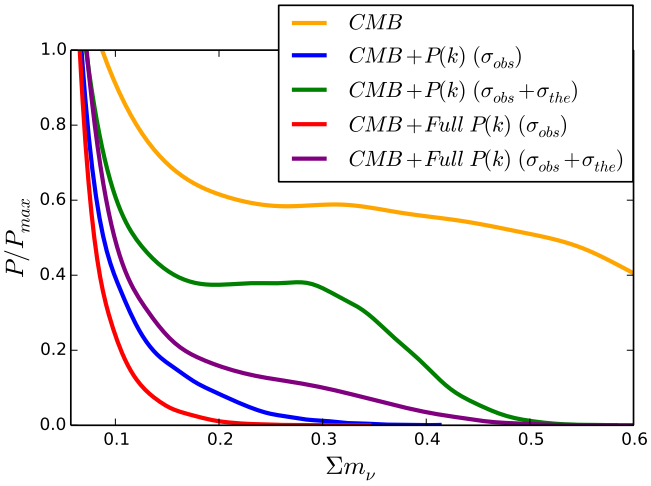

Figure 2. Neutrino mass posterior (relative to its maximum) of modified gravity models for several datasets. The posterior wide tail of the *CMB* dataset is considerably damped when power spectrum data is added. Significantly, heavy neutrinos, considered in the previous section, are highly disfavoured once we include information coming from the expansion history.

fiducial model: `GR+M150`; this has the same cosmological parameters of `GR+M0` but it includes the `M150` neutrino mass model. In both cases we fixed the values of $(c_K, c_T, z_{\rm th}, \Delta z)$ to $(10, 0, 100, 50)$, choosing this value for the tensor speed excess because its impact on the growth of structures is negligible. In each chain the varying parameters were the six standard cosmological parameters, the coefficients of the braiding and the Planck mass run-rate (c_B and c_M) and the neutrino mass Σm_ν, under the simplifying assumptions of normal mass ordering. For each varying parameter we assumed uniform priors.

We show the posterior distributions in figure 2 for different datasets. The broad tail in the *CMB* posterior indicates that this dataset alone is not able to tightly constrain neutrino mass, allowing neutrinos to be quite massive ($\sum m_\nu \lesssim 0.761\ eV$ at 95% CL). We also considered power spectra datasets, where we implemented different combinations of observational error $\sigma_{\rm obs}$, theoretical error $\sigma_{\rm the}$ and effects coming from changes in the expansion history. Neutrino mass constraints come mainly from the small scales, where few percent observational errors lead to tight constraints. On the other hand, non-linear effects and modelling systematics both in neutrinos and modified gravity physics appear precisely at these scales, so even a theoretical error rough estimate, as adopted here, can show how our constraints weaken. Comparing curves with and without the theoretical error we can see that, if we don't take into account effects coming from different expansion histories (*CMB+P(k) ($\sigma_{\rm obs}+\sigma_{\rm the}$)* dataset), inaccurate modelling at small scales could really modify the high mass tail of the distribution ($\sum m_\nu \lesssim 0.400\ eV$ at 95% CL). The expansion history information enclosed in *Full P(k)* is able to play a significant role in constraining neutrino mass (compare *CMB+Full P(k)* to *CMB+P(k)*), but these constraints could weaken by changing the Hubble expansion rate $H(z)$ or the angular diameter distance $D_A(z)$ through a suitable choice of equation of state parameter for dark energy, away from the cosmological constant value, $w_\phi(z) \neq -1$.

In the case of the `M0` fiducial model, considering the most constraining dataset, MG can hide neutrino masses up to 160 meV at 95% CL. On the contrary, a large neutrino mass

JCAP02(2017)043

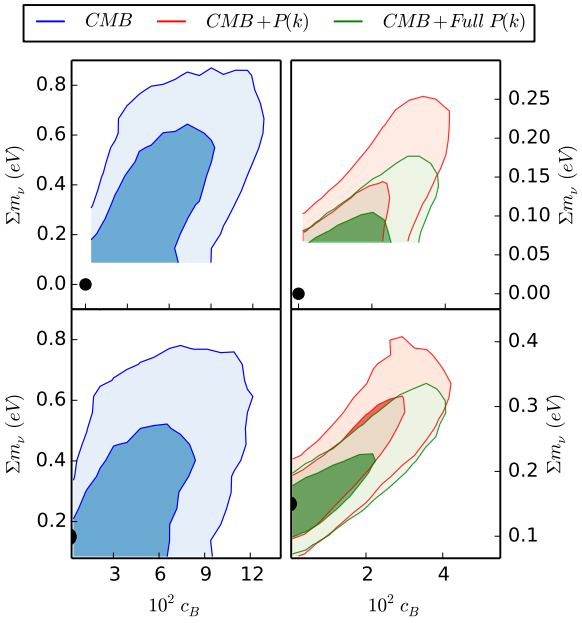

Figure 3. Correlation between c_B and Σm_ν assuming a fiducial model `GR+M0` (upper panels) or `GR+M150` (lower panels). Fiducials are represented as black dots. Contours are shown for the 68% and 95% CL when considering *CMB* (left panels), *CMB+P(k)* and *CMB+Full P(k)* (right panels) datasets. In the latter case we have plotted the case with only observational errors, which is the most constraining case. Cuts in the correlations appear as a result of our assumptions: in our model c_B cannot be negative without triggering instabilities and Σm_ν cannot be less than $\simeq 0.06\,\mathrm{eV}$ since we imposed that neutrinos obey the normal ordering mass scheme.

compatible with present bounds (`M150` fiducial model) can not be hidden by MG as shown in figure 3, where the analysis with the largest dataset finds a minimum mass of 100 meV at 95% CL.

Our results show that the neutrino mass is degenerate with the c_B parameter, as illustrated in figure 3 for the two fiducial models `GR+M0` and `GR+M150`. c_B is the only parameter (at the linear level) in our models that can hide the suppression induced in the power spectrum by massive neutrinos. We can draw this conclusion also by looking at the *CMB* MCMC result, since we included in the dataset also the power spectrum of the weak lensing CMB deflection angle, which in turns depends on the gravitational potentials along the line of sight. Adding power spectrum observations also shows the $c_B - \sum m_\nu$ correlation, with a neutrino mass range partially limited.

6 Conclusions

In this work, we have explored the nature of the degeneracy between neutrino masses and modified gravity. We focussed on widely applicable results by using the Horndeski generalized scalar-tensor theories of gravity. These generic models contain, in the linear regime, few redshift dependent functions that here are tuned to maximize the impact on the neutrino mass determination. We have studied the parameter space of the number of modified gravity

JCAP02(2017)043

parameters (6) in the model for several neutrino mass schemes and considered mock state-of-the-art CMB data sets and forthcoming galaxy redshift surveys. Among other minor contributions, one parameter describing one of the four Hordenski functions is the dominant source of degeneracy with neutrino masses. Not unexpectedly this is the braiding, which physically arises from a mixing between the kinetic terms of the metric and the scalar and it modifies the growth of perturbations boosting small scale power.

We have shown the cancellation of the impact of the neutrino mass with a modified gravity model in the power spectrum in the linear regime. This cancellation is very efficient at a particular redshift; combinations of several redshifts may lift the degeneracy and we have explored the potential of future datasets in doing so. We find that future data such as those provided by an Euclid-like survey would limit, but not fully cancel, the degeneracy of neutrino mass with one of the Hordenski parameters, c_B. Here we have only considered galaxy redshift surveys as large-scale structure probes. Of course the weak gravitational lensing signal could further help, but consideration of this probe is left to future work.

Acknowledgments

NB is supported by the Spanish MINECO under grant BES-2015-073372. BH is partially supported by a Beatriu de Pinos grant and the Chinese National Youth Thousand Talents Program. We acknowledge support by Spanish Mineco grants AYA2014-58747-P, FPA2014-57816-P, GVA grant PROMETEOII/2014/050, MDM-2014-0369 of ICCUB (Unidad de Excelencia Maria de Maeztu) and EU projects H2020-MSCA-ITN-2015//674896-ELUSIVES and H2020-MSCA-RISE-2015.

References

[1] Planck collaboration, P.A.R. Ade et al., *Planck 2015 results. XIII. Cosmological parameters*, *Astron. Astrophys.* **594** (2016) A13 [arXiv:1502.01589] [INSPIRE].

[2] Planck collaboration, P.A.R. Ade et al., *Planck 2015 results. XIV. Dark energy and modified gravity*, *Astron. Astrophys.* **594** (2016) A14 [arXiv:1502.01590] [INSPIRE].

[3] T. Clifton, P.G. Ferreira, A. Padilla and C. Skordis, *Modified Gravity and Cosmology*, *Phys. Rept.* **513** (2012) 1 [arXiv:1106.2476] [INSPIRE].

[4] J.R. Kristiansen, G. La Vacca, L.P.L. Colombo, R. Mainini and S.A. Bonometto, *Coupling between cold dark matter and dark energy from neutrino mass experiments*, *New Astron.* **15** (2010) 609 [arXiv:0902.2737] [INSPIRE].

[5] G. La Vacca, J.R. Kristiansen, L.P.L. Colombo, R. Mainini and S.A. Bonometto, *Do WMAP data favor neutrino mass and a coupling between Cold Dark Matter and Dark Energy?*, *JCAP* **04** (2009) 007 [arXiv:0902.2711] [INSPIRE].

[6] G. La Vacca and J.R. Kristiansen, *Dynamical Dark Energy model parameters with or without massive neutrinos*, *JCAP* **07** (2009) 036 [arXiv:0906.4501] [INSPIRE].

[7] M. Baldi, F. Villaescusa-Navarro, M. Viel, E. Puchwein, V. Springel and L. Moscardini, *Cosmic degeneracies — I. Joint N-body simulations of modified gravity and massive neutrinos*, *Mon. Not. Roy. Astron. Soc.* **440** (2014) 75 [arXiv:1311.2588] [INSPIRE].

[8] A. Barreira, B. Li, C. Baugh and S. Pascoli, *Modified gravity with massive neutrinos as a testable alternative cosmological model*, *Phys. Rev.* **D 90** (2014) 023528 [arXiv:1404.1365] [INSPIRE].

JCAP02(2017)043

[9] J. Shim, J. Lee and M. Baldi, *Breaking the Cosmic Degeneracy between Modified Gravity and Massive Neutrinos with the Cosmic Web*, arXiv:1404.3639 [INSPIRE].

[10] G.W. Horndeski, *Second-order scalar-tensor field equations in a four-dimensional space*, *Int. J. Theor. Phys.* **10** (1974) 363 [INSPIRE].

[11] C. Deffayet, S. Deser and G. Esposito-Farese, *Generalized Galileons: All scalar models whose curved background extensions maintain second-order field equations and stress-tensors*, *Phys. Rev.* **D 80** (2009) 064015 [arXiv:0906.1967] [INSPIRE].

[12] T. Kobayashi, M. Yamaguchi and J. Yokoyama, *Generalized G-inflation: Inflation with the most general second-order field equations*, *Prog. Theor. Phys.* **126** (2011) 511 [arXiv:1105.5723] [INSPIRE].

[13] G. Gubitosi, F. Piazza and F. Vernizzi, *The Effective Field Theory of Dark Energy*, *JCAP* **02** (2013) 032 [arXiv:1210.0201] [INSPIRE].

[14] J.K. Bloomfield, E.E. Flanagan, M. Park and S. Watson, *Dark energy or modified gravity? An effective field theory approach*, *JCAP* **08** (2013) 010 [arXiv:1211.7054] [INSPIRE].

[15] J. Gleyzes, D. Langlois, F. Piazza and F. Vernizzi, *Essential Building Blocks of Dark Energy*, *JCAP* **08** (2013) 025 [arXiv:1304.4840] [INSPIRE].

[16] B. Hu, M. Raveri, N. Frusciante and A. Silvestri, *Effective Field Theory of Cosmic Acceleration: an implementation in CAMB*, *Phys. Rev.* **D 89** (2014) 103530 [arXiv:1312.5742] [INSPIRE].

[17] E. Bellini and I. Sawicki, *Maximal freedom at minimum cost: linear large-scale structure in general modifications of gravity*, *JCAP* **07** (2014) 050 [arXiv:1404.3713] [INSPIRE].

[18] E.V. Linder, G. Sengör and S. Watson, *Is the Effective Field Theory of Dark Energy Effective?*, *JCAP* **05** (2016) 053 [arXiv:1512.06180] [INSPIRE].

[19] E. Bellini, A.J. Cuesta, R. Jimenez and L. Verde, *Constraints on deviations from ΛCDM within Horndeski gravity*, *JCAP* **02** (2016) 053 [arXiv:1509.07816] [INSPIRE].

[20] D. Alonso, E. Bellini, P.G. Ferreira and M. Zumalacarregui, *The Observational Future of Cosmological Scalar-Tensor Theories*, arXiv:1610.09290 [INSPIRE].

[21] L. Perenon, C. Marinoni and F. Piazza, *Diagnostic of Horndeski Theories*, *JCAP* **01** (2017) 035 [arXiv:1609.09197] [INSPIRE].

[22] PLANCK collaboration, N. Aghanim et al., *Planck intermediate results. XLVI. Reduction of large-scale systematic effects in HFI polarization maps and estimation of the reionization optical depth*, *Astron. Astrophys.* **596** (2016) A107 [arXiv:1605.02985] [INSPIRE].

[23] PLANCK collaboration, J. Tauber et al., *The Scientific programme of Planck*, astro-ph/0604069 [INSPIRE].

[24] A. Lewis, A. Challinor and A. Lasenby, *Efficient computation of CMB anisotropies in closed FRW models*, *Astrophys. J.* **538** (2000) 473 [astro-ph/9911177] [INSPIRE].

[25] L. Perotto, J. Lesgourgues, S. Hannestad, H. Tu and Y.Y.Y. Wong, *Probing cosmological parameters with the CMB: Forecasts from full Monte Carlo simulations*, *JCAP* **10** (2006) 013 [astro-ph/0606227] [INSPIRE].

[26] T. Okamoto and W. Hu, *CMB lensing reconstruction on the full sky*, *Phys. Rev.* **D 67** (2003) 083002 [astro-ph/0301031] [INSPIRE].

[27] A. Lewis, *Lensed CMB simulation and parameter estimation*, *Phys. Rev.* **D 71** (2005) 083008 [astro-ph/0502469] [INSPIRE].

[28] EUCLID THEORY WORKING GROUP collaboration, L. Amendola et al., *Cosmology and fundamental physics with the Euclid satellite*, *Living Rev. Rel.* **16** (2013) 6 [arXiv:1206.1225] [INSPIRE].

JCAP02(2017)043

[29] B. Audren, J. Lesgourgues, S. Bird, M.G. Haehnelt and M. Viel, *Neutrino masses and cosmological parameters from a Euclid-like survey: Markov Chain Monte Carlo forecasts including theoretical errors*, *JCAP* **01** (2013) 026 [arXiv:1210.2194] [INSPIRE].

[30] M. Zumalacárregui, E. Bellini, I. Sawicki and J. Lesgourgues, *hi_class: Horndeski in the Cosmic Linear Anisotropy Solving System*, arXiv:1605.06102 [INSPIRE].

[31] J. Lesgourgues, *The Cosmic Linear Anisotropy Solving System (CLASS) I: Overview*, arXiv:1104.2932 [INSPIRE].

[32] D. Blas, J. Lesgourgues and T. Tram, *The Cosmic Linear Anisotropy Solving System (CLASS) II: Approximation schemes*, *JCAP* **07** (2011) 034 [arXiv:1104.2933] [INSPIRE].

[33] J. Lesgourgues and T. Tram, *The Cosmic Linear Anisotropy Solving System (CLASS) IV: efficient implementation of non-cold relics*, *JCAP* **09** (2011) 032 [arXiv:1104.2935] [INSPIRE].

[34] B. Audren, J. Lesgourgues, K. Benabed and S. Prunet, *Conservative Constraints on Early Cosmology: an illustration of the Monte Python cosmological parameter inference code*, *JCAP* **02** (2013) 001 [arXiv:1210.7183] [INSPIRE].

[35] I. Sawicki and E. Bellini, *Limits of quasistatic approximation in modified-gravity cosmologies*, *Phys. Rev.* **D 92** (2015) 084061 [arXiv:1503.06831] [INSPIRE].

JCAP02(2017)043

Part II

PRIMORDIAL BLACK HOLES

3

PRIMORDIAL BLACK HOLES AS DARK MATTER

What the nature of dark matter is remains very hard to assess, despite decades of direct, indirect and colliders experiments, see e.g., Refs. [33, 34] and references therein.

Even if dark matter can be composed by Beyond Standard Model particles, which we might need to solve some of Standard Model puzzles, other dark matter candidates are still allowed by current data. During the past years one of them, Primordial Black Holes (PBHs), started to attract more attention, thanks to the detection of gravitational waves coming from mergers of black hole binaries. In fact the properties of the ten confirmed events of the first two runs [35] showed some unexpected properties, namely large masses of the progenitors and low effective spin of the binary. While these properties can potentially being explained by stellar models, they also fit quite well some of the predictions for PBHs.

PBHs are black hole that formed deep in the radiation-dominated era. They differ from astrophysical black holes, i.e., those created at the end of stellar evolution, because PBHs mass can span a huge range, from $M_{\rm PBH} \simeq 10^{-38}\ M_\odot$ if they formed at time $t_f \simeq 10^{-43}$ s to $M_{\rm PBH} \simeq 10^{5}\ M_\odot$ if born at time $t_f \simeq 1$ s. Moreover, in some formation scenario as the collapse of a large overdensity, they are naturally expected to have small spin [36–38].

In this chapter I present two works, "Primordial black holes as dark matter: converting constraints from monochromatic to extended mass distributions" [39] and "GW×LSS: chasing the progenitors of merging binary black holes" [40], which discuss two crucial problems: defining which is the correct present-day maximum fraction of dark matter made of PBHs and confirming whether detected black holes have a primordial or astrophysical origin. Addressing these issues is a key step in defining if PBHs constitute the majority, or at least a part, of dark matter.

The phenomenology of PBHs is very rich, in part due to the extended range of masses they can have (in contrast to black holes generated as end-point of stellar evolution), but also because they are extended compact objects generating a strong gravitational field and not just particles. Establishing the present-day abundance of PBHs represents a delicate issue, which has sometimes been overlooked: in most of the cases, current constraints are computed assuming a monochromatic mass distribution, i.e., that all the black holes have the same mass. This assumption is not realistic, in fact there are several known processes that change the black hole mass distribution,

as accretion in environments with different baryon density or black holes mergers. Therefore we need a consistent, yet fast, way to generalise these monochromatic constraints to the case of extended mass distributions without involving long analysis, in order to quickly explore the parameter space of possible PBHs mass distributions. At the same time, we must keep under control whether all the assumptions made in obtaining the constraint are still valid, at least to preserve the robustness of the constraint under analysis.

After having determined the maximum fraction of dark matter that can be made up of PBHs, we need to identify which black hole detected by the LIGO/Virgo Collaboration, or by future gravitational waves observatories as Einstein Telescope, has a primordial origin. In fact the existing gravitational wave observatory network (which soon will include also KAGRA and LIGO India) has the potential to discover compact objects whose mass ranges from subsolar masses to hundreds of solar masses. Any black hole with subsolar mass can form only in radiation-domination, however for larger masses both channels are possible. Therefore finding different avenues to infer the origin of detected black holes is crucial, since any eventual confirmation that PBHs exist must be supported by multiple evidence.

Journal of Cosmology and Astroparticle Physics
An IOP and SISSA journal

Primordial black holes as dark matter: converting constraints from monochromatic to extended mass distributions

Nicola Bellomo,[a,b] **José Luis Bernal,**[a,b] **Alvise Raccanelli**[a] **and Licia Verde**[a,c]

[a]ICC, University of Barcelona, IEEC-UB,
Martí i Franquès, 1, E08028 Barcelona, Spain
[b]Dept. de Física Quàntica i Astrofísica, Universitat de Barcelona,
Martí i Franquès 1, E08028 Barcelona, Spain
[c]ICREA, Pg. Lluís Companys 23, 08010 Barcelona, Spain

E-mail: nicola.bellomo@icc.ub.edu, joseluis.bernal@icc.ub.edu, alvise@icc.ub.edu, liciaverde@icc.ub.edu

Received September 28, 2017
Accepted November 23, 2017
Published January 8, 2018

Abstract. The model in which Primordial Black Holes (PBHs) constitute a non-negligible fraction of the dark matter has (re)gained popularity after the first detections of binary black hole mergers. Most of the observational constraints to date have been derived assuming a single mass for all the PBHs, although some more recent works tried to generalize constraints to the case of extended mass functions. Here we derive a general methodology to obtain constraints for any PBH Extended Mass Distribution (EMD) and any observables in the desired mass range. Starting from those obtained for a monochromatic distribution, we convert them into constraints for EMDs by using an equivalent, effective mass $M_{\rm eq}$ that depends on the specific observable. We highlight how limits of validity of the PBH modelling affect the EMD parameter space. Finally, we present converted constraints on the total abundance of PBH from microlensing, stellar distribution in ultra-faint dwarf galaxies and CMB accretion for Lognormal and Power Law mass distributions, finding that EMD constraints are generally stronger than monochromatic ones.

Keywords: primordial black holes, dark matter theory

ArXiv ePrint: 1709.07467

 https://doi.org/10.1088/1475-7516/2018/01/004

JCAP01(2018)004

Contents

1 Introduction

The ΛCDM model has become the cosmological standard model thanks to its ability to provide a good description to a wide range of observations, see e.g., [1]. However, it remains a phenomenological model with no fundamental explanations on the nature of some of its key ingredients, e.g., of dark matter, see e.g., [2]. Several possible dark matter candidates have been proposed, ranging from yet undetected exotic particles like WIMPs [3] or axions [4], to compact objects such as black holes [5], including the ones possibly forming at early times, therefore called Primordial Black Holes (PBHs).

Since so far none of the numerous undergoing direct dark matter detection experiments has given positive results (neither for WIMPs [6] nor for axions [7]), PBHs have started to (re)gain interest after the first gravitational waves detection by the LIGO collaboration [8]. Those gravitational waves were generated by a merger of two black holes with masses around $30M_\odot$. Given the large mass of the progenitors, some authors [9, 10] have proposed that it could be the first detection of PBHs, whose merger rate is indeed compatible with LIGO observations. Since PBHs were first proposed as a candidate for dark matter, there have been considerable efforts from both theoretical and observational sides to constrain such theory. PBHs might produce a large variety of different effects because the theoretically allowed mass range spans many order of magnitude. As a consequence, the set of constraints coming from a variety of observables is broad too. Starting from the lower allowed mass, constraints come from γ-rays derived from black holes evaporation [11], quantum gravity [12], γ-rays femtolensing [13], white-dwarf explosions [14], neutron-star capture [15], microlensing of stars [16–20] and quasars [21], stellar distribution in ultra-faint dwarf galaxies [22], X-ray and radio emission [23], wide-binaries disruption [24], dynamical friction [25], quasars millilensing [26], large-scale structure [27] and accretion effects [28–31]; given the strong interest in the model, there have been recently suggestions for obtaining constraints from e.g. the cross-correlation of gravitational waves with galaxy maps [32, 33], eccentricity of the binary orbits [34], fast radio bursts lensing [35], the black hole mass function [36, 37] and merger rates [38].

These constraints have been obtained (mostly) for a PBH population with a Monochromatic Mass Distribution (MMD). This distribution has been always considered as stationary,

JCAP01(2018)004

even if during its life any black hole changes its mass due to different processes, such as Hawking evaporation [39], gravitational waves emission, accretion [29] and mergers events [9]. The magnitude of such effects has been analysed recently. In ref. [40] the authors investigate the importance of evaporation and Bondi accretion during the whole Universe history. They found that PBHs with mass $10^{-17} M_\odot \lesssim M \lesssim 10^2 M_\odot$ neither accrete or evaporate significantly in a Hubble time (unless they are in a baryon-rich environment). On the other hand, the mass lost in gravitational waves emission due to mergers has to be small, since the fraction of dark matter converted into radiation after recombination cannot exceed the 1%[1] [41]. This finding rejects the possibility of an intense merging period at $z \leq 1000$. Although these effects are small compared to current experimental precision and theoretical uncertainties in the modelling of the processes involving PBHs, a comprehensive treatment must eventually include a description of their evolution.

More importantly, a large variety of formation mechanisms directly produce Extended Mass Distributions (EMDs) for PBHs. Such mechanisms generate PBHs as the result of, among other precesses, collapse of large primordial inhomogeneities [42] arising from quantum fluctuations produced by inflation [43], spectator fields [44] or phase transitions, like bubble collisions [45] or collapse of cosmic string [46], necklaces [47] and domain walls [48].

As pointed out in ref. [49], no EMD can be directly compared to MMD constraints. Since re-computing the constraints for any specific EMD can be time-consuming, at least two different techniques [49, 50] have been proposed so far to infer EMDs constraints from the well-known MMD ones. In this paper we propose a new and improved way to compare EMDs to MMD constraints, directly based on the physical processes when PBHs with different masses are involved.

The paper is organized as follows. In section 2 we present our method to convert between monochromatic constraints and EMD ones and compare it with existing ones. In section 3 first we introduce the EMDs we will analyse, then we provide some practical examples of how our technique works for three different observables, namely microlensing 3.1, ultra-faint dwarf galaxies 3.2 and the cosmic microwave background 3.3. In section 4 we derive constraints for EMDs and discuss the validity of the limits found in previous sections. Finally, we conclude in section 5.

2 Equivalent monochromatic mass distribution

Most of the constraints derived in previous works have been obtained under the simplifying assumption that PBHs have a MMD, despite the fact that such distribution is unrealistic from a physical point of view. Since EMDs have more robust theoretical motivations, it is extremely important to derive accurate constraints for EMDs in order to establish if PBHs could be a valid candidate for (at least a large fraction of) dark matter.

As pointed out for the first time in ref. [49] and then in ref. [51], it is not straightforward to interpret MMD constraints in terms of EMD. It is therefore important to derive constraints precisely using directly the chosen EMD or to provide an approximated technique to convert between MMD and EMD constraints, as done in [49, 50]. Advantages and shortcomings of the presently available methods to convert between MMD and EMD constraints have been discussed in ref. [51]; in short they may bias (i.e., overestimate or underestimate depending on the EMD) the inferred constraints.

[1] A single merger event may surpass this limit, for example the LIGO event GW150914 has been estimated to have converted about 5% of the mass in GW. Here however what matters is the overall integrated conversion.

JCAP01(2018)004

As it is customary, hereafter $f_{\rm PBH}$ denotes the fraction of dark matter in primordial black holes, $f_{\rm PBH} = \frac{\Omega_{\rm PBH}}{\Omega_{\rm dm}}$. The fundamental quantity in our approach is the PBHs differential fractional abundance

$$\frac{df_{\rm PBH}}{dM} \equiv f_{\rm PBH} \frac{d\Phi_{\rm PBH}}{dM}, \tag{2.1}$$

defined in such a way that $f_{\rm PBH}$ represents the normalisation and the distribution $\frac{d\Phi_{\rm PBH}}{dM}$ describes the *shape* (i.e., the mass dependence) of the EMD and it is normalized to unity. By definition this function is related to the differential PBH energy density or, equivalently, to the differential PBH number density by

$$\frac{d\rho_{\rm PBH}}{dM} = \frac{dn_{\rm PBH}}{d\log M} = f_{\rm PBH}\rho_{\rm dm}\frac{d\Phi_{\rm PBH}}{dM}, \tag{2.2}$$

since PBHs are a dynamically cold form of matter. Each EMD is specified by a different number of parameters $\{\zeta_j\}$ that define its shape and the mass range $[M_{\rm min}, M_{\rm max}]$ where the distribution is defined. Known theoretically-motivated models provide a variety of EMDs; in what follows we consider two popular EMDs families, namely the *Power Law* (*PL*) and the *Lognormal* (*LN*) ones, which we will describe in section 3 (for other examples of EMD, see e.g., ref. [52]).

We start from the same consideration done in ref. [50], where it was noticed that PBHs with different masses contributes independently to the most commonly considered observables. In order to account for a PBHs EMD, when calculating PBHs effects on astrophysical observables we have to perform an integral of the form

$$\int dM \frac{df_{\rm PBH}}{dM} g(M, \{p_j\}), \tag{2.3}$$

where $g(M, \{p_j\})$ is a function which encloses the details of the underlying physics and depends on the PBH mass, M, and a set of astrophysical parameters, $\{p_j\}$. Therefore, $g(M, \{p_j\})$ is different for each observable (some example of these functions are provided in section 3). Because of this integral over the mass distribution, there is an implicit degeneracy between different EMDs, which means that two distributions (indicated below by the subscripts 1 and 2) such that

$$f_{\rm PBH,1}\int dM \frac{d\Phi_1}{dM} g(M, \{p_j\}) = f_{\rm PBH,2}\int dM \frac{d\Phi_2}{dM} g(M, \{p_j\}) \tag{2.4}$$

will be observationally indistinguishable. As the constraints for MMDs have already been computed in the literature, we set one of the two distributions in equation 2.4 to be a MMD and the other to be an arbitrary EMD i.e., $\frac{df_{\rm PBH,1}}{dM} = f_{\rm PBH}^{\rm MMD}\delta(M - M_{\rm eq})$ and $\frac{df_{\rm PBH,2}}{dM} = f_{\rm PBH}^{\rm EMD}\frac{d\Phi_{\rm EMD}}{dM}$, so that we can easily rewrite equation 2.4 as

$$f_{\rm PBH}^{\rm MMD} g(M_{\rm eq}, \{p_j\}) = f_{\rm PBH}^{\rm EMD}\int dM \frac{d\Phi_{\rm EMD}}{dM} g(M, \{p_j\}), \tag{2.5}$$

where $M_{\rm eq}$ will be called *Equivalent Mass* (EM). The equivalent mass is, by definition, the effective mass associated with a monochromatic PBHs population such that the observable effects produced by the latter are equivalent to the ones produced by the EMD under consideration.

Constraints for EMDs can be extracted from the previous equation through the following procedure.

JCAP01(2018)004

(A) Fix the ratio $r_f = f_{\rm PBH}^{\rm EMD}/f_{\rm PBH}^{\rm MMD}$ to a specific value. Here, since we want to reinterpret $f_{\rm PBH}^{\rm MMD}$ as a $f_{\rm PBH}^{\rm EMD}$ and solve for $M_{\rm eq}$ we set $r_f = 1$, that is we assume that PBHs total abundance in both scenarios is the same. In principle and for other applications one may want to work with other values of r_f or one may want to fix $M_{\rm eq}$ and solve for r_f. For this reason in our equations we have left r_f indicated explicitly, but in explicit calculations it is set to unity.

(B) Given the (known, see e.g., section 3) function g for the selected observable, solve for $M_{\rm eq}$ the equation

$$g(M_{\rm eq}, \{p_j\}) = r_f \int dM \frac{d\Phi_{\rm EMD}}{dM} g(M, \{p_j\}) \tag{2.6}$$

to calculate the equivalent mass $M_{\rm eq}(r_f, \{\zeta_j\})$ as a function of the parameters of the EMD. As we will see below, in some case this can be done analytically (see e.g., equation (3.20)), but in other cases must be done numerically (see e.g., equation (3.16)). The dependence of $M_{\rm eq}$ on the EMD parameters describing its shape is helpful to understand which observable effects are produced by a certain EMD.

(C) The allowed PBHs abundance (for the considered observable) is given by

$$f_{\rm PBH}^{\rm EMD}(\{\zeta_j\}) = r_f f_{\rm PBH}^{\rm MMD}\left(M_{\rm eq}(r_f, \{\zeta_j\})\right) , \tag{2.7}$$

where $f_{\rm PBH}^{\rm MMD}(M_{\rm eq})$ is the largest allowed abundance for a MMD with $M = M_{\rm eq}$. If we are interested in just one constraint in particular, then this formalism allows us to immediately state if a given EMD is compatible or not with observations. If instead we want to account for several constraints at once, we have to a find the set of Equivalent Masses associated to each function g. Every mass calculated in this way has a maximum allowed (MMD) PBHs fraction (e..g, as found in the literature); of these $f_{\rm PBH}$ values, the minimum one that satisfies all the constraints at once is the largest allowed PBH abundance of that EMD. This is illustrated in figure 1. Hereafter we refer to the maximum allowed value of the PBH fraction as $\hat{f}_{\rm PBH}$.

In figure 1 we consider two specific EMDs, a *PL* (left) and a *LN* (right) and four observational constraints obtained for MMD: microlensing, ultra-faint dwarf galaxies (UFDG) and CMB. The adopted functions g for these observables will be described in section 3. For each observable and each EMD we show the corresponding $M_{\rm eq}$ (dashed vertical lines) and maximum allowed PBHs fraction $\hat{f}_{\rm PBH}$. For the *PL* EMD the maximum allowed $\hat{f}_{\rm PBH}$ is the lowest of the four i.e., the one obtained from EROS2 microlensing (for its corresponding EM). On the other hand, for the chosen *LN* distribution the maximum allowed $\hat{f}_{\rm PBH}$ is that provided by the UFDG for their EM.

An additional feature of this approach is that it allows one to understand which part of a EMD (e.g., low-mass or high-mass tail) is more relevant for a given observational constraint. Such information can be inferred from the value of the equivalent mass i.e., from the position of the vertical dotted lines in figure 1.

Our method extend existing ones [49, 50] in several ways. First of all it introduces a clear physical connection between the effects of EMDs and those of a MMD thanks to the introduction of the new concept of the Equivalent Mass. Thanks to this concept one can predict the approximated strength of the constraint even without computing it, since

JCAP01(2018)004

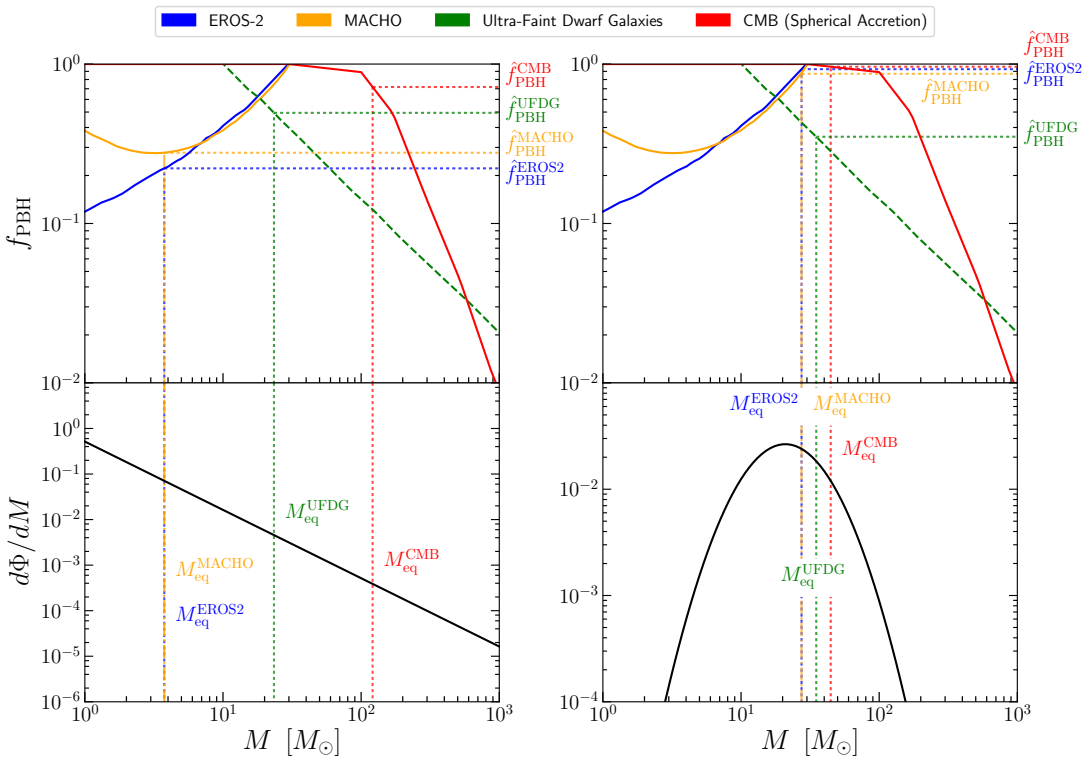

Figure 1. Illustration of the new method proposed in this paper. *Upper Panels*: microlensing (EROS-2, MACHO), ultra-faint dwarf galaxies (UFDG) and cosmic microwave background (CMB) constraints for MMD. Solid lines are used for constraints generally considered robust to astrophysical assumptions, while dashed lines are used for constraints which robustness has yet to be fully discussed in the literature. *Lower Panels*: examples of Power Law (on the left) and Lognormal (on the right) mass distributions. The vertical dotted lines highlight the position of the equivalent mass for each observable, calculated from equations (3.12), (3.16) and (3.20). From their intersection with the corresponding constraint in the upper panels, we extract the set of four maximum PBHs allowed fractions $\hat{f}_{\rm PBH}$. The fraction of PBHs that satisfies the four constraints at once is the minimum of the four, i.e. $\hat{f}^{\rm EROS2}_{\rm PBH}$ for the Power Law and $\hat{f}^{\rm UFDG}_{\rm PBH}$ for the Lognormal. This is then the maximum $f_{\rm PBH}$ allowed for that EMD and that combination of observables.

the EM highlights which part of an arbitrary EMD is more relevant for the physics of a given observable. Secondly, our method allows to calculate constraints coming from single experiments taking into account properly the effects coming from the EMD low- and high-mass tails, since the integrals are performed over the whole mass range and not only where $\hat{f}^{\rm MMD}_{\rm PBH} < 1$. One advantage of such formulation is the possibility to easily check the validity of the assumptions of the underlying modelling (see e.g., section 4).

3 Application to different observables

In light of recent observations by LIGO [8], we focus on the $\mathcal{O}(10)$ $M_\odot$ window in the theoretically allowed PBHs mass range. This particular window is limited on the lower mass end by microlensing constraints and on the higher mass end by UFDG and CMB constraints,

JCAP01(2018)004

which could in principle rule out the possibility that PBHs make up the entirety of the DM, under certain assumptions (e.g., if PBHs form an accreting disk [30]). Inside this mass range there are other constraints, e.g. those coming from PBHs radio and X-ray emission [23]. We chose not to consider this probe since the constraints are extremely sensitive to one particular poorly known parameter, the accretion efficiency relative to the Bondi-Hoyle rate λ, to the point that mildly different values of λ, all consistent with current literature, make the constraint disappear, as pointed out by the same authors of ref. [23].

In order to obtain equivalence relations between the MMD and the EMD cases, we will introduce some approximations that will be described in each specific case. Given all the astrophysical uncertainties that enter in the computation of the limits, one has to keep in mind that constraints have to be considered as orders of magnitude. Therefore the performance of our proposed approach should be evaluated keeping in mind this underlying limitation. Even under our stated simplifying assumptions, here we show the potential of our method to mimic the effects of a MMD and easily obtain constraints for any EMD.

Finally, it should be kept in mind that, even for a MMD, every constraint has been derived under some approximation that determines the range of masses where the same constraint is meaningful. Since our method does not change such assumptions, it should be used for EMDs contained, or at least peaked, in the valid mass domain, in order to extract consistent constraints. We comment on such limitations at the end of each subsection and at the beginning of section 4.

We consider two different families of EMDs:

- A *Power Law (PL)* distribution of the form

$$\frac{d\Phi_{\rm PBH}}{dM} = \frac{\mathcal{N}_{PL}}{M^{1-\gamma}}\Theta(M - M_{\rm min})\Theta(M_{\rm max} - M), \tag{3.1}$$

  characterized by an exponent γ, a mass range $(M_{\rm min}, M_{\rm max})$ and a normalization factor $\mathcal{N}_{PL}$ that reads

$$\mathcal{N}_{PL}(\gamma, M_{\rm min}, M_{\rm max}) = \begin{cases} \dfrac{\gamma}{M_{\rm max}^{\gamma} - M_{\rm min}^{\gamma}}, & \gamma \neq 0, \\ \log^{-1}\left(\dfrac{M_{\rm max}}{M_{\rm min}}\right), & \gamma = 0. \end{cases} \tag{3.2}$$

  Such EMDs appear, for instance, when PBHs are generated by the collapse of large density fluctuations [42] or of cosmic strings [46]. The epoch of the collapse determines the exponent γ, in fact, if we call $w = \frac{p}{\rho}$ the equation of state parameter of universe at PBHs formation, $\gamma = -\frac{2w}{1+w}$ and spans the range $[-1, 1]$, assuming that this process happens in an expanding Universe ($w > -1/3$). Interesting values of the exponent are $\gamma = -0.5$ ($w = 1/3$) and $\gamma = 0$ ($w = 0$), corresponding to formation during radiation and matter dominated eras, respectively.

- A *Lognormal (LN)* distribution

$$\frac{d\Phi_{\rm PBH}}{dM} = \frac{e^{-\frac{\log^2(M/\mu)}{2\sigma^2}}}{\sqrt{2\pi}\sigma M}, \tag{3.3}$$

  defined by the mean and a standard deviation of the logarithm of the mass, μ and σ, respectively. This distribution gives a good approximation to real EMDs when PBHs form from a symmetric peak in the inflationary power spectrum, as proven numerically in [51] and analytically in [53].

JCAP01(2018)004

3.1 Microlensing

Microlensing is the temporary magnification of a background source which occurs when a compact object passes close to its line of sight [54] and crosses the so-called "microlensing tube". The compact object, a PBH in our case, usually (and in this work) belongs to our galaxy halo, but in some works (see e.g., [17]) the background source (M31) was external to the Milky Way and PBHs could belong to either halo. The microlensing tube is the region where the PBH amplification of the background source is larger than some threshold value A_T. For the standard value $A_T = 1.34$, the radius of the microlensing tube is given by the Einstein radius

$$R_E(x) = 2\sqrt{\frac{GML\,x(1-x)}{c^2}}, \tag{3.4}$$

where G is Newton's gravitational constant, L is the distance to the source and x is the distance to the PBH in units of L. Standard analyses usually assume for our galaxy a cored isothermal dark matter (either made by PBHs or not) halo model, for which the density profile reads as

$$\rho(r) = \rho_0 \frac{r_c^2 + r_0^2}{r_c^2 + r^2}, \tag{3.5}$$

where r_c is the halo core radius, r_0 is the Galactocentric radius of the Sun and ρ_0 is the local dark matter density. The duration of each event is the Einstein tube crossing time for the compact object involved. Therefore globally (considering the entire Milky Way halo), the differential microlensing event rate for a single source, for PBHs with an EMD, i.e., how many events we should expected for every Einstein diameter crossing time Δt, is [55–57]

$$\frac{d\Gamma}{d\Delta t} = \frac{512G^2L\rho_0(r_c^2 + r_0^2)}{\Delta t^4 c^4 v_c^2} \int_0^1 dx \frac{x^2(1-x)^2}{A + Bx + x^2} f_{\rm PBH} \int dM \frac{d\Phi}{dM} M e^{-Q(x,\Delta t,M)}, \tag{3.6}$$

where

$$A = \frac{r_c^2 + r_0^2}{L^2}, \qquad B = -2\frac{r_0}{L}\cos b \cos l, \qquad Q(x,t,M) = \left(\frac{2R_E}{v_c \Delta t}\right)^2, \tag{3.7}$$

(b, l) are the galactic latitude and longitude of the source (usually the Magellanic Clouds) and v_c is local circular velocity.[2] For a specific survey, the number of expected microlensing events will be

$$N_{\rm exp} = E \int d\Delta t \frac{d\Gamma}{d\Delta t} \varepsilon(\Delta t), \tag{3.8}$$

where the exposure E and the detection efficiency $\varepsilon(\Delta t)$ depend on the specific experiment and instrument. The choice $\varepsilon(\Delta t) = 1$ correspond to the theoretical number of expected events $N_{\rm exp}^{\rm the}$.

The average microlensing tube crossing time scales as $M^{1/2}$. This suggests that the mass and time dependence in $Q\left(x, \frac{M}{\Delta t^2}\right)$ can be described by a single parameter y. We change the old variables $(M, \Delta t)$ to new ones $\left(M, y = \frac{M}{\Delta t^2}\right)$, obtaining in this way that

$$N_{\rm exp} \propto \int dx f(x) \int dy\; y^{1/2} e^{-Q(x,y)} f_{\rm PBH} \int dM \frac{\varepsilon\left(\sqrt{M/y}\right)}{M^{1/2}} \frac{d\Phi}{dM}, \tag{3.9}$$

[2] In this paper we use $\rho_0 = 0.008\ M_\odot pc^{-3}$, $r_0 = 8.5\ kpc$, $r_c = 5.0\ kpc$, $L = 50\ kpc$, $v_c = 220\ km\ s^{-1}$, $(b, l) = (-33^o, 280^o)$.

JCAP01(2018)004

which we use to find the equivalent mass. Since M and y are coupled by the detection efficiency, the function g introduced in section 2 reads as

$$g(M,\{p_j\}) = \int dx f(x) \int dy\; y^{1/2} e^{-Q(x,y)} \frac{\varepsilon\left(\sqrt{M/y}\right)}{M^{1/2}}, \tag{3.10}$$

where we have already dropped all the constant factors in equation (3.6), since they are present in both side of equation (2.5). Moreover, when we focus on $N_{\rm exp}^{\rm the}$, for which $\varepsilon = 1$, the mass dependence can be decoupled, the common (x, y)-dependent factor cancels and the final g function simplifies to

$$g(M) = M^{-1/2}. \tag{3.11}$$

Now we can use Equation 2.5 to obtain

$$M_{\rm eq}^{-1/2} = r_f \begin{cases} \mathcal{N}_{PL} \dfrac{M_{\rm max}^{\gamma-1/2} - M_{\rm min}^{\gamma-1/2}}{\gamma - \frac{1}{2}}, & PL, \quad \gamma \neq \dfrac{1}{2}, \\ \mathcal{N}_{PL} \log \dfrac{M_{\rm max}}{M_{\rm min}}, & PL, \quad \gamma = \dfrac{1}{2}, \\ e^{\frac{\sigma^2}{8}} \mu^{-1/2}, & LN. \end{cases} \tag{3.12}$$

To validate our approximation, since we are interested in converting MMD to EMD constraints, the relevant quantity is the ratio between the expected microlensing events for the two mass distributions: $N_{\rm exp}^{\rm EMD}/N_{\rm exp}^{\rm MMD}$, which should be unity. To quantify the performance of the approximation $\varepsilon = 1$ (which enabled us to provide an analytic solution) we also consider an $\varepsilon(\Delta t)$ of a form[3] similar to that of the MACHO survey (see figure 8 of ref. [57]).

The duration of detected candidates events was typically ~ 50 days, which for high amplification yields a typical mass of $0.3 M_\odot$ according to the expected scaling (see e.g., ref. [55]). For illustration purposes we therefore set the equivalent mass $M_{\rm eq} = 0.3 M_\odot$. For the PL EMD we set $M_{\rm max} = 100 M_\odot$ and consider two cases for the exponent ($\gamma = -0.5$ and $\gamma = 0$) which implies (equation (3.12)) that $M_{\rm min} = 0.079 M_\odot$ and $M_{\rm min} = 0.015 M_\odot$, respectively; and for the LN we have $\sigma = 1.0$ and $\mu = 0.385 M_\odot$. The left panel of figure 2 shows the theoretical ($\varepsilon = 1$) differential event rate as a function of duration for the four mass distributions and reports the ratio $N_{\rm exp}^{\rm EMD}/N_{\rm exp}^{\rm MMD}$. The fact that this ratio is the unity indicates that the effective mass approach works well. The right panel is the same as the left panel but the number of expected events is now computed with our adopted $\varepsilon(\Delta t)$. In this case the performance of the approach (quantified by $(N_{\rm exp}^{\rm EMD}/N_{\rm exp}^{\rm MMD} - 1) \sim 10 - 25\%$) introduces errors smaller than, or at worst comparable, to those introduced by other assumptions in the model (e.g., the PBHs velocity dispersion choice of the halo model, see figure 3 in [58]). For instance, using the same parameters, a 10% change in the velocity dispersion yields a 25% change in $N_{\rm exp}^{\rm MMD}$. A detailed analysis of the effects of astrophysical uncertainties on PBH constraints from microlensing can be found in [58].

The range of validity of this approach for microlensing is given by the observational window i.e., by the experimental efficiency $\varepsilon(\Delta t)$, characteristic of every given experiment. In particular, below the minimum $\Delta t_{\rm min}$ and above the maximum $\Delta t_{\rm max}$ sampled, the efficiency drops to zero, along with the capability to detect PBHs. Through the above mentioned scaling relation, we can translate the crossing time window sampled by the experiment to a sampled

[3] $\varepsilon(t) = \exp\left[-\frac{\log^2(t/\mu_t)}{2\sigma_t^2}\right] / \sqrt{2\pi\sigma_t^2}$, with time, t, in days, $\mu_t = 70$ days and $\sigma_t = 1.25$.

JCAP01(2018)004

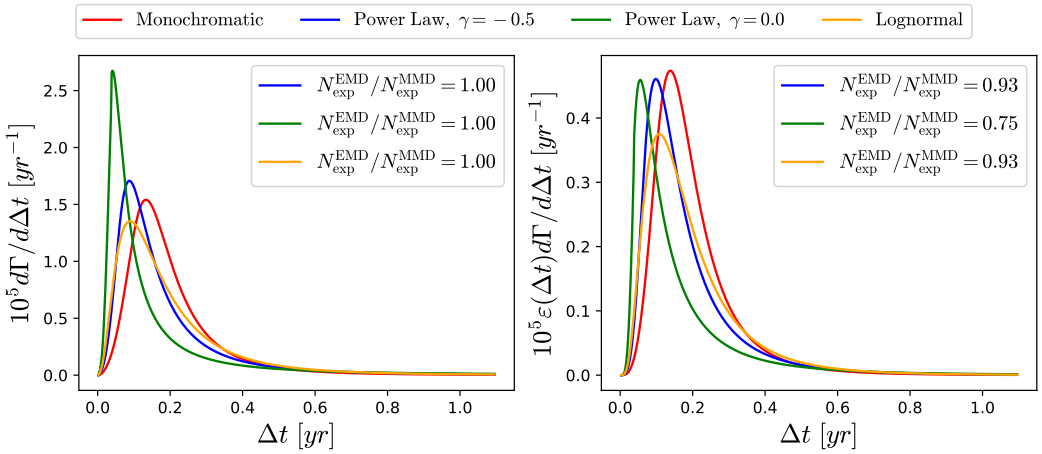

Figure 2. Theoretical ($\varepsilon(\Delta t) = 1$) and experimental differential event rate for a MMD with $M_{\rm eq} = 0.3 M_\odot$, two *PL* and a *LN* with $M_{\rm max} = 100 M_\odot$ and $\sigma = 1.0$. $M_{\rm min}$ and μ have been obtained with equation (3.12) imposing the same equivalent mass of the MMD. The stars source is the LMC, whose parameters can be found in [51, 58]. We assume $f_{\rm PBH} = 1$ for every distribution to calculate the EM. Notice the level of concordance of the expected number of events.

mass range. For this approach to be valid, $M_{\rm min}$ and $M_{\rm max}$ appearing in equation (3.12) must be within the sampled mass range. In general, properly computed lensing constraints would require a detailed modelling including simulations, which is beyond the scope of this paper. Since PBHs constraints are indicative, we followed the most common modelling.

3.2 Ultra-faint dwarf galaxies

In dwarf galaxies, dominated by dark matter, the stellar population can be dynamically heated by gravitational two-body interaction between PBHs and stars. These interactions tend to equalize energy of different mass groups, but if PBHs have a mass larger than one solar mass (average mass of a star), stars will extract energy from them and the stellar system will expand [59]. Since this is the case commonly considered in the literature we will limit ourselves to consider cases in which $M_{\rm PBH} > M_\odot$.

For a generic PBHs mass distribution, the half-light radius of the stellar population evolves according to [22]

$$\frac{dr_h}{dt} = \frac{4\sqrt{2}\pi G f_{\rm PBH}}{\sigma_{\rm PBH}\left(\frac{\alpha M_\star}{\rho_{\rm core} r_h^2} + 2\beta r_h\right)} \int dM \frac{d\Phi}{dM} M \log\Lambda(M), \tag{3.13}$$

where M and $\sigma_{\rm PBH}$ are the PBH mass and velocity dispersion, $M_\star$ is the galaxy stellar mass, $\rho_{\rm core}$ is the dark matter core density, α and β are constants that depend on the mass distribution of the dwarf galaxy and the Coulomb logarithm reads as

$$\log\Lambda(M) = \log\frac{r_h \sigma_{\rm PBH}^2}{G(M_\odot + M)}. \tag{3.14}$$

In general, there should also be a cooling term, which becomes important only if the mass of the PBH is smaller than the mass of the stars. Moreover this modelling is valid if there is no central black hole massive enough to stabilise the stellar distribution [60, 61].

JCAP01(2018)004

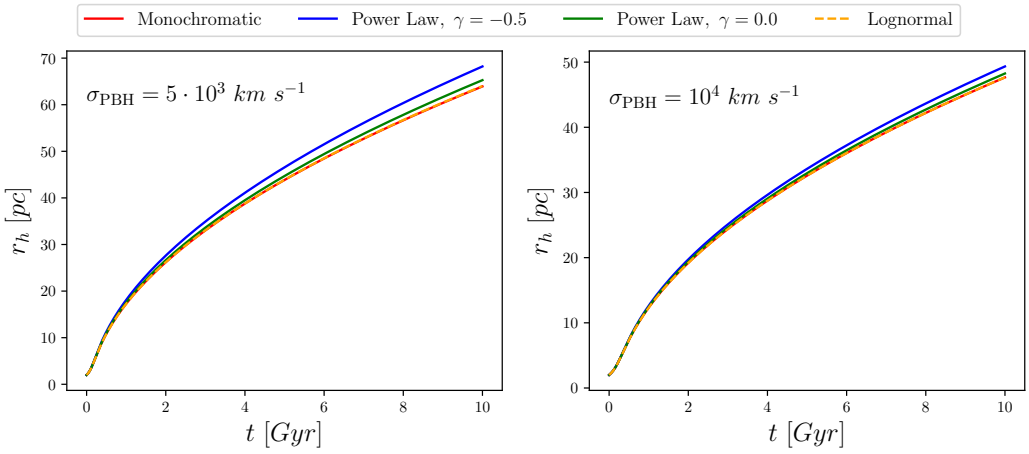

Figure 3. Half-light radius evolution for different values of the PBHs velocity dispersion. The PBHs distributions considered here are a MMD with $M_{\rm eq} = 30M_\odot$, a Power Law with two different exponents and a Lognormal, all with the same Equivalent Mass. In the *PL* case we fixed γ and $M_{\rm min} = 2M_\odot$, while in the *LN* we have fixed $\sigma = 0.5$; $M_{\rm max}$ and μ were calculated using equation (3.16) and assuming $f_{\rm PBH} = 1$ for every distribution.

Aside from common factors we are not interested in, the g function for this observable, directly read from equation (3.13), is given by

$$g(M, r_h, \sigma_{\rm PBH}) = M \log \Lambda(M) = M \log \frac{r_h \sigma^2_{\rm PBH}}{G(M_\odot + M)}. \tag{3.15}$$

We find that Equation 2.5 with this particular choice of g reads as

$$M_{\rm eq} \log \Lambda(M_{\rm eq}) = r_f \begin{cases} \dfrac{\mathcal{N}_{PL}}{1+\gamma} \left(M_{\rm max}^{1+\gamma} \log \left[\Lambda(M_{\rm max}) e^{\frac{1-{}_2F_1(1,1+\gamma,2+\gamma,-M_{\rm max})}{1+\gamma}} \right] - \right. \\ \qquad \left. - M_{\rm min}^{1+\gamma} \log \left[\Lambda(M_{\rm min}) e^{\frac{1-{}_2F_1(1,1+\gamma,2+\gamma,-M_{\rm min})}{1+\gamma}} \right] \right), & PL, \gamma \neq -1, \\ \mathcal{N}_{PL} \left[\log \Lambda(0) \log \dfrac{M_{\rm max}}{M_{\rm min}} + {\rm Li}_2(-M_{\rm max}) - {\rm Li}_2(-M_{\rm min}) \right], & PL, \gamma = -1, \\ \mu e^{\frac{\sigma^2}{2}} \log \Lambda(\mu e^{\sigma^2} - M_\odot), & LN \end{cases} \tag{3.16}$$

where the *PL* result is exact but for the *LN* case we assumed that the EMD was peaked at $M \gtrsim M_\odot$ to have on average PBHs more massive than stars, in order for stars to extract energy from the PBHs.

In figure 3 we show the evolution of the half light radius for different EMDs with the same equivalent mass and the corresponding MMD, for the fiducial dwarf galaxies model

[4] Gaussian Hypergeometric function.
[5] Polylogarithm function.

JCAP01(2018)004

considered in [22]. We have fixed $M_{\rm eq} = 30 M_\odot$ and we have used the same halo parameters[6] of figure 3 of ref. [22]. We fixed $M_{\rm min} = 2\ M_\odot$ for the *PL* EMDs and $\sigma = 0.5$ for the *LN*. Then, by using equation (3.16), we obtain $M_{\rm max}$ and μ for two *PL* and one *LN* distributions, respectively. In the three cases we used the initial value of the half-light radius r_{h0} to calculate the equivalent mass (recall that the equivalent mass has a logarithmic dependence on r_h). As it can be seen in figure 3, our equivalence relations provide a good match between the MMD and the EMDs, which in turn will give an accurate interpretation of abundance constraints.

Beside the requirement that $M_{\rm PBH} \gtrsim M_\odot$ for the PBH to heat the star system, one should also impose $M \lesssim \sigma^2_{\rm PBH} r_h/G - 1$, otherwise the assumption of PBHs travelling in an homogeneous star field will not be valid [62]. Moreover if an EMD provides enough PBHs with masses $\gtrsim 10^2 M_\odot$, it is reasonable to believe that some of these may be placed at the centre of dwarf galaxies and may thus stabilise the stellar distribution, making equation (3.13) invalid [60, 61]. Therefore, in order to obtain constraints for EMDs using equation (3.13), EMDs should not have significant contribution outside this mass range. The sensitivity of the PBH abundance constraints to astrophysical uncertainties in this technique has yet to be fully analysed and discussed in the literature. However given the discussion above in what follows we present separately combined constraints with and without this probe and specific constraints from this probe are indicated by a different line-style.

3.3 Cosmic microwave background

The impact that PBHs have on CMB observables derives from the energy they inject into the plasma. In fact, the extra radiation is responsible for the heating, excitation and ionization of the gas. We refer the interested reader to refs. [29, 30], where the authors presented an updated treatment of the underlying physics of the energy injection for spherical and disk accretion, respectively, and to ref. [31], where cosmological effects of PBHs are described and investigated in detail. In order to include an EMD in this framework, one should integrate the volumetric rate of energy injection over the whole mass range spanned by PBHs as

$$\dot{\rho}_{\rm inj} = \rho_{\rm dm} f_{\rm PBH} \int dM \frac{d\Phi}{dM} \frac{\langle L(M) \rangle}{M}, \tag{3.17}$$

where $\langle L(M) \rangle$ is the velocity-averaged luminosity of a PBH with mass M. We immediately read that

$$g(M, \{p_j\}) = \frac{\langle L(M) \rangle}{M}. \tag{3.18}$$

In general, the averaged luminosity will depend not only on the mass but also on redshift, gas temperature, free electron fraction and ionization regime. Here we will make the simplifying assumption that these dependencies can be factored out, and focus on the mass dependence. Using the results obtained for spherical accretion [29], we can estimate the mass dependence of the integrand as

$$\frac{\langle L \rangle}{M} \propto \frac{L}{M} \propto \frac{\dot{M}^2/L_{\rm Edd}}{M} \propto \frac{M^4 \lambda^2(M)/M}{M} = M^2 \lambda^2(M), \tag{3.19}$$

where L is the luminosity of an accreting black hole, $\dot{M}$ is the black hole growth rate, $L_{\rm Edd}$ is the Eddington luminosity and $\lambda(M)$ is the dimensionless accretion rate. As can be seen in figure 4 of [29], PBHs with different masses accrete in different manners at different redshift.

[6] In this paper we use $r_{h0} = 2\ pc$, $M_\star = 3000 M_\odot$, $\rho_{\rm core} = 1\ M_\odot pc^{-3}$, $\alpha = 0.4$, $\beta = 10$.

JCAP01(2018)004

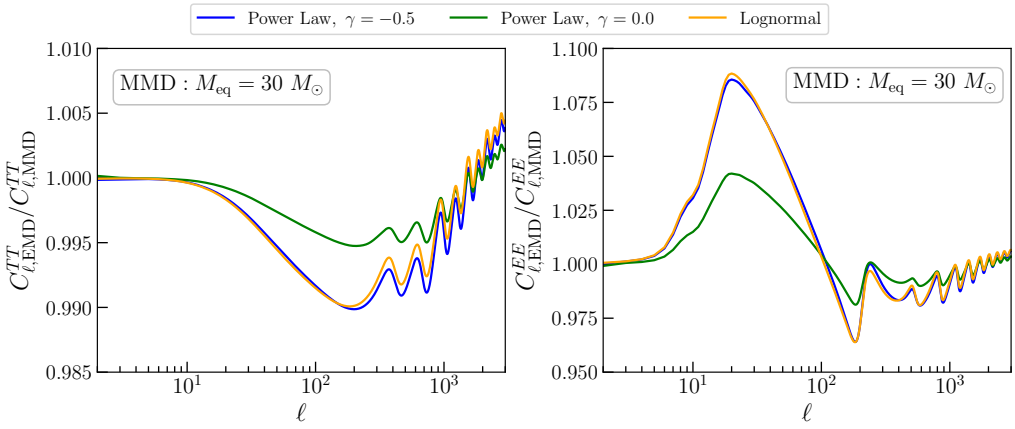

Figure 4. Relative difference in temperature (*left panel*) and polarization (*right panel*) power spectra for two *PL* and one *LN* distributions with respect to a MMD with $M_{\rm eq} = 30M_\odot$, all of them with the same Equivalent Mass. In the *PL* case we fixed γ and $M_{\rm min} = 1M_\odot$, while in the *LN* we have fixed $\sigma = 1.0$; $M_{\rm max}$ and μ were calculated using equation (3.20) and assuming $f_{\rm PBH} = 1$ for every distribution. We chose to show the photoionization limit case, since it is the most constraining case. Finally we have used $\alpha = 0.2$ because it keeps the differences with respect to the MMD case under the cosmic variance level.

In particular, heavy (light) PBHs mostly accrete, and therefore inject energy, after (before) decoupling. However, in the same figure it can be noticed that $\lambda \sim \mathcal{O}(1/2)$ for $z \lesssim 1700$[7] for a wide range of masses. Assuming $\lambda = $ const is a possibility. However, a much better option is to parametrize the accretion rate as $\lambda(M) = M^{\alpha/2}$ (neglecting the redshift dependence), where α is a parameter to be tuned numerically a posteriori to minimize differences in the relevant observable quantity between the EMD case and the equivalent monochromatic case.

Equation (2.5) thus becomes

$$M_{\rm eq}^{2+\alpha} = r_f \begin{cases} \mathcal{N}_{PL} \dfrac{M_{\rm max}^{\gamma+2+\alpha} - M_{\rm min}^{\gamma+2+\alpha}}{\gamma + 2 + \alpha}, & PL, \\ \mu^{2+\alpha} e^{\frac{(2+\alpha)^2\sigma^2}{2}}, & LN. \end{cases} \tag{3.20}$$

In figure 4, produced with a modified version of `HYREC` [31, 63, 64], we compare temperature and polarization power spectra of three different EMDs chosen so that their equivalent mass is $M_{\rm eq} = 30M_\odot$ with those of a fiducial MMD with $M_{\rm eq} = 30M_\odot$, assuming $f_{\rm PBH} = 1$ in the photoionization limit. We have explored α in the interval $[0.0, 0.4]$ but we have plotted the C_ℓs only for the intermediate value $\alpha = 0.2$, since it guarantees that differences are kept under the cosmic variance limit for every $\ell \lesssim 3 \times 10^3$, especially for the E-mode polarization. The choice of α can be further optimised depending on the experiment. For example experiments not limited by cosmic variance at $\ell \gg 10^3$, such as Planck, may require a different value of α, since they have the smallest error bar at lower ℓ [31]. Despite the good agreement, we stress that no choice of this parameter is able to simultaneously match early (before decoupling, for $\ell > 200$) and late time (after decoupling, for $\ell < 200$) energy injection.

[7] The modified `HYREC` version calculates the modified thermal history for $z < 1700$, redshift of the beginning of Hydrogen Recombination.

JCAP01(2018)004

Values of α larger than the adopted one suppress deviations with respect to the MMD case for $\ell < 200$ in both spectra, but increase deviations for $\ell > 200$. Deviations from the fiducial MMD model are larger for EMDs that exhibit a wider high-mass tail, as in the *PL* case with negative exponent or in the *LN* case. We refer the interested reader to reference [31], where these equivalence relations (equation (3.20)) are used, along with a full MCMC treatment, to quantify the performance of our approach. The differences in the obtained PBHs abundance constraints are below the 10%.

Finally one should keep in mind that all constraints (including the monochromatic ones) are derived under the steady-state approximation, which is valid only for PBHs with masses $M \lesssim 10^4 M_\odot$. Hence effects of an EMD high-mass tail beyond this critical value are not properly accounted for.

4 Practical considerations and observational constraints

Before calculating experimental constraints, some important considerations are in order. For a MMD one can unambiguously check if the validity conditions (of the adopted modelling, code, equations etc.) that depend on the PBH mass hold: e.g., the mass is in the sampled mass range for microlensing (section 3.1), PBHs cede energy to the stellar system and travel in a homogeneous field for UFDG and there is no central black hole to stabilise the system (section 3.2), steady-state approximation is valid for CMB constraints (section 3.3). In other words the adopted modelling defines a mass range of validity; outside this range, results (if any) are not reliable and sometimes even unphysical. On the other hand, for non-monochromatic cases, parts of the EMDs can lie outside the mass range of validity. This issue is not only important for our equivalent mass formalism (as discussed previously), but also for every analysis dealing with extended distributions.

In the case of a *PL* distribution, it is always possible to tune $M_{\rm min}$ and $M_{\rm max}$ to restrict the mass range where the distribution is defined, but the *LN* is infinitely extended and the effects of the tails can be relevant. In order to account for them, we propose to compare the amplitude of the EMD at the lower and upper boundaries (if both exist, otherwise just at the relevant one) of the mass range of validity which we indicate as $M^{\pm}_{\rm lim}$, to the amplitude of the EMD maximum, situated at $M_{\rm peak}$. Then require the relative amplitude to be smaller than an arbitrarily chosen threshold δ where[8] $\delta \leq 1$. Without any loss of generality, for any EMD and δ, we can define a mass M_δ through

$$\left.\frac{d\Phi}{dM}\right|_{M_\delta} = \delta \left.\frac{d\Phi}{dM}\right|_{M_{\rm peak}}. \tag{4.1}$$

By solving equation (4.1) for M_δ in the case of a *LN* EMD, we find two solutions, symmetric with respect to the peak:

$$M^{\pm}_\delta = \mu e^{-\sigma^2 \pm \sigma\sqrt{\log(\delta^{-2})}}. \tag{4.2}$$

Finally, by requiring that

$$M^-_{\rm lim} \leq M^-_\delta, \quad M^+_\delta \leq M^+_{\rm lim}, \tag{4.3}$$

[8] Here we have in mind the lognormal distribution. In general this approach applies for EMD that are monotonic around and beyond each of the $M^{\pm}_{\rm lim}$. This is not the only viable criteria, in fact one could directly impose some upper bound on the integrals $\int_{M^+_{\rm lim}}^{\infty} dM \frac{d\Phi}{dM} g(M, \{p_j\})$ and $\int_0^{M^-_{\rm lim}} dM \frac{d\Phi}{dM} g(M, \{p_j\})$ instead of on the EMD.

JCAP01(2018)004

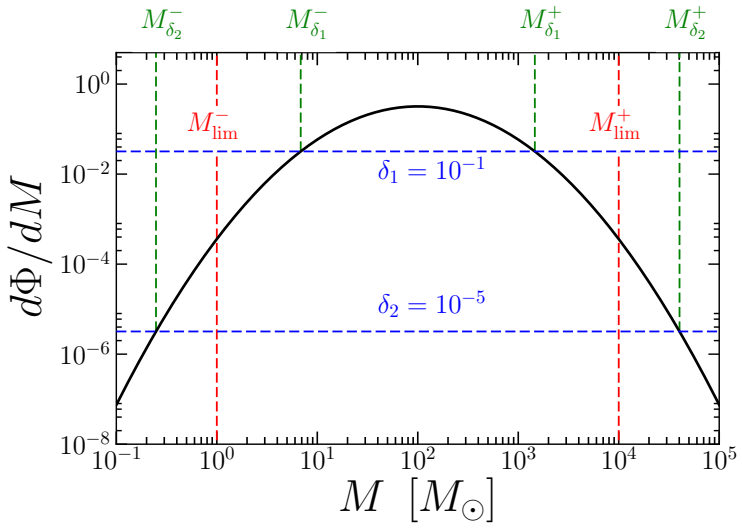

Figure 5. Schematic representation of the criterion proposed to ensure that an EMD does not have significant contributions from masses outside the range of validity for a given observable and the adopted modelling. The mass rage of validity is indicated by $M^{\pm}_{\rm lim}$, δ quantifies a tolerance i.e, how much the EMD is required to drop from its maximum before we accept that the tails of the distribution may extend beyond the range of validity. In this example, for $\delta = 10^{-1}$ this EMD is considered in the range of valid. This is not the case for the more stringent $\delta = 10^{-5}$ tolerance level.

we find the set of inequalities

$$\begin{cases} \sigma^2 + \sigma\sqrt{\log(\delta^{-2})} - \log\dfrac{\mu}{M^-_{\rm lim}} \leq 0, \\ \sigma^2 - \sigma\sqrt{\log(\delta^{-2})} - \log\dfrac{\mu}{M^+_{\rm lim}} \geq 0\,, \end{cases} \tag{4.4}$$

which satisfies the condition that the amplitude of the tails is smaller than the desired amplitude $\delta \left.\frac{d\Phi}{dM}\right|_{M_{\rm peak}}$. This procedure translates the mass range of validity to a range of validity for the parameters describing the EMD. The smaller the δ, the more reliable the abundance constraint will be. At the same time, low values of δ disqualify wider regions of the EMD parameter space. A schematic representation of this criterion is shown in figure 5.

In the following we calculate the *LN* EMD allowed parameter regions for CMB and UFDG constraints. For the CMB, we have just an upper bound $M^+_{\rm lim} \simeq 10^4 M_\odot$, but for UFDG we have an upper and a lower bound. We consider two sub-cases: in UFDG-1 we take $M^-_{\rm lim} \simeq 1 M_\odot$ and $M^+_{\rm lim} \simeq 10^4 M_\odot$, considering just limits that come from equation (3.13), while in UFDG-2 we take $M^-_{\rm lim} \simeq 1 M_\odot$ and $M^+_{\rm lim} \simeq 10^2 M_\odot$, adding the further condition of not having stabilizing PBHs at the center of the dwarf galaxy. Inserting these values in equation (4.4), we obtain the allowed region of parameter space for three different values of δ. We show it in figure 6. In the CMB case, unless a really small value of δ is chosen, the parameter space is not heavily constrained. We refer the interested reader to ref. [31] to see how these limitations apply to the concrete case of CMB-derived abundance constraints. On the other hand, in the case of UFDG we observe that there is a limited region of validity

JCAP01(2018)004

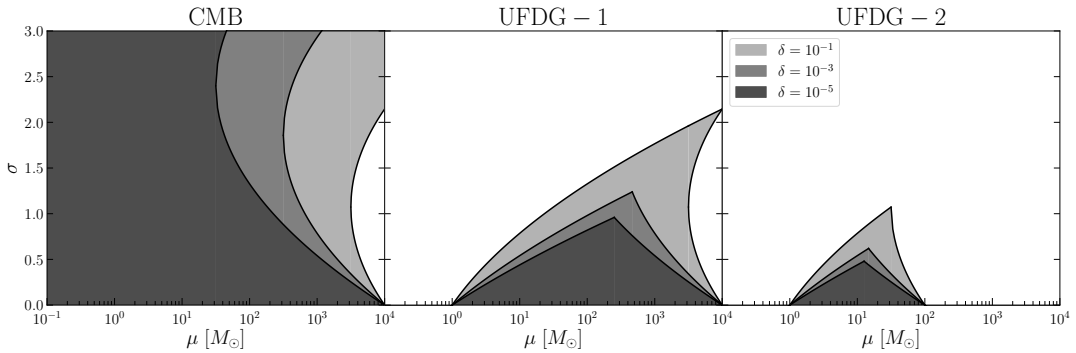

Figure 6. Parameter-space region of validity (in gray) for Lognormal distributions, in the cases of CMB (*left panel*) and UFDG (*central and right panel*) formalism. The region have been obtained according to the limits presented in section 3 and different values of δ. We show two different cases for ultra-faint dwarf galaxies. In the central panel, we considered just the mass limits that come with the description of equation (3.13), while in the right panel we include limitations due to the presence of a central PBH that further stabilises the dwarf galaxy.

in the EMD parameter space, even for quite high values of δ. This does not mean that lognormal distributions outside the gray region in figure 6 are ruled out! It means that the adopted modelling for computing $f_{\rm PHB}$ constraints for these observable is not valid outside the gray region and therefore nothing can be said about distributions corresponding to that region of parameters.

Once established which part of the parameter space is consistent with the modelling, we focus on calculating PBHs constraints in the $10 - 100 M_\odot$ window using the equivalent mass approach we presented here. We are interested in assessing whether for these EMD the allowed window remain open. On the contrary, it would rule out the possibility for PBHs with *PL* or *LN* EMDs to make all the dark matter in that mass range.

This is shown in figures 7 and 8. The color coding is the same used in figure 1, i.e. solid lines represent constraints more robust with respect to astrophysical uncertainties, dashed lines are used for other constraints and dotted lines (when present) represent the MMD constraints. In figure 8, on top of UFDG constraints, we have also introduced diamond markers to highlight the region where the constraints satisfy validity conditions with $\delta = 10^{-3}$ (see central panel of figure 6).

For the *PL* EMDs, figure 7 show the maximum allowed PBH fraction $\hat{f}_{\rm PBH}$ as a function of $M_{\rm max}$ for fixed $M_{\rm min}$ and vice versa. By construction, for $M_{\rm max} = M_{\rm min}$ the monochromatic constraints are recovered. For illustrating the *LN* EMD, we select two representative values of the distribution width σ. By looking at figure 6 one can immediately see that for such values of the EMD width, the mean value μ has only a small range of validity for the UFDG probe around $\mu = 10^2 M_\odot$. Conveniently, the UFDG $\hat{f}_{\rm PBH}$ limits are most stringent and useful exactly in this mass range. Figure 8 shows the maximum allowed PBHs fraction $\hat{f}_{\rm PBH}$ for the *LN* EMD as a function of the mean μ (solid lines). For comparison also the MMD constraint is shown for $M = \mu$ (dashed lines). By construction a *LN* tends to a MMD of mass set by μ for vanishing σ. When the width increases, the window starts shrinking since microlensing constraints drift towards larger mass values while UFDG and CMB constraint drift in the opposite direction.

JCAP01(2018)004

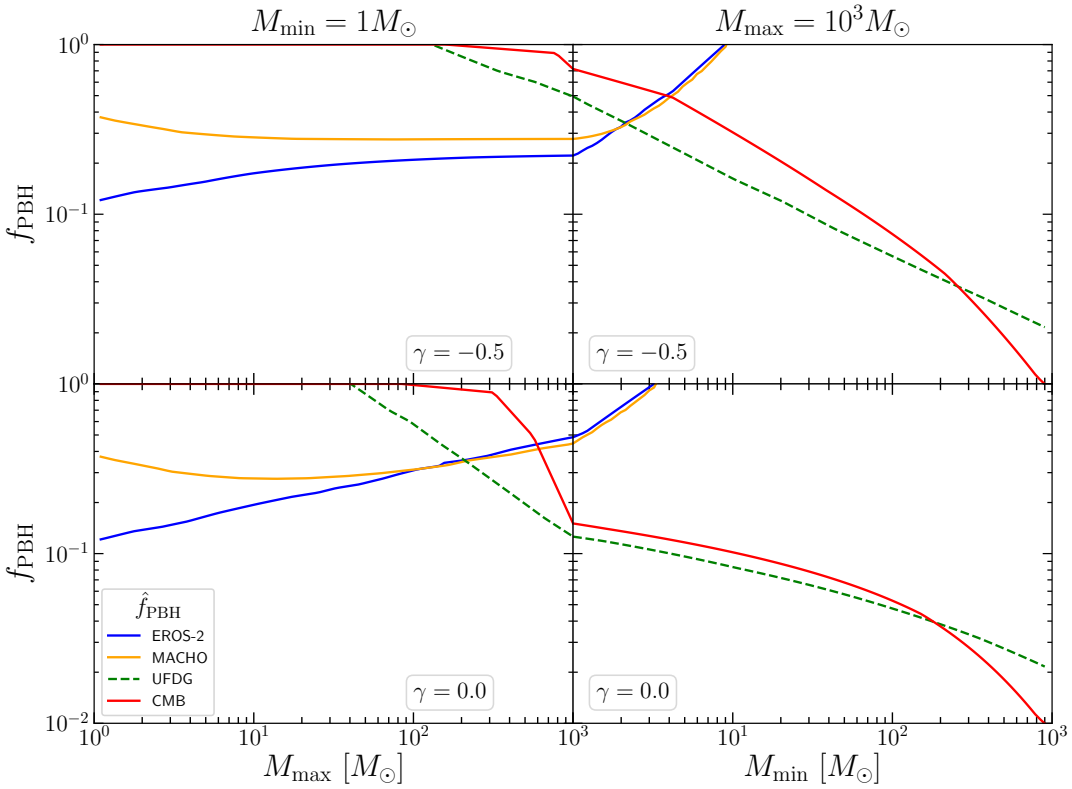

Figure 7. Power Law constraints for $\gamma = -0.5$ (*upper panels*) and $\gamma = 0.0$ (*lower panels*). Solid lines are used for constraints generally considered robust while dashed lines for constraints which dependence on astrophysical assumptions is less known. *Left panels*: $M_{\rm min} = 1\ M_\odot$, $M_{\rm max}$ varying. *Right panels*: $M_{\rm min}$ varying, $M_{\rm max} = 10^3\ M_\odot$.

Finally, to analyse the behaviour of the window where $f_{\rm PBH} \sim 1$ is allowed by the data, we explore the 2D/3D parameter space for the *LN* and *PL* distributions in figures 9 and 10, respectively. In both scenarios we find that with EMDs the PBHs fraction allowed by the combination of all the observables is lower than for a MMD. From the figures we can derive the combination of parameters for each EMD that allow the highest PBHs fraction. Even if in these two figures we have shown wide regions of the parameter space, we want to stress again that constraints can be considered valid only in the subspace allowed by validity conditions, marked with black lines.

The *LN* EMD is shown in figure 9 (the same conventions are kept as in figure 10). The dashed line indicates the boundary of the valid region for UFDG for $\delta = 10^{-3}$ as of figure 6. We notice that to have large $f_{\rm PBH}$ allowed by the whole set of data, the value of μ is quite constrained, and peaked around $20 M_\odot$, while the set of possible σ is wider.

The top and central panels of figure 10 show the maximum allowed $f_{\rm PBH}$ as a function of $M_{\rm min}$ and $M_{\rm max}$ for several choices of γ. We chose to explore the parameter space for the extreme values of γ because the behaviour of any intermediate exponent can be extrapolated from the three cases shown. The bottom panels show sections of the maximum $f_{\rm PBH}$ allowed as a function of $M_{\rm min}$ for fixed $M_{\rm max}$. These sections are chosen to intercept the maximum.

JCAP01(2018)004

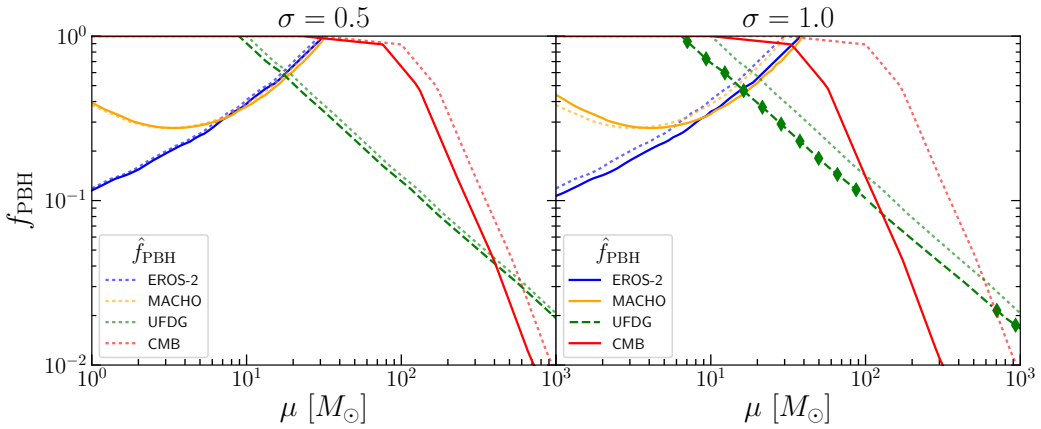

Figure 8. Lognormal (*solid lines*) and Monochromatic (*dotted lines*) constraints for different σ. Solid lines are used for constraints generally considered robust while dashed lines for constraints which dependence on astrophysical assumptions is less known. Diamond markers have been added on top of dashed lines in parameter space regions where validity conditions (for $\delta = 10^{-3}$) are not fulfilled. The $10 - 100\ M_\odot$ window closes as soon as σ starts growing. When σ decreases, EMD constraints tend to MMD ones.

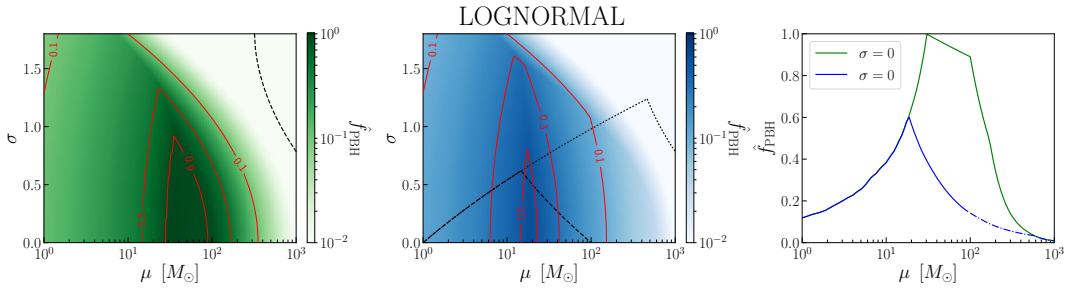

Figure 9. Maximum allowed PBHs fraction for LN distributions for different sets of observables. *Left panel*: microlensing and CMB constraints. The black dashed line corresponds to the $\delta = 10^{-3}$ curve shown in the left panel of figure 6. *Central panel*: microlensing, UFDG and CMB constraints. The black dotted and dashed line corresponds to the $\delta = 10^{-3}$ curve shown in the central and right panel of figure 6. Only constraints below these lines can be considered as theoretically consistent. *Right panels*: sections, chosen to intercept the maximum, of the maximum $f_{\rm PBH}$ allowed as a function of μ. Blue dotted-dashed line signals the region of shallower validity conditions

By looking at the $\hat{f}_{\rm PBH} > 0.5$ region in the central panels, we can confirm the findings of [50], i.e. that in the $\gamma < 0$ ($\gamma > 0$) case the relevant boundary is $M_{\rm min}$ ($M_{\rm max}$), while in the $\gamma = 0$ case both boundary values are equally relevant.

5 Conclusions

PBHs as a dark matter candidate has recently become a popular scenario. Because of the rich phenomenology implied by this possibility, a wide set of different observables can be used

JCAP01(2018)004

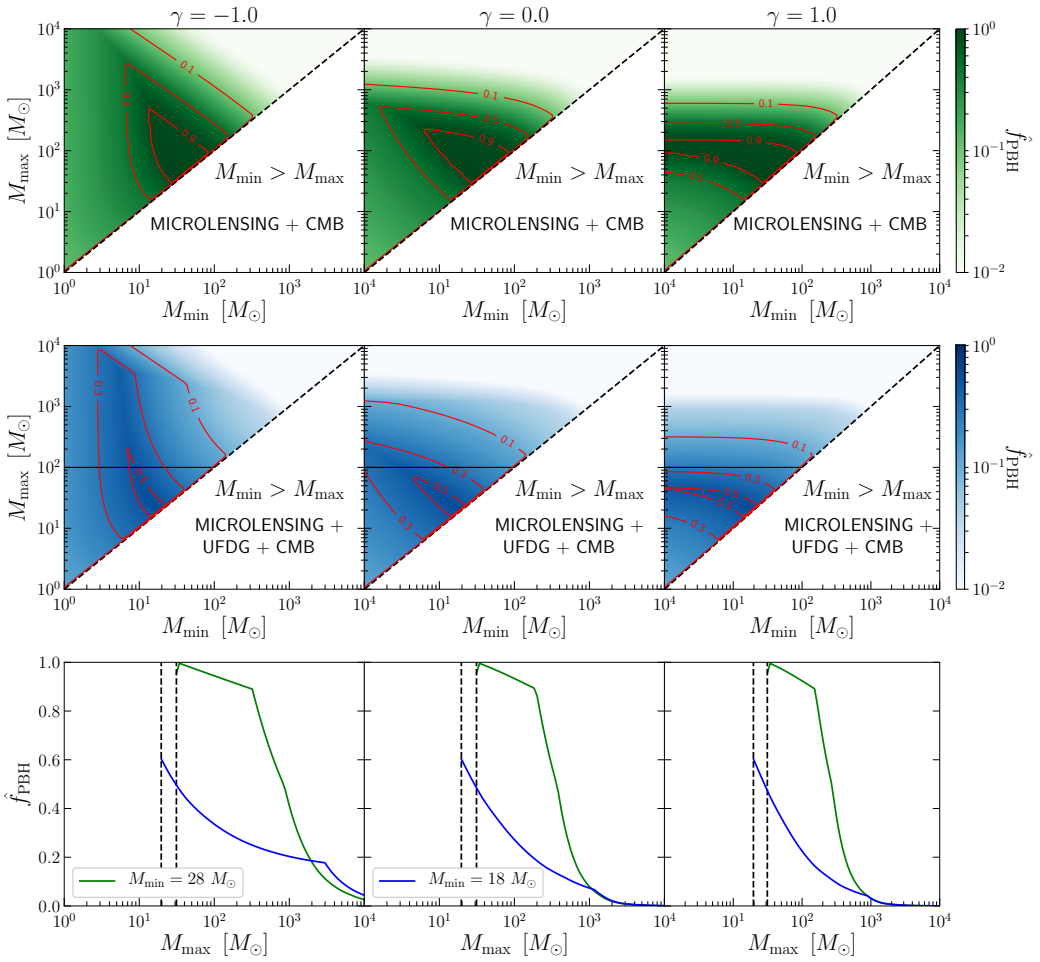

Figure 10. Maximum allowed PBHs fraction for PL distributions for different γ and sets of observables. *Upper panels*: microlensing and CMB constraints. *Central panels*: microlensing, UFDG and CMB constraints. Black solid lines signals the region of tighter validity conditions while black dashed lines signals the region $M_{\rm min} > M_{\rm max}$. *Lower panels*: sections, chosen to intercept the maximum, of the maximum $f_{\rm PBH}$ allowed as a function of $M_{\rm min}$ for fixed $M_{\rm max}$. Black dashed lines signals the region $M_{\rm min} > M_{\rm max}$.

to test and set constraints on this scenario. However, to date most of the PBH constraints have been derived assuming a monochromatic mass distribution, which is over-simplistic.

In this paper we provide a new way to compare extended to monochromatic mass distribution constraints and translate MMD constraints on the maximum allowed PBH abundance to EMD constraints. The aim of our approach is to provide the most accurate and physically-motivated framework to date, while still being quick and easy to implement. For every observable and EMD, we show that there is a corresponding MMD with an "Equivalent Mass" which produces the same physical and observational effects.

JCAP01(2018)004

We provide three practical examples of our method, considering the MMD constraints of the maximum allowed fraction of PBH from microlensing, ultra-faint dwarf galaxies and CMB constraints. We then focus on the mass window at tens of $M_\odot$ — where for MMD a $f_{\rm PBH} \sim 1$ is allowed — for two popular and physically motivated families of EMDs: Power Law and Lognormal. When considering EMDs and their observational constraints, it is important to consider carefully their regime of validity. In fact the modelling of each observable relies on several assumptions which, while valid for a MMD, may not be for an EMD, especially if it has extended tails. Ignoring this important fact may lead to unreliable or even unphysical constraints. This is a danger not only for the approach presented here but of any study of PBH constraints with EMDs: we study this issue in detail and present an easy to use reference to avoid this pitfall.

We find that in both cases (lognormal and power law EMDs), for a consistent and valid choice of distribution parameters, the $\hat{f}_{PBH} \sim 1$ mass window shrinks or is displaced, allowing a lower PBHs abundance compared to MMD calculations. Before exploring a larger EMD parameter space, the physical description behind constraints from microlensing, dynamics of dwarf galaxies and CMB energy injection must be improved to be valid over a wider mass range.

As it is well known, because of all the theoretical uncertainties, all constraints on the maximum allowed $f_{\rm PBH}$ have to be considered as order of magnitudes rather than exact numbers. Similarly the behaviour of this window, where $\hat{f}_{\rm PBH} \sim 1$ is allowed, for the considered EMDs should not be thought as general, in fact it could well become wider and allow a larger $f_{\rm PBH}$ for other EMDs. A window that is closed for a MMD can open for an EMD. We leave the exploration of other windows in other mass range for future work. We envision that our effective "equivalent mass" technique will be useful to study systematically different EMDs and a broad range of observables.

Acknowledgments

We thank Yacine Ali-Haïmoud for sharing his modified version of HyRec and Enrico Barausse, Julian B. Muñoz and Tommi Tenkanen for useful comments on this manuscript. Funding for this work was partially provided by the Spanish MINECO under projects AYA2014-58747-P AEI/FEDER UE and MDM-2014-0369 of ICCUB (Unidad de Excelencia Maria de Maeztu). NB is supported by the Spanish MINECO under grant BES-2015-073372. JLB is supported by the Spanish MINECO under grant BES-2015-071307, co-funded by the ESF. AR has received funding from the People Programme (Marie Curie Actions) of the European Union H2020 Programme under REA grant agreement number 706896 (COSMOFLAGS). LV acknowledges support of European Union's Horizon 2020 research and innovation programme (BePreSySe, grant agreement 725327).

References

[1] Planck collaboration, P.A.R. Ade et al., *Planck 2015 results. XIII. Cosmological parameters*, *Astron. Astrophys.* **594** (2016) A13 [arXiv:1502.01589] [INSPIRE].

[2] G. Bertone, D. Hooper and J. Silk, *Particle dark matter: Evidence, candidates and constraints*, *Phys. Rept.* **405** (2005) 279 [hep-ph/0404175] [INSPIRE].

[3] G. Jungman, M. Kamionkowski and K. Griest, *Supersymmetric dark matter*, *Phys. Rept.* **267** (1996) 195 [hep-ph/9506380] [INSPIRE].

JCAP01(2018)004

[4] J. Preskill, M.B. Wise and F. Wilczek, *Cosmology of the Invisible Axion*, *Phys. Lett.* **120B** (1983) 127 [INSPIRE].

[5] G.F. Chapline, *Cosmological effects of primordial black holes*, *Nature* **253** (1975) 251.

[6] G. Arcadi, M. Dutra, P. Ghosh, M. Lindner, Y. Mambrini, M. Pierre et al., *The Waning of the WIMP? A Review of Models, Searches and Constraints*, arXiv:1703.07364 [INSPIRE].

[7] I. Stern, *ADMX Status*, PoS(ICHEP2016)198 [arXiv:1612.08296] [INSPIRE].

[8] VIRGO, LIGO SCIENTIFIC collaborations, B.P. Abbott et al., *Observation of Gravitational Waves from a Binary Black Hole Merger*, *Phys. Rev. Lett.* **116** (2016) 061102 [arXiv:1602.03837] [INSPIRE].

[9] S. Bird, I. Cholis, J.B. Muñoz, Y. Ali-Haïmoud, M. Kamionkowski, E.D. Kovetz et al., *Did LIGO detect dark matter?*, *Phys. Rev. Lett.* **116** (2016) 201301 [arXiv:1603.00464] [INSPIRE].

[10] S. Clesse and J. García-Bellido, *The clustering of massive Primordial Black Holes as Dark Matter: measuring their mass distribution with Advanced LIGO*, *Phys. Dark Univ.* **15** (2017) 142 [arXiv:1603.05234] [INSPIRE].

[11] B.J. Carr, K. Kohri, Y. Sendouda and J. Yokoyama, *New cosmological constraints on primordial black holes*, *Phys. Rev.* **D 81** (2010) 104019 [arXiv:0912.5297] [INSPIRE].

[12] A. Raccanelli, F. Vidotto and L. Verde, *Effects of primordial black holes quantum gravity decay on galaxy clustering*, arXiv:1708.02588 [INSPIRE].

[13] A. Barnacka, J.F. Glicenstein and R. Moderski, *New constraints on primordial black holes abundance from femtolensing of gamma-ray bursts*, *Phys. Rev.* **D 86** (2012) 043001 [arXiv:1204.2056] [INSPIRE].

[14] P.W. Graham, S. Rajendran and J. Varela, *Dark Matter Triggers of Supernovae*, *Phys. Rev.* **D 92** (2015) 063007 [arXiv:1505.04444] [INSPIRE].

[15] F. Capela, M. Pshirkov and P. Tinyakov, *Constraints on primordial black holes as dark matter candidates from capture by neutron stars*, *Phys. Rev.* **D 87** (2013) 123524 [arXiv:1301.4984] [INSPIRE].

[16] K. Griest, A.M. Cieplak and M.J. Lehner, *Experimental Limits on Primordial Black Hole Dark Matter from the First 2 yr of Kepler Data*, *Astrophys. J.* **786** (2014) 158 [arXiv:1307.5798] [INSPIRE].

[17] H. Niikura, M. Takada, N. Yasuda, R.H. Lupton, T. Sumi, S. More et al., *Microlensing constraints on primordial black holes with the Subaru/HSC Andromeda observation*, arXiv:1701.02151 [INSPIRE].

[18] EROS-2 collaboration, P. Tisserand et al., *Limits on the Macho Content of the Galactic Halo from the EROS-2 Survey of the Magellanic Clouds*, *Astron. Astrophys.* **469** (2007) 387 [astro-ph/0607207] [INSPIRE].

[19] S. Calchi Novati, S. Mirzoyan, P. Jetzer and G. Scarpetta, *Microlensing towards the SMC: a new analysis of OGLE and EROS results*, *Mon. Not. Roy. Astron. Soc.* **435** (2013) 1582 [arXiv:1308.4281] [INSPIRE].

[20] MACHO collaboration, R.A. Allsman et al., *MACHO project limits on black hole dark matter in the 1-30 solar mass range*, *Astrophys. J.* **550** (2001) L169 [astro-ph/0011506] [INSPIRE].

[21] E. Mediavilla, J.A. Muñoz, E. Falco, V. Motta, E. Guerras, H. Canovas et al., *Microlensing-Based Estimate of the Mass Fraction in Compact Objects in Lens*, *Astrophys. J.* **706** (2009) 1451 [arXiv:0910.3645] [INSPIRE].

[22] T.D. Brandt, *Constraints on MACHO Dark Matter from Compact Stellar Systems in Ultra-Faint Dwarf Galaxies*, *Astrophys. J.* **824** (2016) L31 [arXiv:1605.03665] [INSPIRE].

[23] D. Gaggero et al., *Searching for Primordial Black Holes in the radio and X-ray sky*, *Phys. Rev. Lett.* **118** (2017) 241101 [arXiv:1612.00457] [INSPIRE].

JCAP01(2018)004

[24] D.P. Quinn, M.I. Wilkinson, M.J. Irwin, J. Marshall, A. Koch and V. Belokurov, *On the reported death of the MACHO era*, *Mon. Not. Roy. Astron. Soc. Lett.* **396** (2009) L11 [arXiv:0903.1644].

[25] B.J. Carr and M. Sakellariadou, *Dynamical constraints on dark compact objects*, *Astrophys. J.* **516** (1999) 195 [INSPIRE].

[26] P.N. Wilkinson, D.R. Henstock, I.W.A. Browne, A.G. Polatidis, P. Augusto, A.C.S. Readhead et al., *Limits on the cosmological abundance of supermassive compact objects from a search for multiple imaging in compact radio sources*, *Phys. Rev. Lett.* **86** (2001) 584 [astro-ph/0101328] [INSPIRE].

[27] N. Afshordi, P. McDonald and D.N. Spergel, *Primordial black holes as dark matter: The Power spectrum and evaporation of early structures*, *Astrophys. J.* **594** (2003) L71 [astro-ph/0302035] [INSPIRE].

[28] M. Ricotti, J.P. Ostriker and K.J. Mack, *Effect of Primordial Black Holes on the Cosmic Microwave Background and Cosmological Parameter Estimates*, *Astrophys. J.* **680** (2008) 829 [arXiv:0709.0524] [INSPIRE].

[29] Y. Ali-Haïmoud and M. Kamionkowski, *Cosmic microwave background limits on accreting primordial black holes*, *Phys. Rev.* **D 95** (2017) 043534 [arXiv:1612.05644] [INSPIRE].

[30] V. Poulin, P.D. Serpico, F. Calore, S. Clesse and K. Kohri, *CMB bounds on disk-accreting massive primordial black holes*, *Phys. Rev.* **D 96** (2017) 083524 [arXiv:1707.04206] [INSPIRE].

[31] J. Luis Bernal, N. Bellomo, A. Raccanelli and L. Verde, *Cosmological implications of Primordial Black Holes*, *JCAP* **10** (2017) 052 [arXiv:1709.07465] [INSPIRE].

[32] A. Raccanelli, E.D. Kovetz, S. Bird, I. Cholis and J.B. Muñoz, *Determining the progenitors of merging black-hole binaries*, *Phys. Rev.* **D 94** (2016) 023516 [arXiv:1605.01405] [INSPIRE].

[33] A. Raccanelli, *Gravitational wave astronomy with radio galaxy surveys*, *Mon. Not. Roy. Astron. Soc.* **469** (2017) 656 [arXiv:1609.09377] [INSPIRE].

[34] I. Cholis et al., *Orbital eccentricities in primordial black hole binaries*, *Phys. Rev.* **D 94** (2016) 084013 [arXiv:1606.07437] [INSPIRE].

[35] J.B. Muñoz, E.D. Kovetz, L. Dai and M. Kamionkowski, *Lensing of Fast Radio Bursts as a Probe of Compact Dark Matter*, *Phys. Rev. Lett.* **117** (2016) 091301 [arXiv:1605.00008] [INSPIRE].

[36] E.D. Kovetz, I. Cholis, P.C. Breysse and M. Kamionkowski, *Black hole mass function from gravitational wave measurements*, *Phys. Rev.* **D 95** (2017) 103010 [arXiv:1611.01157] [INSPIRE].

[37] E.D. Kovetz, *Probing Primordial-Black-Hole Dark Matter with Gravitational Waves*, *Phys. Rev. Lett.* **119** (2017) 131301 [arXiv:1705.09182] [INSPIRE].

[38] Y. Ali-Haïoud, E.D. Kovetz and M. Kamionkowski, *The merger rate of primordial-black-hole binaries*, arXiv:1709.06576 [INSPIRE].

[39] S.W. Hawking, *Black hole explosions?*, *Nature* **248** (1974) 30 [INSPIRE].

[40] J.R. Rice and B. Zhang, *Cosmological evolution of primordial black holes*, *JHEAp* **13-14** (2017) 22 [arXiv:1702.08069] [INSPIRE].

[41] M. Raidal, V. Vaskonen and H. Veermäe, *Gravitational Waves from Primordial Black Hole Mergers*, *JCAP* **09** (2017) 037 [arXiv:1707.01480] [INSPIRE].

[42] B.J. Carr, *The Primordial black hole mass spectrum*, *Astrophys. J.* **201** (1975) 1 [INSPIRE].

[43] S. Clesse and J. García-Bellido, *Massive Primordial Black Holes from Hybrid Inflation as Dark Matter and the seeds of Galaxies*, *Phys. Rev.* **D 92** (2015) 023524 [arXiv:1501.07565] [INSPIRE].

JCAP01(2018)004

[44] B. Carr, T. Tenkanen and V. Vaskonen, *Primordial black holes from inflaton and spectator field perturbations in a matter-dominated era*, *Phys. Rev.* **D 96** (2017) 063507 [arXiv:1706.03746] [INSPIRE].

[45] S.W. Hawking, I.G. Moss and J.M. Stewart, *Bubble Collisions in the Very Early Universe*, *Phys. Rev.* **D 26** (1982) 2681 [INSPIRE].

[46] S.W. Hawking, *Black Holes From Cosmic Strings*, *Phys. Lett.* **B 231** (1989) 237 [INSPIRE].

[47] T. Matsuda, *Primordial black holes from cosmic necklaces*, *JHEP* **04** (2006) 017 [hep-ph/0509062] [INSPIRE].

[48] V.A. Berezin, V.A. Kuzmin and I.I. Tkachev, *Thin wall vacuum domains evolution*, *Phys. Lett.* **B 120** (1983) 91 [INSPIRE].

[49] B. Carr, F. Kühnel and M. Sandstad, *Primordial Black Holes as Dark Matter*, *Phys. Rev.* **D 94** (2016) 083504 [arXiv:1607.06077] [INSPIRE].

[50] B. Carr, M. Raidal, T. Tenkanen, V. Vaskonen and H. Veermäe, *Primordial black hole constraints for extended mass functions*, *Phys. Rev.* **D 96** (2017) 023514 [arXiv:1705.05567] [INSPIRE].

[51] A.M. Green, *Microlensing and dynamical constraints on primordial black hole dark matter with an extended mass function*, *Phys. Rev.* **D 94** (2016) 063530 [arXiv:1609.01143] [INSPIRE].

[52] J. Yokoyama, *Cosmological constraints on primordial black holes produced in the near critical gravitational collapse*, *Phys. Rev.* **D 58** (1998) 107502 [gr-qc/9804041] [INSPIRE].

[53] K. Kannike, L. Marzola, M. Raidal and H. Veermäe, *Single Field Double Inflation and Primordial Black Holes*, *JCAP* **09** (2017) 020 [arXiv:1705.06225] [INSPIRE].

[54] B. Paczynski, *Gravitational microlensing by the galactic halo*, *Astrophys. J.* **304** (1986) 1 [INSPIRE].

[55] K. Griest, *Galactic Microlensing as a Method of Detecting Massive Compact Halo Objects*, *Astrophys. J.* **366** (1991) 412 [INSPIRE].

[56] A. De Rújula, P. Jetzer and E. Massó, *Dark mass moments*, *Mon. Not. Roy. Astron. Soc.* **250** (1991) 348 [INSPIRE].

[57] MACHO collaboration, C. Alcock et al., *The MACHO project LMC microlensing results from the first two years and the nature of the galactic dark halo*, *Astrophys. J.* **486** (1997) 697 [astro-ph/9606165] [INSPIRE].

[58] A.M. Green, *Astrophysical uncertainties on stellar microlensing constraints on multi-Solar mass primordial black hole dark matter*, *Phys. Rev.* **D 96** (2017) 043020 [arXiv:1705.10818] [INSPIRE].

[59] S.M. Koushiappas and A. Loeb, *Dynamics of Dwarf Galaxies Disfavor Stellar-Mass Black Holes as Dark Matter*, *Phys. Rev. Lett.* **119** (2017) 041102 [arXiv:1704.01668] [INSPIRE].

[60] DES collaboration, T.S. Li et al., *Farthest Neighbor: The Distant Milky Way Satellite Eridanus II*, *Astrophys. J.* **838** (2017) 8 [arXiv:1611.05052] [INSPIRE].

[61] J. Silk, *Feedback by Massive Black Holes in Gas-rich Dwarf Galaxies*, *Astrophys. J.* **839** (2017) L13 [arXiv:1703.08553] [INSPIRE].

[62] J. Binney and S. Tremaine, *Galactic Dynamics*, second edition, Princeton University Press (2008).

[63] Y. Ali-Haïmoud and C.M. Hirata, *Ultrafast effective multi-level atom method for primordial hydrogen recombination*, *Phys. Rev.* **D 82** (2010) 063521 [arXiv:1006.1355] [INSPIRE].

[64] Y. Ali-Haïmoud and C.M. Hirata, *HyRec: A fast and highly accurate primordial hydrogen and helium recombination code*, *Phys. Rev.* **D 83** (2011) 043513 [arXiv:1011.3758] [INSPIRE].

JCAP01(2018)004

Journal of Cosmology and Astroparticle Physics
An IOP and SISSA journal

GW×LSS: chasing the progenitors of merging binary black holes

Giulio Scelfo,[a,b] **Nicola Bellomo,**[b,c] **Alvise Raccanelli,**[b] **Sabino Matarrese**[a,d,e,f] **and Licia Verde**[b,g]

[a]Dipartimento di Fisica e Astronomia G. Galilei, Università degli Studi di Padova, via Marzolo 8, I-35131 Padova, Italy
[b]ICC, University of Barcelona, IEEC-UB, Martí i Franquès, 1, E-08028 Barcelona, Spain
[c]Dept. de Física Quàntica i Astrofísica, Universitat de Barcelona, Martí i Franquès 1, E-08028 Barcelona, Spain
[d]INFN — Sezione di Padova, via F. Marzolo 8, I-35131 Padova, Italy
[e]INAF — Osservatorio Astronomico di Padova, vicolo dell'Osservatorio 5, I-35122 Padova, Italy
[f]Gran Sasso Science Institute, viale F. Crispi 7, I-67100 L'Aquila, Italy
[g]ICREA, Pg. Lluis Companys 23, Barcelona, E-08010, Spain
E-mail: giulio.scelfo@studenti.unipd.it, nicola.bellomo@icc.ub.edu, alvise@icc.ub.edu, sabino.matarrese@pd.infn.it, liciaverde@icc.ub.edu

Received September 14, 2018
Accepted September 15, 2018
Published September 25, 2018

Abstract. Are the stellar-mass merging binary black holes, recently detected by their gravitational wave signal, of stellar or primordial origin? Answering this question will have profound implications for our understanding of the Universe, including the nature of dark matter, the early Universe and stellar evolution. We build on the idea that the clustering properties of merging binary black holes can provide information about binary formation mechanisms and origin. The cross-correlation of galaxy with gravitational wave catalogues carries information about whether black hole mergers trace more closely the distribution of dark matter — indicative of primordial origin — or that of stars harboured in luminous and massive galaxies — indicative of a stellar origin. We forecast the detectability of such signal for several forthcoming and future gravitational wave interferometers and galaxy surveys, including, for the first time in such analyses, an accurate modelling for the different merger rates, lensing magnification and other general relativistic effects. Our results show that forthcoming experiments could allow us to test most of the parameter space of the still viable models investigated, and shed more light on the issue of binary black hole origin and evolution.

Keywords: gravitational waves / experiments, power spectrum, primordial black holes, redshift surveys

ArXiv ePrint: 1809.03528

https://doi.org/10.1088/1475-7516/2018/09/039

JCAP09(2018)039

Contents

1 Introduction

The first detection of gravitational waves (GWs) emitted by the coalescence of two black holes (BHs) of approximately 30 $M_\odot$ [1, 2] opened the era of gravitational waves astronomy, not only by confirming General Relativity predictions, but also establishing a new way to observe and analyse the cosmos. Even if some authors expected such massive progenitors to be the first sources to be detected, see e.g., refs. [3–6], this fact was hailed by part of the community as unexpected and led some researchers to suggest that such events may not be uncommon. Indeed other GWs events followed [7–10] and confirmed that apparently a significant fraction of the detected progenitors has masses between 20 and 40 $M_\odot$. Such large masses of the progenitors are not incompatible with classical stellar/binary evolution [11–13]. Nevertheless the possibility that BHs with an origin different from the standard end-point of stellar evolution and constituting a significant fraction of the dark matter regained interest [14, 15].

The authors of refs. [16–18] were the first to show analytically that, because of large density fluctuations in the primordial cosmic fluid, some extremely overdense regions in the primordial Universe may have overcome pressure forces and have collapsed to give birth to so-called Primordial Black Holes (PBHs). These results were later confirmed by the authors of ref. [19], who were the first to provide general relativistic numerical computations of PBHs formation during the radiation-dominated era. Even if the PBHs formation mechanism is unknown, many proposals have been made, including collapse of cosmic string loops [20–22] and domain walls [23, 24], bubble collisions [25, 26], through the collapse of large fluctuations produced during inflation as pioneered in refs. [27–29] or even through the collapse of (interacting) dark matter clumps [30].

Given the high interest in PBHs as dark matter candidates, a remarkable amount of different observational constraints have been obtained, including constraints coming from

JCAP09(2018)039

gravitational lensing effects [31–40], dynamical effects [41–46] and accretion effects [47–51]. Even if these constraints cover the whole mass range and seem to disfavour PBHs as a significant fraction of the dark matter, these results are far from being conclusive due to the variety of assumptions involved, see e.g., [52, 53]. Some mass "windows" still exist, for instance one around $10^{-10}\ M_\odot$ and another 10 $M_\odot$, where the latter one can be probed by future GWs observatories as Advanced LIGO (aLIGO) [54] or Einstein Telescope (ET) [55].

Despite the fact PBHs may not constitute the totality of the dark matter, it is valuable to explore different ways to determine if mergers progenitors' origin is stellar or primordial. Several proposals have been made, including testing the cross-correlation between galaxy and GW maps [56–58], BHs binaries orbital eccentricity [59], fast radio bursts [60], the BHs mass function [61, 62].

In this work we focus on developing further the cross-correlation approach suggested by the authors of ref. [56], who show that the statistical properties of the type of galaxy (or halo) hosting a GWs event can provide information about the system origin (stellar or primordial). In fact, in more massive halos the typical velocities are higher than those in the less massive ones (the reader can think of the virial theorem or check numerical simulations [63]). As a consequence, it is much more probable that two PBHs form a gravitationally bound binary through GWs emission in low-mass halos, since the cross section of such process is inversely proportional to some power of the relative velocity of the progenitors. The higher velocity dispersion of high-mass halos make this process for PBHs less likely to happen. In addition, low-mass halos tend to be less luminous [64] than high-mass ones and trace more closely the dark matter distribution than high-mass halos. On the other hand the merger probability for stellar black holes is more likely to correlate with galaxies' (or halos') stellar mass, hence stellar black holes mergers tend to happen in more luminous and massive halos. Recall that star formation efficiency increases with halo mass for halo of masses below $10^{12} M_\odot$. It decrease for higher mass-halos but these are very rare and more closely associated to galaxy clusters rather than galaxies. We refer the interested reader to ref. [65] and references therein.

Therefore, once a significant number of GWs coming from BHs mergers will be detected, it will be useful to correlate the corresponding events map with a map of galaxies. If the BHs progenitors were mostly of stellar origin, GWs events would be associated with massive halos, and thus would be highly correlated with luminous galaxies. On the other hand, if these progenitors were more likely to have primordial origin, GWs would come mostly from low mass halos (i.e., they would be poorly correlated with luminous galaxies). While mergers of BHs of primordial origin tend to trace the filaments (dark-matter/low mass-halos distribution[1]) of the large-scale structure, stellar-BHs mergers tend to trace the distribution of galaxies of high stellar mass. The clustering properties of these two populations and the statistical properties the two maps are different. Low-mass halos tracing filaments are less strongly clustered than high (stellar) mass galaxies: in particular they have different *bias* parameters. The bias parameter governs the ratio of clustering amplitude of the selected tracer to that of the dark matter.

At the moment too few GWs events have been detected to measure the auto and cross correlation of maps of GWs events and galaxies, but during next LIGO's runs, thousands of events are likely to be detected due to the improved sensitivity. On the other hand, during the next decade a large volume of the Universe at high redshift will be surveyed thanks

[1]Since we are performing a statistical analysis, the presence of subhalos inside high mass halos does not affect significantly the results because of their relative abundance compared to "field" halos (located in lower density regions such as filaments) of the same mass.

JCAP09(2018)039

to several surveys, as EMU [66], DESI [67] or SKA [68], which we consider in the rest of the paper. Here we develop a Fisher and a $\Delta\chi^2$ analysis to forecast the ability of future surveys to accomplish this goal. We improve the treatment of ref. [56] in different ways. Firstly, we consider both cross and auto correlation terms between our tracers (more details in section 2), whereas the latter ones were previously neglected. Secondly, our computations include all possible general relativistic effects which, as we will show, can influence the results. Thirdly, we use a theoretically-motivated PBHs merger rate without neglecting its redshift dependence. Finally, when modelling the GWs events distribution, we provide for the first time an analytic expression for the magnification bias of gravitational waves. This is a step forward in the study of the lensing of gravitational waves coming from black holes or neutron stars mergers and can provide significant insight on BHs binary formation and evolution [69–71], on estimates of the luminosity distance [72] or even on alternatives to General Relativity [73].

The paper is structured as follows: in section 2 we explain the methodology used in this work and introduce the multi-tracer cross-correlation formalism, in section 3 we characterize the galaxies (3.1) and GWs (3.2) tracers considered while in section 4 we present the results of the forecast. Finally we conclude in section 5.

2 Methodology and galaxy-GW correlation

Since BH-BH mergers do not have an electromagnetic counterpart, the identification of their host object is impossible even if the event is measured by more than three detectors. Because of the poor localisation in the sky of the GWs events, the GWs maps are typically very "low resolution". For this reason we approach the problem in a statistical way, by using measurements and statistical properties of their number counts. In particular, we work in harmonic space and we consider the number counts angular power spectrum, C_ℓ, where only low multipoles ℓ are considered because of the maps' low angular resolution. The maximum multipole $\ell_{\rm max}$ is determined by the angular resolution θ that can be achieved: $\ell_{\rm max} \sim 180^o/\theta$. For the aLIGO+Virgo network $\ell_{\rm max} = 20$, once also LIGO-India and KAGRA are included, we improve the spatial resolution up to $\ell_{\rm max} = 50$ and finally with the futuristic Einstein Telescope, $\ell_{\rm max} = 100$ will be reached. The interested reader can check refs. [74–77]. We discuss the benefits of having higher resolution in GWs maps in section 4.2.

In the following we assume to have (tomographic) maps of GWs events and of galaxies (i.e., the *tracers*). The observed harmonic coefficients used to compute the angular power spectra are given by

$$a^X_{\ell m}(z_i) = s^X_{\ell m}(z_i) + n^X_{\ell m}(z_i), \tag{2.1}$$

where $s^X_{\ell m}$ and $n^X_{\ell m}$ are the partial wave coefficients of the signal and of the noise for tracer X. We consider the noise angular power spectrum to be given only by a shot noise term $\mathcal{N}^X_\ell(z_i)$ and we assume that the noise terms from different experiments and different redshift bins are uncorrelated, which means that

$$\langle n^X_{\ell m}(z_i) n^{Y^*}_{\ell' m'}(z_j)\rangle = \delta_{\ell\ell'}\delta_{mm'}\delta_{XY}\delta_{ij}\mathcal{N}^X_\ell(z_i), \tag{2.2}$$

where δ denotes the Kronecker delta. The expectation value of the signal gives the C_ℓs [78, 79],

$$\langle s^X_{\ell m}(z_i) s^{Y^*}_{\ell' m'}(z_j)\rangle = \delta_{\ell\ell'}\delta_{mm'}C^{XY}_\ell(z_i, z_j), \tag{2.3}$$

JCAP09(2018)039

while the signal-cross-noise expectation value is given by

$$\langle s^X_{\ell m}(z_i) n^{Y^*}_{\ell' m'}(z_j)\rangle = 0, \tag{2.4}$$

since we assume signal and noise to be statistically independent. Finally, the observed angular power spectrum $\tilde{C}^{XY}_\ell(z_i, z_j)$ reads as

$$\langle a^X_{\ell m}(z_i) a^{Y^*}_{\ell' m'}(z_i)\rangle = \delta_{\ell\ell'}\delta_{mm'}\tilde{C}^{XY}_\ell(z_i, z_j) = \delta_{\ell\ell'}\delta_{mm'}\left[C^{XY}_\ell(z_i, z_j) + \delta_{XY}\delta_{ij}\mathcal{N}^X_\ell(z_i)\right]. \tag{2.5}$$

Following the notation of ref. [80] (which is re-arranged differently than the standard way, but reflects how the public code `CLASS` [81, 82] is structured) and generalizing their formalism to the case of multiple tracers we can write the angular power spectrum as

$$C^{XY}_\ell(z_i, z_j) = \frac{2}{\pi}\int \frac{dk}{k}\mathcal{P}(k)\Delta^{X,z_i}_\ell(k)\Delta^{Y,z_j}_\ell(k), \tag{2.6}$$

where $\{X, Y\}$ stands for the different tracers (galaxies and GWs in our case), $\mathcal{P}(k) = k^3 P(k)$ is the primordial power spectrum and

$$\Delta^{X,z_i}_\ell(k) = \int_{z_i-\Delta z}^{z_i+\Delta z} dz \frac{dN_X}{dz} W(z, z_i)\Delta^X_\ell(k, z), \tag{2.7}$$

where we have introduced a window function[2] $W(z, z_i)$, centered at redshift z_i with bin half-width Δz, the source number density per redshift interval $\frac{dN_X}{dz}$, and the tracer X angular number count fluctuation $\Delta^X_\ell(k, z)$. The integral of $W(z, z_i)\dfrac{dN_X}{dz}$ is normalized to unity. In general the observed number count fluctuation receives contributions from density (den), velocity (vel), lensing (len) and gravity (gr) effects [80, 83]:

$$\Delta_\ell(k, z) = \Delta^{\rm den}_\ell(k, z) + \Delta^{\rm vel}_\ell(k, z) + \Delta^{\rm len}_\ell(k, z) + \Delta^{\rm gr}_\ell(k, z). \tag{2.8}$$

We report in appendix A the complete form of the various terms in equation (2.8). Even if the bias parameter b_X of the tracer X enters only in the density contribution $\Delta^{\rm den}_\ell(k, z)$, we cannot overlook the effect of the other terms on the signal-to-noise, as sometimes done in the literature. Since the public code `CLASS` allows us to choose whether include or not the velocity, lensing and gravity effects in the computation of the C_ℓ, we estimate the error one would introduce by neglecting these contributions in section 4.1. The reader interested in a more in general discussion on the importance of a correct modelling of an observable can check ref. [84]. To compute the angular power spectra we extend the public code `CLASS` to include the possibility to have different tracers ($X \neq Y$). We present this new version of `CLASS`, called `Multi_CLASS`, in ref. [84]. It should be noticed that, in the case of different tracers, the angular projections are not symmetrical under the exchange of redshift $z_i \longleftrightarrow z_j$, therefore, if we have n redshift bins, we have to compute n^2 different C_ℓ, while for identical tracers we have to compute only $n(n+1)/2$ angular power spectra.

Hereafter we consider two tracers, galaxies and gravitational waves, labelled by $\{\mathrm{g}, \mathrm{GW}\}$. For illustrative purposes, the tracers have been divided in three redshift bins with central redshift values $\{z_1,\ z_2,\ z_3\} = \{1.5,\ 2.5,\ 3.5\}$ and bin half-width $\Delta z = 0.5$. This choice refers to the main generic case discussed in section 4.1; in section 4.2, we also provide results for specific surveys: EMU [66] (a wide-field radio continuum survey planned for the new

[2] In this work we use a Top-Hat window function.

JCAP09(2018)039

Australian Square Kilometre Array Pathfinder telescope), DESI [67] (a Stage IV ground-based dark energy experiment planned to study baryon acoustic oscillations and the growth of structure through redshift-space distortions with a wide-area galaxy and quasar redshift survey), and SKA [68] (as a radio continuum survey with 5 μJy flux limit at redshift $z < 5$). For gravitational waves experiments we consider aLIGO [54] (a GWs experiment which currently being developed with enough sensitivity to detect 30 $M_\odot$ binary black holes mergers up a redhsift $z_{\rm max} = 0.4$), LIGO-India [85] and KAGRA [86] (we also include these last two detectors as to improve event localization in the sky and thus increase the resolution of the resulting GW map) and Einstein Telescope (ET) [55] (a planned GWs detector with higher sensitivity and resolution than aLIGO).

We estimate the capability of future surveys to determine BHs mergers progenitors' origin in two different ways, one more conservative that follows the approach suggested in ref. [56], the other more optimal and closer to an actual data analysis but that relies on modelling well some properties of the tracers that are currently still uncertain. We perform what can be seen as a null hypothesis testing, comparing two models, one in which progenitors origin is stellar, the other in which is primordial. We assume one model as fiducial and we check if the alternative model can be differentiated from the fiducial one by computing a Signal-to-Noise ratio S/N. The null hypothesis is that the model is indistinguishable from the fiducial, which happens for low values of the Signal-to-Noise ratio ($S/N \lesssim 1$).

The first procedure relies on a standard Fisher analysis, where we consider a parameter set $\{\theta_\alpha\}$, given by the cold dark matter physical density $\omega_{\rm cdm}$, the baryon physical density $\omega_{\rm b}$, the angular scale of the sound horizon at decoupling $100\theta_s$, the amplitude of scalar perturbations $\log 10^{10} A_s$, the spectral index n_s and an effective bias $B_{\rm g}$ and $B_{\rm GW}$ of galaxies and GWs, respectively.[3] More details on how we calculate the effective bias of the tracers are given in section 3. Following the authors of refs. [87–89], we write the upper triangular part of the covariance matrix $\mathcal{C}_\ell$ as

$$\mathcal{C}_\ell = \begin{bmatrix} \tilde{C}_\ell^{\rm gg}(z_1,z_1) & \tilde{C}_\ell^{\rm gg}(z_1,z_2) & \tilde{C}_\ell^{\rm gg}(z_1,z_3) & \tilde{C}_\ell^{\rm gGW}(z_1,z_1) & \tilde{C}_\ell^{\rm gGW}(z_1,z_2) & \tilde{C}_\ell^{\rm gGW}(z_1,z_3) \\ & \tilde{C}_\ell^{\rm gg}(z_2,z_2) & \tilde{C}_\ell^{\rm gg}(z_2,z_3) & \tilde{C}_\ell^{\rm gGW}(z_2,z_1) & \tilde{C}_\ell^{\rm gGW}(z_2,z_2) & \tilde{C}_\ell^{\rm gGW}(z_2,z_3) \\ & & \tilde{C}_\ell^{\rm gg}(z_3,z_3) & \tilde{C}_\ell^{\rm gGW}(z_3,z_1) & \tilde{C}_\ell^{\rm gGW}(z_3,z_2) & \tilde{C}_\ell^{\rm gGW}(z_3,z_3) \\ & & & \tilde{C}_\ell^{\rm GWGW}(z_1,z_1) & \tilde{C}_\ell^{\rm GWGW}(z_1,z_2) & \tilde{C}_\ell^{\rm GWGW}(z_1,z_3) \\ & & & & \tilde{C}_\ell^{\rm GWGW}(z_2,z_2) & \tilde{C}_\ell^{\rm GWGW}(z_2,z_3) \\ & & & & & \tilde{C}_\ell^{\rm GWGW}(z_3,z_3) \end{bmatrix}, \tag{2.10}$$

where the lower triangular part can be easily obtained noticing that the covariance matrix is symmetric. The covariance matrix is then used to compute the Fisher matrix elements as

$$F_{\alpha\beta} = f_{\rm sky} \sum_\ell \frac{2\ell+1}{2} {\rm Tr}\left[{\mathcal{C}_\ell}^{-1}(\partial_\alpha \mathcal{C}_\ell){\mathcal{C}_\ell}^{-1}(\partial_\beta \mathcal{C}_\ell)\right], \tag{2.11}$$

where ∂_α indicates the derivative with respect to the parameter θ_α and $f_{\rm sky}$ is the fraction of the sky covered by (the intersection of) both surveys. Notice that, since we are not

[3] The fiducial values of the five standard cosmological parameters reads as

$$\{\omega_{\rm cdm}, \omega_{\rm b}, 100\theta_s, \log 10^{10} A_s, n_s\} = \{0.12038, 0.022032, 1.042143, 3.0980, 0.9619\}. \tag{2.9}$$

The fiducial values of the effective galaxy and GWs bias, $B_{\rm g}$ and $B_{\rm GW}$, are discussed in detail in section 3, but see also table 1, where results discussed in section 3 are summarized.

JCAP09(2018)039

interested in the cosmological parameters but only on the GW bias, we marginalise over all other parameters, also using a prior for the six standard cosmological parameters coming from Planck[4] data [90]. In this first approach the significance for distinguishing a fiducial model (hereafter "fiducial") from an alternative one (hereafter "alternative") is given by the difference between the effective GWs bias parameters (see section 3), after marginalising over all other parameters:

$$\left(\frac{S}{N}\right)^2_{\Delta B/B} = \frac{\left(B_{\rm GW}^{\rm Alternative} - B_{\rm GW}^{\rm Fiducial}\right)^2}{\sigma^2_{B_{\rm GW}^{\rm Fiducial}}}, \tag{2.12}$$

where $B_{\rm GW}$ is the effective bias defined in equation (3.1) and $\sigma_{B_{\rm GW}^{\rm Fiducial}}$ is the Fisher-estimated marginal error on $B_{\rm GW}$.

In the second way we quantify the distance of an alternative model from the fiducial using a $\Delta\chi^2$ statistics. In our case the $\Delta\chi^2$ is given by the logarithm of a likelihood, in particular we assume a likelihood quadratic in the angular power spectra. The resulting $\Delta\chi^2$ statistics reads as

$$\left(\frac{S}{N}\right)^2_{\sqrt{\Delta\chi^2}} \sim \Delta\chi^2 := f_{\rm sky}\sum_{2}^{\ell_{\rm max}}(2\ell+1)(\mathbf{C}_\ell^{\rm Alternative}-\mathbf{C}_\ell^{\rm Fiducial})^T{\rm Cov}_\ell^{-1}(\mathbf{C}_\ell^{\rm Alternative}-\mathbf{C}_\ell^{\rm Fiducial}), \tag{2.13}$$

where the vector $\mathbf{C}_\ell$ contains the same data of the covariance matrix $\mathcal{C}_\ell$ in equation (2.10) but organized as

$$\mathbf{C}_\ell = \begin{pmatrix} C_\ell^{\rm gg}(z_1,z_1) \\ \vdots \\ C_\ell^{\rm gGW}(z_1,z_1) \\ \vdots \\ C_\ell^{\rm GWGW}(z_1,z_1) \\ \vdots \end{pmatrix}, \tag{2.14}$$

and where the ${\rm Cov}_\ell$ is a new covariance matrix, computed from angular power spectra of the fiducial model. We can associate to every element $I = 1,\ldots,21$ of the $\mathbf{C}_\ell$ vector two indices (I_1, I_2), corresponding to the two tracers (in a given redshift bin) that produce the angular power spectra that appear in the $I^{\rm th}$ row; for instance we associate to $I = 1$, corresponding to $C_\ell^{\rm gg}(z_1,z_1)$, the couple of indices $(I_1 = {\rm g}_{z_1}, I_2 = {\rm g}_{z_1})$. Then the elements of the new covariance matrix ${\rm Cov}_\ell$ read as

$$({\rm Cov}_\ell)_{IJ} = \tilde{C}_\ell^{I_1J_1}\tilde{C}_\ell^{I_2J_2} + \tilde{C}_\ell^{I_1J_2}\tilde{C}_\ell^{I_2J_1}, \tag{2.15}$$

where the $\tilde{C}_\ell$ are those defined in equation (2.5).

Notice that in both cases the ability to distinguish between two scenarios can differ according to which model is the alternative model and which one is the fiducial, since the covariance matrix and thus the errors depend (sometimes strongly) on the fiducial model adopted. The Fisher and $\Delta\chi^2$ methods do not have to give the same results because they are two different approximations. The Fisher approach is based on a quadratic approximation of the log-likelihood, estimating its curvature around the fiducial scenario, while the $\Delta\chi^2$ approach is based directly on the log-likelihood and assumes all other parameters are perfectly known.

[4] http://pla.esac.esa.int/pla/.

JCAP09(2018)039

B_X	Generic	EMU	DESI	SKA
Galaxies	1.55	0.83	1.37	1.58
Primordial-Early Binaries	1.00	1.00	1.00	1.00
Primordial-Late Binaries	0.50	0.50	0.50	0.50
End-point of Stellar Evolution	1.81	0.84	1.53	1.85

Table 1. Effective bias for different scenarios and surveys calculated according to equation (3.1).

3 Tracers

In this section we describe the two tracers we consider in this work, galaxies and GWs. For cosmological purposes, each of these tracers is characterised by a source number density per redshift bin and square degree $d^2N_X/dzd\Omega$, bias $b_X(z)$, magnification bias $s_X(z)$ and evolution bias $f_X^{\rm evo}(z)$ parameters, which will be defined in detail below. While some of these quantities are uncertain at the moment, in the following we will attempt to keep track of these uncertainty and how they may affect the final results.

In particular, the two methods presented in section 2 allow us to assess the effect of the uncertainty on the redshift dependence of the bias, in fact in the Fisher analysis case, starting from the source number density and bias, we associate to a given tracer X an *effective* bias parameter

$$B_X = \frac{\int_{z_{\rm min}}^{z_{\rm max}} dz\; b_X(z) \dfrac{d^2N_X}{dzd\Omega}}{\int_{z_{\rm min}}^{z_{\rm max}} dz \dfrac{d^2N_X}{dzd\Omega}} \tag{3.1}$$

over the entire redshift range $[z_{\rm min}, z_{\rm max}]$ of the survey, while in the $\Delta\chi^2$ statistics case, we assume that $b_X(z)$ is known. We summarize the values of the effective bias for the different tracers, scenarios and surveys in table 1. In the first case we assume that only the averaged, effective bias is the relevant quantity known well enough to be used as a model parameter, neglecting the information coming from its redshift dependence, while in the second one we are exploiting it to maximize the differences between the two models.

While the procedure to obtain such quantities for galaxies is well established, in the case of GWs this is quite a new field, and an accurate modelling would involve not only the knowledge of the physics behind the merging process but also an understanding of GWs detection efficiency for mergers events detectors. For this initial investigation we have to make assumptions that may need to be revised and improved in the future. For this reason we present a step-by-step introduction in the GWs section 3.2, guiding the reader through all the details.

3.1 Galaxies

Depending on the experimental set up under consideration, we choose as luminous tracers emission-line galaxies in the redshift range $[0.6 - 1.7]$, targeted by DESI, or star-forming galaxies, targeted by EMU and SKA in the redshift range $[0.0 - 5.0]$. In particular the latter will be mapped up to relatively high redshift by forthcoming radio surveys, as extensively discussed in ref. [91], where they dominate the total number of sources. For the generic case we use radio galaxies, as in the SKA case.

JCAP09(2018)039

In all the three surveys we find that we can model the number density per redshift bin and square degree as

$$\frac{d^2N_{\rm g}}{dzd\Omega} = a_1 z^{a_2} e^{-a_3 z}, \tag{3.2}$$

where different surveys have different parameters a_1, a_2, a_3.[5] For DESI we used figure 3.12 of ref. [67], while for EMU and SKA we used the Tiered Radio Extragalactic Continuum Simulation (T-RECS) [92] catalogue with different detection threshold (100 μJy for EMU and 5 μJy for SKA). We report in the top left panel of figure 1 the three normalized number densities.

The bias for emission-line galaxies is taken to be $b_{\rm g}(z) = 0.84/D(z)$ [67], where $D(z)$ is the linear growth factor normalized to unity today, while the bias for EMU and SKA star-forming galaxies is modelled as [93]

$$b_{\rm g}(z) = \begin{cases} b_0 e^{z b_1}, & z < 3, \\ b_0 e^{3 b_1}, & z \geq 3, \end{cases} \tag{3.3}$$

where $b_0 = 0.755$ and $b_1 = 0.368$. Following the prescription of ref. [94], the bias is assumed to be constant after redshift $z = 3$ to avoid unrealistically high values. We show the bias redshift dependence in the bottom left panel of figure 1. The effective bias of equation (3.1) for these surveys yields $B_{\rm g,EMU} = 0.83$, $B_{\rm g,DESI} = 1.37$ and $B_{\rm g,SKA} = 1.58$.

Gravitational lensing changes the sources surface density on the sky in two competing ways [95], by increasing the area, which in turn decreases the projected number density, but also by magnifying individual sources and promoting faint objects above the magnitude limit. These effects change the observed number density $n_{\rm obs}$ in a flux-limited survey as

$$n_{\rm obs} = n_{\rm g}\left[1 + (5s_{\rm g} - 2)\kappa\right], \tag{3.4}$$

where $n_{\rm g}$ is the intrinsic galaxies number density, $s_{\rm g}$ is called galaxy magnification bias parameter and κ is the convergence [96], namely an isotropic increase or decrease of source size, defined as $\kappa = \frac{1}{2}\nabla^2\psi$, where ψ is the lensing potential. The change in the number of observed sources depends the value of the slope of the faint-end of the luminosity function [97–99]

$$s_{\rm g}(z) = \left.\frac{d\log_{10}\frac{d^2N_{\rm g}(z,m<m_{\rm lim})}{dzd\Omega}}{dm}\right|_{m_{\rm lim}} = -\frac{2}{5}\left.\frac{d\log_{10}\frac{d^2N_{\rm g}(z,L>L_{\rm lim})}{dzd\Omega}}{d\log_{10}L}\right|_{L_{\rm lim}}, \tag{3.5}$$

where m is the apparent magnitude, L is the intrinsic source luminosity and $m_{\rm lim}$, $L_{\rm lim}$ are the maximum detectable magnitude and the minimum detectable source luminosity of the survey. The magnification bias enters in the velocity, lensing and gravity terms of equation (2.8) (see also appendix A), however its main contribution is in the lensing part, which dominates the amplitude of the signal in the cross-bin case. The reader should keep in mind that the specific value $s_{\rm g} = 0.4$ is the one associated to a compensation between the two competing effects, therefore it is the one that cancels lensing contributions. For DESI we use figure 3.11 of ref. [67], while for EMU and SKA we use the T-RECS catalogue [92] to compute it. We report the magnification bias parameter $s_{\rm g}(z)$ in the bottom right panel of figure 1.

Finally, it should be noted that the number of galaxies does not have to be conserved as function of redshift, e.g., galaxies can form, therefore their number density does not scale

[5] For EMU we find $a_1^{\rm EMU} = 1236.0$, $a_2^{\rm EMU} = 0.77$, $a_3^{\rm EMU} = 1.39$; for DESI we have $a_1^{\rm DESI} = 56491.0$, $a_2^{\rm DESI} = 1.89$, $a_3^{\rm DESI} = 3.70$ while for SKA we have $a_1^{\rm SKA} = 57642.0$, $a_2^{\rm SKA} = 1.05$, $a_3^{\rm SKA} = 1.36$.

[September 30, 2019 at 6:32 – classicthesis v4.6]

JCAP09(2018)039

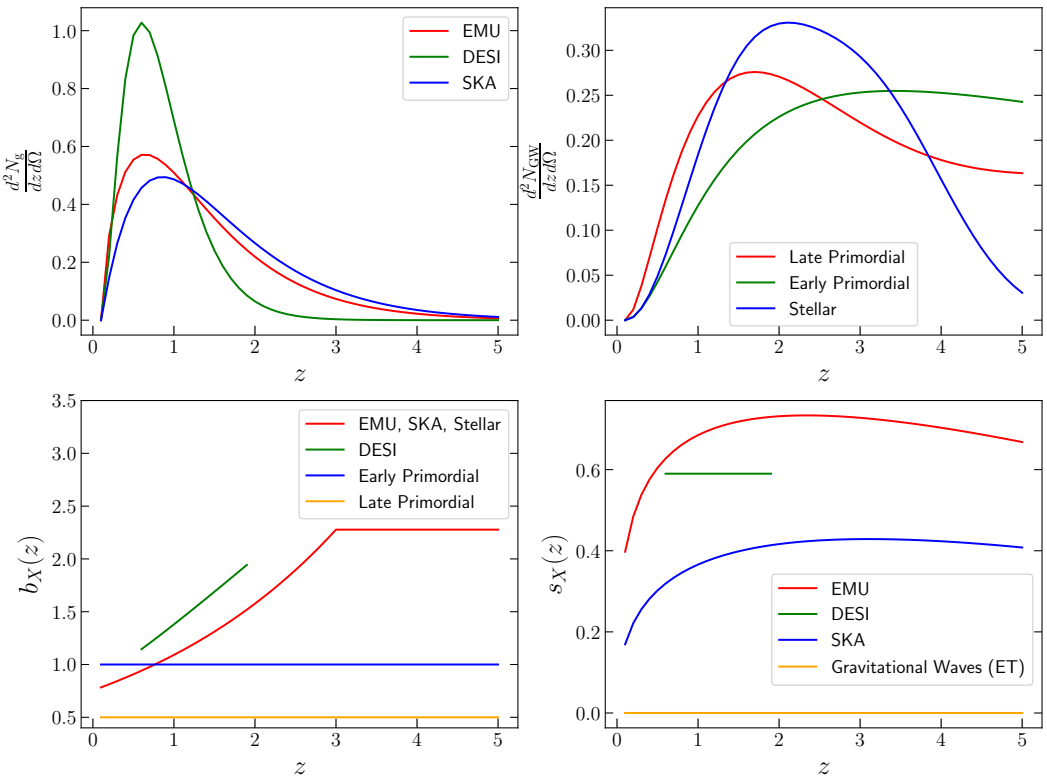

Figure 1. *Top panels*: normalized number density distribution per redshift bin per square degree $\frac{d^2N_X}{dzd\Omega}$ for galaxies (*top left*) and GWs (*top right*). *Bottom panels*: bias $b_X(z)$ (*bottom left*) and magnification bias parameter $s_X(z)$ (*bottom right*) for galaxies and GWs. We report the GWs magnification bias parameter associated to a BHs population with monochromatic mass distribution detected by an interferometer with characteristics similar to those of ET.

JCAP09(2018)039

as a^{-3}, where a is the scale factor. To account for the creation of new galaxies we include also the evolution bias $f_X^{\rm evo}$ defined as [100–102]

$$f_{\rm g}^{\rm evo}(z) = \frac{d\log\left(a^3\frac{d^2N_{\rm g}}{dzd\Omega}\right)}{d\log a}. \tag{3.6}$$

This term enters in the velocity and gravity contributions in equation (2.8) (see also appendix A). Since it appears only in subleading terms and since there are significant uncertainties in the modelling of galactic evolution, we can use in the definition of evolution bias the observed number density instead of the true one, without adding significant errors.

3.2 Gravitational waves

The number density of detected GWs events per redshift bin per square degree can be estimated as

$$\frac{d^2N_{\rm GW}}{dzd\Omega} = T_{\rm obs}\frac{c\chi^2(z)}{(1+z)H(z)}\mathcal{R}_{\rm tot}(z)F_{\rm GW}^{\rm detectable}(z), \tag{3.7}$$

where $T_{\rm obs}$ is the total observational time,[6] $\chi(z)$ is the comoving distance, $H(z)$ is the Hubble expansion rate, $\mathcal{R}_{\rm tot}(z)$ is the total comoving merger rate, $F_{\rm GW}^{\rm detectable}(z)$ is the fraction of detectable events, that depends on the Signal-to-Noise cut $\varrho_{\rm lim}$ imposed at the GWs observatory. The total merger rate depends on the progenitors origin. In section 3.2.1 we consider a scenario where mergers are from PBHs; in section 3.2.2 a scenario with BHs of stellar origin. We comment in section 3.2.3 how we compute $F_{\rm GW}^{\rm detectable}(z)$. Starting from the observed number density, we can calculate GWs evolution bias $f_{\rm GW}^{\rm evo}(z)$ using equation (3.6).

Here we should mention that the uncertainty in the total merger rate $\mathcal{R}_{\rm tot}$ is of orders of magnitude, however what enters in the calculation of the angular power spectra C_ℓ^{XY} (i.e., the signal) is the shape of $\frac{d^2N}{dzd\Omega}$, not the global amplitude. On the other hand, the merger rate (and its normalisation) affects the signal-to-noise ratio (i.e., the error-bars): a larger number density will decrease the shot noise, improving the constraints on the cosmological parameters of interest.

3.2.1 Primordial scenario

In the case where BHs have primordial origin and form a significant part of the dark matter there are at least two important processes that lead to BHs binary formation. In the *late primordial* formation scenario the binary forms when progenitors are already part of dark matter halos [14] and become a bound system by emitting GWs, while in the *early primordial* formation scenario the bound pair forms during radiation-dominated era [45, 103, 104]. In particular, the first mechanism, effective at late times, yields merger rate compatible with those of LIGO. The second mechanism, according to theoretical estimates done in ref. [45], provides a preferred present-day merger rate thait is already excluded by the LIGO constraints. Nevertheless, given the large theoretical uncertainties that these estimates involve, we keep both scenarios into account, adjusting the merger rate value of the early primordial case to make it compatible with LIGO current constraints (we discuss this in more details in section 4).

In the following we focus on the late primordial scenario and we briefly review the theoretical modelling of ref. [14], reporting only the most important results and extending their formalism to the case where PBHs have an extended mass distribution instead of a monochromatic one. In this model, the total merger rate $\mathcal{R}_{\rm tot}(z)$ is expressed as a function of the merger rate per halo $\mathcal{R}_{\rm halo}$ as

$$\mathcal{R}_{\rm tot}(z) = \int_{M_{\rm halo,min}}^{M_{\rm halo,max}} dM_{\rm halo} \frac{dn(M_{\rm halo}, z)}{dM_{\rm halo}} \mathcal{R}_{\rm halo}(M_{\rm halo}, z), \tag{3.8}$$

where $M_{\rm halo,min}, M_{\rm halo,max}$ are the minimum and maximum mass of dark matter halos and $\frac{dn(M_{\rm halo}, z)}{dM_{\rm halo}}$ is the halo mass function [105]. Following the notation of ref. [53] and extending their formalism, for a completely general PBHs mass distribution, the merger rate per halo is given by

$$\mathcal{R}_{\rm halo}(M_{\rm halo}, z) = f_{\rm PBH}^2 \int d^3r dM_1 dM_2 \frac{d\Phi_{\rm PBH}}{dM_1} \frac{d\Phi_{\rm PBH}}{dM_2} \frac{\langle \sigma_{\rm PF} v_{\rm PBH} \rangle}{2M_1 M_2} \rho_{\rm halo}^2(r), \tag{3.9}$$

where $f_{\rm PBH}$ is the fraction of dark matter composed by PBHs,[7] $\frac{d\Phi_{\rm PBH}}{dM}$ describes the shape of the mass distribution and is normalized to unity, M_1, M_2 are progenitors masses, $\sigma_{\rm PF}$

[6] We assume as fiducial observational time $T_{\rm obs} = 10$ years.

[7] In this work we assume that PBHs compose the totality of dark matter, i.e., $f_{\rm PBH} = 1$.

JCAP09(2018)039

is the pair-formation cross section [106, 107], $v_{\rm PBH}$ is the relative velocity between two PBHs, angle brackets $\langle \cdot \rangle$ stand for the average over PBHs relative velocity distribution (a Maxwell-Boltzmann distribution with a cut-off at virial velocity) and $\rho_{\rm halo}(r)$ is the halo radial profile which we choose to be a Navarro-Frenk-White (NFW) [108]. The NFW profile is governed by the so-called concentration parameter that can be calibrated on numerical simulations [109, 110], in turn the "typical" value of the concentration parameter depends only the halo mass and on the redshift. Since the pair-formation cross section $\sigma_{\rm PF}$ scales as $(M_1 + M_2)^{10/7} M_1^{2/7} M_2^{2/7}$ with progenitors masses, the black holes mass dependence of the halo merger rate can be factorized as

$$\mathcal{M}_{\rm PBH} = \int dM_1 dM_2 \frac{d\Phi_{\rm PBH}}{dM_1} \frac{d\Phi_{\rm PBH}}{dM_2} \frac{(M_1 + M_2)^{10/7}}{M_1^{5/7} M_2^{5/7}}. \tag{3.10}$$

Therefore, in the case where the two merging objects come from a monochromatic mass distribution, i.e., a Dirac delta centred at a certain value $M_{\rm PBH}$, equation (3.10) simplifies to $\mathcal{M}_{\rm PBH}^{\rm Monochromatic} = 4^{5/7}$, independently from where the mass distribution is centred.

Since perfectly monochromatic mass distributions are unphysical, we estimate how the merger rate in this model changes when considering two popular extended mass distributions (see ref. [53] for more details about them). We focus on *Power Law* distributions

$$\frac{d\Phi_{\rm PBH}}{dM} = \frac{\mathcal{N}_{PL}}{M^{1-\gamma}} \Theta(M - M_{\rm min}) \Theta(M_{\rm max} - M), \tag{3.11}$$

characterized by an exponent $\gamma \in [-1, +1]$, a mass range $(M_{\rm min}, M_{\rm max})$ and a normalization factor $\mathcal{N}_{PL}$ and on *Lognormal* distributions

$$\frac{d\Phi_{\rm PBH}}{dM} = \frac{e^{-\frac{\log^2(M/\mu)}{2\sigma^2}}}{\sqrt{2\pi}\sigma M}, \tag{3.12}$$

where $\log \mu$ and σ are the mean and standard deviation of the logarithm of the mass, respectively. It is not possible to find an analytical result of the integral in equation (3.10) for these two distributions, however we provide in figure 2 the ratio between merger rates calculated for an extended and a monochromatic mass distribution, which is equivalent to the ratio $\mathcal{M}_{\rm PBH}^{\rm Extended} / \mathcal{M}_{\rm PBH}^{\rm Monochromatic}$ between the factors calculated in equation (3.10). As can be appreciated from the figure, the ratio is always a factor few bigger than unity. This important result allows us to generalize to the extended mass distribution case (for distributions centred in the $\mathcal{O}(10)\ M_\odot$ window) conclusions we draw for the monochromatic one in section 4, just by rescaling the merger rate by some numerical factor. Furthermore, in the case of a *Lognormal* distribution, the ratio depends on the width of the distribution but not on the "scale" μ.[8]

Since the total merger rate in equation (3.8) is dominated by low-mass halo, the choice of the minimum halo mass may have a big impact on the final result. The minimum mass is set by requiring that the small halos evaporation time is larger the Hubble time. The authors of ref. [45] pointed out that the presence of Poisson fluctuations significantly affects the estimation of the characteristic density and velocity dispersion, increasing the initial estimate of the minimum allowed halo mass in ref. [14] by one order of magnitude. However, still in ref. [45], it was also found that the total merger rate computed including Poisson

[8] This result is exact, in fact the scale μ disappears from equation (3.10) once that we rescale the masses through a change of variables.

JCAP09(2018)039

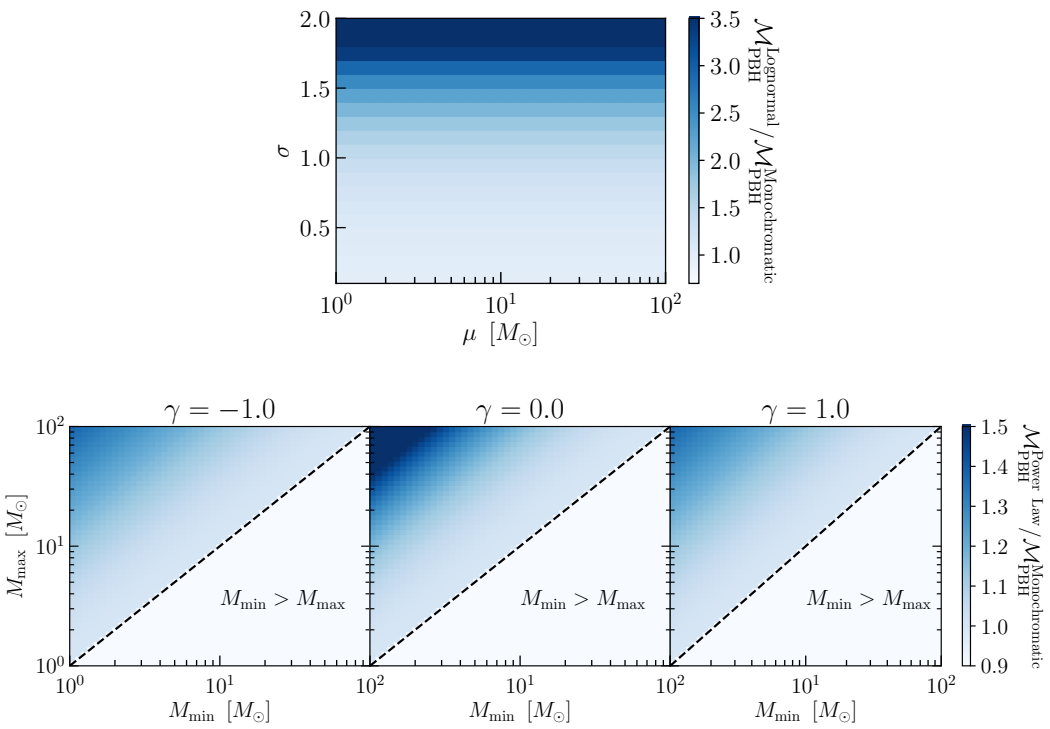

Figure 2. Ratio between the mass-dependent factor $\mathcal{M}_{\rm PBH}$ of different extended mass distribution, centred in the $\mathcal{O}(10)$ $M_\odot$ window, with respect to the monochromatic case $\mathcal{M}_{\rm PBH}^{\rm Monochromatic} = 4^{5/7}$. *Top panel: Lognormal* distribution. *Bottom panel: Power Law* distribution. In both cases the $\mathcal{M}_{\rm PBH}$ factor does not deviate significantly from the one obtained in the monochromatic case.

fluctuations is of the same order of magnitude of that found in ref. [14]. These results have been obtained assuming that the initial clustering of PBHs is Poissonian, however this assumption is still a matter of discussion. If PBHs are born strongly clustered, merger rate estimates could be heavily affected, see e.g., refs. [111–115].

The second scenario we consider is the early primordial formation mechanism. In this case PBHs binaries form in the early Universe and can merge in less than a Hubble time. The estimated total merger rate for this scenario is five orders of magnitude larger than the one given by the late primordial scenario, however there are several theoretical uncertainties; the interested reader can check ref. [45] to find a broad discussion on these uncertainties. Finally we mention that other binary formation mechanisms exist, see e.g., ref. [58], however we do not consider them since uncertainties at play are even larger.

Let's turn our attention on the bias the GWs associated to different binary formation mechanism. If the progenitors have primordial origin, the estimates in ref. [45] indicate that the merger rate is heavily dominated the early primordial one. In this scenario the PBHs trace the dark matter, therefore they have constant bias $b_{\rm GW}(z) \equiv 1$ and constant effective bias $B_{\rm GW} \equiv 1$. However, if primordial binaries are disrupted during the history of the Universe and the merger rate is dominated by the late primordial mechanism, then the merger events trace low-velocity dispersion low-mass halos ($M_{\rm halo} < 10^6 M_\odot$). The bias of these halos is

JCAP09(2018)039

given by [116]

$$b_{\rm lmh}(z) = 1 + \frac{\nu^2 - 1}{\delta_{\rm sc}}, \tag{3.13}$$

where $\nu = \delta_{\rm sc}/\sigma(M_{\rm halo}, z)$ is the dimensionless peak height, $\delta_{\rm sc} = 1.686$ is the spherical collapse threshold and $\sigma(M_{\rm halo}, z)$ is the root-mean-squared density fluctuation at redshift z for a smoothing scale corresponding to mass $M_{\rm halo}$ in a Press-Schechter-like philosophy. Since the bias does not evolve significantly in redshift, we consider it as a constant, therefore in this second case its effective value is $B_{\rm GW} = 0.5$.

3.2.2 End-point of stellar evolution scenario

Several authors have estimated the merger rate of BH binaries coming from stellar evolution, see e.g., refs. [117–119]. In this work we use the prescriptions given by ref. [119] who obtain the merger rate of stellar BH binaries by combining the Illustris cosmological simulation with population-synthesis simulations of black hole binaries. They rely on up-to-date prescriptions for stellar winds and core collapse Supernovae. In this merger rate all three populations of stars are included. We consider as our fiducial model the fiducial merger rate of figure 1 of [119]. We can model their merger rate as

$$\mathcal{R}_{\rm tot}(z) = \mathcal{A}\left(1 + \left(\frac{z}{z_0}\right)^{p_1}\right)^{p_2} e^{-(z-z_1)^2/2} \tag{3.14}$$

where $\mathcal{A} = 786.0$, $z_0 = 3.0$, $z_1 = 1.8$, $p_1 = 4.9$ and $p_2 = 1.4$. Other models (based on different properties of the population-synthesis simulations, using different prescriptions for Supernovae, natal kicks distribution, Hertzsprung gap stars and common envelope phase efficiency) still have approximately the same shape, but a different amplitude $\mathcal{A}$. Uncertainties in this case are around one order of magnitude. We report the normalized number density of sources per redshift bin per square degree compute using this total merger rate in the top right panel of figure 1.

When progenitors of a merging event have stellar origin, they are more likely correlated with higher-mass halos that had a higher star-formation rate, therefore their bias will be the same of the galaxies under consideration, i.e. $b_{\rm GW}(z) = b_{\rm g}(z)$, where the different bias are reported in section 3.1 and figure 1. In these cases the effective bias reads as $B_{\rm GW,EMU} = 0.84$, $B_{\rm GW,DESI} = 1.53$ and $B_{\rm GW,SKA} = 1.85$.

3.2.3 Gravitational waves signal-to-noise ratio and event detectability

In this section we calculate the expected signal-to-noise ratio for BH-BH merger events. Given the uncertainties in the final design of future GWs observatories, we take several simplifying assumptions. However, we try to be as realistic as possible striking a balance between being conservative but not over-conservative. Our main findings are robust against changes of specific details.

We define the GW averaged[9] signal-to-noise ratio measured at a given GWs observatory as $\sqrt{\langle \varrho^2 \rangle}$. This is obtained via (see e.g., ref. [120]),

$$\langle \varrho^2 \rangle = \frac{1}{5} \int_{f_{\rm min}}^{f_{\rm max}} df \frac{h_c^2(f)}{f^2 S_n(f)}, \tag{3.15}$$

[9] Here the average is over the system-detector relative orientation and over waves polarization.

JCAP09(2018)039

where f is the observed frequency, $h_c(f)$ is the characteristic strain amplitude, $S_n(f)$ is the one-sided noise power spectral density and $f_{\rm min}$ and $f_{\rm max}$ are the minimum and maximum frequencies the detector is sensible to. We choose $(f_{\rm min}, f_{\rm max}) = (10, 10^4)$ when considering aLIGO and $(f_{\rm min}, f_{\rm max}) = (1, 10^4)$ when considering ET. To be more precise, the $1/5$ factor slightly depends on the characteristics of the analysed system considered, however it is usually very close to the value we have chosen [121].

The characteristic strain amplitude depends on the physical phenomenon one is interested in. In this work we consider a two body system, the merging binary, with progenitors masses M_1 and M_2, total mass $M_{\rm tot}$ and reduced mass $\mu_{\rm r}$. The characteristic strain is related to its spectral energy distribution dE/df_s as [122]

$$h_c(f) = \frac{2^{1/2}}{\pi\chi(z)}\sqrt{\frac{dE}{df_s}}, \tag{3.16}$$

where $f_s = (1+z)f$ is the frequency of the emitted wave at the source, located at redshift z. Every merger event is characterized by three different phases, inspiraling (I), merging (M) and ringdown (R), that correspond to the emission in three different and separate frequency ranges with different spectral energy distributions (see ref. [122] for specific details). In the following we consider only the first two phases (inspiraling and merging) since during the third one the strain is rapidly damped. These phases are associated to the observed frequency ranges

$$I: \quad f < \frac{f_m}{1+z}, \qquad M: \quad \frac{f_m}{1+z} < f < \frac{f_r}{1+z}, \tag{3.17}$$

where $f_m = 4100\ (M_\odot/M_{\rm tot})\ s^{-1}$ and $f_r = 28600\ (M_\odot/M_{\rm tot})\ s^{-1}$ are the so called merger and ringdown frequencies.

Given that different merger phases do not share the same frequency domain, the signal-to-noise ratio can be computed separately for each phase and then combined:

$$\begin{aligned}
\langle\varrho^2\rangle &= \langle\varrho^2\rangle_I + \langle\varrho^2\rangle_M\,, \\
\langle\varrho^2\rangle_I &= \frac{2\mu_{\rm r} M_{\rm tot}^{2/3} G^{5/3}}{15\pi^{4/3}c^3}\frac{(1+z)^{-1/3}}{\chi^2(z)}\int_{f_{\rm min}}^{f^I_{\rm up}(z)} df\,\frac{f^{-7/3}}{S_n(f)}, \\
\langle\varrho^2\rangle_M &= \frac{32 G\mu_{\rm r}^2\epsilon}{5\pi^2 M_{\rm tot} c(f_r - f_m)}\frac{1}{\chi^2(z)}\int_{f^M_{\rm low}(z)}^{f^M_{\rm up}(z)} df\,\frac{f^{-2}}{S_n(f)},
\end{aligned} \tag{3.18}$$

where ϵ is the fraction of the total mass emitted in GW and typically assumes values around $\epsilon \sim 0.05$ (this is the value we assume). The signal-to-noise ratio for the different phases are non-zero only if $f_{\rm min} < f^I_{\rm up}(z)$ and $f^M_{\rm low}(z) < f^M_{\rm up}(z)$, where

$$f^I_{\rm up}(z) = \min\left(f_{\rm max}, \frac{f_m}{1+z}\right), \quad f^M_{\rm low}(z) = \max\left(f_{\rm min}, \frac{f_m}{1+z}\right), \quad f^M_{\rm up}(z) = \min\left(f_{\rm max}, \frac{f_r}{1+z}\right). \tag{3.19}$$

Each of the observatories we consider (aLIGO starting in the next decade and, beyond that, ET) is characterised by its sensitivity or, equivalently, by its own noise power spectral density $S_n(f)$. The interested reader can find these details in ref. [123] for aLIGO and in ref. [124] for ET.

To define the fraction of detectable events $F_{\rm GW}^{\rm detectable}$ introduced in equation (3.7), we impose $\sqrt{\langle\varrho^2\rangle} > \varrho_{\rm lim}$; following existing literature we choose the typical minimum value $\varrho_{\rm lim} = 8$.

JCAP09(2018)039

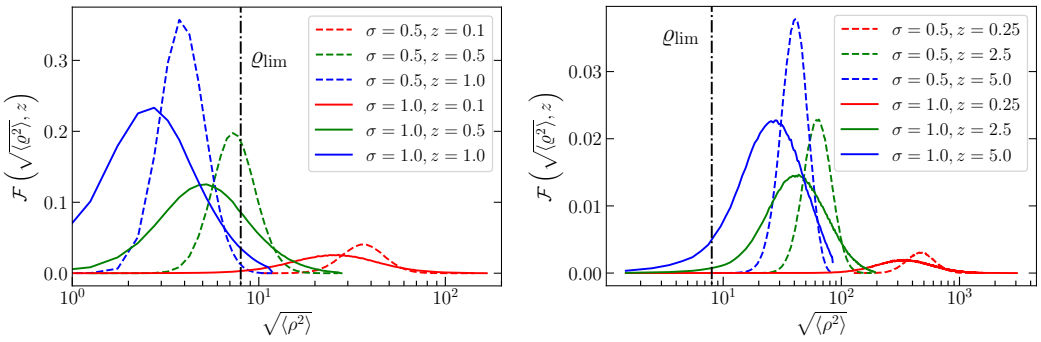

Figure 3. Probability distribution function of the signal-to-noise for Lognormal black holes extended mass distribution with $(\mu, \sigma) = (30, 0.5)$ (*dashed line*) and $(\mu, \sigma) = (30, 1.0)$ (*solid line*) at different redshift. *Left panel:* aLIGO detector. *Right panel:* ET detector. The black dotted-dashed line represents the detection threshold at $\varrho_{\rm lim} = 8$.

The distribution of detected signal-to-noise ratio at different redshift, that we denote with $\mathcal{F}\left(\sqrt{\langle\varrho^2\rangle}, z\right)$, expected from different BHs mass distributions is computed as follows.

In the case where the BHs have a monochromatic mass distribution, all the mergers have the same averaged signal-to-noise ratio at a given redshift, therefore in this approximation we are able to detect all the merger events up to some maximum redshift $z_{\rm max}$ such that $\sqrt{\langle\varrho^2(z_{\rm max})\rangle} = \varrho_{\rm lim}$. We calculate that $z_{\rm max}^{\rm aLIGO} = 0.4$ for aLIGO and $z_{\rm max}^{\rm ET} > 5$ for ET. In this case $F_{\rm GW}^{\rm detectable} \equiv 1$ up to the maximum redshift.

For an extended mass distribution we simulate 10^5 BH mergers at different redshift with progenitors masses drawn from two *Lognormal* mass distributions, one narrow ($\sigma = 0.5$), the other wider ($\sigma = 1.0$), both having $\mu = 30.0\ M_\odot$. We calculate the averaged signal-to-noise ratio distribution using the aLIGO [123] and ET [124] expected sensitivity. We report the probability distribution $\mathcal{F}\left(\sqrt{\langle\varrho^2\rangle}, z\right)$ in figure 3 for different redshift. For the aLIGO detector details of the extended mass distribution can be relevant, in fact in both cases of narrow and broad mass distribution, a significant fraction of events may lie below detection threshold, up to half of the total events in the broad distribution case for redshift $z = 0.4$, corresponding to $F_{\rm GW}^{\rm detectable}(z = 0.4) \simeq 0.5$. However, the next generation of GWs observatories will overcome this limitation. In particular ET sensitivity will be so large that in the narrow mass distribution case all the event are detectable, therefore $F_{\rm GW}^{\rm detectable} \equiv 1$. In the broad mass distribution case we observe that part of the tail is below the threshold, however even at redshift $z = 5$ the overall effect is very small, in fact we find that $F_{\rm GW}^{\rm detectable} \gtrsim 0.97$. Since in the ET case the effect of an extended mass distribution is so small, every conclusion we draw for the monochromatic case applies also the extended one.

The GW averaged signal-to-noise ratio and the distribution of detected signal-to-noise ratio as a function of redshift are also a key inputs to compute the magnification bias.

3.2.4 Gravitational waves magnification bias

In this section we calculate for the first time the magnification bias for GWs. As for galaxies, the magnification bias contains the information on which of the two effects of gravitational

JCAP09(2018)039

lensing, explained in section 3.1, dominates. It enters in the velocity, lensing and gravity terms of equation (2.8) (see also appendix A).

In complete analogy to what has been done for galaxies in equation (3.5), we identify the galaxy apparent magnitude m with the GWs averaged signal-to-noise ratio $\sqrt{\langle\varrho^2\rangle}$ measured at a given GWs observatory. As in equation (3.5), instead of a maximum apparent magnitude $m_{\rm lim}$, we define a minimum average signal-to-noise ratio $\varrho_{\rm lim} = 8$ to claim the detection of an event. Finally, we define the GWs magnification bias parameter as

$$s_{\rm GW}(z) = -\left.\frac{d\log_{10}\frac{d^2N_{\rm GW}(z,\sqrt{\langle\varrho^2\rangle}>\varrho_{\rm lim})}{dzd\Omega}}{d\sqrt{\langle\varrho^2\rangle}}\right|_{\varrho_{\rm lim}}, \tag{3.20}$$

where the minus sign has been introduced to preserve the interpretation of a positive or negative magnification bias parameter. Notice that instead of the averaged signal-to-noise ratio $\sqrt{\langle\varrho^2\rangle}$ one could have defined the GWs magnification bias using just the signal-to-noise ratio ϱ. In that case one should consider not only the mass distribution but also the system orientation and GWs polarization distribution. This goes beyond the purposes of this article and is left to future work.

The distribution of detected signal-to-noise ratio at different redshifts $\mathcal{F}\left(\sqrt{\langle\varrho^2\rangle}, z\right)$ and different BHs mass distributions (see section 3.2.3) is the key quantity to estimate the GWs magnification bias. For a monochromatic mass distribution, all the mergers have the same averaged signal-to-noise ratio at a given redshift and we observe all the events (or none of them), hence the magnification bias parameter for a BHs monochromatic population is identically zero ($s_{\rm GW}(z) \equiv 0.0$) except in an infinitely thin redshift shell around $z_{\rm max}$.

On the other hand, for an extended mass distribution, the magnification bias parameter can be non-zero since, especially for the broad mass distribution, in fact we potentially have events above and below the detection threshold at every redshift. As shown in figure 3 and discussed in section 3.2.3, the ET sensitivity guarantees that for narrow mass distribution all events are detectable, $s_{\rm GW} \equiv 0.0$, as in the monochromatic mass distribution case. In the broad mass distribution case only few events are missed and we find $s_{\rm GW} \lesssim 0.01$ at redshift $z = 5$. For the aLIGO case we find $s_{\rm GW} \lesssim 0.07$ at redshift $z = 0.4$ in both cases. In general, for any given extended mass distribution, more sensitive experiments, as the ET, have smaller magnification bias parameter. Since the values of the magnification bias parameter are so close to zero, the error coming from working with a monochromatic mass distribution are subdominant with respect to other uncertainties in the modelling. Therefore we can safely extrapolate our results for monochromatic cases to extended mass distribution cases.

4 Results

Beside the tracer's bias, the merger rates are also poorly known, both on the observational and theoretical side, spanning several orders of magnitude and affecting the overall expected number of GWs events. After the first run of LIGO, the observational merger rate today is estimated to be [125]

$$\mathcal{R}^{\rm LIGO}_{\rm today} \simeq 9 - 240\ {\rm Gpc}^{-3}{\rm yr}^{-1}, \tag{4.1}$$

while the theoretically predicted merger rates for the stellar and late primordial scenario are

$$\begin{aligned}\mathcal{R}^{\rm Stellar}_{\rm today} &\simeq 150\ {\rm Gpc}^{-3}{\rm yr}^{-1},\\ \mathcal{R}^{\rm Late\ Primordial}_{\rm today} &\simeq 4\ {\rm Gpc}^{-3}{\rm yr}^{-1}.\end{aligned} \tag{4.2}$$

JCAP09(2018)039

The predicted merger rate for the early primordial scenario is approximately 10^5 Gpc^{-3}yr^{-1} or even higher [126], therefore ruling out this scenario. However, given the high uncertainties in its computation which could significantly lower this value [45], in this work we consider a fiducial value for this scenario of

$$\mathcal{R}_{\rm today}^{\text{Early Primordial}} \simeq 200 \text{ Gpc}^{-3}\text{yr}^{-1}, \tag{4.3}$$

which is consistent with LIGO constraints. Nevertheless, these uncertainties act mainly as a rescaling of the number of events, thus of the noise and of the resulting signal-to-noise ratio.

We parametrize the uncertainty on the number of GWs events (3.7) by introducing a new parameter r constant in redshift. In the stellar case r reads as

$$r^{\rm Stellar} = \frac{T_{\rm obs}}{10 \text{ years}} \times \frac{\mathcal{R}}{\mathcal{R}_{\rm today}^{\rm Stellar}}, \tag{4.4}$$

where $\mathcal{R}/\mathcal{R}_{\rm today}^{\rm Stellar}$ parametrizes the uncertainty coming from the chosen fiducial model in ref. [119]. In the primordial scenarios we have

$$\begin{aligned} r^{\text{Late Primordial}} &= \frac{T_{\rm obs}}{10 \text{ years}} \times f_{\rm PBH}^2 \times \frac{\mathcal{M}_{\rm PBH}^{\rm Extended}}{\mathcal{M}_{\rm PBH}^{\rm Monochromatic}} \times \left\langle F_{\rm GW}^{\rm detectable} \right\rangle \times \frac{\mathcal{R}}{\mathcal{R}_{\rm today}^{\text{Late Primordial}}}, \\ r^{\text{Early Primordial}} &= \frac{T_{\rm obs}}{10 \text{ years}} \times \frac{\mathcal{R}}{\mathcal{R}_{\rm today}^{\text{Early Primordial}}}, \end{aligned} \tag{4.5}$$

where in the late primordial formation scenario we have explicitly separated the contributions analysed in section 3.2, even if the dependence on the observational time $T_{\rm obs}$, the fraction $f_{\rm PBH}$ of PBHs that constitutes the dark matter, the choice of PBHs mass distribution (extended or monochromatic) and the average fraction of observables events $\left\langle F_{\rm GW}^{\rm detectable} \right\rangle$ can be generalized also to the early primordial formation scenario. The quantity $\mathcal{R}/\mathcal{R}_{\rm today}^{\text{Late, Early Primordial}}$ contains any possible uncertainty related to the modelling of the merger rate that affects its overall normalisation, expressing deviations from the fiducial values of equations (4.2) and (4.3). The values $r^{\text{Stellar, Late, Early Primordial}} = 1$ correspond to the merger rates reported in equations (4.2) and (4.3). To account for several theoretical uncertainties that can influence the merger rates, we provide results for a range $r^{\text{Stellar, Late, Early Primordial}} \in [10^{-1}, 10]$.

Finally, we report in table 2 the details of the survey we analyse in section 4.1 and 4.2, in particular the combinations of GWs observatories and large scale structure surveys, the covered fraction of the sky, the maximum multipole, connected to the maximum angular resolution achievable (see section 2) and the redshift binning we choose.

4.1 Generic case and importance of projection effects

In this section we study a generic case to highlight the importance of projection effects. In terms of angular resolution and covered fraction of the sky, this generic case can be thought as a ET×SKA in the redshift range $[1.0, 4.0]$ (see table 2).

We perform the Fisher and $\Delta\chi^2$ analyses adding one by one the effects listed in equation (2.8) to estimate their importance, in particular we consider only density and velocity contributions (den + vel case), then we add lensing (den + vel + len case) and finally gravity effects (den + vel + len + gr case). In particular we call *projection effects* the combination of the latter two, namely lensing and gravity contributions (len + gr). We refer the interested

JCAP09(2018)039

SURVEYS COMBINATION	$f_{\rm sky}$	$\ell_{\rm max}$	REDSHIFT BINNING
GENERIC CASE	0.75	100	$1.0 \leq z_1 \leq 2.0$ $2.0 \leq z_2 \leq 3.0$ $3.0 \leq z_3 \leq 4.0$
aLIGO $\times$ EMU	0.75	50	$0.0 \leq z_1 \leq 0.4$
ET $\times$ DESI	0.34	100	$0.60 \leq z_1 \leq 1.15$ $1.15 \leq z_2 \leq 1.70$
ET $\times$ SKA	0.73	100	$1.0 \leq z_1 \leq 2.0$ $2.0 \leq z_2 \leq 3.0$ $3.0 \leq z_3 \leq 4.0$ $4.0 \leq z_4 \leq 5.0$

Table 2. Prescription used for the forecast. We report the GWs observatory and the galaxy surveys, the covered fraction of the sky $f_{\rm sky}$, the maximum achievable multipole $\ell_{\rm max}$ of the GWs observatory and redshift binning. Note that we take the value $\ell_{\rm max} = 50$ for aLIGO, because we assume that KAGRA and LIGO India will also be running, improving the source localisation and resolution of the resulting GWs events map.

reader to ref. [84], where a broader discussion on the importance of the full modelling can be found. Results from the Fisher analysis, with and without a Planck prior, are reported in figure 4, both for the stellar and primordial black holes scenarios. As expected, adding the CMB prior improves the results, lowering the value of the error $\sigma_{B_{\rm GW}^{\rm Fiducial}}$ defined in equation (2.12), due to the extra power in constraining the standard cosmological parameters. We also find lensing effects have a large impact on determining the final Signal-to-Noise and that gravity contributions barely affects the final results, since they are relevant mostly at horizon scales.

We argue here that even if projection effects (lensing, gravity) do not depend on the signal one is trying to measure — the bias in this case — their contributions cannot necessarily be ignored in a Fisher error forecast for two reasons: *i)* they must be included in the covariance matrix as they act as an effective source of "noise" — think of the cosmic variance contribution — as such ignoring them would underestimate the resulting error, *ii)* they do depend on other "extra" parameters, i.e. the cosmological parameters. When marginalizing over these extra parameters, the presence of projection effects help constraining them and thus improve the overall error-bars. The interplay and balance between these two trends yields a combined effect on the resulting forecasts, which we investigate now in more details.

We show on top panels of figure 5 how the inclusion of projection effects affects the results obtained through the Fisher analysis, depending on the value of the parameter r and on the adoption of the Planck prior. In particular we appreciate that without adding Planck prior projection effects yield an improvement while adding it we observe a small degradation. This counter-intuitive result can be understood as follows. The lensing contribution does not directly depend on the bias parameter (see appendix A) but it dominates the global C_ℓ signal, especially for the cross-bin angular power spectrum, acting as an effective source of "noise", since bigger C_ℓ yield smaller Fisher matrix elements (see equation (2.11)) and, consequently, a higher error $\sigma_{B_{\rm GW}^{\rm Fiducial}}$. On the other hand, lensing effects can improve forecasts on the other (cosmological) parameters considered in the Fisher analysis, increasing the corresponding Fisher elements. In the presence of degeneracies this can lead to an improvement on the bias parameter determination. This can be seen explicitly in the top left panel of figure 5: in the three cases, for high enough values of r, the improvement of other cosmological parameters estimates breaks degeneracies, improving the forecasts on GWs bias $B_{\rm GW}$. This is not so evident for low values of the parameter r, as the higher shot noise works against the lensing-

JCAP09(2018)039

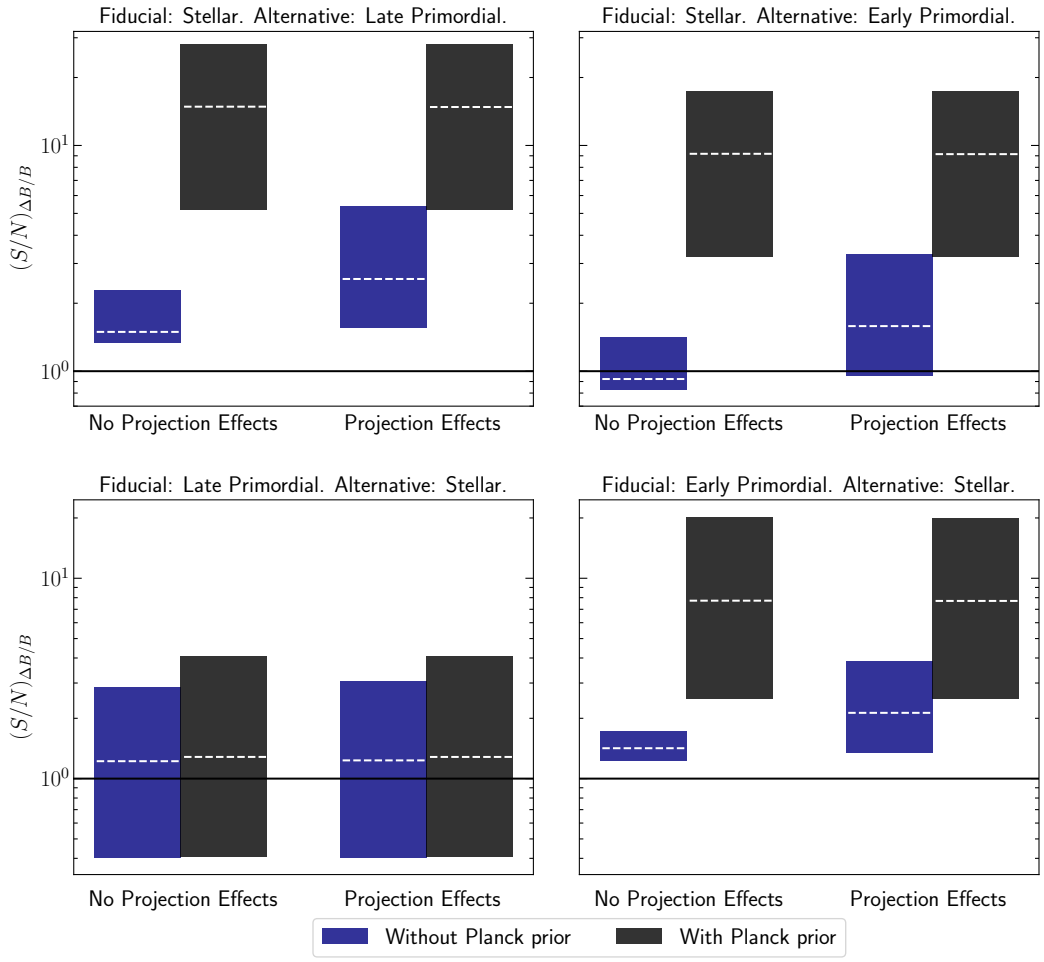

Figure 4. Generic case. Signal-to-Noise $(S/N)_{\Delta B/B}$ estimates from the Fisher analysis for different fiducial and alternative models, including and neglecting projection effects and the Planck prior on cosmological parameters. We assume $T_{\rm obs} = 10$ years. The lower (upper) edge of the coloured bars corresponds to $r = 0.1$ ($r = 10$), while the white dashed line corresponds to the fiducial value $r = 1$. The fiducial and the alternative models are indicated on top of each panel.

induced improvements on cosmological parameters. We have seen that in this method the inclusion of projection effects can change the forecast errors up to a factor of 2, therefore we argue that in general they cannot simply be neglected, even if there could be situations where the change is not so significant. When using the strong Planck prior, whose Fisher matrix elements are orders of magnitude bigger than those of the clustering, the lensing improvement on cosmological parameter forecasts is not significant any more, and we observed only the increased "noise" effect on $\sigma_{B_{\rm GW}^{\rm fiducial}}$.

In the lower panels of figure 5 we observe the same effect, this time with the $\Delta\chi^2$ method. In this case cosmological parameters are assumed to be known, and thus the lensing effect does not add signal, it only increases the noise.

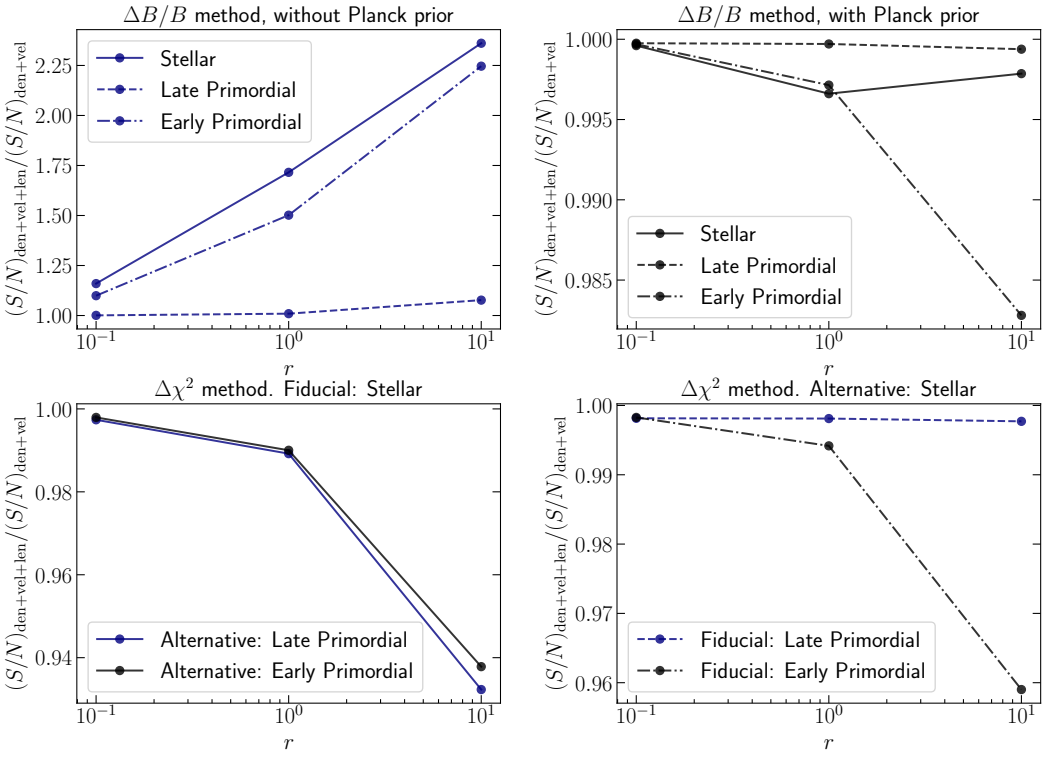

Figure 5. Generic case. *Upper panels:* ratio of the Signal-to-Noise $(S/N)_{\Delta B/B}$ obtained with the Fisher analysis, including and neglecting projection effects, for different values of r, including (*right panel*) or not (*left panel*) the Planck prior. Lines indicates the assumed fiducial model. *Lower panels:* ratio of the Signal-to-Noise $(S/N)_{\sqrt{\Delta\chi^2}}$ obtained with the $\Delta\chi^2$ analysis, including and neglecting projection effects, for different values of r, for the stellar as fiducial model (*left panel*) or as alternative model (*right panel*).

4.2 Forecast for future large scale structure surveys

In this section we provide forecasts for those specific combinations of GWs observatories and large scale structure surveys given in table 2.

We report the Signal-to-Noise forecasts, obtained with both methods described in section 2, in figure 6 (stellar as fiducial model), figure 7 (late primordial as fiducial model) and figure 8 (early primordial as fiducial model). In each of these figures we show four panels: the upper ones show results coming from the Fisher analysis, while the lower ones come from the $\Delta\chi^2$ formalism. In the left panels we show bar charts obtained for different values of the parameter r at fixed maximum multipole $\ell_{\rm max}$, while in the right panels we report the scaling of the Signal-to-Noise for different values of the maximum angular resolution when $r^{\text{Stellar, Late, Early Primordial}} = 1$, corresponding to the merger rates reported in equations (4.4) and (4.5).

We show that surveys covering a bigger volume (or redshift range) have can discriminate better between different models, i.e. have higher Signal-to-Noise ratios, as expected from surveys with smaller shot noise. In the case where the stellar model is assumed as fiducial, it

JCAP09(2018)039

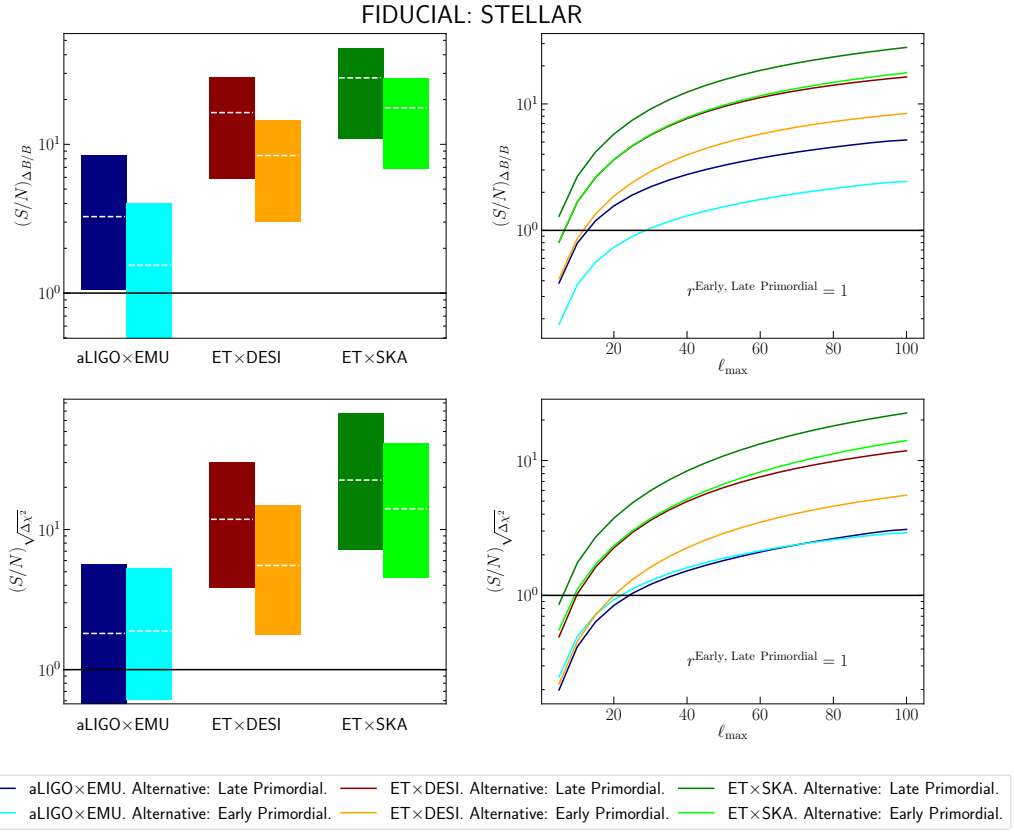

Figure 6. Specific surveys. Signal-to-Noise S/N estimates coming from Fisher analyses, along with the Planck prior, (*upper panels*) and $\Delta\chi^2$ formalism (*lower panels*) for specific surveys combinations. *Left panels:* Signal-to-Noise S/N estimates as a function of r, assuming a fixed ℓ_{max} (50 for aLIGO and 100 for ET). The horizontal dashed white lines refer to the $r = 1$ case. *Right panels:* Signal-to-Noise S/N estimates as a function of ℓ_{max} for the fiducial merger rate case $r = 1$. The fiducial scenario assumed is the stellar, to be distinguished by the early and late primordial alternative models. We choose as observation time $T_{\text{obs}} = 10$ years.

is generally more difficult to distinguish the early primordial scenario than the late primordial, since the former has a bias (or an effective bias) closer the stellar model one. Notice also that in the cases of stellar and early primordial as fiducial, we have better Signal-to-Noise ratio than in the late primordial scenario, due to higher merger rates, thus higher number of detected sources and lower shot noise.

In general we can conclude that future surveys will enable us to address questions about binary BHs mergers given enough observation time and resolution. One caveat is that this does not always happen for the aLIGO×EMU combination, which will have a Signal-to-Noise lower or very close to unity in some cases (especially if mergers come from the late primordial formation mechanism). This is due to the fact that this combination of GWs observatory and large scale structure survey can only cover a low redshift range, where the biases (or the effective biases) are very similar (see e.g., the bottom left panel of figure 1) and we have an higher shot noise due to the scarce number of detected objects.

JCAP09(2018)039

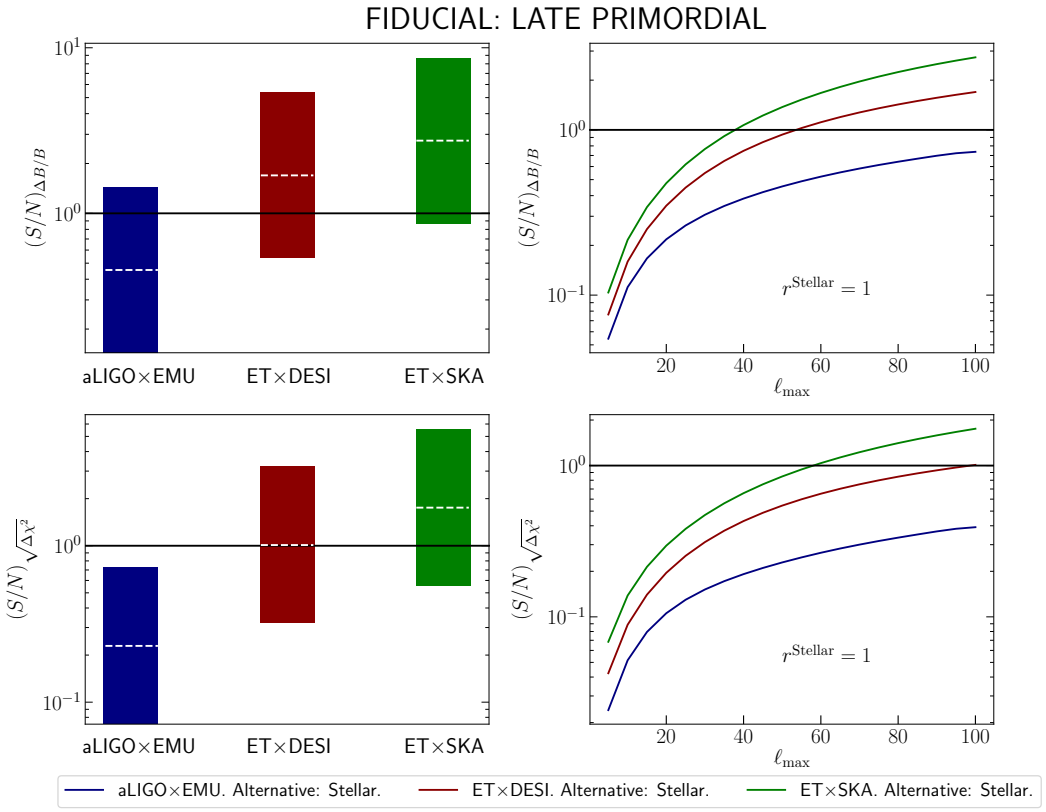

Figure 7. Specific surveys. Signal-to-Noise S/N estimates coming from Fisher analyses, along with the Planck prior, (*upper panels*) and $\Delta\chi^2$ formalism (*lower panels*) for specific surveys combinations. *Left panels:* Signal-to-Noise S/N estimates as a function of r, assuming a fixed $\ell_{\rm max}$ (50 for aLIGO and 100 for ET). The horizontal dashed white lines refer to the $r = 1$ case. *Right panels:* Signal-to-Noise S/N estimates as a function of $\ell_{\rm max}$ for the fiducial merger rate case $r = 1$. The horizontal dashed white lines refer to $r = 1$. The fiducial scenario assumed is the late primordial, to be distinguished by the stellar model. We choose as observation time $T_{\rm obs} = 10$ years.

5 Conclusions

The renewed interest in primordial black holes has highlighted their importance not only as a possible constituent of the dark matter but also because their existence (if confirmed) would have profound implications about the physics of the early Universe. It is therefore essential to explore new ways to discriminate between primordial or stellar origin of the black holes which mergers have been observed with laser interferometers. Beyond the standard ways to constrain the existence of stellar mass primordial black holes through lensing or the effect on cosmic backgrounds, a complementary approach is to assess whether the GWs signal from merging binary BHs we detect are produced by objects of primordial origin or not.

Here we build on the idea that the cross-correlation of galaxy catalogues with GWs (from the merger of binary BHs) maps is a powerful tool to statistically study the origin of the progenitors of BHs mergers [56]. This will be possible once the next generation of GWs detectors will provide localization of enough events to make low resolution maps. Galaxy

JCAP09(2018)039

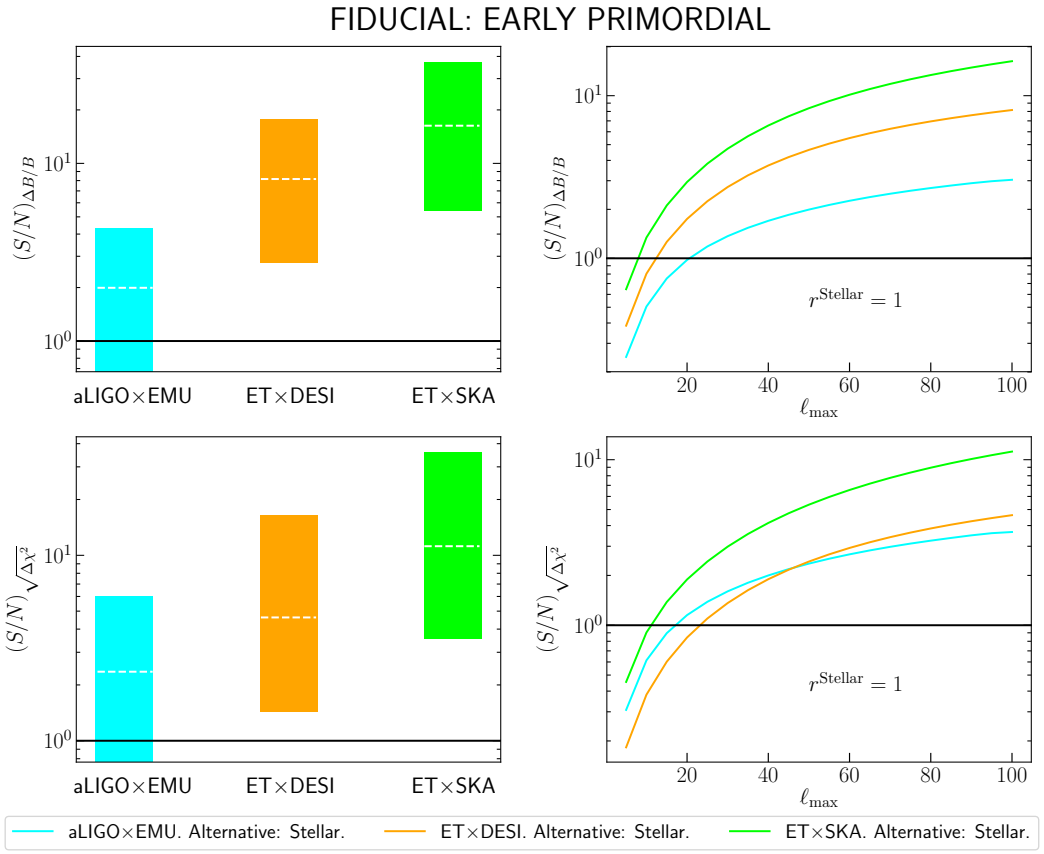

Figure 8. Specific surveys. Signal-to-Noise S/N estimates coming from Fisher analyses, along with the Planck prior, (*upper panels*) and $\Delta\chi^2$ formalism (*lower panels*) for specific surveys combinations. *Left panels:* Signal-to-Noise S/N estimates as a function of r, assuming a fixed $\ell_{\rm max}$ (50 for aLIGO and 100 for ET). The horizontal dashed white lines refer to the $r = 1$ case. *Right panels:* Signal-to-Noise S/N estimates as a function of $\ell_{\rm max}$ for the fiducial merger rate case $r = 1$. The fiducial scenario assumed is the early primordial, to be distinguished by the stellar model. We choose as observation time $T_{\rm obs} = 10$ years.

catalogues covering a significant fraction of the sky and an overlapping redshift range are also under construction or at an advanced planning stage. Then, by measuring the bias of the halos hosting the binary BHs mergers, as well as the variation in their number counts due to lensing magnification and projection effects, we can infer the clustering properties of the progenitors of the binary BHs. Clustering properties matching those of luminous, high velocity-dispersion, high stellar-mass galaxies, would indicate a stellar origin, while clustering properties more similar to those of low-mass galaxies preferentially populating the filamentary structure of large-scale structures indicate a primordial origin. Moreover, this approach could also set constraints on the abundance of PBHs, and hence on the fraction of dark matter that can be comprised of them.

We consider different models for the binary BHs formation, accretion mechanism, merger rate and clustering properties, both for the stellar and primordial nature of the BHs. We generalize similar studies on the cross-correlation between galaxy and gravitational wave maps

JCAP09(2018)039

by performing a full multi-tracer analysis that accounts for different redshift distributions, galaxy bias evolution, magnification bias of luminous sources as well as GWs, and relativistic projection effects. To perform such analyses one need to include a variety of different quantities and physical effects that are still poorly understood. For this reason, we investigated several possible scenarios and reported our results for a wide range of values of uncertain parameters, so that our results are quite general and can be still used once some of such quantities will be better understood.

Before studying specific forthcoming experiments, we highlighted the importance of projections effects on the estimate capability of a given experiment to differentiate between different origins of BHs mergers. Then, we find that the near future combination of aLIGO×EMU would be able to address the nature of observed mergers in the case where their origin is mostly stellar or, if primordial, dominated by early binaries, due to a higher merger rate. If instead BHs have a late primordial origin, the corresponding merger rate would be too low to make it possible to distinguish this scenario from the stellar one with current observations. On the other hand, more futuristic survey combinations, such as ET×DESI or ET×SKA, would allow a real discrimination between all possible model combinations. Our results show that forthcoming experiments could allow us to test most of the parameter space of the still viable models investigated, and shed more light on the issue of binary black hole origin and evolution.

However, it is important to keep in mind some of the assumptions made in this work, that we will list below; it will therefore be important to keep refining these studies in order to have a robust model, formalism and pipeline once laser interferometers will deliver large GWs maps ready to be correlated with other datasets. Most of all, it is very difficult to understand, in the absence of full simulations, the process of binary formation and evolution of early binaries for PBHs scenarios. Related to this, another major source of uncertainty is the BHs accretion mechanism and efficiency across different cosmic epochs; estimates available in literature vary by several orders of magnitude.

In this work we considered PBHs with a monochromatic mass distribution peaked around $30M_{\odot}$; while we verified that our results hold when considering instead some commonly used extended mass distributions, these types of analyses will differ when considering very different mass ranges. Finally, for the stellar model, uncertainties in the star formation rate, existence and distribution of sub-halos, massive star ejections and the epoch of first star formation can as well influence conclusions drawn from the GW×LSS cross-correlation, and therefore need to be further studied. Nonetheless, we believe that the present work can contribute to further develop the new avenue of GW-LSS synergies, and that the vast range of parameters and models explored here make our results general enough to provide a realistic forecast of what this can teach us on the nature of binary BHs progenitors in the next decade.

Acknowledgments

We thank Sathyaprakash Bangalore, Enrico Barausse, José Luis Bernal, Yacine Ali-Haïmoud, Ely Kovetz, Julien Lesgourgues, Antonio Riotto and Matteo Viel for comments on the draft. We also thank Stefano Camera, Neal Dalal, Vincent Desjacques, Raul Jimenez and Sergey Sibiryakov for discussion. Funding for this work was partially provided by the Spanish MINECO under projects AYA2014-58747-P AEI/FEDER, UE, and MDM-2014-0369 of ICCUB (Unidad de Excelencia María de Maeztu). GS was supported by the Erasmus+ for Trainership grant during the early stages of this work, subsequently by grant from the "Maria de Maeztu de Ciències del Cosmos" project mentioned above. NB is supported by the Span-

JCAP09(2018)039

ish MINECO under grant BES-2015-073372. AR has received funding from the People Programme (Marie Curie Actions) of the European Union H2020 Programme under REA grant agreement number 706896 (COSMOFLAGS). SM acknowledges partial financial support by ASI Grant No. 2016-24-H.0. LV acknowledges support by European Union's Horizon 2020 research and innovation programme ERC (BePreSySe, grant agreement 725327). LV acknowledges the Radcliffe Institute for Advanced Study of Harvard University for hospitality during the latest stages of this work.

A Relativistic number counts

In this appendix we explicitly report relativistic number counts effects, following the notation of ref. [82]. The elements of equation (2.8) read as

$$
\begin{aligned}
\Delta_\ell^{\rm den}(k,z) &= b_X \delta(k,\tau_z) j_\ell, \\
\Delta_\ell^{\rm vel}(k,z) &= \Delta_\ell^{\rm rsd}(k,z) + \Delta_\ell^{\rm dop}(k,z), \\
\Delta_\ell^{\rm rsd}(k,z) &= \frac{k}{\mathcal{H}} j_\ell'' V(k,\tau_z), \\
\Delta_\ell^{\rm dop}(k,z) &= \left[(f_X^{\rm evo} - 3)\frac{\mathcal{H}}{k} j_\ell + \left(\frac{\mathcal{H}'}{\mathcal{H}^2} + \frac{2-5s_X}{r(z)\mathcal{H}} + 5s_X - f_X^{\rm evo} \right) j_\ell' \right] V(k,\tau_z), \\
\Delta_\ell^{\rm len}(k,z) &= \ell(\ell+1)\frac{2-5s_X}{2} \int_0^{r(z)} dr \frac{r(z)-r}{r(z)r} [\Phi(k,\tau_z) + \Psi(k,\tau_z)] j_\ell(kr), \\
\Delta_\ell^{\rm gr}(k,z) &= \left[\left(\frac{\mathcal{H}'}{\mathcal{H}^2} + \frac{2-5s_X}{r(z)\mathcal{H}} + 5s_X - f_X^{\rm evo} + 1 \right) \Psi(k,\tau_z) + (-2+5s_X)\Phi(k,\tau_z) + \mathcal{H}^{-1}\Phi'(k,\tau_z) \right] j_\ell \\
&\quad + \int_0^{r(z)} dr \frac{2-5s_X}{r(z)} [\Phi(k,\tau) + \Psi(k,\tau)] j_\ell(kr), \\
&\quad + \int_0^{r(z)} dr \left(\frac{\mathcal{H}'}{\mathcal{H}^2} + \frac{2-5s_X}{r(z)\mathcal{H}} + 5s_X - f_X^{\rm evo} \right)_{r(z)} \left[\Phi'(k,\tau) + \Psi'(k,\tau) \right] j_\ell(kr).
\end{aligned}
\tag{A.1}
$$

According to the notation of ref. [82], r is the conformal distance of on the light cone, $\tau = \tau_0 - r$ is the conformal time, $\tau_z = \tau_0 - r(z)$, b_X is the bias parameter, s_X is the magnification bias parameter, $f_X^{\rm evo}$ is the evolution bias parameter, Bessel functions and their derivatives j_ℓ, $j_\ell' = \frac{dj_\ell}{dy}$, $j_\ell'' = \frac{d^2 j_\ell}{dy^2}$ are evaluated at $y = kr(z)$ unless explicitly stated, $\mathcal{H}$ is the conformal Hubble parameter, a prime $'$ indicates derivatives with respect to conformal time, δ is the density contrast in comoving gauge, V is the peculiar velocity, Φ and Ψ are Bardeen potentials.

The velocity term $\Delta_\ell^{\rm vel}(k,z)$ has been written in terms of the pure (Kaiser) redshift-space distortions term $\Delta_\ell^{\rm rsd}(k,z)$ and in term of Doppler contributions $\Delta_\ell^{\rm dop}(k,z)$. Notice that the magnification and evolution bias enter only in the Doppler term.

References

[1] Virgo and LIGO Scientific collaborations, B.P. Abbott et al., *Observation of gravitational waves from a binary black hole merger*, *Phys. Rev. Lett.* **116** (2016) 061102 [arXiv:1602.03837] [inSPIRE].

[2] Virgo and LIGO Scientific collaborations, B.P. Abbott et al., *Properties of the binary black hole merger GW150914*, *Phys. Rev. Lett.* **116** (2016) 241102 [arXiv:1602.03840] [inSPIRE].

[3] K. Belczynski, M. Dominik, T. Bulik, R. O'Shaughnessy, C.L. Fryer and D.E. Holz, *The effect of metallicity on the detection prospects for gravitational waves*, *Astrophys. J.* **715** (2010) L138 [arXiv:1004.0386] [INSPIRE].

[4] M. Dominik et al., *Double compact objects I: the significance of the common envelope on merger rates*, *Astrophys. J.* **759** (2012) 52 [arXiv:1202.4901] [INSPIRE].

[5] M. Dominik et al., *Double compact objects II: cosmological merger rates*, *Astrophys. J.* **779** (2013) 72 [arXiv:1308.1546] [INSPIRE].

[6] M. Dominik et al., *Double compact objects III: gravitational wave detection rates*, *Astrophys. J.* **806** (2015) 263 [arXiv:1405.7016] [INSPIRE].

[7] VIRGO and LIGO SCIENTIFIC collaborations, B.P. Abbott et al., *GW*151226*: observation of gravitational waves from a* 22*-solar-mass binary black hole coalescence*, *Phys. Rev. Lett.* **116** (2016) 241103 [arXiv:1606.04855] [INSPIRE].

[8] VIRGO and LIGO SCIENTIFIC collaborations, B.P. Abbott et al., *GW*170104*: observation of a* 50*-solar-mass binary black hole coalescence at redshift* 0.2, *Phys. Rev. Lett.* **118** (2017) 221101 [arXiv:1706.01812] [INSPIRE].

[9] VIRGO and LIGO SCIENTIFIC collaborations, B.P. Abbott et al., *GW*170608*: observation of a* 19*-solar-mass binary black hole coalescence*, *Astrophys. J.* **851** (2017) L35 [arXiv:1711.05578] [INSPIRE].

[10] VIRGO and LIGO SCIENTIFIC collaborations, B.P. Abbott et al., *GW*170814*: a three-detector observation of gravitational waves from a binary black hole coalescence*, *Phys. Rev. Lett.* **119** (2017) 141101 [arXiv:1709.09660] [INSPIRE].

[11] K. Belczynski, D.E. Holz, T. Bulik and R. O'Shaughnessy, *The first gravitational-wave source from the isolated evolution of two* 40–100 *Msun stars*, *Nature* **534** (2016) 512 [arXiv:1602.04531] [INSPIRE].

[12] K. Belczynski, T. Bulik, C.L. Fryer, A. Ruiter, J.S. Vink and J.R. Hurley, *On the maximum mass of stellar black holes*, *Astrophys. J.* **714** (2010) 1217 [arXiv:0904.2784] [INSPIRE].

[13] K. Belczynski et al., *The effect of pair-instability mass loss on black hole mergers*, *Astron. Astrophys.* **594** (2016) A97 [arXiv:1607.03116] [INSPIRE].

[14] S. Bird et al., *Did LIGO detect dark matter?*, *Phys. Rev. Lett.* **116** (2016) 201301 [arXiv:1603.00464] [INSPIRE].

[15] S. Clesse and J. García-Bellido, *The clustering of massive primordial black holes as dark matter: measuring their mass distribution with advanced LIGO*, *Phys. Dark Univ.* **15** (2017) 142 [arXiv:1603.05234] [INSPIRE].

[16] Y.B. Zel'dovich and I. Novikov, *The hypothesis of cores retarded during expansion and the hot cosmological model*, *Sov. Astron.* **10** (1967) 602.

[17] S. Hawking, *Gravitationally collapsed objects of very low mass*, *Mon. Not. Roy. Astron. Soc.* **152** (1971) 75 [INSPIRE].

[18] B.J. Carr and S.W. Hawking, *Black holes in the early universe*, *Mon. Not. Roy. Astron. Soc.* **168** (1974) 399 [INSPIRE].

[19] I. Musco, J.C. Miller and L. Rezzolla, *Computations of primordial black hole formation*, *Class. Quant. Grav.* **22** (2005) 1405 [gr-qc/0412063] [INSPIRE].

[20] A. Polnarev and R. Zembowicz, *Formation of primordial black holes by cosmic strings*, *Phys. Rev.* **D 43** (1991) 1106 [INSPIRE].

[21] S.W. Hawking, *Black holes from cosmic strings*, *Phys. Lett.* **B 231** (1989) 237 [INSPIRE].

JCAP09(2018)039

[22] U.F. Wichoski, J.H. MacGibbon and R.H. Brandenberger, *Astrophysical constraints on primordial black hole formation from collapsing cosmic strings*, *Phys. Rept.* **307** (1998) 191 [astro-ph/9804341] [INSPIRE].

[23] V.A. Berezin, V.A. Kuzmin and I.I. Tkachev, *Thin wall vacuum domains evolution*, *Phys. Lett.* **B 120** (1983) 91 [INSPIRE].

[24] J. Ipser and P. Sikivie, *The gravitationally repulsive domain wall*, *Phys. Rev.* **D 30** (1984) 712 [INSPIRE].

[25] M. Crawford and D.N. Schramm, *Spontaneous generation of density perturbations in the early universe*, *Nature* **298** (1982) 538 [INSPIRE].

[26] D. La and P.J. Steinhardt, *Bubble percolation in extended inflationary models*, *Phys. Lett.* **B 220** (1989) 375 [INSPIRE].

[27] P. Ivanov, P. Naselsky and I. Novikov, *Inflation and primordial black holes as dark matter*, *Phys. Rev.* **D 50** (1994) 7173 [INSPIRE].

[28] P. Ivanov, *Nonlinear metric perturbations and production of primordial black holes*, *Phys. Rev.* **D 57** (1998) 7145 [astro-ph/9708224] [INSPIRE].

[29] J. García-Bellido, A.D. Linde and D. Wands, *Density perturbations and black hole formation in hybrid inflation*, *Phys. Rev.* **D 54** (1996) 6040 [astro-ph/9605094] [INSPIRE].

[30] S. Shandera, D. Jeong and H.S.G. Gebhardt, *Gravitational waves from binary mergers of subsolar mass dark black holes*, *Phys. Rev. Lett.* **120** (2018) 241102 [arXiv:1802.08206] [INSPIRE].

[31] A. Barnacka, J.-F. Glicenstein and R. Moderski, *New constraints on primordial black holes abundance from femtolensing of gamma-ray bursts*, *Phys. Rev.* **D 86** (2012) 043001 [arXiv:1204.2056] [INSPIRE].

[32] A. Katz, J. Kopp, S. Sibiryakov and W. Xue, *Femtolensing by dark matter revisited*, submitted to *JCAP* (2018) [arXiv:1807.11495] [INSPIRE].

[33] K. Griest, A.M. Cieplak and M.J. Lehner, *Experimental limits on primordial black hole dark matter from the first 2 yr of Kepler data*, *Astrophys. J.* **786** (2014) 158 [arXiv:1307.5798] [INSPIRE].

[34] H. Niikura et al., *Microlensing constraints on primordial black holes with the Subaru/HSC Andromeda observation*, arXiv:1701.02151 [INSPIRE].

[35] EROS-2 collaboration, P. Tisserand et al., *Limits on the Macho content of the galactic halo from the EROS-2 survey of the Magellanic clouds*, *Astron. Astrophys.* **469** (2007) 387 [astro-ph/0607207] [INSPIRE].

[36] S. Calchi Novati, S. Mirzoyan, P. Jetzer and G. Scarpetta, *Microlensing towards the SMC: a new analysis of OGLE and EROS results*, *Mon. Not. Roy. Astron. Soc.* **435** (2013) 1582 [arXiv:1308.4281] [INSPIRE].

[37] MACHO collaboration, R.A. Allsman et al., *MACHO project limits on black hole dark matter in the 1–30 solar mass range*, *Astrophys. J.* **550** (2001) L169 [astro-ph/0011506] [INSPIRE].

[38] E. Mediavilla et al., *Microlensing-based estimate of the mass fraction in compact objects in lens*, *Astrophys. J.* **706** (2009) 1451 [arXiv:0910.3645] [INSPIRE].

[39] P.N. Wilkinson et al., *Limits on the cosmological abundance of supermassive compact objects from a search for multiple imaging in compact radio sources*, *Phys. Rev. Lett.* **86** (2001) 584 [astro-ph/0101328] [INSPIRE].

[40] M. Zumalacarregui and U. Seljak, *Limits on stellar-mass compact objects as dark matter from gravitational lensing of type-IA supernovae*, arXiv:1712.02240 [INSPIRE].

JCAP09(2018)039

[41] P.W. Graham, S. Rajendran and J. Varela, *Dark matter triggers of supernovae*, *Phys. Rev.* **D 92** (2015) 063007 [arXiv:1505.04444] [INSPIRE].

[42] F. Capela, M. Pshirkov and P. Tinyakov, *Constraints on primordial black holes as dark matter candidates from capture by neutron stars*, *Phys. Rev.* **D 87** (2013) 123524 [arXiv:1301.4984] [INSPIRE].

[43] D.P. Quinn, M.I. Wilkinson, M.J. Irwin, J. Marshall, A. Koch and V. Belokurov, *On the reported death of the MACHO era*, *Mon. Not. Roy. Astron. Soc.* **396** (2009) 11 [arXiv:0903.1644] [INSPIRE].

[44] T.D. Brandt, *Constraints on MACHO dark matter from compact stellar systems in ultra-faint dwarf galaxies*, *Astrophys. J.* **824** (2016) L31 [arXiv:1605.03665] [INSPIRE].

[45] Y. Ali-Haïmoud, E.D. Kovetz and M. Kamionkowski, *Merger rate of primordial black-hole binaries*, *Phys. Rev.* **D 96** (2017) 123523 [arXiv:1709.06576] [INSPIRE].

[46] R. Magee et al., *Methods for the detection of gravitational waves from sub-solar mass ultracompact binaries*, arXiv:1808.04772 [INSPIRE].

[47] D. Gaggero et al., *Searching for primordial black holes in the radio and X-ray sky*, *Phys. Rev. Lett.* **118** (2017) 241101 [arXiv:1612.00457] [INSPIRE].

[48] M. Ricotti, J.P. Ostriker and K.J. Mack, *Effect of primordial black holes on the cosmic microwave background and cosmological parameter estimates*, *Astrophys. J.* **680** (2008) 829 [arXiv:0709.0524] [INSPIRE].

[49] Y. Ali-Haïmoud and M. Kamionkowski, *Cosmic microwave background limits on accreting primordial black holes*, *Phys. Rev.* **D 95** (2017) 043534 [arXiv:1612.05644] [INSPIRE].

[50] V. Poulin, P.D. Serpico, F. Calore, S. Clesse and K. Kohri, *CMB bounds on disk-accreting massive primordial black holes*, *Phys. Rev.* **D 96** (2017) 083524 [arXiv:1707.04206] [INSPIRE].

[51] J. Luis Bernal, N. Bellomo, A. Raccanelli and L. Verde, *Cosmological implications of primordial black holes*, *JCAP* **10** (2017) 052 [arXiv:1709.07465] [INSPIRE].

[52] D. Aloni, K. Blum and R. Flauger, *Cosmic microwave background constraints on primordial black hole dark matter*, *JCAP* **05** (2017) 017 [arXiv:1612.06811] [INSPIRE].

[53] N. Bellomo, J.L. Bernal, A. Raccanelli and L. Verde, *Primordial black holes as dark matter: converting constraints from monochromatic to extended mass distributions*, *JCAP* **01** (2018) 004 [arXiv:1709.07467] [INSPIRE].

[54] LIGO Scientific collaboration, J. Aasi et al., *Advanced LIGO*, *Class. Quant. Grav.* **32** (2015) 074001 [arXiv:1411.4547] [INSPIRE].

[55] B. Sathyaprakash et al., *Scientific objectives of Einstein telescope*, *Class. Quant. Grav.* **29** (2012) 124013 [*Erratum ibid.* **30** (2013) 079501] [arXiv:1206.0331] [INSPIRE].

[56] A. Raccanelli, E.D. Kovetz, S. Bird, I. Cholis and J.B. Muñoz, *Determining the progenitors of merging black-hole binaries*, *Phys. Rev.* **D 94** (2016) 023516 [arXiv:1605.01405] [INSPIRE].

[57] A. Raccanelli, *Gravitational wave astronomy with radio galaxy surveys*, *Mon. Not. Roy. Astron. Soc.* **469** (2017) 656 [arXiv:1609.09377] [INSPIRE].

[58] H. Nishikawa, E.D. Kovetz, M. Kamionkowski and J. Silk, *Primordial-black-hole mergers in dark-matter spikes*, arXiv:1708.08449 [INSPIRE].

[59] I. Cholis et al., *Orbital eccentricities in primordial black hole binaries*, *Phys. Rev.* **D 94** (2016) 084013 [arXiv:1606.07437] [INSPIRE].

[60] J.B. Muñoz, E.D. Kovetz, L. Dai and M. Kamionkowski, *Lensing of fast radio bursts as a probe of compact dark matter*, *Phys. Rev. Lett.* **117** (2016) 091301 [arXiv:1605.00008] [INSPIRE].

JCAP09(2018)039

[61] E.D. Kovetz, I. Cholis, P.C. Breysse and M. Kamionkowski, *Black hole mass function from gravitational wave measurements*, *Phys. Rev.* **D 95** (2017) 103010 [arXiv:1611.01157] [INSPIRE].

[62] E.D. Kovetz, *Probing primordial-black-hole dark matter with gravitational waves*, *Phys. Rev. Lett.* **119** (2017) 131301 [arXiv:1705.09182] [INSPIRE].

[63] E. Munari, A. Biviano, S. Borgani, G. Murante and D. Fabjan, *The relation between velocity dispersion and mass in simulated clusters of galaxies: dependence on the tracer and the baryonic physics*, *Mon. Not. Roy. Astron. Soc.* **430** (2013) 2638 [arXiv:1301.1682] [INSPIRE].

[64] A. Vale and J.P. Ostriker, *Linking halo mass to galaxy luminosity*, *Mon. Not. Roy. Astron. Soc.* **353** (2004) 189 [astro-ph/0402500] [INSPIRE].

[65] D.K. Erb, *Feedback in low-mass galaxies in the early universe*, *Nature* **523** (2015) 169 [arXiv:1507.02374] [INSPIRE].

[66] R.P. Norris et al., *EMU: Evolutionary Map of the Universe*, *Publ. Astron. Soc. Austral.* **28** (2011) 215 [arXiv:1106.3219] [INSPIRE].

[67] DESI collaboration, A. Aghamousa et al., *The DESI experiment part I: science, targeting and survey design*, arXiv:1611.00036 [INSPIRE].

[68] SKA Cosmology SWG collaboration, R. Maartens, F.B. Abdalla, M. Jarvis and M.G. Santos, *Overview of cosmology with the SKA*, PoS(AASKA14)016 [arXiv:1501.04076] [INSPIRE].

[69] L. Dai, T. Venumadhav and K. Sigurdson, *Effect of lensing magnification on the apparent distribution of black hole mergers*, *Phys. Rev.* **D 95** (2017) 044011 [arXiv:1605.09398] [INSPIRE].

[70] M. Oguri, *Effect of gravitational lensing on the distribution of gravitational waves from distant binary black hole mergers*, *Mon. Not. Roy. Astron. Soc.* **480** (2018) 3842 [arXiv:1807.02584] [INSPIRE].

[71] Y. Wang, A. Stebbins and E.L. Turner, *Gravitational lensing of gravitational waves from merging neutron star binaries*, *Phys. Rev. Lett.* **77** (1996) 2875 [astro-ph/9605140] [INSPIRE].

[72] D. Bertacca, A. Raccanelli, N. Bartolo and S. Matarrese, *Cosmological perturbation effects on gravitational-wave luminosity distance estimates*, *Phys. Dark Univ.* **20** (2018) 32 [arXiv:1702.01750] [INSPIRE].

[73] S. Camera and A. Nishizawa, *Beyond concordance cosmology with magnification of gravitational-wave standard sirens*, *Phys. Rev. Lett.* **110** (2013) 151103 [arXiv:1303.5446] [INSPIRE].

[74] B.F. Schutz, *Networks of gravitational wave detectors and three figures of merit*, *Class. Quant. Grav.* **28** (2011) 125023 [arXiv:1102.5421] [INSPIRE].

[75] S. Klimenko et al., *Localization of gravitational wave sources with networks of advanced detectors*, *Phys. Rev.* **D 83** (2011) 102001 [arXiv:1101.5408] [INSPIRE].

[76] T. Sidery et al., *Reconstructing the sky location of gravitational-wave detected compact binary systems: methodology for testing and comparison*, *Phys. Rev.* **D 89** (2014) 084060 [arXiv:1312.6013] [INSPIRE].

[77] T. Namikawa, A. Nishizawa and A. Taruya, *Anisotropies of gravitational-wave standard sirens as a new cosmological probe without redshift information*, *Phys. Rev. Lett.* **116** (2016) 121302 [arXiv:1511.04638] [INSPIRE].

[78] A. Raccanelli et al., *A reassessment of the evidence of the Integrated Sachs-Wolfe effect through the WMAP-NVSS correlation*, *Mon. Not. Roy. Astron. Soc.* **386** (2008) 2161 [arXiv:0802.0084] [INSPIRE].

JCAP09(2018)039

[79] A. Pullen, T.-C. Chang, O. Dore and A. Lidz, *Cross-correlations as a carbon monoxide detector*, *Astrophys. J.* **768** (2013) 15 [arXiv:1211.1397] [INSPIRE].

[80] C. Bonvin and R. Durrer, *What galaxy surveys really measure*, *Phys. Rev.* **D 84** (2011) 063505 [arXiv:1105.5280] [INSPIRE].

[81] D. Blas, J. Lesgourgues and T. Tram, *The Cosmic Linear Anisotropy Solving System (CLASS) II: approximation schemes*, *JCAP* **07** (2011) 034 [arXiv:1104.2933] [INSPIRE].

[82] E. Di Dio, F. Montanari, J. Lesgourgues and R. Durrer, *The CLASSgal code for relativistic cosmological large scale structure*, *JCAP* **11** (2013) 044 [arXiv:1307.1459] [INSPIRE].

[83] A. Challinor and A. Lewis, *The linear power spectrum of observed source number counts*, *Phys. Rev.* **D 84** (2011) 043516 [arXiv:1105.5292] [INSPIRE].

[84] N. Bellomo, J.L. Bernal, A. Raccanelli, G. Scelfo and L. Verde, *On the importance of a correct modelling*, to appear in the arXiv, October 2018.

[85] C.S. Unnikrishnan, *IndIGO and LIGO-India: scope and plans for gravitational wave research and precision metrology in India*, *Int. J. Mod. Phys.* **D 22** (2013) 1341010 [arXiv:1510.06059] [INSPIRE].

[86] KAGRA collaboration, K. Somiya, *Detector configuration of KAGRA: the Japanese cryogenic gravitational-wave detector*, *Class. Quant. Grav.* **29** (2012) 124007 [arXiv:1111.7185] [INSPIRE].

[87] E.F. Bunn, *Statistical analysis of cosmic microwave background anisotropy*, Ph.D. thesis, University of California, Berkeley, CA, U.S.A., (1995).

[88] M. Tegmark, A. Taylor and A. Heavens, *Karhunen-Loève eigenvalue problems in cosmology: how should we tackle large data sets?*, *Astrophys. J.* **480** (1997) 22 [astro-ph/9603021] [INSPIRE].

[89] M.S. Vogeley and A.S. Szalay, *Eigenmode analysis of galaxy redshift surveys I. Theory and methods*, *Astrophys. J.* **465** (1996) 34 [astro-ph/9601185] [INSPIRE].

[90] PLANCK collaboration, P.A.R. Ade et al., *Planck* 2015 *results. XIII. Cosmological parameters*, *Astron. Astrophys.* **594** (2016) A13 [arXiv:1502.01589] [INSPIRE].

[91] M.J. Jarvis et al., *Cosmology with SKA radio continuum surveys*, arXiv:1501.03825 [INSPIRE].

[92] A. Bonaldi et al., *The Tiered Radio Extragalactic Continuum Simulation (T-RECS)*, arXiv:1805.05222 [INSPIRE].

[93] A. Raccanelli et al., *Cosmological measurements with forthcoming radio continuum surveys*, *Mon. Not. Roy. Astron. Soc.* **424** (2012) 801 [arXiv:1108.0930] [INSPIRE].

[94] R.J. Wilman et al., *A semi-empirical simulation of the extragalactic radio continuum sky for next generation radio telescopes*, *Mon. Not. Roy. Astron. Soc.* **388** (2008) 1335 [arXiv:0805.3413] [INSPIRE].

[95] E.L. Turner, J.P. Ostriker and J.R. Gott, III, *The statistics of gravitational lenses: the distributions of image angular separations and lens redshifts*, *Astrophys. J.* **284** (1984) 1 [INSPIRE].

[96] M. Bartelmann and P. Schneider, *Weak gravitational lensing*, *Phys. Rept.* **340** (2001) 291 [astro-ph/9912508] [INSPIRE].

[97] L. Hui, E. Gaztanaga and M. LoVerde, *Anisotropic magnification distortion of the 3D galaxy correlation. 1. Real space*, *Phys. Rev.* **D 76** (2007) 103502 [arXiv:0706.1071] [INSPIRE].

[98] J. Liu, Z. Haiman, L. Hui, J.M. Kratochvil and M. May, *The impact of magnification and size bias on weak lensing power spectrum and peak statistics*, *Phys. Rev.* **D 89** (2014) 023515 [arXiv:1310.7517] [INSPIRE].

JCAP09(2018)039

[99] F. Montanari and R. Durrer, *Measuring the lensing potential with tomographic galaxy number counts*, *JCAP* **10** (2015) 070 [arXiv:1506.01369] [INSPIRE].

[100] A. Challinor and A. Lewis, *The linear power spectrum of observed source number counts*, *Phys. Rev.* **D 84** (2011) 043516 [arXiv:1105.5292] [INSPIRE].

[101] D. Jeong, F. Schmidt and C.M. Hirata, *Large-scale clustering of galaxies in general relativity*, *Phys. Rev.* **D 85** (2012) 023504 [arXiv:1107.5427] [INSPIRE].

[102] D. Bertacca, R. Maartens, A. Raccanelli and C. Clarkson, *Beyond the plane-parallel and Newtonian approach: wide-angle redshift distortions and convergence in general relativity*, *JCAP* **10** (2012) 025 [arXiv:1205.5221] [INSPIRE].

[103] T. Nakamura, M. Sasaki, T. Tanaka and K.S. Thorne, *Gravitational waves from coalescing black hole MACHO binaries*, *Astrophys. J.* **487** (1997) L139 [astro-ph/9708060] [INSPIRE].

[104] M. Raidal, V. Vaskonen and H. Veermäe, *Gravitational waves from primordial black hole mergers*, *JCAP* **09** (2017) 037 [arXiv:1707.01480] [INSPIRE].

[105] J.L. Tinker et al., *Toward a halo mass function for precision cosmology: the limits of universality*, *Astrophys. J.* **688** (2008) 709 [arXiv:0803.2706] [INSPIRE].

[106] H. Mouri and Y. Taniguchi, *Runaway merging of black holes: analytical constraint on the timescale*, *Astrophys. J.* **566** (2002) L17 [astro-ph/0201102] [INSPIRE].

[107] G.D. Quinlan and S.L. Shapiro, *Dynamical evolution of dense clusters of compact stars*, *Astrophys. J.* **343** (1989) 725.

[108] J.F. Navarro, C.S. Frenk and S.D.M. White, *The structure of cold dark matter halos*, *Astrophys. J.* **462** (1996) 563 [astro-ph/9508025] [INSPIRE].

[109] F. Prada, A.A. Klypin, A.J. Cuesta, J.E. Betancort-Rijo and J. Primack, *Halo concentrations in the standard ΛCDM cosmology*, *Mon. Not. Roy. Astron. Soc.* **423** (2012) 3018 [arXiv:1104.5130] [INSPIRE].

[110] A.D. Ludlow et al., *The mass-concentration-redshift relation of cold and warm dark matter haloes*, *Mon. Not. Roy. Astron. Soc.* **460** (2016) 1214 [arXiv:1601.02624] [INSPIRE].

[111] J.R. Chisholm, *Clustering of primordial black holes: basic results*, *Phys. Rev.* **D 73** (2006) 083504 [astro-ph/0509141] [INSPIRE].

[112] J.R. Chisholm, *Clustering of primordial black holes. II. Evolution of bound systems*, *Phys. Rev.* **D 84** (2011) 124031 [arXiv:1110.4402] [INSPIRE].

[113] Y. Ali-Haïmoud, *Correlation function of high-threshold regions and application to the initial small-scale clustering of primordial black holes*, *Phys. Rev. Lett.* **121** (2018) 081304 [arXiv:1805.05912] [INSPIRE].

[114] V. Desjacques and A. Riotto, *The spatial clustering of primordial black holes*, arXiv:1806.10414 [INSPIRE].

[115] G. Ballesteros, P.D. Serpico and M. Taoso, *On the merger rate of primordial black holes: effects of nearest neighbours distribution and clustering*, arXiv:1807.02084 [INSPIRE].

[116] H.J. Mo and S.D.M. White, *An analytic model for the spatial clustering of dark matter halos*, *Mon. Not. Roy. Astron. Soc.* **282** (1996) 347 [astro-ph/9512127] [INSPIRE].

[117] K. Belczynski, T. Ryu, R. Perna, E. Berti, T.L. Tanaka and T. Bulik, *On the likelihood of detecting gravitational waves from population III compact object binaries*, *Mon. Not. Roy. Astron. Soc.* **471** (2017) 4702 [arXiv:1612.01524] [INSPIRE].

[118] O.D. Elbert, J.S. Bullock and M. Kaplinghat, *Counting black holes: the cosmic stellar remnant population and implications for LIGO*, *Mon. Not. Roy. Astron. Soc.* **473** (2018) 1186 [arXiv:1703.02551] [INSPIRE].

JCAP09(2018)039

[119] M. Mapelli, N. Giacobbo, E. Ripamonti and M. Spera, *The cosmic merger rate of stellar black hole binaries from the Illustris simulation*, *Mon. Not. Roy. Astron. Soc.* **472** (2017) 2422 [arXiv:1708.05722] [INSPIRE].

[120] C.J. Moore, R.H. Cole and C.P.L. Berry, *Gravitational-wave sensitivity curves*, *Class. Quant. Grav.* **32** (2015) 015014 [arXiv:1408.0740] [INSPIRE].

[121] M. Vallisneri and C.R. Galley, *Non-sky-averaged sensitivity curves for space-based gravitational-wave observatories*, *Class. Quant. Grav.* **29** (2012) 124015 [arXiv:1201.3684] [INSPIRE].

[122] E.E. Flanagan and S.A. Hughes, *Measuring gravitational waves from binary black hole coalescences: I. Signal-to-noise for inspiral, merger and ringdown*, *Phys. Rev.* **D 57** (1998) 4535 [gr-qc/9701039] [INSPIRE].

[123] P. Ajith, *Addressing the spin question in gravitational-wave searches: waveform templates for inspiralling compact binaries with nonprecessing spins*, *Phys. Rev.* **D 84** (2011) 084037 [arXiv:1107.1267] [INSPIRE].

[124] E.A. Huerta and J.R. Gair, *Intermediate-mass-ratio-inspirals in the Einstein telescope: I. Signal-to-noise ratio calculations*, *Phys. Rev.* **D 83** (2011) 044020 [arXiv:1009.1985] [INSPIRE].

[125] VIRGO and LIGO SCIENTIFIC collaborations, B.P. Abbott et al., *Binary black hole mergers in the first advanced LIGO observing run*, *Phys. Rev.* **X 6** (2016) 041015 [arXiv:1606.04856] [INSPIRE].

[126] K. Hayasaki and A. Loeb, *Detection of gravitational wave emission by supermassive black hole binaries through tidal disruption flares*, *Sci. Repts.* **6** (2016) 35629 [arXiv:1510.05760] [INSPIRE].

JCAP09(2018)039

Part III

INFLATION

4

CONSTRAINING THE INFLATIONARY SCENARIO

The simplest inflationary models, i.e., those belonging to the single-field slow-roll class, have passed numerous tests, namely they generate a flat, isotropic and homogeneous Universe, they create super-horizon scalar perturbations with Gaussian statistics, the power spectrum of these perturbations is almost scale-invariant and reads as

$$\mathcal{P}_\zeta(k) = A_s \left(\frac{k}{k_\star}\right)^{n_s - 1}, \tag{4.1}$$

where A_s and n_s are the scalar perturbation amplitude and tilt and $k_\star$ is a pivot scale.

Assuming that a single-field inflationary model is slow-rolling is equivalent to require that the kinetic energy of the scalar field is significantly smaller than the potential one, i.e., $\dot{\phi}^2 \ll V$, and that the acceleration of the field is negligible with respect to its velocity, i.e., $\ddot{\phi} \ll H_{\rm inf}\dot{\phi}$. Alternatively, we can express the same set of conditions in terms of the slow-roll parameters

$$\epsilon = \frac{M_p^2}{2}\left(\frac{\partial_\phi V}{V}\right)^2, \qquad \eta = M_p^2 \frac{\partial_\phi^2 V}{V}, \tag{4.2}$$

which describe the steepness of the scalar field potential and how fast the scalar field moves along it: slow-roll means that we require $\epsilon \ll 1$ and $|\eta| \ll 1$. The dynamics of the field is also encoded in the two-point function of the perturbations, in fact we have that

$$A_s \propto \frac{H_{\rm inf}^2}{\epsilon M_p^2}, \qquad n_s - 1 = 2\eta - 6\epsilon, \tag{4.3}$$

therefore measurements of Late Universe properties can actually put constraints on the dynamics of the Early Universe.

However, we are still missing the so called "smoking gun" of inflation: the gravitational waves produced as tensor fluctuations in the metric and stretched to super-horizon scales by the exponential expansion, as in the case of scalar perturbations. Also tensor perturbations are predicted to have an almost scale-invariant power spectrum, namely

$$\mathcal{P}_h(k) = A_t \left(\frac{k}{k_\star}\right)^{n_t}, \tag{4.4}$$

where A_t and n_t are the tensor perturbations amplitude and tilt, in analogy with scalar perturbations. The standard predictions is that

the tilt reads as $n_t = -2\epsilon$ while the amplitude is suppressed with respect to scalar perturbation: this suppression is typically quantified by the tensor-to-scalar ratio at pivot scale $r = A_t/A_s = 16\epsilon$. Therefore measuring properties of tensor modes in the Late Universe helps in breaking the degeneracy between the energy scale of inflation $H_{\rm inf}$ and the slow-roll parameters ϵ and η.

In this chapter I present two works, "Measuring the energy scale of inflation using large scale structures" [41] and "From primordial black holes abundance to primordial curvature power spectrum (and back)" [42]. In both works I propose a novel way to measure properties of the Early Universe.

The first article I investigate how to measure the energy scale of inflation, i.e., the Hubble expansion parameter $H_{\rm inf}$, through a measurement of the tensor-to-scalar ratio r. The only model-independent lower limit we have comes from Big Bang Nucleosynthesis, which bound inflation to happen at energies greater than $\mathcal{O}(\text{MeV})$. We also have an upper limit of $\mathcal{O}(10^{16}\ \text{GeV})$ coming from the upper limit on B-modes amplitude, which bounds $r \lesssim \mathcal{O}(10^{-1})$ [9]. In this work I propose a method to measure r using the data coming from the large scale structure of the Universe, providing an alternative to classical CMB B-modes detection or to detect a primordial gravitational waves background using next generation detectors as LISA, BBO or DECIGO. The determination of this energy scale is a key step in addressing other open questions in the ΛCDM, for instance related to the physics of reheating or how baryons and matter-antimatter asymmetry was created. Moreover, the inflaton itself would represent the first Beyond Standard Model particle to be ever detected in a range of energies inaccessible by any laboratory on Earth.

In several inflationary scenario, the scalar field is not slow-rolling indefinitely, and possible deviations from slow-roll might boost the power spectrum at very small scales, which has not been probed yet. If the boost is large enough, the mildly non-linear or non-linear perturbations created might be able to collapse and form compact objects, PBHs, already during the radiation-dominated era. In the second paper I put on a firm theoretical ground the correspondence between PBHs abundance in present-day Universe and the primordial curvature power spectrum. Eventual detections of PBHs would shed light on a completely new range of scales orders of magnitude smaller than cosmological scales. At the same time, we would be able to probe the dynamics of the inflation in a new regime completely different by the slow-roll one, which is totally incompatible with the existence even of a single PBH in our Universe.

Journal of Cosmology and Astroparticle Physics
An IOP and SISSA journal

Measuring the energy scale of inflation with large scale structures

Nicola Bellomo,[a,b] **Nicola Bartolo,**[c,d,e] **Raul Jimenez,**[a,f] **Sabino Matarrese**[c,d,e,g] **and Licia Verde**[a,f]

[a]ICC, University of Barcelona, IEEC-UB, Martí i Franquès, 1, E-08028 Barcelona, Spain
[b]Departament de Física Quàntica i Astrofísica, Universitat de Barcelona, Martí i Franquès 1, E-08028 Barcelona, Spain
[c]Dipartimento di Fisica e Astronomia G. Galilei, Università degli Studi di Padova, via F. Marzolo 8, I-35131, Padova, Italy
[d]INFN, Sezione di Padova, via F. Marzolo 8, I-35131, I-35131 Padova, Italy
[e]INAF — Osservatorio Astronomico di Padova, vicolo dell'Osservatorio 5, I-35122 Padova, Italy
[f]ICREA, Pg. Lluis Companys 23, Barcelona, E-08010, Spain
[g]Gran Sasso Science Institute, viale F. Crispi 7, I-67100 L'Aquila, Italy

E-mail: nicola.bellomo@icc.ub.edu, nicola.bartolo@pd.infn.it, raul.jimenez@icc.ub.edu, sabino.matarrese@pd.infn.it, liciaverde@icc.ub.edu

Received September 25, 2018
Revised November 12, 2018
Accepted November 15, 2018
Published November 26, 2018

Abstract. The determination of the inflationary energy scale represents one of the first step towards the understanding of the early Universe physics. The (very mild) non-Gaussian signals that arise from any inflation model carry information about the energy scale of inflation and may leave an imprint in some cosmological observables, for instance on the clustering of high-redshift, rare and massive collapsed structures. In particular, the graviton exchange contribution due to interactions between scalar and tensor fluctuations leaves a specific signature in the four-point function of curvature perturbations, thus on clustering properties of collapsed structures. We compute the contribution of graviton exchange on two- and three-point function of halos, showing that at large scales $k \sim 10^{-3}\,\mathrm{Mpc}^{-1}$ its magnitude is comparable or larger to that of other primordial non-Gaussian signals discussed in the literature. This provides a potential route to probe the existence of tensor fluctuations which is alternative and highly complementary to B-mode polarisation measurements of the cosmic microwave background radiation.

Keywords: inflation, power spectrum
ArXiv ePrint: 1809.07113

We dedicate this paper to the memory of our friend and colleague Bepi Tormen who did pioneering work in the understanding of the abundance and clustering of dark matter halos.

https://doi.org/10.1088/1475-7516/2018/11/043

JCAP11(2018)043

Contents

1 Introduction

The inflationary paradigm has passed four major tests: there are super-horizon perturbations, as shown for the first time in ref. [1]; the power spectrum of these fluctuations is nearly scale invariant [2] but deviates by a small amount from it, as first shown compellingly in refs. [3, 4]; the Universe is essentially spatially flat [3, 5–7] and appears homogeneous and isotropic on large scales [8–10]; initial conditions are very nearly Gaussian [1, 11–14].

The fact that the inflationary paradigm has passed these tests does not mean it has been verified. Indeed, alternative models exist that also pass the above tests [15, 16]. What is unique of the inflationary paradigm is the existence of an accelerated expansion phase that results in a (quasi) exponential growth of the scale-factor of the metric. This, in turn, facilitates that tensor fluctuations in the metric will manifest themselves as potentially observable gravitational waves [17]. This crucial feature of inflation has not yet been measured. Obviously, measuring it would be momentous as it would open up a window into inflation and the early Universe physics not explored before, and would offer the possibility to understand physical mechanisms at play at the energy scale of inflation.

In the simplest inflationary models the amplitude of tensor modes (usually parametrised by the parameter r, the tensor-to-scalar ratio at a given scale) can be related to the energy scale of inflation, given by the inflaton potential V, by

$$V^{1/4} = \left(\frac{3}{2}\pi^2 r \mathcal{P}_\zeta\right)^{1/4} M_P \sim 3.3 \times 10^{16}\ r^{1/4}\,\mathrm{GeV}, \tag{1.1}$$

where $\mathcal{P}_\zeta$ is the power spectrum[1] of curvature perturbations on uniform energy density hypersurfaces ζ and $M_P = \sqrt{\hbar c/(8\pi G)}$ is the reduced Planck mass. The firm lower limit on

[1] Here we refer to the almost scale-invariant power spectrum

$$\mathcal{P}_\zeta = \frac{k^3}{2\pi^2} P_\zeta = \frac{1}{2M_P^2 \epsilon}\left(\frac{H_\star}{2\pi}\right)^2 \left(\frac{k}{aH_\star}\right)^{n_s - 1},$$

determined by the Hubble expansion rate during inflation $H_\star$ and the slow-roll parameter $\epsilon = \frac{M_P^2}{2}\left(\frac{\partial_\varphi V}{V}\right)^2$, where ∂_φ represents the partial derivative with respect to the inflaton field. Past experiments have already measured with great precision the scalar power spectrum amplitude $2\pi^2 A_s = \frac{H_\star^2}{4\epsilon M_P^2}$ and the scalar tilt n_s. In this work we use $A_s = 2.105 \cdot 10^{-9}$ and $n_s = 0.9665$ [7].

JCAP11(2018)043

the energy scale of inflation is around the MeV scale, to guarantee hydrogen and helium production during Big Bang Nucleosynthesis [18–21].

An inflationary stochastic background of gravitational waves could in principle be measured directly via future(istic) gravitational wave detection experiments as LISA [22] (see also [23–25]), DECIGO [26] or BBO [27], or indirectly via its effect on the polarization of the cosmic microwave background radiation (CMB, see e.g., refs. [28, 29]). The current observational limit on the tensor-to-scalar ratio is $r \lesssim 0.1$ [6, 7]. Proposed experiments, as CMBPol [30], PRISM [31] and CORE [32], can reach the 10^{-3} level, however it is well known that measuring $r < 10^{-4}$ via CMB polarisation is extremely challenging (see e.g., ref. [33]) and the cosmic variance limit is at the 10^{-5} level [34]. This implies that the measurement of the CMB polarisation signal can only access inflationary energy scales above 10^{15} GeV, only less than an order of magnitude away from the current limit.

A third way one could use to determine the scale of inflation is by probing primordial non-Gaussianities using the information contained in the large-scale structure of the Universe. During the next decade, several galaxy surveys, as DESI [35], LSST [36] and Euclid [37], will probe a large volume of our Universe, providing an unprecedented amount of new data. In this context, measuring higher-order statistics, such as the three- or the four-point functions, will extend our knowledge on the inflationary dynamics, which in turn can be used to discriminate between minimal, slow-roll inflationary paradigm and more complex models. On the other hand the specific details of these higher-order statistics can be highly model dependent, therefore the interpretation of the results can be not so straightforward. The non-Gaussian signature arising from particle exchange between scalar fluctuations has recently received attention [38, 39]. In this work we concentrate on a particular non-Gaussian signal called *graviton exchange* (GE) [40]. This signal arises from correlations between inflaton fluctuations mediated by a graviton and enters in the four-point function of scalar curvature perturbations. The magnitude of this non-Gaussian effect is directly proportional to the tensor-to-scalar ratio r, therefore by isolating this contribution we can extract a direct information (or a stronger upper bound) on the energy scale of inflation. Moreover, this GE contribution contains much more information about inflationary dynamics, in particular on whether inflation is a strong isotropic attractor, as discussed in ref. [41].

The paper is organised as follows: in section 2 we review the main results on non-Gaussianities relevant for this work, in section 3 we review the framework of excursion regions and halo n-points functions and in section 4 we investigate the magnitude of graviton exchange contribution in large scale structure, in particular to the halo power spectrum 4.1 and to the halo bispectrum 4.2. Finally we conclude in section 5. In section A we discuss bispetrum templates. In this work we use the $M_P = 1$ convention.

2 Non-Gaussianity

Primordial fluctuations have been found to be consistent with being Gaussian to a very stringent level [13, 14], however some small deviations from Gaussianity are unavoidable, even in the simplest models, due to the coupling of the inflaton to gravity [42–46]. The information on how these deviations are created is encoded in the connected part of n-point correlators $\langle \zeta_{\mathbf{k}_1} \cdots \zeta_{\mathbf{k}_n} \rangle$ (with $n \geq 2$), where ζ is the curvature perturbation (on uniform energy density hypersurfaces), which is conserved on super-horizon scales for single-field models of inflation. Since curvature perturbations are small (typically $\zeta \sim \mathcal{O}(10^{-5})$ at cosmological scales), it is naively believed that the $(n+1)$-point function is just a small

JCAP11(2018)043

correction to the n-point function, however this statement does not take into account the numerous possible mechanisms that can generate a non-Gaussian signal. Moreover, existing small non-Gaussianities can be boosted in the clustering of high density regions that underwent gravitational collapse, as the peaks of the matter density field, that today host virialized structures.

Since the goal of this work is to provide a new way to constrain the energy scale of inflation, we want to identify some non-Gaussian signal whose strength is directly proportional to the tensor-to-scalar ratio r. In particular, in this work we consider the GE contribution to the four-point function and its contribution to the two- and three-point correlation function of collapsed structures. This signal is contaminated by other non-Gaussian signals, such as those coming from the primordial three-point function, which has not been measured yet. For this reason we consider different scenarios, to cover as many inflationary single-field models as possible.

The curvature perturbation ζ, generated by scalar field(s) during inflation, can be connected to the scalar field(s) fluctuation $\delta\varphi$ on an initial spatially-flat hypersurface. The computation of higher-order correlators can be performed using the so-called in-in or Schwinger-Keldysh formalism [47–50], which allows to follow the evolution of the correlators from sub- to super-horizon scales. One can also use other methods, such as second- and higher-order perturbation theory [45, 51], or using the so-called δN formalism [42, 52–56]. The latter is equivalent to integrating the evolution of the curvature perturbation on super-horizon scales from horizon exit until some later time after inflation. The correlators of the scalar field(s) fluctuation $\delta\varphi$ at horizon-crossing can then be calculated in an expanding or curved background spacetime using the in-in method. Numerous results have been obtained in this context using these well-established formalisms, both at the level of the bispectrum in single- [42, 43, 45, 46, 57] and multi-field inflation, see, e.g., [58–61], and at the level of the trispectrum in single- and multi-fields inflationary scenarios [62–64]. In this work we consider for simplicity single-field slow-roll inflationary models.

When considering the three-point function, we commonly express it in terms of the bispectrum as

$$\langle \zeta_{\mathbf{k}_1} \zeta_{\mathbf{k}_2} \zeta_{\mathbf{k}_3} \rangle = (2\pi)^3 \delta^D \left(\mathbf{k}_{123}\right) B_\zeta(\mathbf{k}_1, \mathbf{k}_2, \mathbf{k}_3), \tag{2.1}$$

where δ^D is the Dirac delta, $\mathbf{k}_{ij\ldots n} = \mathbf{k}_i + \mathbf{k}_j + \cdots + \mathbf{k}_n$ and the details and the assumptions on the inflationary dynamics are encoded in the B_ζ function. For completeness, following ref. [63], we also report the curvature bispectrum:

$$B_\zeta(\mathbf{k}_1, \mathbf{k}_2, \mathbf{k}_3) = (\partial_\varphi N)^3 B_{\delta\varphi}(\mathbf{k}_1, \mathbf{k}_2, \mathbf{k}_3) + (\partial^2_\varphi N)(\partial_\varphi N)^2 \left[P_{\delta\varphi}(k_1) P_{\delta\varphi}(k_2) + (2\,\text{perms.})\right], \tag{2.2}$$

where $P_{\delta\varphi}$ and $B_{\delta\varphi}$ are the scalar field fluctuation power spectrum and bispectrum, N is the number of e-foldings, $\partial^n_\varphi N \sim \mathcal{O}(\epsilon^{(n-2)/2})$ is the n-th derivative of the number of e-folding with respect to the scalar field and it scales with the slow-roll parameter $\epsilon = \frac{1}{2}\left(\partial_\varphi V/V\right)^2$ as indicated. In particular, it has been calculated by Maldacena [46] that in the simplest single-field slow-roll inflationary scenario, at leading order in the slow-roll parameters, the bispectrum reads as

$$B_\zeta^{\text{Maldacena}}(\mathbf{k}_1, \mathbf{k}_2, \mathbf{k}_3) = \frac{1}{2}\left(\frac{H^2_\star}{4\epsilon}\right)^2 \frac{\sum k_j^3}{\prod k_j^3} \left[(1 - n_s) + \epsilon \left(\frac{\sum_{i\neq j} k_i k_j^2 + 8\frac{\sum_{i>j} k_i^2 k_j^2}{k_t}}{\sum k_j^3} - 3\right)\right] \tag{2.3}$$

JCAP11(2018)043

where $k_t = \sum_{j=1}^{3} k_j$. The term in squared parenthesis, as expected [65], has a shape-dependent part explicitly suppressed by the slow-roll parameter ϵ. In the limit of one momentum going to zero (squeezed triangular configurations) the term in round parenthesis goes to zero and the whole bispectrum is proportional to $(1 - n_s)$, while in equilateral triangular configurations the same term is maximal and equal to 5/3. Typically the entire squared parenthesis is written in terms of a $f_{\rm NL}^{\zeta}$ constant parameter (modulus some proportionality constant), to compare data with theory in a simpler way.[2] Notice that non-Gaussianities of this type include also a prominent local contribution (the one proportional to $(1 - n_s)$) associated in real space to the well-known quadratic local model [43, 66, 67]

$$\zeta = \zeta_G + \frac{3}{5} f_{\rm NL}^{\zeta} \left[\zeta_G^2 - \left\langle \zeta_G^2 \right\rangle\right], \tag{2.4}$$

where ζ_G is a Gaussian curvature perturbation.

There is a current debate in the literature about whether the $(1 - n_s)$ term in equation (2.3) represents the minimum amount of non-Gaussianities that can be observed in the squeezed limit. While some authors argue that it is indeed an intrinsic property of the inflaton that gets imprinted in the dark matter density field [68], others argue that it is simply a gauge quantity that will only manifest itself on higher-order terms with a suppressed value of $f_{\rm NL}^{\zeta} \propto \left(\frac{k_L}{k_S}\right)^2 (1 - n_s)$, where k_L and k_S are a long and a short mode, respectively (see e.g., ref. [69] and refs. therein). We point out that it is still an open question which one is the truly gauge invariant quantity in which the calculation can be performed. It should describe the perturbations behaviour on super-horizon scales and connect the fluctuations in early and late Universe to be used to model the corresponding observables. We also refer the interested reader to ref. [70], where a third view on the subject has been presented.

On the other hand, in this work we are mainly interested in the four-point function or trispectrum, in particular its connected part (the disconnected part is always present even in the purely Gaussian case). The complete form of the curvature perturbation trispectrum in single-field inflation, up to second order in slow-roll parameters, reads as [63]

$$\begin{aligned} T_{\zeta}(\mathbf{k}_1, \mathbf{k}_2, \mathbf{k}_3, \mathbf{k}_4) = {} & (\partial_{\varphi} N)^4 T_{\delta\varphi}(\mathbf{k}_1, \mathbf{k}_2, \mathbf{k}_3, \mathbf{k}_4) \\ & + (\partial_{\varphi}^2 N)(\partial_{\varphi} N)^3 \left[P_{\delta\varphi}(k_1) B_{\delta\varphi}(k_{12}, k_3, k_4) + (11\,\text{perms})\right] \\ & + (\partial_{\varphi}^2 N)^2 (\partial_{\varphi} N)^2 \left[P_{\delta\varphi}(k_{13}) P_{\delta\varphi}(k_3) P_{\delta\varphi}(k_4) + (11\,\text{perms})\right] \\ & + (\partial_{\varphi}^3 N)(\partial_{\varphi} N)^3 \left[P_{\delta\varphi}(k_2) P_{\delta\varphi}(k_3) P_{\delta\varphi}(k_4) + (3\,\text{perms})\right], \end{aligned} \tag{2.5}$$

where $T_{\delta\varphi}$ is the scalar field fluctuation trispectrum. By using the linear relation $\zeta \propto \epsilon^{-1/2} \delta\varphi$ we notice that the third and fourth lines of the r.h.s. of equation (2.5) are order ϵ^2 while the order of the first and second line remains to be determine through an explicit computation. The last two lines have also the typical scale dependence coming from the cubic local model

[2] Notice that in the literature there are a series of equivalent, but slightly different parameters. If we would have written the correlators in term of the curvature perturbations on comoving hypersurfaces $\mathcal{R}$ we would have worked with $f_{\rm NL}^{\mathcal{R}}$, while if we have used with the Bardeen's gauge invariant potential Φ, corresponding to the gravitational potential on subhorizon scales, therefore more suitable to work in relation to late times large scale structures, we would have found some constant $f_{\rm NL}^{\Phi}$. Since the three perturbations mentioned above are connected to each other at superhorizon scales by $\Phi = \frac{3(1+w)}{5+3w}\mathcal{R} = -\frac{3(1+w)}{5+3w}\zeta$, the parameters are also connected to each other by $f_{\rm NL}^{\Phi} = f_{\rm NL}^{\mathcal{R}} = -f_{\rm NL}^{\zeta}$, for perturbations entering the horizon during matter domination (if ones uses $\Phi = \Phi_G + f_{\rm NL}^{\Phi}\left[\Phi_G^2 - \langle \Phi_G^2 \rangle\right]$).

JCAP11(2018)043

in real space:

$$\zeta = \zeta_G + \frac{1}{2}\left(\tau^{\zeta}_{\rm NL}\right)^{1/2}\left[\zeta_G^2 - \langle\zeta_G^2\rangle\right] + \frac{9}{25}g^{\zeta}_{\rm NL}\left[\zeta_G^3 - 3\zeta_G\langle\zeta_G^2\rangle\right], \tag{2.6}$$

where we have introduced two non-linearity parameters $\tau^{\zeta}_{\rm NL}$ and $g^{\zeta}_{\rm NL}$ that generate the third and fourth line of equation (2.5), respectively. These two parameters are expected to be of second order in slow-roll parameters. Finally, notice that only in single-field inflation there is a one-to-one correspondence between $f^{\zeta}_{\rm NL}$ and $\tau^{\zeta}_{\rm NL}$.

In ref. [62] it was demonstrated that the scalar field and the metric remain coupled even in an exact de Sitter space, therefore curvature fluctuations are unavoidably non-Gaussian and there is always a connected four-point function, while naively one would have expected it to be zero. This four-point function is associated to so-called contact interactions, that in terms of Feynman diagrams are associated to a diagram with four scalar external legs. The strength of contact interactions has been roughly estimated to be order ϵ [62], disfavouring the possibility of a detection, however, in successive works [40, 64] it has been noticed that non-linear interactions mediated by tensor fluctuations should also be accounted for, in particular the amplitude of the trispectrum generated by the GE is in general comparable to that generated by contact interactions. More details on the GE contribution can be found in section 4.

3 Dark matter halos

Even if some level of non-Gaussianity is imprinted in the primordial field ζ, the most relevant quantity for observations is the late-time (smoothed) matter density field. In particular, the effect of non-Gaussianity is enhanced on higher-order correlations of excursion regions which are traced by potentially observable objects such as dark matter halos (or the galaxies these halos host). We define the smoothed linear overdensity field as

$$\delta_R(\mathbf{x}) = \int d^3y W_R(\mathbf{x}-\mathbf{y})\delta(\mathbf{y}), \tag{3.1}$$

where W_R is a window function of characteristic radius R and δ is the linear overdensity field. We identify regions corresponding to collapsed objects as those where the smoothed density field exceeds a suitable threshold, namely when

$$\delta_R(\mathbf{x}) > \delta_c(z_f) = \frac{\Delta_c(z_f)}{D(z_f)}, \tag{3.2}$$

where z_f is the formation redshift of the dark matter halo and we assume that it is very similar to the observed redshift ($z_f \simeq z_o = z$), $\delta_c(z)$ is the collapse threshold, $\Delta_c(z)$ is the linearly extrapolated overdensity for spherical collapse (1.686 in the Einstein-de Sitter and slightly redshift-dependent for more general cosmologies) and $D(z)$ the linear growth factor. The Fourier transform of the (smoothed) linear overdensity field is related to the Bardeen potential Φ and to the curvature perturbation ζ via the Poisson equation

$$\delta_R(\mathbf{k},z) = \frac{2}{3}\frac{T(k)k^2D(z)}{H_0^2\Omega_{m0}}W_R(k)\Phi(\mathbf{k}) = -\frac{2}{5}\frac{T(k)k^2D(z)}{H_0^2\Omega_{m0}}W_R(k)\zeta(\mathbf{k}) \equiv \mathcal{M}_R(k,z)\zeta(\mathbf{k}), \tag{3.3}$$

where H_0 is today's Hubble expansion rate, Ω_{m0} is the present day matter density fraction, $T(k)$ is the matter transfer function[3] and $W_R(k)$ is the Fourier transform of the window

[3] In this work we use for the transfer function the analytical estimation provided in ref. [71], after checking that it does not differ more than 10% at large k from the transfer function obtained from Boltzmann codes as `CLASS` [72]. To compute the transfer function we use the cosmological parameters $\omega_{\rm b} = 0.02242$, $\omega_{\rm cdm} = 0.11933$ and $h = 0.6766$ [7].

JCAP11(2018)043

function in real space $W_R(r)$.[4] The linear growth factor $D(z)$ depends on the background cosmology and reads as $D(z) = (1+z)^{-1} g(z)/g(0)$, where $g(z)$ is the growth suppression factor for non Einstein-de Sitter universes.

The two-point function of the smoothed matter field reads as

$$\left\langle \delta_R(\mathbf{k}, z) \delta_R(\mathbf{k}', z) \right\rangle = (2\pi)^3 \delta^D(\mathbf{k} + \mathbf{k}') P_R(k, z), \tag{3.4}$$

where $P_R(k,z) = \mathcal{M}_R^2(k,z) P_\zeta(k)$ is the smoothed matter field power spectrum and it is the Fourier transform of the two-point correlation function of the smoothed overdensity field $\xi_R(r,z)$. Finally, we define the variance of the underlying smoothed overdensity field as

$$\xi_R(0,z) = \sigma_R^2(z) = \int \frac{d^3k}{(2\pi)^3} P_R(k,z). \tag{3.5}$$

For Gaussian or slightly non-Gaussian fields, virtually all regions above a high threshold are peaks and therefore will eventually host virialized structures (i.e., massive dark matter halos). Non-Gaussianities change the clustering properties of halos. For regions above a high threshold (and therefore to an extremely good approximation for massive halos), the two-point correlation function reads [73–75]

$$\xi_{\rm halo}(\mathbf{r}) = \exp\left[\sum_{N=2}^{\infty} \sum_{j=1}^{N-1} \frac{\nu^N \sigma_R^{-N}}{j!(N-j)!} \xi_R^{(N)} (\underbrace{\mathbf{x}_1, \ldots, \mathbf{x}_1}_{j \text{ times}}, \underbrace{\mathbf{x}_2, \ldots, \mathbf{x}_2}_{(N-j) \text{ times}}) \right] - 1, \tag{3.6}$$

where $\mathbf{r} = \mathbf{x}_1 - \mathbf{x}_2$, $\nu(z,M) = \Delta_c(z)/\sigma_R(z)$ is the dimensionless peak height, $\xi_R^{(N)} = \langle \underbrace{\delta_R \cdots \delta_R}_{N \text{ times}} \rangle$ are the N-point connected correlation functions and $\xi_R^{(2)} \equiv \xi_R$. The generalization of equation (3.6) to the three-point correlation function is [74]

$$\begin{aligned} \Xi_{\rm halo}(\mathbf{x}_1, \mathbf{x}_2, \mathbf{x}_3) = F(\mathbf{x}_1, \mathbf{x}_2, \mathbf{x}_3) \left[\prod_{i<j} \xi_{\rm halo}(\mathbf{x}_i, \mathbf{x}_j) + [\xi_{\rm halo}(\mathbf{x}_1, \mathbf{x}_2) \xi_{\rm halo}(\mathbf{x}_2, \mathbf{x}_3) + (2 \,\text{perms.})] \right] \\ + [F(\mathbf{x}_1, \mathbf{x}_2, \mathbf{x}_3) - 1] \left[\sum_{i<j} \xi_{\rm halo}(\mathbf{x}_i, \mathbf{x}_j) + 1 \right], \end{aligned} \tag{3.7}$$

where

$$F(\mathbf{x}_1, \mathbf{x}_2, \mathbf{x}_3) = \exp\left[\sum_{N=3}^{\infty} \sum_{j=1}^{N-2} \sum_{k=1}^{N-j-1} \frac{\nu^N \sigma_R^{-N}}{j!k!(N-j-k)!} \xi_R^{(N)} (\underbrace{\mathbf{x}_1, \ldots, \mathbf{x}_1}_{j \text{ times}}, \underbrace{\mathbf{x}_2, \ldots, \mathbf{x}_2}_{k \text{ times}}, \underbrace{\mathbf{x}_3, \ \ldots, \ \mathbf{x}_3}_{(N-j-k) \text{ times}}) \right]. \tag{3.8}$$

[4] In this work we use a top-hat filter of radius R, of enclosed mass (possibly corresponding to a collapsed object at late times) given by

$$M = \frac{3 H_0^2 \Omega_{m0}}{8\pi G} \times \frac{4}{3} \pi R^3.$$

In the rest of this work we use $R = 1.824\,\text{Mpc}$, corresponding to $M_{\rm halo} = 10^{12}\ M_\odot$ dark matter halos. At redshift $z = 0$ these halos cannot be considered very massive, however, as we explain in the following section, our goal is to use the information coming from the high redshift Universe, where e.g., $M_{\rm halo} = 10^{14}\ M_\odot$ dark matter halos (corresponding to $R = 8.45\,\text{Mpc}$) are not common. Nevertheless we explicitly checked that at large scales the choice of a different smoothing radius does not change significantly the results.

JCAP11(2018)043

Here we notice that the N-th order term scales with redshift as $D(z)^{-N}$, hence going to high redshift we observe enhanced non-Gaussian features with respect to redshift $z = 0$. In fact, from our definitions, we have that $(\nu/\sigma_R)^N \propto D(z)^{-2N}$ and $\xi_R^{(N)} \propto D(z)^N$, since in the N-point function each δ_R comes along with a $D(z)$ factor, independently on the Gaussian or non-Gaussian origin of such N-point connected correlation function. Therefore going to higher redshift boosts the non-Gaussian signal with respect to its magnitude at redshift $z = 0$, even if we don't expand the exponential in equations (3.6) and (3.8).

In the limit of purely Gaussian initial conditions, where $\xi_R^{(N\geq 3)} \equiv 0$ hence $F(\mathbf{x}_1, \mathbf{x}_2, \mathbf{x}_3) = 1$, the two- [76–78] and three-point [74] functions of excursion regions becomes

$$\begin{aligned} \xi^G_{\rm halo}(\mathbf{r}) &= \exp\left[\frac{\nu^2}{\sigma_R^2}\xi_R^{(2)}(\mathbf{r})\right] - 1, \\ \Xi^G_{\rm halo}(\mathbf{x}_1, \mathbf{x}_2, \mathbf{x}_3) &= \left[\prod_{i<j} \xi^G_{\rm halo}(\mathbf{x}_i, \mathbf{x}_j) + \left[\xi^G_{\rm halo}(\mathbf{x}_1, \mathbf{x}_2)\xi^G_{\rm halo}(\mathbf{x}_2, \mathbf{x}_3) + (2\,\text{perms.})\right]\right]. \end{aligned} \tag{3.9}$$

The above equations are typically expanded in the limit of high-density peaks ($\nu \gg 1$) and large separation between halos (large scale limit, $r \gg R$, where $\xi_R^{(N)} \ll 1$). In this limit, we expect δ_R to be small, therefore we can identify it as a small parameter in which the expansion is done and we can roughly estimate the N-point correlation functions as $\xi_R^{(N)} \sim \mathcal{O}(\delta_R^N)$. We choose to expand equations (3.9) up to second order, to check that higher order corrections do not contaminate the non-Gaussian signal we are interested in. In particular for the two- and three-point point correlation functions we obtain

$$\begin{aligned} \xi^G_{\rm halo}(\mathbf{r}) &\approx b_L^2\xi_R^{(2)}(\mathbf{r}) + \frac{b_L^4}{2}\left[\xi_R^{(2)}(\mathbf{r})\right]^2, \\ \Xi^G_{\rm halo}(\mathbf{x}_1, \mathbf{x}_2, \mathbf{x}_3) &\approx b_L^4\left[\xi_R^{(2)}(\mathbf{x}_1, \mathbf{x}_2)\xi_R^{(2)}(\mathbf{x}_2, \mathbf{x}_3) + (2\,\text{perms.})\right] \\ &\quad + b_L^6\xi_R^{(2)}(\mathbf{x}_1, \mathbf{x}_2)\xi_R^{(2)}(\mathbf{x}_2, \mathbf{x}_3)\xi_R^{(2)}(\mathbf{x}_1, \mathbf{x}_3) \\ &\quad + \frac{b_L^6}{2}\left[\xi_R^{(2)}(\mathbf{x}_1, \mathbf{x}_2)\left[\xi_R^{(2)}(\mathbf{x}_2, \mathbf{x}_3)\right]^2 + (2\,\text{perms.})\right], \end{aligned} \tag{3.10}$$

where $b_L(z) = \nu(z)/\sigma_R(z) = \Delta_c(z)/\sigma_R^2(z)$ is the Lagrangian linear bias. As noted for the first time by the authors of ref. [74], even if initial conditions are perfectly Gaussian, the three-point correlation function of excursion regions is non-zero and constitutes an unavoidable background signal from which the true primordial non-Gaussian signal has to be extracted. We further analyse the form of the Gaussian part in section 4.2, however we stress that it is not unexpected for the filtering procedure to introduce some feature in correlations functions of all orders, since the smoothing procedure is highly nonlocal and nonlinear. We refer the interested reader to ref. [79], where the authors investigate the effects of the smoothing procedure on dark matter halos bias.

On the other hand, for non-Gaussian initial conditions, other terms appear in the above Taylor expansion. By expanding up to $N = 4$ order to include the four-point correlation function contribution, we have that the non-Gaussian part of the two- and three-point functions

JCAP11(2018)043

read as [80, 81]

$$\xi^{NG}_{\rm halo}(\mathbf{r}) \approx \xi^{G}_{\rm halo}(\mathbf{r}) + b_L^3 \xi_R^{(3)}(\mathbf{x}_1,\mathbf{x}_1,\mathbf{x}_2) + b_L^4 \left[\frac{\xi_R^{(4)}(\mathbf{x}_1,\mathbf{x}_1,\mathbf{x}_1,\mathbf{x}_2)}{3} + \frac{\xi_R^{(4)}(\mathbf{x}_1,\mathbf{x}_1,\mathbf{x}_2,\mathbf{x}_2)}{4} \right] + b_L^5 \xi_R^{(2)}(\mathbf{x}_1,\mathbf{x}_2)\xi_R^{(3)}(\mathbf{x}_1,\mathbf{x}_1,\mathbf{x}_2), \tag{3.11}$$

$$\Xi^{NG}_{\rm halo}(\mathbf{x}_1,\mathbf{x}_2,\mathbf{x}_3) \approx \Xi^{G}_{\rm halo}(\mathbf{x}_1,\mathbf{x}_2,\mathbf{x}_3) + b_L^3 \xi_R^{(3)}(\mathbf{x}_1,\mathbf{x}_2,\mathbf{x}_3) + b_L^4 \left[\frac{\xi_R^{(4)}(\mathbf{x}_1,\mathbf{x}_1,\mathbf{x}_2,\mathbf{x}_3)}{2} + \frac{\xi_R^{(4)}(\mathbf{x}_1,\mathbf{x}_2,\mathbf{x}_2,\mathbf{x}_3)}{2} + \frac{\xi_R^{(4)}(\mathbf{x}_1,\mathbf{x}_2,\mathbf{x}_3,\mathbf{x}_3)}{2} \right] + b_L^5 \xi_R^{(3)}(\mathbf{x}_1,\mathbf{x}_2,\mathbf{x}_3) \sum_{i<j} \xi_R^{(2)}(\mathbf{x}_i,\mathbf{x}_j), \tag{3.12}$$

where in the last lines of equations (3.11) and (3.12) we report also the first Gaussian/non-Gaussian mixed contribution, even if it is expected to be one order of magnitude lower in δ_R than the trispectrum contribution. To leading order, the non-Gaussian correction to the n-points functions of massive halos is a -truncated- sum of contributions of the three- and four-point (primordial) functions, enhanced by powers (third and fourth powers respectively) of bias, b_L. Notice that so far these results are very generic, in fact the equations above do not assume any specific origin of the three- and four-point correlation functions and constitute the starting point of our analysis.

The validity of the approach described above has been repeatedly tested against numerical simulations with Gaussian and non-Gaussian initial conditions, finding that theory agrees with simulations. In particular, on large enough scales, we have that $b_L^N \xi_R^{(N)}$ is small and the series expansion does not have convergence issues. The interested reader can check e.g., refs. [82–88].

4 Graviton exchange signal in large scale structure

The trispectrum generated by GE was derived in detail in ref. [40]. Very recently Baumann and collaborators [39] re-derived the GE-induced higher order correlations in a more general context. We leave the analysis of their findings to future work and consider here the GE trispectrum of ref. [40]. In principle there are two distinct ways to measure the GE contribution in large scale structure data.

The first one is to look for it directly in the trispectrum of the dark matter or low-to-moderate biased tracers of it. In this case, as pointed out by ref. [40] some configurations are particularly interesting and well suited since the size of non-Gaussianity is amplified. These configurations are associated to the so-called counter-collinear limit, where the sum of two momenta goes to zero (e.g., when $k_{12} \ll k_1 \approx k_2, k_3 \approx k_4$). We show in figure 1 the two possible (dual) configurations, called *kite*, if the momenta summing up to zero are on opposite sides of the parallelogram, and *folded kite*, if the momenta summing up to zero are on contiguous side of the parallelogram. In these configurations, where all momenta are finite, the GE contribution diverges (e.g., scaling as k_{12}^{-3}) opening the possibility for amplifying the signal.

A direct measurement of the primordial trispectrum has been done at the CMB level in refs. [12–14, 90–93]. However doing so from large-scale structure surveys may be challenging because of the number of trispectrum modes involved and the low-signal to noise per mode; for this reason very few attempt have been done so far [94].

JCAP11(2018)043

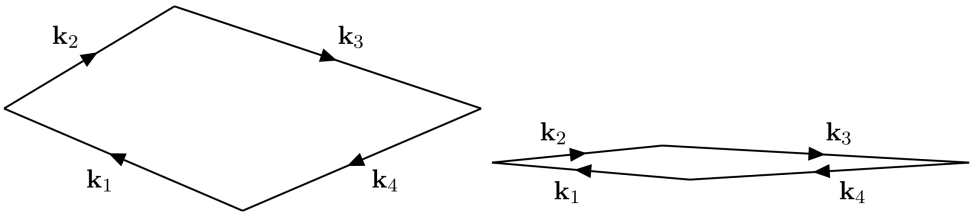

Figure 1. Kite (*left panel*) and folded kite (*right panel*) diagrams. In the left diagram we have $k_{13} \ll k_1 \sim k_3, k_2 \sim k_4$, while in the right one we have $k_{12} \ll k_1 \sim k_2, k_3 \sim k_4$. Diagrams have been drawn with Ti*k*Z-Feynman [89].

In this section we consider the alternative approach of looking at the effect of the GE trispectrum contribution in the halo two- and three-point functions. The trispectrum due to a graviton exchange is given by [40]

$$\begin{aligned}\langle\zeta_{\mathbf{k}_1}\zeta_{\mathbf{k}_2}\zeta_{\mathbf{k}_3}\zeta_{\mathbf{k}_4}\rangle^{\rm GE} = (2\pi)^3\delta(\mathbf{k}_{1234})\left(\frac{H_\star^2}{4\epsilon}\right)^3\frac{r/4}{\prod_j k_j^3}\\ \times\left[\frac{k_1^2k_3^2}{k_{12}^3}\left[1-(\hat{\mathbf{k}}_1\cdot\hat{\mathbf{k}}_{12})^2\right]\left[1-(\hat{\mathbf{k}}_3\cdot\hat{\mathbf{k}}_{12})^2\right]\cos 2\chi_{12,34}\cdot(\mathcal{I}_{1234}+\mathcal{I}_{3412})+\right.\\ +\frac{k_1^2k_2^2}{k_{13}^3}\left[1-(\hat{\mathbf{k}}_1\cdot\hat{\mathbf{k}}_{13})^2\right]\left[1-(\hat{\mathbf{k}}_2\cdot\hat{\mathbf{k}}_{13})^2\right]\cos 2\chi_{13,24}\cdot(\mathcal{I}_{1324}+\mathcal{I}_{2413})+\\ \left.+\frac{k_1^2k_2^2}{k_{14}^3}\left[1-(\hat{\mathbf{k}}_1\cdot\hat{\mathbf{k}}_{14})^2\right]\left[1-(\hat{\mathbf{k}}_2\cdot\hat{\mathbf{k}}_{14})^2\right]\cos 2\chi_{14,23}\cdot(\mathcal{I}_{1423}+\mathcal{I}_{2314})\right],\end{aligned} \tag{4.1}$$

where $\cos\chi_{ij,kl} = (\hat{\mathbf{k}}_i\times\hat{\mathbf{k}}_j)\cdot(\hat{\mathbf{k}}_k\times\hat{\mathbf{k}}_l)$ is the angle between the two planes formed by $\{\mathbf{k}_i,\mathbf{k}_j\}$ and $\{\mathbf{k}_k,\mathbf{k}_l\}$,

$$\begin{aligned}\mathcal{I}_{1234}+\mathcal{I}_{3412} = \frac{k_1+k_2}{a_{34}^2}\left[\frac{1}{2}(a_{34}+k_{12})(a_{34}^2-2b_{34})+k_{12}^2(k_3+k_4)\right]+(1,2\leftrightarrow 3,4)\\ +\frac{k_1k_2}{k_t}\left[\frac{b_{34}}{a_{34}}-k_{12}+\frac{k_{12}}{a_{12}}\left(k_3k_4-k_{12}\frac{b_{34}}{a_{34}}\right)\left(\frac{1}{k_t}+\frac{1}{a_{12}}\right)\right]+(1,2\leftrightarrow 3,4)\\ -\frac{k_{12}}{a_{12}a_{34}k_t}\left[b_{12}b_{34}+2k_{12}^2k_p\left(\frac{1}{k_t^2}+\frac{1}{a_{12}a_{34}}+\frac{k_{12}}{k_ta_{12}a_{34}}\right)\right],\end{aligned} \tag{4.2}$$

$a_{ij} = k_i + k_j + k_{ij}$, $b_{ij} = (k_i + k_j)k_{ij}$, $k_t = \sum_{j=1}^4 k_j$ and $k_p = \prod_{j=1}^4 k_j$.[5]

In principle there are a multitude of late-time, non-primordial effects that should be taken into account when measuring non-Gaussianity in large scale structure. Here, we are interested in estimating only the size of specific effects, and we refer the interested reader e.g., to ref. [95] for a comprehensive analysis.

[5]Note that scalar and vector products in the above equation can be uniquely computed using spherical coordinates as

$$\begin{aligned}\hat{\mathbf{k}}_i\cdot\hat{\mathbf{k}}_j &= \sin\theta_i\sin\theta_j\cos(\phi_i-\phi_j)+\cos\theta_i\cos\theta_j,\\ \hat{\mathbf{k}}_i\times\hat{\mathbf{k}}_j &= (\sin\theta_i\sin\phi_i\cos\theta_j-\cos\theta_i\sin\theta_j\sin\phi_j)\,\hat{\mathbf{k}}_x\\ &\quad+(\cos\theta_i\sin\theta_j\cos\phi_j-\sin\theta_i\cos\phi_i\cos\theta_j)\,\hat{\mathbf{k}}_y\\ &\quad+\ \sin\theta_i\sin\theta_j\sin(\phi_j-\phi_i)\hat{\mathbf{k}}_z.\end{aligned}$$

JCAP11(2018)043

In this work we use the public `Cubature`[6] package to compute the multidimensional integrals. Notice that in doing the integrals, besides the obvious singularity when one of the momenta goes to zero that the package can easily deal with, there is another singularity, i.e., the counter-collinear limit, when the sum of two momenta goes to zero. Since the region where this happens has some non-trivial shape, we decided to regularize the integrand close to the singularity by multiplying each term (lines two, three and four) in equation (4.1) by $e^{-k_{\rm hor}/k_{ij}}$, where $k_{\rm hor}$ is a mode entering the horizon at late time and k_{ij} is the respective momentum at the denominator. The physical interpretation of such regularization is straightforward: we cannot probe wave numbers smaller than those that are crossing the horizon today, since smaller wave numbers appear as an uniform background. In doing so we are removing extremely folded configurations (that might be related to "gauge-invariance" considerations). On the one hand our regularisation method artificially suppresses modes $k \lesssim k_{\rm hor}$, on the other hand we explicitly checked that this procedure does not introduce any significant bias in the magnitude of the GE contribution when $k \gg k_{\rm hor}$. We choose $k_{\rm hor} = 10^{-6}\,{\rm Mpc}^{-1}$, much less than $k_{\rm hor}^{\rm today} \sim \mathcal{O}(10^{-4})\,{\rm Mpc}^{-1}$, in order not to affect the modes that are of cosmological interest. This phenomenological procedure represents a first attempt to tackle the long-standing problem of a correct treatment of super-horizon modes. The improvement of this method is left for future work.

The GE contribution was derived in the context of standard single-field slow-roll inflation, namely using standard kinetic term, no modified gravity, Bunch-Davies vacuum and others [40]. However, in order to help the readers to compare these contributions to other bispectrum templates they may be familiar with, we include in the figures of the following sections also the bispectrum templates of appendix A, which arise when different assumptions are taken. We choose as reference values for non-Gaussianity parameters $r = 0.1$ (maximum value allowed by current CMB data [7]), $\epsilon = r/16 = 0.00625$ and $|f_{\rm NL}^{\zeta}| = (1 - n_s)/12 = 0.00279$. It should be noticed that Cosmic Microwave Background data currently allow higher values of $|f_{\rm NL}^{\zeta}| \sim \mathcal{O}(1\text{–}10)$, depending on the bispectrum template, see e.g., ref. [13]. However, in the cases we are interested in, r and $f_{\rm NL}^{\zeta}$ act only as an overall amplitude rescaling factor, therefore the reader can simply shift vertically the lines to match with the desired value of such parameters.

4.1 Signal in the halo power spectrum

To compute the halo power spectrum, in the equations below we take the Fourier transform (FT $\{\cdot\}$) of equation (3.11),

$$P_{\rm halo}^{NG}(k,z) \approx P_{\rm halo}^{G}(k,z) + B_{112}(k,z) + T_{1112}(k,z) + T_{1122}(k,z) + M_{12-112}(k,z), \tag{4.3}$$

where we recognise the Gaussian halo power spectrum,

$$P_{\rm halo}^{G}(k,z) \approx b_L^2(z) P_R(k,z) + \frac{b_L^4(z)}{2} \int \frac{d^3q}{(2\pi)^3} P_R(q,z) P_R(|\mathbf{k}-\mathbf{q}|,z), \tag{4.4}$$

[6]The package has be written by Steven G. Johnson and can be found in GitHub https://github.com/stevengj/cubature.

JCAP11(2018)043

the purely non-Gaussian contributions,

$$
\begin{aligned}
B_{112}(k,z) &= b_L^3(z)\mathrm{FT}\left\{\xi_R^{(3)}(\mathbf{x}_1,\mathbf{x}_1,\mathbf{x}_2)\right\} \\
&= b_L^3(z)\int \frac{d^3q}{(2\pi)^3}\mathcal{M}_R(q,z)\mathcal{M}_R(|\mathbf{k}-\mathbf{q}|,z)\mathcal{M}_R(k,z)B_\zeta(\mathbf{q},\mathbf{k}-\mathbf{q},-\mathbf{k}), \\
T_{1112}(k,z) &= \frac{b_L^4(z)}{3}\mathrm{FT}\left\{\xi_R^{(4)}(\mathbf{x}_1,\mathbf{x}_1,\mathbf{x}_1,\mathbf{x}_2)\right\} \\
&= \frac{b_L^4(z)}{3}\int \frac{d^3q_1}{(2\pi)^3}\frac{d^3q_2}{(2\pi)^3}\mathcal{M}_R(q_1,z)\mathcal{M}_R(q_2,z)\mathcal{M}_R(|\mathbf{k}-\mathbf{q}_{12}|,z)\mathcal{M}_R(k,z) \\
&\qquad\qquad \times T_\zeta(\mathbf{q}_1,\mathbf{q}_2,\mathbf{k}-\mathbf{q}_{12},-\mathbf{k}), \\
T_{1122}(k,z) &= \frac{b_L^4(z)}{4}\mathrm{FT}\left\{\xi_R^{(4)}(\mathbf{x}_1,\mathbf{x}_1,\mathbf{x}_2,\mathbf{x}_2)\right\} \\
&= \frac{b_L^4(z)}{4}\int \frac{d^3q_1}{(2\pi)^3}\frac{d^3q_2}{(2\pi)^3}\mathcal{M}_R(|\mathbf{k}-\mathbf{q}_1|,z)\mathcal{M}_R(q_1,z)\mathcal{M}_R(q_2,z)\mathcal{M}_R(|\mathbf{k}+\mathbf{q}_2|,z) \\
&\qquad\qquad \times T_\zeta(\mathbf{k}-\mathbf{q}_1,\mathbf{q}_1,\mathbf{q}_2,-\mathbf{k}-\mathbf{q}_2),
\end{aligned}
\tag{4.5}
$$

and the mixed contribution

$$
\begin{aligned}
M_{12-112}(k,z) &= b_L^5(z)\mathrm{FT}\left\{\xi_R^{(2)}(\mathbf{x}_1,\mathbf{x}_2)\xi_R^{(3)}(\mathbf{x}_1,\mathbf{x}_1,\mathbf{x}_2)\right\} \\
&= b_L^5(z)\int \frac{d^3q_1}{(2\pi)^3}\frac{d^3q_2}{(2\pi)^3}P_R(|\mathbf{k}-\mathbf{q}_{12}|,z)B_R(q_1,q_2,q_{12},z).
\end{aligned}
\tag{4.6}
$$

In the context of quadratic and cubic models of local non-Gaussianities of equations (2.4) and (2.6), the three- and the four-points contribution has already been evaluated by refs. [96, 97], respectively. We compute the GE contribution following the same procedure, by substituting equation (4.1) into the four-point correlation function on the r.h.s. of equation (4.3). Since we are interested only in primordial features, we report in figure 2 the ratio between the primordial non-Gaussian contributions of equation (4.3) and the Gaussian halo power spectrum at different redshift, to compare the relative strength of the signals coming from Gaussian and non-Gaussian processes and the relative strength of the bispectrum and trispectrum terms.

Notice that from an operational point of view, the GE signal should be extracted from the total halo power spectrum by subtracting the bispectrum contribution, which in this case acts as an additional source of "noise". As we explained in section 2, there is an ongoing debate in the literature on the correct form of the bispectrum in the local case, therefore we report both possibilities. Following Cabass [69], we multiply the $(1-n_s)$ factor in equation (2.3) by an additional factor $(k_{\rm longest}/k_{\rm shortest})^2$, where $k_{\rm longest}$ and $k_{\rm shortest}$ are the longest and shortest modes of the considered triangle. We are aware that the GE contribution has not been computed under different assumptions, for example the conditions that give rise to different bispectra shapes such as non Bunch-Davies vacuum states. However the authors of ref. [40] indicate that their results can be extended to more general conditions. Here, for helping the reader to compare these contributions to other bispectra they may be familiar with, we have included also the bispectrum templates, $\mathcal{B}$, defined in equations (A.1), (A.2) and (A.3), which have already been studied in the halo power spectrum context for instance in refs. [98, 99]. As it can be seen in figure 2, depending on the specific model and magnitude of primordial non-Gaussianities, the GE contribution is comparable to or even larger than

JCAP11(2018)043

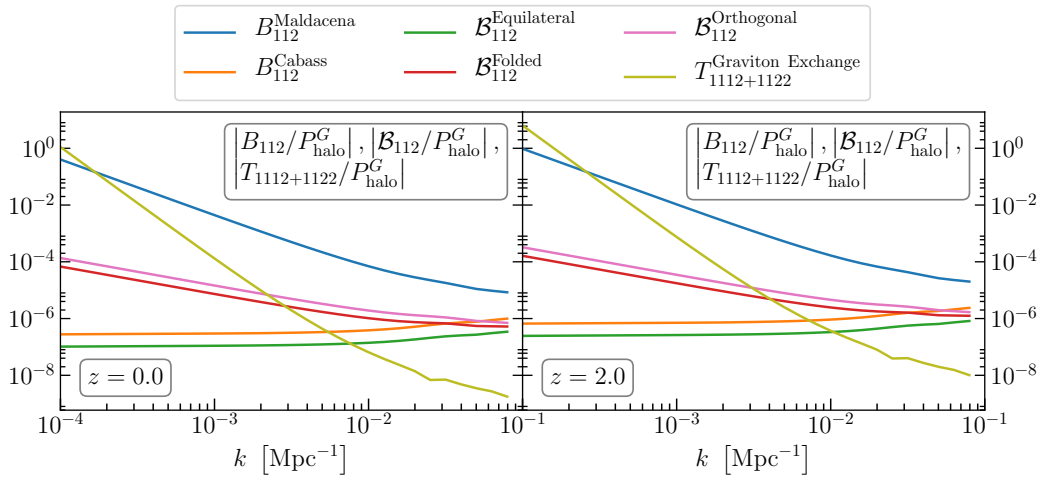

Figure 2. Ratio between different primordial non-Gaussian contribution (bispectra and GE trispectrum) and the Gaussian halo power spectrum at redshift $z = 0$ (*left panel*) and $z = 2$ (*right panel*) for $M_{\rm halo} = 10^{12}\ M_\odot$ dark matter halos. For the Maldacena and Cabass bispectra, indicated by B_{112}, we use $\epsilon = 0.00625$, while for the Equilateral, Folded and Orthogonal templates, indicated by $\mathcal{B}_{112}$, we use $f_{\rm NL} = 0.00279$. In the case of the templates, a different value of $f_{\rm NL}$ would simply rescale vertically the lines. For the GE contribution we use $r = 0.1$ and $k_{\rm hor} = 10^{-6}\,{\rm Mpc}^{-1}$. Also in this case different values of r simply rescales vertically the GE contribution.

the primordial bispectrum signal at the largest scales. By comparing the two panels, we also notice that the importance of the GE increases with redshift.

Although a detailed signal-to-noise and survey forecast calculation is well beyond the scope of this paper, figure 2 indicates that the GE contribution can be singled out and extracted from the measured halo power spectrum thanks to the different scale dependence of the terms in equation (4.3). In particular, at large scales, we have that

$$\begin{aligned} &B_{112}^{\rm Cabass}/P_{\rm halo}^{G},\ \mathcal{B}_{112}^{\rm Equilateral}/P_{\rm halo}^{G} \propto k^{0}(1+z)\frac{g(0)}{g(z)}, \\ &\mathcal{B}_{112}^{\rm Orthogonal}/P_{\rm halo}^{G},\ \mathcal{B}_{112}^{\rm Folded}/P_{\rm halo}^{G} \propto k^{-1}(1+z)\frac{g(0)}{g(z)}, \\ &B_{112}^{\rm Maldacena}/P_{\rm halo}^{G} \propto k^{-2}(1+z)\frac{g(0)}{g(z)}, \end{aligned} \tag{4.7}$$

while the two trispectrum contributions scale as

$$\begin{aligned} T_{1112}/P_{\rm halo}^{G} &\propto k^{-2}\left[(1+z)\frac{g(0)}{g(z)}\right]^{2}, \\ T_{1122}/P_{\rm halo}^{G} &\propto k^{-4}\left[(1+z)\frac{g(0)}{g(z)}\right]^{2}. \end{aligned} \tag{4.8}$$

We have checked that for all the cases of interest, that is bias of order few, the second term in equation (4.4) is subdominant with respect to the first one that scales as D^{-2}, therefore in equations (4.7) and (4.8) only the dominant term matters. Notice also that in equation (4.8) the term $T_{1122}(k)$ dominates over the $T_{1112}(k)$ term at large scales and it has a scale dependence different from any other common bispectrum template. Other terms of the trispectrum

JCAP11(2018)043

could have the same scale dependence, e.g., the terms in the third line of equation (2.5), as found in ref. [97], however these terms are second order in slow-roll parameters, therefore they are suppressed approximately by a factor $\mathcal{O}(\epsilon)$ with respect to the GE contribution. Furthermore we note that the first order correction to the Gaussian halo power spectra in equation (4.4) and the Gaussian/non-Gaussian mixed contribution of equation (4.6) become scale-independent at large scales, namely when taking the $k \to 0$ limit. This further highlights the fact that the GE scale dependence is quite unique, offering an opportunity to separate it from other signals. Moreover, as can be seen in equations (4.7) and (4.8), the bispectrum contribution scales with redshift approximately as $(1+z)$ while for the trispectrum contribution the scaling is proportional to $(1+z)^2$; hence going to high redshift further helps the GE term to dominate over the bispectrum contributions, as can be explicitly seen in figure 2.

In conclusion, looking for this specific scale dependence at high redshift is a possible way to extract this specific signal from the halo power spectrum, providing an alternative way to determine the energy scale of inflation.

4.2 Signal in the halo bispectrum

The Fourier transform of the Gaussian part of equation (3.10) reads as

$$\begin{aligned} B^G_{\rm halo}(k_1,k_2,k_3,z) \approx\, & b_L^4(z)\left[P_R(k_1,z)P_R(k_2,z)+(2\,\text{perms.})\right] \\ & + b_L^6(z)\int \frac{d^3q}{(2\pi)^3} P_R(|\mathbf{k}_1-\mathbf{q}|,z)P_R(|\mathbf{k}_2-\mathbf{q}|,z)P_R(q,z) \\ & + \frac{b_L^6(z)}{2}\left[P_R(k_1,z)\int \frac{d^3q}{(2\pi)^3} P_R(|\mathbf{k}_2-\mathbf{q}|,z)P_R(q,z)+(2\,\text{perms.})\right]. \end{aligned} \tag{4.9}$$

Even if the initial conditions are perfectly Gaussian, we have a well-defined bispectrum of excursion regions. To compute the GE contribution to the halo bispectrum we take the Fourier transform of equation (3.12), obtaining

$$\begin{aligned} B^{NG}_{\rm halo}(k_1,k_2,k_3,z) \approx\, & B^G_{\rm halo}(k_1,k_2,k_3,z) + B_{123}(k_1,k_2,k_3,z) \\ & + T_{1123}(k_1,k_2,k_3,z) + T_{1223}(k_1,k_2,k_3,z) + T_{1233}(k_1,k_2,k_3,z) \\ & + M_{12-123}(k_1,k_2,k_3,z) + M_{23-123}(k_1,k_2,k_3,z) + M_{13-123}(k_1,k_2,k_3,z), \end{aligned} \tag{4.10}$$

where we recognise the non-Gaussian contributions,

$$\begin{aligned} B_{123}(k_1,k_2,k_3,z) &= b_L^3(z)\,\text{FT}\left\{\xi_R^{(3)}(\mathbf{x}_1,\mathbf{x}_2,\mathbf{x}_3)\right\} \equiv b_L^3(z)B_R(k_1,k_2,k_3) \\ &= b_L^3(z)\mathcal{M}_R(k_1,z)\mathcal{M}_R(k_2,z)\mathcal{M}_R(k_3,z)B_\zeta(k_1,k_2,k_3), \\ T_{1123}(k_1,k_2,k_3,z) &= \frac{b_L^4(z)}{2}\,\text{FT}\left\{\xi_R^{(4)}(\mathbf{x}_1,\mathbf{x}_1,\mathbf{x}_2,\mathbf{x}_3)\right\} \\ &= \frac{b_L^4(z)}{2}\int \frac{d^3q}{(2\pi)^3}\mathcal{M}_R(q,z)\mathcal{M}_R(|\mathbf{k}_1-\mathbf{q}|,z)\mathcal{M}_R(k_2,z)\mathcal{M}_R(k_3,z) \\ &\qquad \times T_\zeta(\mathbf{q},\mathbf{k}_1-\mathbf{q},\mathbf{k}_2,\mathbf{k}_3), \\ T_{1223}(k_1,k_2,k_3,z) &= \frac{b_L^4(z)}{2}\,\text{FT}\left\{\xi_R^{(4)}(\mathbf{x}_1,\mathbf{x}_2,\mathbf{x}_2,\mathbf{x}_3)\right\} \\ &= \frac{b_L^4(z)}{2}\int \frac{d^3q}{(2\pi)^3}\mathcal{M}_R(k_1,z)\mathcal{M}_R(|\mathbf{k}_2-\mathbf{q}|,z)\mathcal{M}_R(q,z)\mathcal{M}_R(k_3,z) \\ &\qquad \times T_\zeta(\mathbf{k}_1,\mathbf{k}_2-\mathbf{q},\mathbf{q},\mathbf{k}_3), \end{aligned}$$

JCAP11(2018)043

$$T_{1233}(k_1,k_2,k_3,z) = \frac{b_L^4(z)}{2}\mathrm{FT}\left\{\xi_R^{(4)}(\mathbf{x}_1,\mathbf{x}_2,\mathbf{x}_3,\mathbf{x}_3)\right\}$$
$$= \frac{b_L^4(z)}{2}\int\frac{d^3q}{(2\pi)^3}\mathcal{M}_R(k_1,z)\mathcal{M}_R(k_2,z)\mathcal{M}_R(q,z)\mathcal{M}_R(|\mathbf{k}_3-\mathbf{q}|,z)$$
$$\times T_\zeta(\mathbf{k}_1,\mathbf{k}_2,\mathbf{q},\mathbf{k}_3-\mathbf{q}), \tag{4.11}$$

and the mixed contributions,

$$M_{12-123}+M_{23-123}+M_{13-123} = b_L^5(z)\int\frac{d^3q}{(2\pi)^3}P_R(q,z)\Big[B_R(|\mathbf{k}_1-\mathbf{q}|,|\mathbf{k}_2+\mathbf{q}|,k_{12},z)$$
$$+B_R(k_1,|\mathbf{k}_2-\mathbf{q}|,|\mathbf{k}_{12}-\mathbf{q}|,z)$$
$$+B_R(|\mathbf{k}_1-\mathbf{q}|,k_2,|\mathbf{k}_{12}-\mathbf{q}|,z)\Big]. \tag{4.12}$$

We compute the GE contribution following the same methodology described in the previous section, namely we substitute equation (4.1) into the four-point correlation function on the r.h.s. of equation (4.10). As before, since we are interested only in primordial features, we report in figure 3 the ratio between the primordial non-Gaussian contributions of equation (4.10) and the Gaussian halo power spectrum. This allows us to compare the relative strength of the signals coming from Gaussian and non-Gaussian processes and the relative strength of the primordial bispectrum and trispectrum terms.

In the three panels of figure 3, since the exploration of every possible triangular configuration goes beyond the purpose of this work, we choose to explore just three representative triangular configuration, namely the equilateral ($k_1 = k_2 = k_3$), squeezed ($k_1 = k_2 \approx 10k_3$) and folded ($k_1 = k_2 \approx k_3/2$) configurations. Also in this case we include, for comparison, different primordial bispectrum templates (see figure caption for the choice of normalisation). As seen also in section 4.1, at large scales, in the case there is no primordial non-Gaussianity of any sort down to the "gravitational floor", the GE contribution easily dominates over the one arising from reasonably expected primordial non-Gaussian bispectrum. It is interesting to note that, at scales around $k \sim 10^{-3}\,\mathrm{Mpc}^{-1}$, the trispectrum contribution to the halo bispectrum in the squeezed and equilateral configurations becomes of the same order of the intrinsic halo bispectrum for an initial Gaussian field. In the three panels we can identify the following scale and redshift scalings:

$$B_{123}/B^G_{\rm halo},\ \mathcal{B}_{123}/B^G_{\rm halo} \propto k^{-2}\frac{g(z)}{g(0)(1+z)}, \tag{4.13}$$

which is valid for all models and templates except for those that vanish in specific triangular configurations, e.g., the Equilateral template in squeezed triangular configurations. On the other hand the trispectrum contributions scales as

$$T_{1123+1223+1233}/B^G_{\rm halo} \propto k^{-6}, \tag{4.14}$$

independently from redshift, in contrast to the signal coming from primordial bispectra, which is suppressed approximately by a factor $(1+z)$ going to higher redshift. We do not report the magnitude of primordial bispectra signals in figure 3 for redshift $z > 0$, however the interested reader can simply divide the chosen model by the appropriate redshift factor, while keeping fixed the GE contribution, to get them. Since going to higher redshift shifts the primordial bispectra signal downward, the GE contribution will become even more dominant.

JCAP11(2018)043

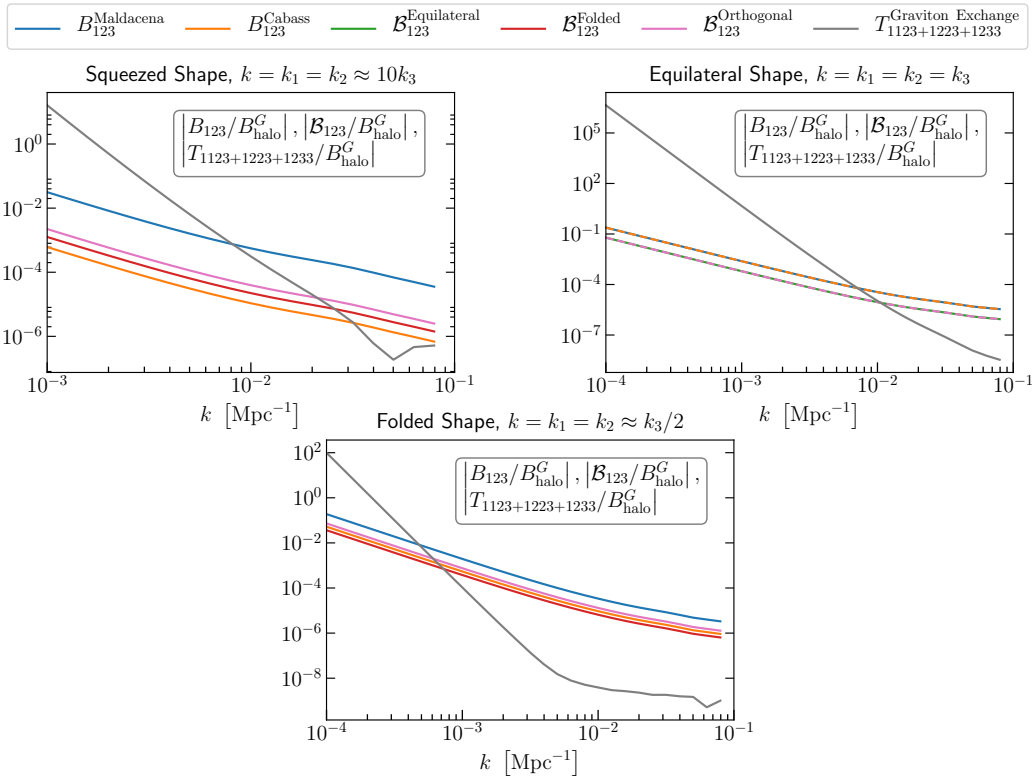

Figure 3. Ratio between different primordial bispectra and GE trispectrum contribution with respect to the Gaussian halo bispectrum for squeezed (*top left panel*), equilateral (*top right panel*) and folded (*bottom panel*) triangular shapes at redshift $z = 0$ for $M_{\rm halo} = 10^{12}\ M_\odot$ dark matter halos. We use $\epsilon = 0.00625$ for Maldacena and Cabass bispectra, indicated by B_{123}, and $f_{\rm NL} = 0.00279$ for the Equilateral, Folded and Orthogonal templates, indicated by $\mathcal{B}_{123}$. For the GE contribution we use $r = 0.1$ and $k_{\rm hor} = 10^{-6}\,{\rm Mpc}^{-1}$. Different values of $f_{\rm NL}$ and r correspond to vertically scaling the Equilateral, Folded, Orthogonal templates and GE contribution, respectively.

Finally, we note that also in this case in all the configurations considered, Gaussian halo bispectrum corrections in equation (4.9) are scale-independent. On the other hand the mixed Gaussian/non-Gaussian term appearing in equation (4.12) exhibits a potential scale dependence when taking the limit $k_1, k_2 \to 0$. We report in figure 4 the magnitude of this contribution relative to the Gaussian halo bispectrum at redshift $z = 0$. As it can be seen from the figure, for our choice of parameters, the magnitude of this contribution is typically smaller than GE one, however, since this ratio grows approximately as $(1+z)$ with redshift, it might dominate over the GE signal at high redshift, depending on the real value of r and $f_{\rm NL}^{\zeta}$. Nevertheless its scale dependence is completely different from the characteristic one of the GE, therefore we still have some way to identify the signal we are interested in.

JCAP11(2018)043

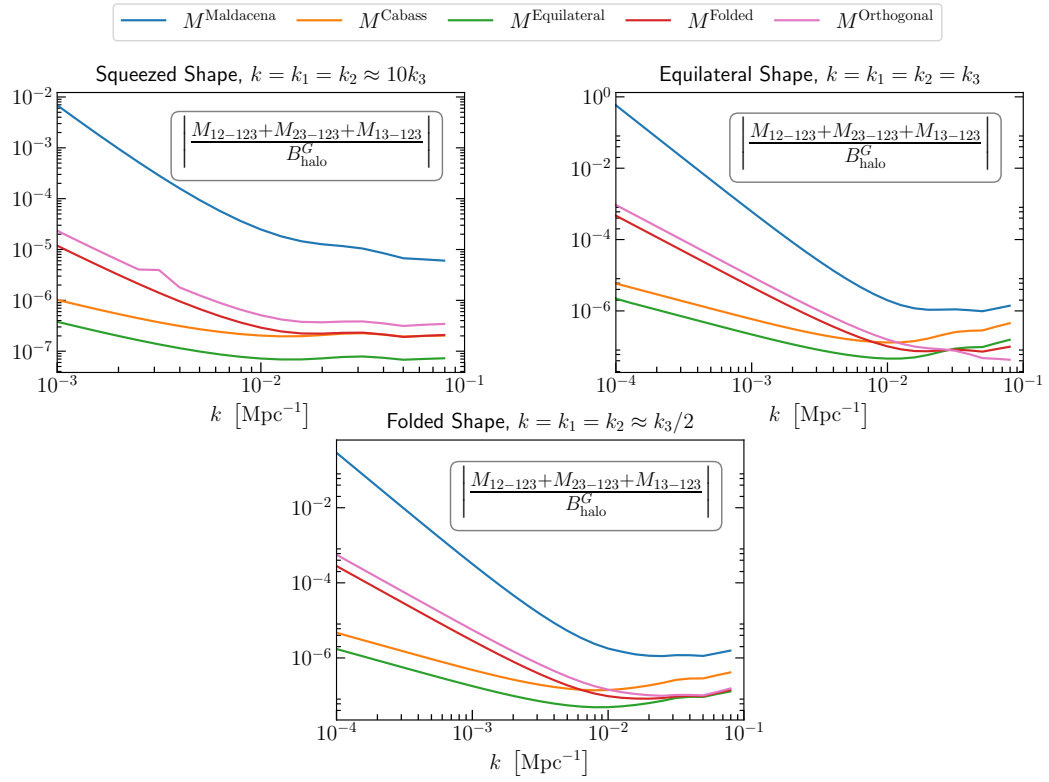

Figure 4. Ratio between different Gaussian/non-Gaussian mixed terms with respect to the Gaussian halo bispectrum for squeezed (*top left panel*), equilateral (*top right panel*) and folded (*bottom panel*) triangular shapes at redshift $z = 0$ for $M_{\rm halo} = 10^{12}\ M_\odot$ dark matter halos. We use $\epsilon = 0.00625$ when Maldacena and Cabass bispectra appear in M, and $f_{\rm NL} = 0.00279$ when the Equilateral, Folded and Orthogonal templates appear in the mixed term. Different values of $f_{\rm NL}$ correspond to vertically scaling the Equilateral, Folded, Orthogonal templates.

5 Conclusions

Determining the underlying physics of inflation is one of the big goals of Cosmology. A first step necessary to accomplish such a goal is determining the inflationary energy scale. In simple single-field slow-roll scenarios, the energy scale of inflation is proportional to the tensor-to-scalar ratio r or, equivalently, to the first slow-roll parameter ϵ. Several cosmological observables have been proposed to measure the value of r, such as B-mode polarization and direct interferometric measurements of gravitational wave stochastic backgrounds. In this work we explore a third avenue, the study of non-Gaussianities.

Non-Gaussianities are unavoidably produced during inflation and they constitute on their own a probe of the inflationary physics. Their importance as window into the self-interaction of the field during inflation is known (see e.g., ref. [100] and references therein). In this work we focused on the so-called graviton exchange, in particular on the specific non-Gaussianity generated by the interaction of scalar and tensor fluctuations at the horizon scale during the epoch of inflation. One of the peculiarities of this contribution to the four-point

JCAP11(2018)043

function is that it is suppressed only by one power of the slow-roll parameter. It becomes therefore interesting to entertain the idea that the GE contribution to the trispectrum could be relevant for future large-scale galaxy surveys. Moreover, this avenue is worth exploring as the signal contains configurations that cannot be "gauged" away. This is not surprising as the graviton exchange is a real quantum effect and not an artefact due to local effects.

We know from CMB observations that non-Gaussianities are small, in fact we have only upper bounds [12–14]. Here we proposed to look at the n-point function of gravitationally collapsed structures to further boost the signal coming from the primordial universe. In particular, we computed the contribution of the graviton exchange to the two- and three-point function of massive dark matter halos. We have shown that at large scales ($k \sim 10^{-4}$–$10^{-3}\,\mathrm{Mpc}^{-1}$) the contribution due to graviton exchange to the power spectrum of rare peaks is comparable to, if not dominant over, the one generated by the primordial three-point function expected from generic inflationary models (e.g., Maldacena and Cabass bispectrum). We have also shown that this contribution has a particular scale dependence and that it scales with increasing redshift faster than the three-point function contribution. Once going to high redshift favours the GE contributions compared to other non-Gaussian signals. The same can be said to the GE contribution to the three-point function of dark matter halos for specifics configurations. This analytical approach to the clustering of peaks is of course an approximation to the clustering of realistic halos. While in detail the bias modelling for realistic halos may be much more complex than adopted here, the good agreement between simulations and the predictions obtained with this approach (see e.g., refs. [82–88]) offers strong support that our initial investigation captures the behaviour of the signal both as a function of scale and redshift.

The effects produced by the GE contribution are significant at large scales, which are notoriously cosmic variance dominated. Since the signal depends on the tracer bias, the multi-tracer approach can be used beat down cosmic variance [101, 102]. These results open an observational window, yet unexplored, but with the potential to help us understand and verify the physics of inflation. This new avenue is highly complementary to direct or indirect (via CMB polarization) detection of primordial gravitational waves. We leave for future work a thorough computation of the observational configurations that have the largest signal-to-noise.

Acknowledgments

NBe. and LV acknowledge Martin Sloth and Filippo Vernizzi for helpful discussions. We thank Antonio Riotto for helpful comments. NBe and LV thank D. Baumann for an inspiring presentation at the "Analytical Methods" workshop of the Institut Henri Poincaré and thank the Center Emile Borel for hospitality during the latest stages of this work. Funding for this work was partially provided by the Spanish MINECO under projects AYA2014-58747-P AEI/FEDER, UE, and MDM-2014-0369 of ICCUB (Unidad de Excelencia María de Maeztu). NBe. is supported by the Spanish MINECO under grant BES-2015-073372. LV acknowledges support by European Union's Horizon 2020 research and innovation programme ERC (BePreSySe, grant agreement 725327). LV and RJ acknowledge the Radcliffe Institute for Advanced Study of Harvard University for hospitality during the latest stages of this work. NBa. and SM acknowledge partial financial support by ASI Grant No. 2016-24-H.0.

JCAP11(2018)043

A Bispectrum templates

In general, the functional form of the primordial bispectrum is complicated and unsuitable for visualisation and data analysis. For this reason bispectrum *templates* have been constructed that are useful to approximate the physical bispectrum and are suitable for data analysis. There is no shortage of inflationary models where non-Gaussianities peak in configurations different from the squeezed one. In fact, if any of the conditions giving the standard, single-field, slow-roll is violated, important non-Gaussian signatures will be produced, and in particular the violation of each condition leaves its signature on specifics triangular configurations, see e.g., ref. [100] and [103] and refs. therein. These types of non-Gaussianities, as shown in ref. [104], are generically well described by a linear combination of three basic bispectrum templates. The widely known and used templates are the so-called, local, equilateral, folded and orthogonal. Of these four templates, only three are independent, the fourth can obtained as a linear combination of the other tree see e.g., [87, 88, 104]. For example the local template is not independent from the other three templates, in fact it can be described as a linear combination of them. Here below we report the most studied templates and in the main text we use them to check whether there is any particular shape that could contaminate the GE signal we are interested in.

The equilateral template [105]

$$\mathcal{B}_\zeta^{\rm Equilateral}(\mathbf{k}_1,\mathbf{k}_2,\mathbf{k}_3) = 6 f_{\rm NL}^\zeta \left(\frac{H_\star^2}{4\epsilon}\right)^2 \frac{\sum k_j^3}{\prod k_j^3}\left[-1+\frac{\sum_{i\neq j} k_i^2 k_j - 2k_p}{\sum k_j^3}\right], \tag{A.1}$$

is used to model non-Gaussianities arising from e.g., inflaton Lagrangians with non-canonical kinetic terms; in this case the bispectrum is peaked on equilateral shapes.

The folded template [106–109]

$$\mathcal{B}_\zeta^{\rm Folded}(\mathbf{k}_1,\mathbf{k}_2,\mathbf{k}_3) = 6 f_{\rm NL}^\zeta \left(\frac{H_\star^2}{4\epsilon}\right)^2 \frac{\sum k_j^3}{\prod k_j^3}\left[1+\frac{3k_p - \sum_{i\neq j} k_i^2 k_j}{\sum k_j^3}\right], \tag{A.2}$$

is used to model non-gaussianities arising from different assumption on the initial vacuum state.

The orthogonal template [104]

$$\mathcal{B}_\zeta^{\rm Orthogonal}(\mathbf{k}_1,\mathbf{k}_2,\mathbf{k}_3) = 6 f_{\rm NL}^\zeta \left(\frac{H_\star^2}{4\epsilon}\right)^2 \frac{\sum k_j^3}{\prod k_j^3}\left[-3+\frac{3\sum_{i\neq j} k_i^2 k_j - 8k_p}{\sum k_j^3}\right], \tag{A.3}$$

where $k_p = \prod_{j=1}^3 k_j$ is the product of the three momenta, has been built to be orthogonal to the equilateral one.

JCAP11(2018)043

References

[1] WMAP collaboration, H.V. Peiris et al., *First year Wilkinson Microwave Anisotropy Probe (WMAP) observations: Implications for inflation*, *Astrophys. J. Suppl.* **148** (2003) 213 [astro-ph/0302225] [INSPIRE].

[2] WMAP collaboration, D.N. Spergel et al., *First year Wilkinson Microwave Anisotropy Probe (WMAP) observations: Determination of cosmological parameters*, *Astrophys. J. Suppl.* **148** (2003) 175 [astro-ph/0302209] [INSPIRE].

[3] PLANCK collaboration, P.A.R. Ade et al., *Planck 2013 results. XVI. Cosmological parameters*, *Astron. Astrophys.* **571** (2014) A16 [arXiv:1303.5076] [INSPIRE].

[4] PLANCK collaboration, P.A.R. Ade et al., *Planck 2013 results. XXII. Constraints on inflation*, *Astron. Astrophys.* **571** (2014) A22 [arXiv:1303.5082] [INSPIRE].

[5] WMAP collaboration, G. Hinshaw et al., *Nine-Year Wilkinson Microwave Anisotropy Probe (WMAP) Observations: Cosmological Parameter Results*, *Astrophys. J. Suppl.* **208** (2013) 19 [arXiv:1212.5226] [INSPIRE].

[6] PLANCK collaboration, P.A.R. Ade et al., *Planck 2015 results. XIII. Cosmological parameters*, *Astron. Astrophys.* **594** (2016) A13 [arXiv:1502.01589] [INSPIRE].

[7] PLANCK collaboration, N. Aghanim et al., *Planck 2018 results. VI. Cosmological parameters*, arXiv:1807.06209 [INSPIRE].

[8] C.L. Bennett et al., *Seven-Year Wilkinson Microwave Anisotropy Probe (WMAP) Observations: Are There Cosmic Microwave Background Anomalies?*, *Astrophys. J. Suppl.* **192** (2011) 17 [arXiv:1001.4758] [INSPIRE].

[9] PLANCK collaboration, P.A.R. Ade et al., *Planck 2013 results. XXIII. Isotropy and statistics of the CMB*, *Astron. Astrophys.* **571** (2014) A23 [arXiv:1303.5083] [INSPIRE].

[10] PLANCK collaboration, P.A.R. Ade et al., *Planck 2015 results. XVI. Isotropy and statistics of the CMB*, *Astron. Astrophys.* **594** (2016) A16 [arXiv:1506.07135] [INSPIRE].

[11] WMAP collaboration, E. Komatsu et al., *First year Wilkinson Microwave Anisotropy Probe (WMAP) observations: tests of Gaussianity*, *Astrophys. J. Suppl.* **148** (2003) 119 [astro-ph/0302223] [INSPIRE].

[12] PLANCK collaboration, P.A.R. Ade et al., *Planck 2013 Results. XXIV. Constraints on primordial non-Gaussianity*, *Astron. Astrophys.* **571** (2014) A24 [arXiv:1303.5084] [INSPIRE].

[13] PLANCK collaboration, P.A.R. Ade et al., *Planck 2015 results. XVII. Constraints on primordial non-Gaussianity*, *Astron. Astrophys.* **594** (2016) A17 [arXiv:1502.01592] [INSPIRE].

[14] PLANCK collaboration, Y. Akrami et al., *Planck 2018 results. X. Constraints on inflation*, arXiv:1807.06211 [INSPIRE].

[15] P.J. Steinhardt, N. Turok and N. Turok, *A Cyclic model of the universe*, *Science* **296** (2002) 1436 [hep-th/0111030] [INSPIRE].

[16] R.H. Brandenberger, *Alternatives to the inflationary paradigm of structure formation*, *Int. J. Mod. Phys. Conf. Ser.* **01** (2011) 67 [arXiv:0902.4731] [INSPIRE].

[17] A.A. Starobinsky, *A New Type of Isotropic Cosmological Models Without Singularity*, *Phys. Lett.* **B 91** (1980) 99 [INSPIRE].

[18] M. Kawasaki, K. Kohri and N. Sugiyama, *MeV scale reheating temperature and thermalization of neutrino background*, *Phys. Rev.* **D 62** (2000) 023506 [astro-ph/0002127] [INSPIRE].

JCAP11(2018)043

[19] G.F. Giudice, E.W. Kolb and A. Riotto, *Largest temperature of the radiation era and its cosmological implications*, *Phys. Rev.* **D 64** (2001) 023508 [hep-ph/0005123] [INSPIRE].

[20] S. Hannestad, *What is the lowest possible reheating temperature?*, *Phys. Rev.* **D 70** (2004) 043506 [astro-ph/0403291] [INSPIRE].

[21] A. Katz and A. Riotto, *Baryogenesis and Gravitational Waves from Runaway Bubble Collisions*, *JCAP* **11** (2016) 011 [arXiv:1608.00583] [INSPIRE].

[22] N. Bartolo et al., *Science with the space-based interferometer LISA. IV: Probing inflation with gravitational waves*, *JCAP* **12** (2016) 026 [arXiv:1610.06481] [INSPIRE].

[23] M.C. Guzzetti, N. Bartolo, M. Liguori and S. Matarrese, *Gravitational waves from inflation*, *Riv. Nuovo Cim.* **39** (2016) 399 [arXiv:1605.01615] [INSPIRE].

[24] C. Caprini and D.G. Figueroa, *Cosmological Backgrounds of Gravitational Waves*, *Class. Quant. Grav.* **35** (2018) 163001 [arXiv:1801.04268] [INSPIRE].

[25] N. Bartolo et al., *Probing non-Gaussian Stochastic Gravitational Wave Backgrounds with LISA*, arXiv:1806.02819 [INSPIRE].

[26] S. Kawamura et al., *The Japanese space gravitational wave antenna - DECIGO*, *J. Phys. Conf. Ser.* **122** (2008) 012006 [INSPIRE].

[27] J. Crowder and N.J. Cornish, *Beyond LISA: Exploring future gravitational wave missions*, *Phys. Rev.* **D 72** (2005) 083005 [gr-qc/0506015] [INSPIRE].

[28] M.J. Rees, *Polarization and spectrum of the primeval radiation in an anisotropic universe*, *Astrophys. J.* **153** (1968) L1.

[29] M. Kamionkowski, A. Kosowsky and A. Stebbins, *Statistics of cosmic microwave background polarization*, *Phys. Rev.* **D 55** (1997) 7368 [astro-ph/9611125] [INSPIRE].

[30] CMBPol Study Team collaboration, D. Baumann et al., *CMBPol Mission Concept Study: Probing Inflation with CMB Polarization*, *AIP Conf. Proc.* **1141** (2009) 10 [arXiv:0811.3919] [INSPIRE].

[31] PRISM collaboration, P. André et al., *PRISM (Polarized Radiation Imaging and Spectroscopy Mission): An Extended White Paper*, *JCAP* **02** (2014) 006 [arXiv:1310.1554] [INSPIRE].

[32] CORE collaboration, F. Finelli et al., *Exploring cosmic origins with CORE: Inflation*, *JCAP* **04** (2018) 016 [arXiv:1612.08270] [INSPIRE].

[33] L. Verde, H. Peiris and R. Jimenez, *Optimizing CMB polarization experiments to constrain inflationary physics*, *JCAP* **01** (2006) 019 [astro-ph/0506036] [INSPIRE].

[34] L. Knox and Y.-S. Song, *A Limit on the detectability of the energy scale of inflation*, *Phys. Rev. Lett.* **89** (2002) 011303 [astro-ph/0202286] [INSPIRE].

[35] DESI collaboration, A. Aghamousa et al., *The DESI Experiment Part I: Science,Targeting and Survey Design*, arXiv:1611.00036 [INSPIRE].

[36] LSST Science and LSST Project collaborations, P.A. Abell et al., *LSST Science Book, Version 2.0*, arXiv:0912.0201 [INSPIRE].

[37] EUCLID collaboration, R. Laureijs et al., *Euclid Definition Study Report*, arXiv:1110.3193 [INSPIRE].

[38] N. Arkani-Hamed and J. Maldacena, *Cosmological Collider Physics*, arXiv:1503.08043 [INSPIRE].

[39] N. Arkani-Hamed, D. Baumann, H. Lee and G.L. Pimentel, *The Cosmological Bootstrap: Inflationary Correlators from Symmetries and Singularities*, arXiv:1811.00024 [INSPIRE].

[40] D. Seery, M.S. Sloth and F. Vernizzi, *Inflationary trispectrum from graviton exchange*, *JCAP* **03** (2009) 018 [arXiv:0811.3934] [INSPIRE].

JCAP11(2018)043

[41] L. Bordin, P. Creminelli, M. Mirbabayi and J. Noreña, *Tensor Squeezed Limits and the Higuchi Bound*, *JCAP* **09** (2016) 041 [arXiv:1605.08424] [INSPIRE].

[42] D.S. Salopek and J.R. Bond, *Nonlinear evolution of long wavelength metric fluctuations in inflationary models*, *Phys. Rev.* **D 42** (1990) 3936 [INSPIRE].

[43] A. Gangui, F. Lucchin, S. Matarrese and S. Mollerach, *The Three point correlation function of the cosmic microwave background in inflationary models*, *Astrophys. J.* **430** (1994) 447 [astro-ph/9312033] [INSPIRE].

[44] N. Bartolo, S. Matarrese and A. Riotto, *Enhancement of non-Gaussianity after inflation*, *JHEP* **04** (2004) 006 [astro-ph/0308088] [INSPIRE].

[45] V. Acquaviva, N. Bartolo, S. Matarrese and A. Riotto, *Second order cosmological perturbations from inflation*, *Nucl. Phys.* **B 667** (2003) 119 [astro-ph/0209156] [INSPIRE].

[46] J.M. Maldacena, *Non-Gaussian features of primordial fluctuations in single field inflationary models*, *JHEP* **05** (2003) 013 [astro-ph/0210603] [INSPIRE].

[47] D.H. Lyth and Y. Rodriguez, *The Inflationary prediction for primordial non-Gaussianity*, *Phys. Rev. Lett.* **95** (2005) 121302 [astro-ph/0504045] [INSPIRE].

[48] J.S. Schwinger, *Brownian motion of a quantum oscillator*, *J. Math. Phys.* **2** (1961) 407 [INSPIRE].

[49] L.V. Keldysh, *Diagram technique for nonequilibrium processes*, *Zh. Eksp. Teor. Fiz.* **47** (1964) 1515 [INSPIRE].

[50] E. Calzetta and B.L. Hu, *Closed Time Path Functional Formalism in Curved Space-Time: Application to Cosmological Back Reaction Problems*, *Phys. Rev.* **D 35** (1987) 495 [INSPIRE].

[51] D. Seery, K.A. Malik and D.H. Lyth, *Non-Gaussianity of inflationary field perturbations from the field equation*, *JCAP* **03** (2008) 014 [arXiv:0802.0588] [INSPIRE].

[52] A.A. Starobinsky, *Multicomponent de Sitter (Inflationary) Stages and the Generation of Perturbations*, *JETP Lett.* **42** (1985) 152 [INSPIRE].

[53] M. Sasaki and E.D. Stewart, *A General analytic formula for the spectral index of the density perturbations produced during inflation*, *Prog. Theor. Phys.* **95** (1996) 71 [astro-ph/9507001] [INSPIRE].

[54] M. Sasaki and T. Tanaka, *Superhorizon scale dynamics of multiscalar inflation*, *Prog. Theor. Phys.* **99** (1998) 763 [gr-qc/9801017] [INSPIRE].

[55] D.H. Lyth and D. Wands, *Conserved cosmological perturbations*, *Phys. Rev.* **D 68** (2003) 103515 [astro-ph/0306498] [INSPIRE].

[56] D.H. Lyth, K.A. Malik and M. Sasaki, *A General proof of the conservation of the curvature perturbation*, *JCAP* **05** (2005) 004 [astro-ph/0411220] [INSPIRE].

[57] D. Seery and J.E. Lidsey, *Primordial non-Gaussianities in single field inflation*, *JCAP* **06** (2005) 003 [astro-ph/0503692] [INSPIRE].

[58] N. Bartolo, S. Matarrese and A. Riotto, *NonGaussianity from inflation*, *Phys. Rev.* **D 65** (2002) 103505 [hep-ph/0112261] [INSPIRE].

[59] D. Seery and J.E. Lidsey, *Primordial non-Gaussianities from multiple-field inflation*, *JCAP* **09** (2005) 011 [astro-ph/0506056] [INSPIRE].

[60] L.E. Allen, S. Gupta and D. Wands, *Non-Gaussian perturbations from multi-field inflation*, *JCAP* **01** (2006) 006 [astro-ph/0509719] [INSPIRE].

[61] F. Vernizzi and D. Wands, *Non-Gaussianities in two-field inflation*, *JCAP* **05** (2006) 019 [astro-ph/0603799] [INSPIRE].

JCAP11(2018)043

[62] D. Seery, J.E. Lidsey and M.S. Sloth, *The inflationary trispectrum*, *JCAP* **01** (2007) 027 [astro-ph/0610210] [INSPIRE].

[63] C.T. Byrnes, M. Sasaki and D. Wands, *The primordial trispectrum from inflation*, *Phys. Rev.* **D 74** (2006) 123519 [astro-ph/0611075] [INSPIRE].

[64] F. Arroja and K. Koyama, *Non-Gaussianity from the trispectrum in general single field inflation*, *Phys. Rev.* **D 77** (2008) 083517 [arXiv:0802.1167] [INSPIRE].

[65] N. Bartolo, E. Komatsu, S. Matarrese and A. Riotto, *Non-Gaussianity from inflation: Theory and observations*, *Phys. Rept.* **402** (2004) 103 [astro-ph/0406398] [INSPIRE].

[66] L. Verde, L.-M. Wang, A. Heavens and M. Kamionkowski, *Large scale structure, the cosmic microwave background and primordial non-Gaussianity*, *Mon. Not. Roy. Astron. Soc.* **313** (2000) L141 [astro-ph/9906301] [INSPIRE].

[67] E. Komatsu and D.N. Spergel, *Acoustic signatures in the primary microwave background bispectrum*, *Phys. Rev.* **D 63** (2001) 063002 [astro-ph/0005036] [INSPIRE].

[68] N. Bartolo et al., *A relativistic signature in large-scale structure*, *Phys. Dark Univ.* **13** (2016) 30 [arXiv:1506.00915] [INSPIRE].

[69] G. Cabass, E. Pajer and F. Schmidt, *How Gaussian can our Universe be?*, *JCAP* **01** (2017) 003 [arXiv:1612.00033] [INSPIRE].

[70] A.A. Abolhasani and M. Sasaki, *Single-field consistency relation and δN-formalism*, *JCAP* **08** (2018) 025 [arXiv:1805.11298] [INSPIRE].

[71] D.J. Eisenstein and W. Hu, *Baryonic features in the matter transfer function*, *Astrophys. J.* **496** (1998) 605 [astro-ph/9709112] [INSPIRE].

[72] D. Blas, J. Lesgourgues and T. Tram, *The Cosmic Linear Anisotropy Solving System (CLASS) II: Approximation schemes*, *JCAP* **07** (2011) 034 [arXiv:1104.2933] [INSPIRE].

[73] B. Grinstein and M.B. Wise, *NonGaussian Fluctuations and the Correlations of Galaxies or Rich Clusters of Galaxies*, *Astrophys. J.* **310** (1986) 19 [INSPIRE].

[74] S. Matarrese, F. Lucchin and S.A. Bonometto, *A path integral approach to large scale matter distribution originated by non-gaussian fluctuations*, *Astrophys. J.* **310** (1986) L21 [INSPIRE].

[75] F. Lucchin, S. Matarrese and N. Vittorio, *Scale Invariant Clustering and Primordial Biasing*, *Astrophys. J.* **330** (1988) L21 [INSPIRE].

[76] N. Kaiser, *On the Spatial correlations of Abell clusters*, *Astrophys. J.* **284** (1984) L9 [INSPIRE].

[77] H.D. Politzer and M.B. Wise, *Relations Between Spatial Correlations of Rich Clusters of Galaxies*, *Astrophys. J.* **285** (1984) L1 [INSPIRE].

[78] L.G. Jensen and A.S. Szalay, *N-point correlations for biased galaxy formation*, *Astrophys. J. Lett.* **305** (1986) L5.

[79] L. Verde, R. Jimenez, F. Simpson, L. Álvarez-Gaumé, A. Heavens and S. Matarrese, *The bias of weighted dark matter haloes from peak theory*, *Mon. Not. Roy. Astron. Soc.* **443** (2014) 122 [arXiv:1404.2241] [INSPIRE].

[80] D. Jeong and E. Komatsu, *Primordial non-Gaussianity, scale-dependent bias and the bispectrum of galaxies*, *Astrophys. J.* **703** (2009) 1230 [arXiv:0904.0497] [INSPIRE].

[81] E. Sefusatti, *1-loop Perturbative Corrections to the Matter and Galaxy Bispectrum with non-Gaussian Initial Conditions*, *Phys. Rev.* **D 80** (2009) 123002 [arXiv:0905.0717] [INSPIRE].

[82] N. Dalal, O. Dore, D. Huterer and A. Shirokov, *The imprints of primordial non-Gaussianities on large-scale structure: scale dependent bias and abundance of virialized objects*, *Phys. Rev.* **D 77** (2008) 123514 [arXiv:0710.4560] [INSPIRE].

JCAP11(2018)043

[83] V. Desjacques, U. Seljak and I. Iliev, *Scale-dependent bias induced by local non-Gaussianity: A comparison to N-body simulations*, *Mon. Not. Roy. Astron. Soc.* **396** (2009) 85 [arXiv:0811.2748] [INSPIRE].

[84] M. Grossi et al., *Large-scale non-Gaussian mass function and halo bias: tests on N-body simulations*, *Mon. Not. Roy. Astron. Soc.* **398** (2009) 321 [arXiv:0902.2013] [INSPIRE].

[85] A. Pillepich, C. Porciani and O. Hahn, *Universal halo mass function and scale-dependent bias from N-body simulations with non-Gaussian initial conditions*, *Mon. Not. Roy. Astron. Soc.* **402** (2010) 191 [arXiv:0811.4176] [INSPIRE].

[86] T. Nishimichi, A. Taruya, K. Koyama and C. Sabiu, *Scale Dependence of Halo Bispectrum from Non-Gaussian Initial Conditions in Cosmological N-body Simulations*, *JCAP* **07** (2010) 002 [arXiv:0911.4768] [INSPIRE].

[87] C. Wagner, L. Verde and L. Boubekeur, *N-body simulations with generic non-Gaussian initial conditions I: Power Spectrum and halo mass function*, *JCAP* **10** (2010) 022 [arXiv:1006.5793] [INSPIRE].

[88] C. Wagner and L. Verde, *N-body simulations with generic non-Gaussian initial conditions II: Halo bias*, *JCAP* **03** (2012) 002 [arXiv:1102.3229] [INSPIRE].

[89] J. Ellis, *TikZ-Feynman: Feynman diagrams with TikZ*, *Comput. Phys. Commun.* **210** (2017) 103 [arXiv:1601.05437] [INSPIRE].

[90] M. Kunz, A.J. Banday, P.G. Castro, P.G. Ferreira and K.M. Górski, *The trispectrum of the 4 year cobe-dmr data*, *Astrophys. J.* **563** (2001) L99 [astro-ph/0111250] [INSPIRE].

[91] G. De Troia et al., *The trispectrum of the Cosmic Microwave Background on sub-degree angular scales: An analysis of the BOOMERanG data*, *Mon. Not. Roy. Astron. Soc.* **343** (2003) 284 [astro-ph/0301294] [INSPIRE].

[92] J. Smidt, A. Amblard, C.T. Byrnes, A. Cooray, A. Heavens and D. Munshi, *CMB Constraints on Primordial non-Gaussianity from the Bispectrum (f_{NL}) and Trispectrum (g_{NL} and τ_{NL}) and a New Consistency Test of Single-Field Inflation*, *Phys. Rev.* **D 81** (2010) 123007 [arXiv:1004.1409] [INSPIRE].

[93] T. Sekiguchi and N. Sugiyama, *Optimal constraint on g_{NL} from CMB*, *JCAP* **09** (2013) 002 [arXiv:1303.4626] [INSPIRE].

[94] L. Verde and A.F. Heavens, *On the trispectrum as a Gaussian test for cosmology*, *Astrophys. J.* **553** (2001) 14 [astro-ph/0101143] [INSPIRE].

[95] D. Karagiannis, A. Lazanu, M. Liguori, A. Raccanelli, N. Bartolo and L. Verde, *Constraining primordial non-Gaussianity with bispectrum and power spectrum from upcoming optical and radio surveys*, *Mon. Not. Roy. Astron. Soc.* **478** (2018) 1341 [arXiv:1801.09280] [INSPIRE].

[96] S. Matarrese and L. Verde, *The effect of primordial non-Gaussianity on halo bias*, *Astrophys. J.* **677** (2008) L77 [arXiv:0801.4826] [INSPIRE].

[97] V. Desjacques and U. Seljak, *Signature of primordial non-Gaussianity of ϕ^3-type in the mass function and bias of dark matter haloes*, *Phys. Rev.* **D 81** (2010) 023006 [arXiv:0907.2257] [INSPIRE].

[98] L. Verde and S. Matarrese, *Detectability of the effect of Inflationary non-Gaussianity on halo bias*, *Astrophys. J.* **706** (2009) L91 [arXiv:0909.3224] [INSPIRE].

[99] F. Schmidt and M. Kamionkowski, *Halo Clustering with Non-Local Non-Gaussianity*, *Phys. Rev.* **D 82** (2010) 103002 [arXiv:1008.0638] [INSPIRE].

[100] E. Komatsu et al., *Non-Gaussianity as a Probe of the Physics of the Primordial Universe and the Astrophysics of the Low Redshift Universe*, arXiv:0902.4759 [INSPIRE].

JCAP11(2018)043

[101] U. Seljak, *Extracting primordial non-Gaussianity without cosmic variance*, *Phys. Rev. Lett.* **102** (2009) 021302 [arXiv:0807.1770] [INSPIRE].

[102] P. McDonald and U. Seljak, *How to measure redshift-space distortions without sample variance*, *JCAP* **10** (2009) 007 [arXiv:0810.0323] [INSPIRE].

[103] X. Chen, *Primordial Non-Gaussianities from Inflation Models*, *Adv. Astron.* **2010** (2010) 638979 [arXiv:1002.1416] [INSPIRE].

[104] L. Senatore, K.M. Smith and M. Zaldarriaga, *Non-Gaussianities in Single Field Inflation and their Optimal Limits from the WMAP 5-year Data*, *JCAP* **01** (2010) 028 [arXiv:0905.3746] [INSPIRE].

[105] D. Babich, P. Creminelli and M. Zaldarriaga, *The Shape of non-Gaussianities*, *JCAP* **08** (2004) 009 [astro-ph/0405356] [INSPIRE].

[106] X. Chen, M.-x. Huang, S. Kachru and G. Shiu, *Observational signatures and non-Gaussianities of general single field inflation*, *JCAP* **01** (2007) 002 [hep-th/0605045] [INSPIRE].

[107] X. Chen, R. Easther and E.A. Lim, *Large Non-Gaussianities in Single Field Inflation*, *JCAP* **06** (2007) 023 [astro-ph/0611645] [INSPIRE].

[108] R. Holman and A.J. Tolley, *Enhanced Non-Gaussianity from Excited Initial States*, *JCAP* **05** (2008) 001 [arXiv:0710.1302] [INSPIRE].

[109] P.D. Meerburg, J.P. van der Schaar and P.S. Corasaniti, *Signatures of Initial State Modifications on Bispectrum Statistics*, *JCAP* **05** (2009) 018 [arXiv:0901.4044] [INSPIRE].

JCAP11(2018)043

CERN-TH-2019-056

Prepared for submission to JCAP

From Primordial Black Holes Abundance to Primordial Curvature Power Spectrum (and back)

Alba Kalaja,[a,b,c] **Nicola Bellomo,**[b,d] **Nicola Bartolo,**[a,e,f] **Daniele Bertacca,**[a,e] **Sabino Matarrese,**[a,e,f,g] **Ilia Musco,**[b] **Alvise Raccanelli,**[b,h] **Licia Verde**[b,i]

[a]Dipartimento di Fisica e Astronomia G. Galilei, Università degli Studi di Padova, I-35131 Padova, Italy.

[b]ICC, University of Barcelona, IEEC-UB, Martí i Franquès, 1, E-08028 Barcelona, Spain.

[c]Van Swinderen Institute for Particle Physics and Gravity, University of Groningen, Nijenborgh 4, 9747 AG Groningen, The Netherlands.

[d]Dept. de Física Quàntica i Astrofísica, Universitat de Barcelona, Martí i Franquès 1, E-08028 Barcelona, Spain.

[e]INFN, Sezione di Padova, via F. Marzolo 8, I-35131, I-35131 Padova, Italy.

[f]INAF - Osservatorio Astronomico di Padova, vicolo dell'Osservatorio 5, I-35122 Padova, Italy.

[g]Gran Sasso Science Institute, viale F. Crispi 7, I-67100 L'Aquila, Italy.

[h]Theoretical Physics Department, CERN, 1 Esplanade des Particules, CH-1211 Geneva 23, Switzerland.

[i]ICREA, Pg. Lluis Companys 23, Barcelona, E-08010, Spain.

E-mail: a.kalaja@rug.nl, nicola.bellomo@icc.ub.edu, nicola.bartolo@pd.infn.it, daniele.bertacca@pd.infn.it, sabino.matarrese@pd.infn.it, iliamusco@icc.ub.edu, alvise.raccanelli@cern.ch, liciaverde@icc.ub.edu

Abstract. In the model where Primordial Black Holes (PBHs) form from large primordial curvature (C) perturbations, i.e., CPBHs, constraints on PBH abundance provide in principle constraints on the primordial curvature power spectrum. This connection however depends necessarily on the details of PBH formation mechanism. In this paper we provide, for the first time, constraints on the primordial curvature power spectrum from the latest limits on PBH abundance, taking into account all the steps from gravitational collapse in real space to PBH formation. In particular, we use results from numerical relativity simulations and peak theory to study the conditions for PBH formation for a range of perturbation shapes, including non-linearities, perturbation profile and a careful treatment of smoothing and filtering scales. We then obtain updated PBH formation conditions and translate that into primordial spectrum constraints for a wide range of shapes and abundances. These updated constraints cover a range of scales not probed by other cosmological observables. Our results show that the correct and accurate modelling of non-linearities, filtering and typical perturbation profile, is crucial for deriving meaningful cosmological implications.

Contents

1 Introduction

During the first two runs of the LIGO-Virgo observatory, a considerable fraction of detected events [1–7] shows two characteristics that were generally unexpected by part of the community: large progenitors masses ($\gtrsim 20\ M_\odot$) and low binary effective spin.

Even if such massive progenitors were (by some) expected to be the first detected sources [8–11] and are not incompatible with classical stellar/binary evolution [12–14], this fact suggested that detected black holes could also have an origin different from the standard end-point of stellar evolution and that they may constitute a significant fraction of the dark matter [15–17]. Moreover, black holes of primordial origin, PBHs hereafter, are expected to have low spins, as recently showed in Refs. [18–20], hence they would produce binaries with values of the effective spin parameter compatibles with the observed ones. The observed merger rate is on the upper end of the predicted range for stellar progenitors [21] (even though there are still many uncertainties), and at least some contribution from primordial objects would reconcile theory with observations. Furthermore, PBHs might constitute the seeds of the super-massive black holes [22, 23] that inhabit the center of galaxies [24–27].

Given the interest in this potential dark matter candidate and the rich phenomenology of black holes, a large number of observational constraints on the abundance of PBHs have been obtained so far. They cover a remarkable portion of the allowed mass range and they

include constraints coming from gravitational lensing effects [28–36], dynamical effects [37–48], accretion effects [49–57] and effects on large-scale structure [58, 59]. Two mass ranges remain still open, around 10^{-15} $M_\odot$ and 10^{-12} $M_\odot$. Nonetheless, these constraints are not conclusive because they are computed for monochromatic mass distributions and they involve a variety of assumptions, see e.g., Refs. [60–62]. Therefore, the model in which PBHs constitute at least a non negligible fraction of the dark matter is still allowed by observations.

The idea that an overdense region of the primordial Universe could collapse gravitationally to form a black hole was proposed already fifty years ago [63–66]. Several mechanisms to produce such overdensities have been suggested, including cosmic topological defects [67–75], (interacting) dark matter clumps [76] or large curvature perturbations generated during inflation [77–79]. In the latter formation mechanism, curvature perturbations are generated during inflation, hence they carry a substantial amount of information about the Early Universe. In particular, there are a plethora of inflationary scenarios able to generate PBHs in the late Universe, see e.g., Refs. [80–93]. In this paper we concentrate on this scenario of PBHs generated by primordial curvature (C) perturbations, CPBHs.

CPBHs, apart from providing a dark matter candidate and being the seeds of supermassive black holes, can provide insights on the first moments of our Universe. It has already been established that at cosmological scales ($k \lesssim \mathcal{O}(1)$ Mpc^{-1}) the primordial curvature power spectrum is almost scale-invariant, both in model-dependent and model-independent analyses, see e.g., Ref. [94]. Moreover, during the past two decades, the amplitude and the tilt of the primordial curvature power spectrum has been measured with high accuracy [95–97]. On the other hand we still have very little information about the primordial curvature power spectrum on small scales ($k > \mathcal{O}(1)$ Mpc^{-1}). Several authors have proposed different ways to probe such scales, including CMB spectral distortions [98], analyses of Silk damping effects [99], exploiting WIMP properties [100, 101] (in the last case assuming they are the main component of dark matter), reconstructing quasar light curves [102] or through the detection of gravitational waves generated by large scalar perturbations, see e.g., Refs. [103–111] and references therein for constraints coming from ongoing (PTA [112–114]) and future (SKA [115, 116], LISA [115, 117]) experiments.

An additional method to set constraints on the amplitude and shape of the power spectrum consists in using PBH abundance [118–120]. CPBH formation requires at least mildly non-linear fluctuations to form during radiation domination, hence it requires an inflationary dynamics that deviates significantly from the standard slow-roll paradigm. It is generally accepted that in the simplest standard, single-field slow-roll inflationary models, initial perturbations are very close to Gaussian and their power spectrum is an almost scale invariant power law; hence perturbations large enough to go non-linear in the early Universe are exceedingly rare. Therefore constraints on PBH abundance can be translated into constraints on the Early Universe physics. This connection was pioneered in Ref. [121] and later extended in Refs. [122–124] to include an early matter-dominated era. We refer the interested reader also to Refs. [125, 126], where the authors report constraints on the primordial power spectrum amplitude from the most updated PBH abundance constraints, and to Ref. [127], where the authors investigated the effects of critical collapse and non-sphericities on the primordial power spectrum constraints.

In the previous literature a series of approximations and shortcuts were used. Given the potential implications of an accurate and robust connection between PBH abundance constraints and early Universe physics, we argue that these approximations should be revisited. The goal of this work is to extend previous works and to put constraints on the primordial

curvature power spectrum on a firmer theoretical ground. We aim to do this by building on and improving upon previous analyses as outlined below in section 2.

2 Executive Summary

This work is based on three pillars: the numerical simulations needed to assess the conditions under which PBHs form, the cosmological connection, fundamental to link the properties of the individual peak eventually forming a CPBH to the statistics of random fields and in particular their correlation functions, and peak theory, used to assess CPBH abundance and its link to primordial statistical properties. Each one of these pillars has a dedicated section, 3, 4 and 5 for numerical simulations, cosmological connection and peak theory, respectively. These elements constitute the fundamental building blocks we use to reconstruct the primordial power spectrum.

We improve upon previous analyses by reducing the number of approximations (also in light of recent theoretical developments) and providing new insights on each of the building blocks as follows. We go beyond the linear approximation for the curvature perturbation in modelling CPBH formation and improve the reliability of the estimate of the critical threshold the perturbation has to overcome to collapse. We include information about the profile of the initial density perturbation. We clarify the role of smoothing scales and their relation to the underlying physics and we propose a filtering recipe that respects all the relevant physics. Finally, we go beyond Press-Schechter theory to connect PBH abundance to the primordial power spectrum and adopt the most recent PBH abundance constraints which have changed significantly since the time of Ref. [121].

In section 3 we treat the details of CPBH formation. We perform an advanced study of the effects of non-linearities. In particular we study the impact of the linear approximation of curvature on the typical scale of the collapsing region, on the overdensity profile, on the mass of the final object and on the criterion used to assess whether a PBH forms or not. We prove that none of these quantities is accurately computed using linear theory.

In section 4 we further develop cosmological perturbation theory to be applicable in the context of CPBH formation and to include non-linear effects which are non-negligible. We motivate, on a physical basis, how the filtering/smoothing procedure should be done to avoid introducing artificial features on the filtered field. While numerical simulations treat one density perturbation at the time, cosmological perturbation theory treats the entire density field (made by the superposition of many density perturbations) at once. The density field statistical properties are determined by the primordial curvature power spectrum (and possibly higher-order statistics) and by non-linearities. Here we provide a fully analytical method to include non-linearities and primordial non-Gaussianity contributions to the density field statistics.

In section 5 we connect the results found using numerical simulations to the statistical properties of the density field, which ultimately determines the abundance of PBHs. We comment on how the statistical properties of the density field should be evaluated during radiation-domination and under which conditions the shape of the peak in the density field is connected to statistical properties of the field itself.

We conclude in section 6, where we provide the most updated and accurate limits on the primordial curvature power spectrum amplitude allowed if CPBHs constitute the maximum fraction of the dark matter consistent with observations. Furthermore, we show to which

extent the initial conditions of numerical simulations, corresponding to the threshold for CPBH formation, can be used to reconstruct the shape of the primordial power spectrum.

In this work we use natural units $c = \hbar = G = 1$ unless otherwise specified.

3 Primordial black holes formation

The gravitational collapse of density perturbations in the radiation-dominated era and the subsequent formation of PBHs are highly non-linear processes. Hence their study requires numerical simulations [128–130]. After these pioneering works, the collapse of initial perturbations in the form of primordial curvature fluctuations, was numerically studied in Refs. [131, 132], followed some years afterwards by an extensive numerical analysis by one of us using an explicit Lagrangian hydrodynamics code developed and used in Refs. [133–137] and, recently, by other authors in Refs. [138, 139]. More details about the code and the result of these simulations are discussed in appendix A. Here we rely on results of this code and these simulations.

Numerical simulations of PBH formation have always assumed spherical symmetry. This assumption is quite natural in this context because large perturbations, as in the case of those generating CPBHs, are expected to be quasi-spherical (see also section 5); therefore we will continue assuming spherical symmetry[1]. The simplest form of the metric in a spherically symmetric spacetime is

$$ds^2 = -A^2(t,r)dt^2 + B^2(t,r)dr^2 + R^2(t,r)d\Omega^2, \tag{3.1}$$

where t is the cosmic time, r is a comoving radial coordinate, A, B and R are strictly positive functions, $d\Omega$ is the solid angle measure. The function R is also called areal radius and it measures the physical distance of a point of the space-time with coordinates (t, r) from the centre of symmetry.

3.1 Curvature and density perturbations in the super-horizon regime

Formation of a CPBH requires a cosmological perturbation large enough to collapse, forming an apparent horizon [140, 141] which is obtained from initial conditions characterized by non-linear curvature perturbations. To use the standard description of cosmological adiabatic perturbations behaving as pure growing modes, these initial conditions must be set on super-horizon scales, where the length scale of the perturbation(s) we are considering must be much larger than the cosmological horizon at initial time. This is easy to envision if initial curvature perturbations are generated in the context of cosmological inflation.

In this regime the curvature perturbations are conserved (time-independent) because pressure gradients are negligible and an analytic treatment, usually called the gradient expansion or long-wave length approximation[2], is possible [132, 142]. The metric in equation (3.1) can then be written using a spherically-symmetric spatial curvature perturbation $K(\tilde{r})$ [134]

$$ds^2 \simeq -dt^2 + a^2(t)\left[\frac{d\tilde{r}^2}{1 - K(\tilde{r})\tilde{r}^2} + \tilde{r}^2 d\Omega^2\right], \tag{3.2}$$

[1] Small deviation from non-spherical perturbations could play an important role when computing PBH abundance, however in this work we follow the standard approach.

[2] In this description the exact solution is expanded in a power series of a small parameter that is conveniently identified with the ratio between the Hubble radius and the length-scale of the perturbation.

where $a(t)$ is the scale factor and $\tilde{r}$ is a comoving radial coordinate. This expression is approximated because here for simplicity we neglect the time-dependent components of the metric perturbations, which are small on super-horizon scales. However these components are taken into account when the initial condition of numerical simulations are specified.

For a more expert reader we point out that, although this approach reproduces the time evolution of linear perturbation theory on super-horizon scale, it also allows one to consider non-linear curvature perturbations if the spacetime is sufficiently homogeneous and isotropic on large scales [143]. This is equivalent to say that pressure gradients are negligible and shows that the large initial curvature perturbations, as required for PBH formation, has to appear already at zero order in the background form of the metric.

In a cosmological framework it is more convenient to use a different parametrisation of the curvature perturbation, for instance by using the curvature perturbation on comoving hypersurfaces $\mathcal{R}$ or the curvature perturbation on uniform energy density hypersurfaces ζ.[3] Both can be interpreted as perturbations of the scale factor $a(t)$. Here we choose to work with the latter, where equation (3.2) becomes [143]

$$ds^2 \simeq -dt^2 + a^2(t) e^{-2\zeta(\hat{r})} \left[d\hat{r}^2 + \hat{r}^2 d\Omega^2 \right], \tag{3.3}$$

valid in this form during radiation-domination only on super-horizon scales. Different parametrisations of the curvature perturbation yield different parametrisation of the radial comoving coordinate (see Ref. [149] for an exhaustive discussion on different metrics in the context of CPBH formation), and comparing the two forms of the metric above one finds they are related by [137]

$$\begin{aligned} \tilde{r} &= \hat{r} e^{-\zeta(\hat{r})}, \\ K(\tilde{r})\tilde{r}^2 &= \hat{r} \frac{d\zeta(\hat{r})}{d\hat{r}} \left[2 - \hat{r} \frac{d\zeta(\hat{r})}{d\hat{r}} \right]. \end{aligned} \tag{3.4}$$

From now onwards we assume that the spatial metric perturbations in equations (3.2) and (3.3) describe a peak centred in the coordinates origin. In Refs. [134, 137] the authors analysed the gravitational collapse of density perturbations generated by peaks of the K-curvature perturbation, whose profile is parametrised as

$$K_{\rm peak}(\tilde{r}) = \mathcal{A}_{\rm peak} \exp\left[-\frac{1}{\alpha} \left(\frac{\tilde{r}}{r_t} \right)^{2\alpha} \right], \tag{3.5}$$

where $\mathcal{A}_{\rm peak}$ is the K-curvature peak amplitude, α describes the steepness of the peak profile and r_t, as it will become clearer later, sets the typical scale of the peak. We choose this one-parameter family of profiles because it allows us to study both steep ($\alpha \to 0$) and flat peaks ($\alpha \to \infty$), as we show in the upper left panel of figure 1. This family of profiles assumes a spatially flat background at infinity, i.e., $K(\tilde{r}) \to 0$ when $\tilde{r} \to \infty$. According to the super-horizon regime prescription, the scale r_t has to be much larger than the comoving cosmological horizon $r_{\rm hor} = (aH)^{-1}$ at initial time $t_{\rm ini}$, i.e., $a_{\rm ini} H_{\rm ini} r_t \gg 1$, where H is the Hubble expansion rate, $a_{\rm ini} = a(t_{\rm ini})$ and $H_{\rm ini} = H(t_{\rm ini})$. The simulations show that, if the perturbation amplitude, controlled by the parameter $\mathcal{A}_{\rm peak}$, is larger than a suitable threshold, these curvature profiles lead to CPBH formation. That is, if certain conditions

[3] In cosmology there are different notation conventions regarding the curvature perturbation. Throughout this work we follow the one of Refs. [144–146]; however there are alternative conventions, for instance the one used by the WMAP and Planck Collaborations, see e.g., Refs. [147, 148].

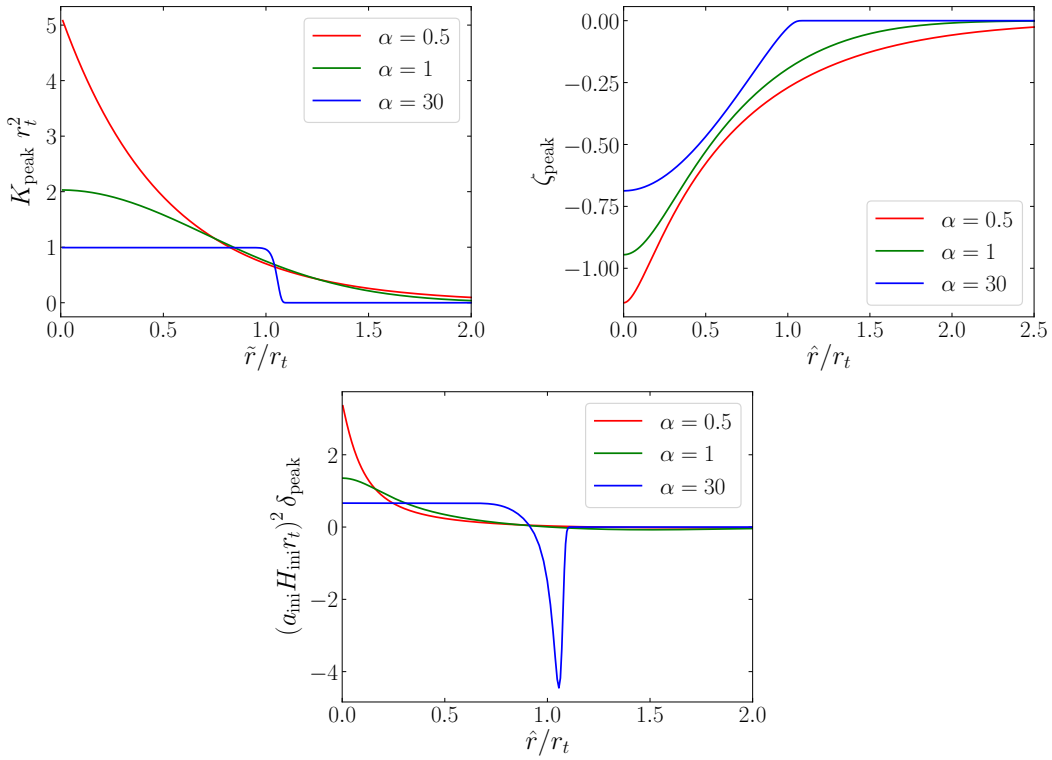

Figure 1: *Upper left panel:* curvature profile $K_{\rm peak} r_t^2$ at initial conditions, on super-horizon scales, for different values of the shape parameter α. We use $\mathcal{A}_{\rm peak} r_t^2 = 5.18,\ 2.03,\ 0.99$ for $\alpha = 0.5,\ 1.0,\ 30$, respectively. While the peak amplitude $\mathcal{A}_{\rm peak}$ changes when the typical scale r_t varies, the quantity $\mathcal{A}_{\rm peak} r_t^2$ is constant. Initial conditions are set up super-horizon, so that the typical scale of the perturbation r_t is much larger than the coming horizon at initial time, i.e., $a_{\rm ini} H_{\rm ini} r_t \gg 1$. *Upper right panel:* Curvature profiles $\zeta_{\rm peak}$, corresponding to the K-curvature peaks of the upper left panel, at initial time $t_{\rm ini}$ for different values of the parameter α. Also in this case the typical scale of the perturbation is r_t. *Lower panel:* Corresponding overdensity profiles at initial time $t_{\rm ini}$.

on the peak profile are satisfied, these curvature profiles generate overdensities that, after crossing the cosmological horizon, are large enough to overcome pressure forces, collapse and form PBHs. These conditions will be discussed in § 3.2.

On super-horizon scales a constant shift in ζ is equivalent to a rescaling of the radial coordinate; therefore, without any loss of generality, we can take $\zeta(\hat{r}) \to 0$ when $\hat{r} \to \infty$. Hence for the family of profiles under consideration, a peak in the K-curvature becomes a trough in the ζ-curvature perturbation which reads as

$$\zeta_{\rm peak}\left[\hat{r}(\tilde{r})\right] = \int_{\infty}^{\tilde{r}} \frac{dr}{r} \left[\frac{1}{\sqrt{1 - K_{\rm peak}(r) r^2}} - 1 \right], \tag{3.6}$$

reported in the upper right panel of figure 1. Despite the naïve idea that peaks in the curvature field correspond to peaks in overdensity, in this case peaks in the metric of equation (3.2)

correspond to troughs in the metric of equation (3.3), even if both perturbations generate a peak in the energy density[4] ρ. The ζ-curvature perturbation generates an overdensity perturbation $\delta_{\rm peak} = \rho/\bar{\rho} - 1$, where $\bar{\rho}$ is the background energy density, given by

$$\begin{aligned}\delta_{\rm peak}(t,\hat{r}) &= \frac{3(1+w)}{5+3w}\left(\frac{1}{aH}\right)^2\left(-\frac{4}{3}\right)e^{5\zeta_{\rm peak}(\hat{r})/2}\nabla^2 e^{-\zeta_{\rm peak}(\hat{r})/2} \\ &= \frac{4}{9}\left(\frac{1}{aH}\right)^2 e^{2\zeta_{\rm peak}(\hat{r})}\left[\nabla^2\zeta_{\rm peak}(\hat{r}) - \frac{1}{2}\nabla\zeta_{\rm peak}(\hat{r})\cdot\nabla\zeta_{\rm peak}(\hat{r})\right],\end{aligned} \tag{3.7}$$

where $w := p/\rho$ is the equation of state for a perfect fluid and p is the pressure[5] ($w = 1/3$ in radiation-dominated era). As it can be seen in the lower panel of figure 1 (and later in figure 4), the peak shows an overdensity in the central region surrounded by an underdense region. We call zero-crossing distance $\hat{r}_0$ the distance from the peak where $\delta_{\rm peak}(\hat{r}_0) = 0$, i.e., where the overdensity becomes an underdensity.

Notice that the relation between the overdensity and curvature perturbations is intrinsically non-linear. A linear relation is recovered only when the curvature perturbation and the gradient of the curvature are small ($|\zeta_{\rm peak}| \ll 1$, $|\nabla\zeta_{\rm peak}| \ll 1$) and we explicitly show in § 3.3 that this approximation is not accurate in the context of CPBH formation. In the following subsection we work with the full non-linear relation between overdensity and curvature.

3.2 Primordial black hole formation criterion

Many criteria have been proposed to assess whether a CPBH forms (see Ref. [137] and references therein for a broad discussion on different criteria). In this work we use the criterion proposed in Ref. [132], based on the so called compaction function. This approach allows us to consistently compare curvature and overdensity profiles with different shapes. The compaction function $\mathcal{C}$ quantifies the magnitude of the gravitational potential and, following Ref. [137], we define it as twice the ratio between the mass excess δM inside a sphere of areal radius R at time t and the areal radius itself:

$$\mathcal{C}(t,r) := 2\frac{\delta M(t,r)}{R(t,r)}. \tag{3.8}$$

Here with r we refer to a generic comoving variable as in equation (3.1), without specifying the particular parametrisation of the curvature profile used.

In the cases where the overdensity perturbation has a single peak, as in those described by equation (3.5), the compaction function has a maximum at some comoving scale r_m. Moreover, it can be shown that the compaction function is conserved [137] (i.e., constant in time) on super-horizon scales, where $R(t,r)H(t) \geq 1$. The condition $R(t,r)H(t) = 1$ defines the horizon crossing time t of the comoving scale r, hence for any $t_\star \leq t$ the cosmological horizon is smaller than the scale of interest r and we have $\mathcal{C}$ constant in time: $\mathcal{C}(t_\star, r) = \mathcal{C}(t,r)$. In the following we take as reference scale r_m and as reference time t_m, defined implicitly by $H_m R_m = 1$, with $R_m = R(t_m, r_m)$ and $H_m = H(t_m)$. In this sense the value of the compaction function can be used as a time-independent measure of the amplitude of the perturbation on super-horizon scales: a CPBH forms if $\mathcal{C}(t_m, r_m)$ is larger than

[4] If we use the curvature perturbation on comoving hypersurfaces $\mathcal{R} \simeq -\zeta$ instead of the curvature perturbation on uniform energy density hypersurfaces ζ, then peaks in the K-curvature correspond to peaks in the $\mathcal{R}$-curvature and both generate peaks in the density.

[5] We refer the interested reader to appendix B of Ref. [140] for more details about the equation of state of a perfect fluid.

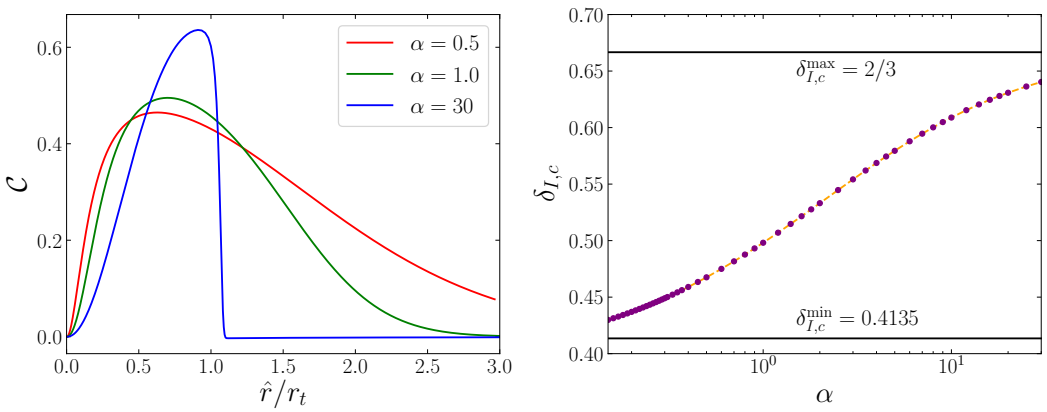

Figure 2: *Left panel:* compaction function $\mathcal{C}$ corresponding to the curvature and density perturbations of figure 1. *Right panel:* Critical threshold as a function of the shape of the perturbation profile. Steep profiles correspond to $\alpha \to 0$, while flat profiles correspond to $\alpha \to \infty$. Purple dots represents values found by numerical simulation, interpolated with the orange line.

some critical threshold [132] whose specific value depends on the particular shape of the peak curvature [137].

By comparing equations (3.1) and (3.3) we find that the areal radius in the second metric reads as $R = a\hat{r}e^{-\zeta_{\rm peak}(\hat{r})}$ and therefore, according to our parametrisation of the peak shape of equation (3.5), the physical scale of the maximum of the compaction function is $R_m = a_m\hat{r}_m e^{-\zeta_{\rm peak}(\hat{r}_m)}$ (with $a_m = a(t_m)$). This is tightly related to the typical comoving scale of the perturbation $r_t \equiv \tilde{r}_m = \hat{r}_m e^{-\zeta_{\rm peak}(\hat{r}_m)}$ defined by the horizon crossing condition $a_m H_m r_t = 1$. Qualitatively, we say that at time t_m the perturbation enters the horizon, i.e., the perturbation enters the horizon when the physical scale R_m (corresponding to the maximum of the compaction function) is crossing the cosmological horizon. We show in figure 2 the compaction function for the overdensity perturbations appearing in figure 1.

For practical purposes, the criterion collapse is often formulated in terms of the integrated overdensity profile δ_I, given by

$$\delta_I(t,r) = \frac{\delta M(t,r)}{\overline{M}(t,r)} = \frac{3}{R^3(t,r)}\int_0^r dx \frac{dX(t,x)}{dx} X^2(t,x)\delta_{\rm peak}(t,x), \tag{3.9}$$

where X and x are physical and comoving coordinates, respectively, and the mass excess

$$\delta M(t,r) = M(t,r) - \overline{M}(t,r) = 4\pi\int_0^r dx \frac{dX(t,x)}{dx} X^2(t,x)\left[\rho(t,x) - \bar{\rho}(t)\right] \tag{3.10}$$

has been measured with respect to an unperturbed sphere of areal radius R, uniform density $\bar{\rho}$ (which in the case considered here corresponds to the background cosmological energy density) and enclosed mass $\overline{M}$. Since we assume spherical symmetry, as in the numerical simulations we use, the mass is defined without ambiguity by the Misner-Sharp mass[6] [152].

[6] In general one should use the Komar mass [150], which is equivalent to Kodama mass [151] and to the Misner-Sharp mass [152] in this context.

However the two criteria are not conflicting, in fact, using the definition of compaction function, we have that on super horizon scales $\mathcal{C}(t,r) = H^2(t)R^2(t,r)\delta_I(t,r)$ [149]. Using the horizon crossing condition $H_m R_m = 1$, our threshold criterion reads as

$$\mathcal{C}(t_m, r_m) = \delta_I(t_m, r_m) > \delta_{I,c}(\alpha), \tag{3.11}$$

where the exact numerical value of the critical threshold $\delta_{I,c}(\alpha)$ has to be found using numerical simulations (see appendix A). We report the critical value of the integrated overdensity amplitude as a function of the parameter α in the right panel of figure 2. We note that the critical threshold is shape-dependent and that it takes values between $\delta_{I,c}^{\min} = 0.4135$ and $\delta_{I,c}^{\max} = 2/3$ for steep ($\alpha \to 0$) and flat ($\alpha \to \infty$) profiles, respectively. The difference in the value of critical threshold is related to the role of pressure gradients during the non-linear evolution [137]: a steeper initial profile needs a lower excess of mass to form a PBH because most of the energy density is already located in the centre and the pressure gradients around r_t are negligible. On the contrary, when the profile is more homogeneous, as for a top-hat profile, the pressure gradients around r_t are very large and the required value of $\delta_{I,c}$ is higher.

The mass of the resulting CPBH follows the scaling law of critical collapse [153] determined by how much the integrated density profile exceeds a critical value and it reads as [131, 135, 153, 154]

$$M_{\rm PBH} = \mathcal{K}(\alpha) M_{\rm hor}(t_m) \left[\delta_I(t_m, r_m) - \delta_{I,c}(\alpha)\right]^{\gamma_{\rm crit}}, \tag{3.12}$$

where $M_{\rm hor}(t_m) = (2H_m)^{-1}$ is the mass contained inside the cosmological horizon at horizon crossing time, $\gamma_{\rm crit} \simeq 0.36$ is a critical exponent for radiation, which depends only on the equation of state parameter w[7] [159] while $\mathcal{K}$ is a numerical coefficient that depends on the specific density profile. This result holds under the condition $M_{\rm PBH} \lesssim M_{\rm hor}$, i.e., for $\delta_I - \delta_{I,c} \lesssim \mathcal{O}(10^{-2})$, beyond these values the scaling law is not very accurate. We discuss further the validity of equation (3.12) in § 5.1. It is important to note here that in equation (3.12) the estimated values of $\mathcal{K}$ and $\gamma_{\rm crit}$ are computed with a $\delta_I(t_m, r_m)$ which comes from the initial conditions linearly extrapolated and rescaled by the background cosmic evolution (i.e., the effects of pressure gradients are neglected). Also this subtlety will be revisited later, in § 5.1.

As we will see in section 5, it is useful to re-interpret equation (3.12) in terms of the peak amplitude $\delta_{\rm peak,0} = \delta_{\rm peak}(t_m, 0)$. Also in this case the peak amplitude is linearly extrapolated from initial conditions by using only the cosmic expansion $1/a^2H^2$ factor. The integrated overdensity is related to the overdensity peak amplitude by a shape-dependent, but time-independent, relation $\mathcal{F}_\delta(\alpha) = \delta_I(t_m, r_m)/\delta_{\rm peak}(t_m, 0)$. Hence equation (3.12) can be re-written as

$$M_{\rm PBH} = \mathcal{K}'(\alpha) M_{\rm hor}(t_m) \left[\delta_{\rm peak,0} - \delta_{\rm peak,0,c}(\alpha)\right]^{\gamma_{\rm crit}}, \tag{3.13}$$

where $\mathcal{K}'(\alpha) = \left[\mathcal{F}_\delta(\alpha)\right]^{\gamma_{\rm crit}} \mathcal{K}(\alpha)$ and the new critical threshold is related to the integrated critical threshold by $\delta_{\rm peak,0,c}(\alpha) = \delta_{I,c}(\alpha)/\mathcal{F}_\delta(\alpha)$.

[7] Notice that the equation of state is not exactly constant during the entire radiation-dominated era. For instance, during the QCD phase transition, the equation of state and the sound speed soften dropping to $\gamma \simeq 0.20 - 0.25$ and the production of PBHs is enhanced [155–158]. This change of the equation of state, not any more characterised only by one parameter, generates a deviation from the scaling law, as simulations suggest [156]. Since refined simulation of PBH formation during the QCD phase transition investigating are still missing, in this work we consider only the standard case where $\gamma \simeq 0.36$.

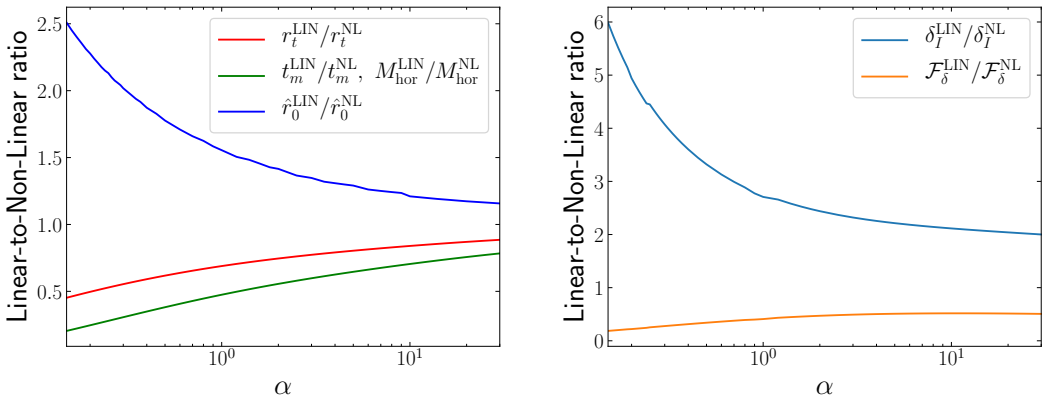

Figure 3: Linear-to-Non-Linear ratio between different physical scales. *Left panel:* ratio of typical comoving scales r_t of the perturbation, horizon crossing times t_m, masses enclosed inside the horizon $M_{\rm hor}$ and overdensity zero-crossing scales $\hat{r}_0$. *Right panel:* ratio of integrated density profiles $\delta_I(t_m, R_m)$ and integrated-density-to-peak-amplitude relation $\mathcal{F}_\delta$.

3.3 Effects of the linear curvature approximation

It is usually assumed, even in the context of CPBH formation, that both the ζ-curvature and curvature gradients are small ($|\zeta_{\rm peak}|$, $|\nabla\zeta_{\rm peak}| \ll 1$) and therefore equations involving them can be linearised. In particular, in equation (3.7) it is often assumed that the exponential damping $e^{2\zeta_{\rm peak}}$ and the quadratic gradient correction ($\nabla\zeta_{\rm peak}\cdot\nabla\zeta_{\rm peak}$) can be neglected, effectively linearising the relation between ζ-curvature perturbation and the overdensity perturbation δ: $\delta^{\rm LIN}_{\rm peak} \propto \nabla^2\zeta_{\rm peak}$.

Even if at initial time the linear approximation is accurate, at horizon crossing time, when both curvature and overdensity perturbations are of order unity, non-linearities have already produced significant effects. Neglecting non-linearities biases the results obtained at every level of the analysis done in this work (the three pillars of section 2). Hence, we use the full non-linear results coming from numerical simulations.

Since, for simplicity, it is tempting to use the linear approximation – and it has been used in the literature not infrequently – in this subsection we explicitly show the effects that the linear approximation generates in the CPBH formation process. To quantify the effects of the linear approximation, we proceed in comparing key quantities evaluated with the full non-linear equation (NL) with the corresponding linear approximation (LIN).

Under linear approximation, the typical scale of the perturbation becomes $r_t^{\rm LIN} = \hat{r}_m$, to be compared against the typical non-linear scale $r_t^{\rm NL} = \hat{r}_m e^{-\zeta_{\rm peak}(\hat{r}_m)}$. Since $\zeta_{\rm peak}$ is negative, linearisation underestimates the real size of the perturbation, i.e., $r_t^{\rm LIN}/r_t^{\rm NL} < 1$. Because in radiation-domination the comoving horizon scales as $r_{\rm hor} \propto t^{1/2}$ and the horizon crossing condition is $a_m H_m r_t = 1$, linearisation also underestimates the horizon crossing time t_m:

$$\frac{t_m^{\rm LIN}}{t_m^{\rm NL}} = \left(\frac{r_t^{\rm LIN}}{r_t^{\rm NL}}\right)^2 < 1. \tag{3.14}$$

The inferred mass of the PBH is also affected by linearisation through a different estimate of the horizon crossing time, as can be seen in equation (3.12). The main effect is that

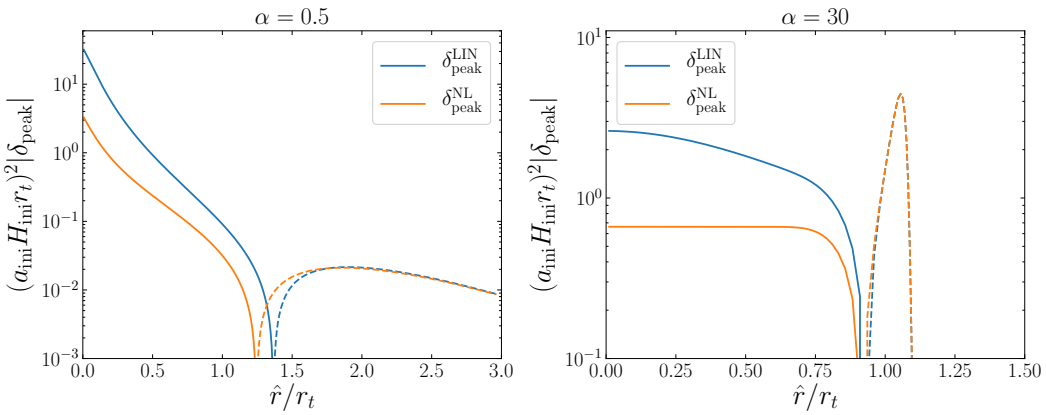

Figure 4: Linear and non-linear overdensity profile of equation (3.7) on super-horizon scales, for a steep profiles with $\alpha = 0.5$ (*left panel*) and a flat profile $\alpha = 30$ (*right panel*). Solid lines indicate overdensity ($\delta_{\rm peak} > 0$) while dashed lines indicate underdensities ($\delta_{\rm peak} < 0$). The profile is showed in units of the typical scale of the perturbation $r_t = \hat{r}_m$ in the linear approximation or $r_t = \hat{r}_m e^{-\zeta_{\rm peak}(\hat{r}_m)}$ in the non-linear case. In both cases the non-linear corrections damps and shrink the overdensity profile significantly with respect to the linear case. We use $\mathcal{A}_{\rm peak} r_t^2 = 5.18,\ 0.99$ for $\alpha = 0.5,\ 30$, respectively.

the linear approximation underestimates the mass inside the horizon, by a factor

$$\frac{M^{\rm LIN}_{\rm hor}}{M^{\rm NL}_{\rm hor}} = \frac{t^{\rm LIN}_m}{t^{\rm NL}_m} < 1. \tag{3.15}$$

We report in the left panel of figure 3 the magnitude of such effects, where we can see that the largest effects are for the steeper profiles.

The second effect of the linear approximation is to change the non-linear relation between overdensity and ζ-curvature perturbations of equation (3.7) yielding:

$$\delta^{\rm LIN}_{\rm peak} = \frac{4}{9}\left(\frac{1}{aH}\right)^2 \nabla^2 \zeta_{\rm peak}. \tag{3.16}$$

We show in figure 4 the comparison between the non-linear overdensity $\delta_{\rm peak} \equiv \delta^{\rm NL}_{\rm peak}$ and its linear counterpart $\delta^{\rm LIN}_{\rm peak}$ on super-horizon scales. Notice that the profiles are presented in terms of their respective typical scale r_t, which we have already showed to be different. Unsurprisingly, the linear approximation clearly fails when curvature and overdensity perturbations are order unity. As we can see from equation (3.7), non-linearities produce two effects: an exponential damping of the peak given by $e^{2\zeta_{\rm peak}}$ and a change in the tails of the profile given by the gradient correction $\nabla\zeta_{\rm peak} \cdot \nabla\zeta_{\rm peak}$. The exponential damping is relevant especially towards the center of the perturbation, where $|\zeta_{\rm peak}| \sim \mathcal{O}(1)$, whereas the gradient-squared correction changes the tails by shifting the zero-crossing scale $\hat{r}_0$. The change in the absolute value of $\hat{r}_0$ is showed in the left panel of figure 3. The exponential damping is relevant for the whole range of profile under consideration, while the gradient correction is significant only for steep profiles. Non-linear effects therefore damp and shrink the overdensity profile computed under the linear approximation. At the same time, they

also shrink the typical scale, as discussed before. The magnitude of these two competing effects depends on the case under consideration.

Finally, since the linearised overdensity profile is different, the compaction function, the integrated overdensity and the threshold criterion will change as well. We show the linear-to-non-linear ratio of the integrated overdensity profiles $\delta_I(t_m, r_m)$ and of the integrated-density-to-peak-amplitude relation $\mathcal{F}_\delta$ in the right panel of figure 3. Since the linearised overdensity is overestimated, it is easier for a perturbation to exceed the critical threshold and to form a CPBH in the linear approximation. Moreover, the mass of the resulting CPBH and, more in general, the CPBHs mass distribution will be shifted with respect to the non-linear case. The magnitude of the shift and the direction (towards lower/higher masses) depend on two competing effects: the change in the horizon crossing time and the change in the threshold criterion. Notice also that the integrated-density-to-peak-amplitude relation $\mathcal{F}_\delta$ changes as well, hence the numerical coefficient $\mathcal{K}'(\alpha)$ derived in the linear approximation is smaller.

While the magnitude of all these effects is specific to the family of profiles we have analysed, the qualitative effects remain in general valid, showing that the linear approximation is inadequate to describe the formation of CPBHs. As a consequence, adopting the linear approximation to compute the inferred statistical properties of the overdensity field yield an incorrect estimate of the global PBH abundance. A discussion on these effects can be found in section 5 and in Refs. [160–162]. Since this require a set of preliminary results that are connected to the standard description of cosmological perturbations, we present them after section 4.

4 The cosmology connection

Our numerical simulations model the collapse of one overdensity peak at a time; however, if CPBHs are the dark matter, we have to construct a self-consistent description of a Universe filled with many of those peaks. Even if the mechanism generating these overdensity perturbations is not known and many of them have been proposed so far, in this work we assume that they are created by large fluctuations of the curvature perturbation, generated during inflation. Hence the information encoded in the overdensity peaks can be connected to the Early Universe physics.

Cosmological perturbation theory provides in principle the necessary framework and tools to connect Early and Late Universe physics. However, in the standard cosmological context and on large cosmological scales, perturbations are typically (almost) linear while we have seen in section 3 that CPBH formation is strongly non-linear and that non-linearities cannot be neglected. Therefore, for this application, standard cosmology perturbation theory has to be extended and modified to account for these effects.

We begin by reviewing cosmological linear theory, which represents our starting point in § 4.1. The first extension we must introduce is connected to the role of the filter functions in the context of CPBH formation, which we discuss in § 4.2 and we motivate their use based on physical arguments. The second extension is the inclusion of non-linearities, hence of non-Gaussainities, both primordial (eventually) and due to gravity: their presence is unavoidable precisely because of the non-linear relation between curvature and overdensity and we quantify their effects in § 4.3.

In this section we always work with the metric defined in equation (3.3), hence for convenience we drop the " $\widehat{\ }$ " symbol on top of spatial comoving coordinates. Notice that

in this section we consider generic overdensity and curvature perturbations (and not only peaks, as in section 3), hence we also drop the " $_{\rm peak}$ " subscript.

4.1 Linear theory

In the standard cosmological framework, linear theory can be used and stretched even to study the collapse of massive objects such as halos (see e.g., the Press Schechter approach [163]). As a warm up exercise, we start by adopting the linear approximation and reviewing the necessary background to be applied to CPBH formation.

In linear theory, as it can be seen in equation (3.16), the overdensity perturbation δ is uniquely determined by the second derivatives of the ζ-curvature perturbation, (i.e., $\delta \propto \nabla^2\zeta$). According to the standard interpretation of cosmological perturbation theory, both perturbations are random fields whose properties are determined by the family of n-point correlators, e.g., $\langle\zeta(\mathbf{x}_1)\cdots\zeta(\mathbf{x}_n)\rangle$ or $\langle\delta(\mathbf{x}_1)\cdots\delta(\mathbf{x}_n)\rangle$, and by the relation between the two random fields. For instance, since the Laplacian is a linear operator, if ζ is a Gaussian random field then also δ will be a Gaussian random field.

It is well-known that random fields are neither continuous or differentiable [164–166], hence it is necessary to smooth out the field on small scales using a filter function, especially to define topological concepts as peaks or troughs of the random field. In full generality, we define a smoothed field, e.g., the overdensity field, as

$$\delta_s(\mathbf{x}) = \int d^3y W_s(|\mathbf{x}-\mathbf{y}|)\delta(\mathbf{y}), \tag{4.1}$$

where W_s is a filter function of comoving radius s. The filter function is typically normalized to unity $\left(\int d^3y W_s(|\mathbf{y}|) = 1\right)$ and it can be written in terms of an unnormalized filter function $w_s(|\mathbf{y}|)$ and a comoving volume normalizing factor $V_w^{\rm com.} = \int d^3y w_s(|\mathbf{y}|)$ as $W_s = w_s/V_w^{\rm com.}$.

Since we are working in the linear approximation, where spatial curvature is assumed to be small, the smoothing can be done directly in comoving coordinates. We discuss the smoothing procedure when spatial curvature is not negligible and the appropriate size of the smoothing radius s in § 4.2. In principle, since the relation between ζ and δ is non-linear, smoothing the curvature field is not equivalent to smoothing directly the over density field. However, at linear order, the two operations are equivalent, in fact by applying the smoothing procedure of equation (4.1) to equation (3.16) we obtain

$$\begin{aligned}
\delta_s(\mathbf{x}) &= \frac{4}{9}\frac{1}{a^2H^2}\int d^3y W_s(|\mathbf{x}-\mathbf{y}|)\nabla^2_{\mathbf{y}}\zeta(\mathbf{y}) \\
&= \frac{4}{9}\frac{1}{a^2H^2}\int d^3y \left\{\zeta(\mathbf{y})\nabla^2_{\mathbf{y}}W_s(|\mathbf{x}-\mathbf{y}|) + \right. \\
&\qquad\qquad \left. +\nabla_{\mathbf{y}}\cdot\left[W_s(|\mathbf{x}-\mathbf{y}|)\nabla_{\mathbf{y}}\zeta(\mathbf{y}) - \zeta(\mathbf{y})\nabla_{\mathbf{y}}W_s(|\mathbf{x}-\mathbf{y}|)\right]\right\} \\
&= \frac{4}{9}\frac{1}{a^2H^2}\nabla^2_{\mathbf{x}}\zeta_s(\mathbf{x})\,.
\end{aligned} \tag{4.2}$$

The surface contribution vanishes under the fairly general assumption that W_s and its derivative vanish at large scales (as for Top-Hat or Gaussian filter functions), where we use $\nabla^2_{\mathbf{y}}W_s = \nabla^2_{\mathbf{x}}W_s$ because of the form of the filter function argument and we recognise $\zeta_s(\mathbf{x}) \equiv \int d^3y W_s(|\mathbf{x}-\mathbf{y}|)\zeta(\mathbf{y})$. Therefore, at linear level, it is completely equivalent to smooth out the overdensity field or the curvature field.

In general, the statistical properties (the n-point correlators) of smoothed fields will be different from those of the original unsmoothed field. In particular, the power spectrum of the smoothed field will be that of the unsmoothed field multiplied by the square of the Fourier transform of the kernel. Moreover, the filter function may introduce non-trivial effects in the context of PBHs abundance constraints such as those presented in Ref. [167] and later re-analysed in Ref. [168] (see also § 4.2) or in Ref. [169] for effects applied to dark matter halos.

Even if so far we have considered the spatial curvature on super-horizon scales as time-independent, on every sub-horizon patch the curvature is actually evolving with time. The evolution of sub-horizon scales is typically described by a transfer function $\mathcal{T}$. By taking the Fourier transform of equation (4.2) and including pressure effects on sub-horizon scales, we have that in linear theory the overdensity field in Fourier space reads as

$$\widehat{\delta}_s(\tau, \mathbf{k}) = -\frac{4}{9}\frac{k^2}{a^2 H^2}\widehat{W}_s(k)\widehat{\mathcal{T}}_{\rm LIN}(\tau, k)\widehat{\zeta}(\mathbf{k}), \tag{4.3}$$

where τ is the conformal time and $\widehat{W}_s$ and $\widehat{\mathcal{T}}_{\rm LIN}$ are the Fourier transform of the filter and linear transfer functions. Under the linear approximation assumption, in the radiation-dominated era, the transfer function reads as [170, 171]

$$\widehat{\mathcal{T}}_{\rm LIN}(\tau, k) = 3\frac{\sin(c_s k\tau) - (c_s k\tau)\cos(c_s k\tau)}{(c_s k\tau)^3}, \tag{4.4}$$

where $c_s^2 = 1/3$ is the sound speed of the relativistic fluid. As can be seen from equation (4.4), pressure effects act as a smoothing and naturally damp perturbations on scales smaller than the sound horizon $r_s(\tau) = c_s\tau = c_s/(aH)$, i.e., for modes $k \gg (c_s\tau)^{-1}$.

The statistical properties of the smoothed overdensity field, i.e., the n-point functions $\left\langle \widehat{\delta}_s(\mathbf{k}_1)\cdots\widehat{\delta}_s(\mathbf{k}_n)\right\rangle$ can be computed using equation (4.3), assuming that we know the entire set of n-point functions of the curvature field, e.g.,

$$\begin{aligned}\left\langle \widehat{\zeta}(\mathbf{k}_1)\widehat{\zeta}(\mathbf{k}_2)\right\rangle &= (2\pi)^3\delta^D\left(\mathbf{k}_{12}\right)P_\zeta(\mathbf{k}_1),\\ \left\langle \widehat{\zeta}(\mathbf{k}_1)\widehat{\zeta}(\mathbf{k}_2)\widehat{\zeta}(\mathbf{k}_3)\right\rangle &= (2\pi)^3\delta^D\left(\mathbf{k}_{123}\right)B_\zeta(\mathbf{k}_1, \mathbf{k}_2, \mathbf{k}_3),\end{aligned} \tag{4.5}$$

etc., where δ^D is the Dirac delta, $\mathbf{k}_{1\ldots n} = \mathbf{k}_1 + \cdots + \mathbf{k}_n$ and P_ζ and B_ζ are the curvature power spectrum and bispectrum, respectively. For instance, the two-point function or, equivalently, the power spectrum of the smoothed density field is

$$P_s(\tau, k) = \frac{16}{81}\frac{k^4}{a^4 H^4}\widehat{W}_s^2(k)\widehat{\mathcal{T}}_{\rm LIN}^2(\tau, k)P_\zeta(k). \tag{4.6}$$

4.2 Filtering random fields

Filtering is a procedure widely used in signal processing that eliminates the power contained in a range of "frequencies" (scales in this case) from some "signal" (the overdensity field in the case under consideration). Operationally, this is done by convolving the signal with a filter/smoothing/window function (all the three names have been used in the literature)[8]. A

[8] Smoothing is usually the result of a low-pass filter, where high-frequencies are suppressed, but high-pass filters are also useful, where low frequency signals that might mimic an almost-DC mode or long baseline variations are suppressed. Here for example, as it will be clear later, long wavelength modes on scales much larger than the typical size of the perturbation of interest are considered as DC modes and effectively ignored in the simulations. In certain cases, see § 5.2, these modes have to be cut out.

low-pass filter is what is mostly used in cosmological settings and it results in a smoother version of the initial signal. Because of this, in the rest of the section we use interchangeably the term filter and smoothing function.

As already emphasized in Refs. [164–166], a filtering procedure is absolutely necessary to define concepts such as peaks or troughs of random fields, which require the field to be at least differentiable. In this sense, the filter function is just a mathematical artefact we introduce to treat analytically random fields, therefore it is fundamental for this procedure not to bias the statistical properties of the random field (or, in case it is unavoidable, one should asses the magnitude of the bias). Notice that in the Press-Schechter formalism of large-scale structure the filter function is used to define the mass of the object of interest (the dark matter halo). In the CPBHs case this does not apply; in fact the mass of the CPBHs is specified by the shape of the overdensity, the horizon crossing time of the perturbation and by how much the integrated overdensity (or the height of the overdensity peak) exceeds some critical threshold (see equations (3.12) and (3.13)).

Since the purpose of the filter function in the large-scale structure and CPBHs frameworks is completely different, we cannot apply directly what is typically done in large-scale structure to CPBHs. In particular we have to re-assess the appropriate smoothing scale and how the filtering is performed when the spatial curvature is non-negligible.

To set the smoothing radius, first we have to establish which scales r (or modes $k := r^{-1}$) play a physical role in the collapse. As we have seen in section 3, we identify the typical scale of a collapsing perturbation in real space with r_t, corresponding to a typical mode $k_t = r_t^{-1}$ in Fourier space[9]. To avoid affecting the shape of the peaks, and the properties of the resulting CPBH, the smoothing should be done on scales much smaller than the typical scale of the fluctuation, i.e., for the "ultra-short" scales $r \ll r_t$ or modes $k \gg k_t$. We show a visual example of an overdensity field and its smoothed version in figure 5, in particular in the zoomed-in panel. The specific details of how these modes (corresponding to "ultra-short" scales) are filtered out should not influence the dynamics of the perturbation on scales $\mathcal{O}(r_t)$, where the gravitational collapse is the dominant process. Note that this procedure is implicitly implemented every time the spacetime is discretized, as in numerical simulations.

The other relevant physical scale is the size of the sound horizon, where pressure gradients effectively smooth the perturbations. As seen in equation (4.4), in linear theory, pressure effects act as an effective filter function that damps perturbations on scales smaller than the sound horizon. At horizon crossing, the size of the sound horizon $r_s(t_m) = c_s/(a_m H_m) = r_t/\sqrt{3}$ is comparable to the typical scale of the perturbation. Hence, a filter function of smoothing radius $r_t \equiv 1/(a_m H_m)$ would artificially increase the damping effect produced by pressure. Finally, the height of the peak $\delta_{\mathrm{peak},0}$, used in equation (3.13) to determine the mass of the PBH, should not depend on how the filtering procedure is performed (see also appendix A).

The condition $s \ll r_t$ thus $s \ll r_s(t_m)$, ensures that: *(i)* what determines the true height of the peaks are pressure effects and not the artificial smoothing, *(ii)* does not alter the relevant properties of the field nor the physics involved in CPBH formation and *(iii)* allows

[9] While in flat space we typically have $k = (2\pi)/r$, in this case, where curvature is non-negligible, the conversion factor between k and r will be different from 2π, with a coefficient that depends on the shape. To avoid discussing scenarios on a case by case basis, we define $k := 1/r$ and we refer the interested reader to Ref. [172] for a broader discussion. Notice that the conversion factor is order unity in all the cases of interest, hence this definition does not influence our conclusions.

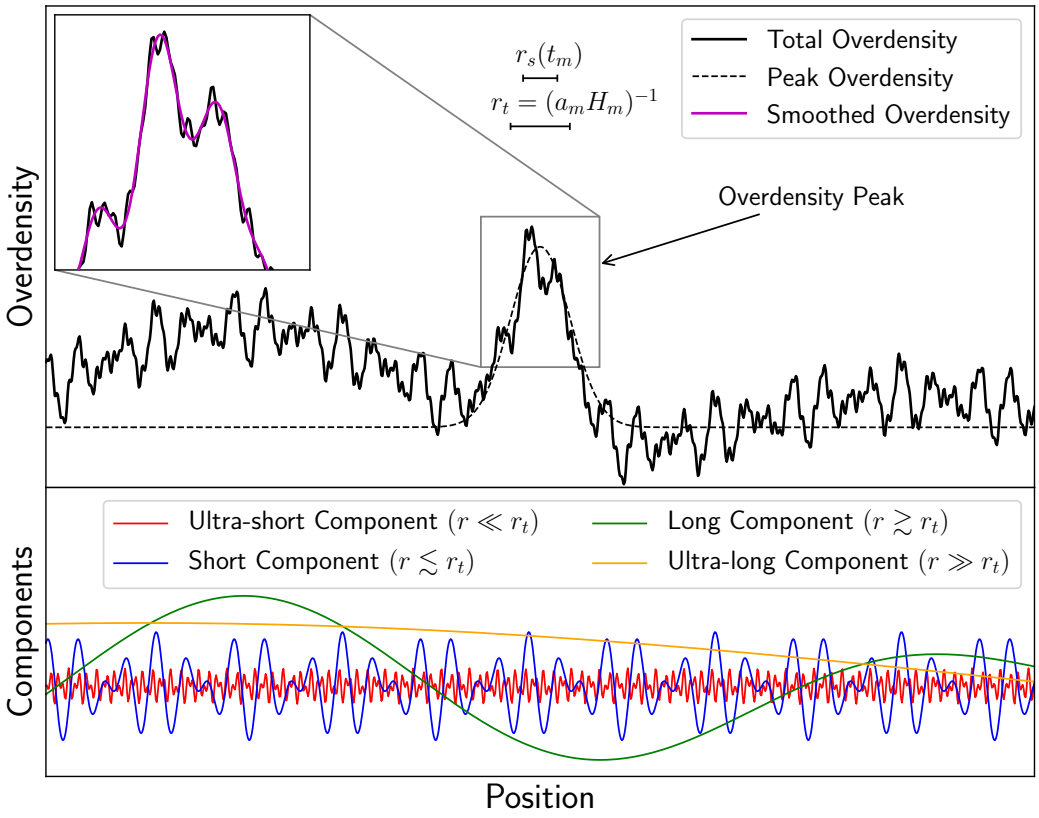

Figure 5: Sketch of the overdensity random field in one spatial dimension. *Upper panel:* total overdensity (*solid line*) given by the sum of a peak overdensity (*dashed line*) with typical scale r_t and the four random fluctuations with different wavelengths illustrated in the lower panel. For completeness we report also the size of the sound horizon $r_s = r_t/\sqrt{3}$. *Zoomed-in panel:* how the peak profile would be before and after smoothing on scale s ($s \ll r_t$, $s \ll r_s$), i.e., removing ultra-short perturbations with frequency $k \gg k_t$. *Lower panel:* the four components of the sketched overdensity with different wavelengths.

us to use all the (cosmological) results about properties of (smoothed) random fields. In other words, the smoothing of the field on small scales should be done on a scale $r_{\rm hor}(t_{\rm ini})$, where $t_{\rm ini}$ is some initial time, much smaller than all the typical horizon re-entry time scales t_m.

In the majority of the existing literature the smoothing radius has been typically chosen to be comparable to the typical scale of the perturbation or, equivalently, to the radius of the cosmological comoving horizon when the perturbation starts to collapse, namely $s \sim \mathcal{O}(r_t \equiv 1/a_m H_m)$. This operation removes both ultra-short and short perturbation of figure 5. Some effects of this choice might be seen in Ref. [167], where it was shown that different window functions with this smoothing radius lead to different CPBH abundance constraints. The choice we propose here, $s \ll r_s(t_m)$, ensures that the details (or even the presence) of the (artificial but unavoidable) smoothing do not affect the dynamic of the collapse and thus the final results including PBH mass and abundance.

It is also important to note that, while the gravitational collapse of a CPBH is a process ongoing at cosmological horizon scales, scales that are well above the horizon at all times during the collapse do not influence sub-horizon dynamics. The collapse is not instantaneous, therefore it is reasonable to expect that long perturbations with modes $k \lesssim k_t$ might influence the process; on the other hand ultra-long scale perturbations associated to modes $k \ll k_t$ appear as a constant background during the collapse, hence they should not play any role in determining whether a CPBH forms or not. We refer the reader to figure 5 for a visualization of these two cases. One way to avoid super-horizon effects is to introduce a second (high pass) filter function W_{s_2} that smooths out scales much larger than the typical scale of the perturbation, i.e., scales $s_2 \gg r_t$ or modes $k_2 \ll k_t$. This is what will be implemented in § 5.2.

The second difference in the smoothing procedure regards the treatment of non-linearities. So far we have neglected spatial curvature and worked with comoving coordinates. But spatial curvature is not negligible; this introduces some subtleties which ultimately lead to a re-interpretation of the filtering procedure. To account for the curvature, the filtering should be done in physical coordinates $\mathbf{Y} = ae^{-\zeta(\mathbf{y})}\mathbf{y}$ instead of comoving coordinates $\mathbf{y}$, as in linear theory. For instance, the filtered overdensity field would be

$$\delta_S(\mathbf{X}) = \int d^3Y W_S(|\mathbf{X}-\mathbf{Y}|)\delta(\mathbf{Y}), \tag{4.7}$$

where W_S is a filter function of smoothing physical scale S. Also in this case the filter function has been normalized to unity and it can be written as $W_S = w_S/V_w^{\text{phys.}}$, where w_S is the unnormalized filter function and $V_w^{\text{phys.}} = \int d^3Y w_S(|\mathbf{Y}|)$ is the physical volume normalization coefficient. Therefore the overdensity field, filtered on a comoving scale s corresponding to a physical scale $S = ae^{-\zeta(\mathbf{s})}s$, becomes in comoving coordinates

$$\begin{aligned}\delta_s(\mathbf{x}) = \delta_{S(s)}\left(\mathbf{X}(\mathbf{x})\right) &= \int d^3y e^{-3\zeta(\mathbf{y})}\left[1-\mathbf{y}\cdot\nabla\zeta(\mathbf{y})\right]\frac{a^3}{V_w^{\text{phys.}}}w_{S(s)}(|\mathbf{X}(\mathbf{x})-\mathbf{Y}(\mathbf{y})|)\delta(\mathbf{y}) \\ &= \int d^3y \frac{a^3}{V_w^{\text{phys.}}}w_{S(s)}(|\mathbf{X}(\mathbf{x})-\mathbf{Y}(\mathbf{y})|)\delta_{\text{new}}(\mathbf{y}),\end{aligned} \tag{4.8}$$

where, using equation (3.7), the "new" overdensity field we want to smooth out reads as

$$\delta_{\text{new}}(\mathbf{y}) = \frac{4}{9}\left(\frac{1}{aH}\right)^2 e^{-\zeta(\mathbf{y})}\left[1-\mathbf{y}\cdot\nabla\zeta(\mathbf{y})\right]\left[\nabla^2\zeta(\mathbf{y}) - \frac{1}{2}\nabla\zeta(\mathbf{y})\cdot\nabla\zeta(\mathbf{y})\right]. \tag{4.9}$$

Notice that in the linear approximation, where curvature and gradients are small ($\zeta \ll 1$, $|\nabla\zeta| \ll 1$), thus $V_w^{\text{phys.}} \to a^3 V_w^{\text{com.}}$ and $w_S \to w_s$[10], we recover exactly the linear theory definition of filtering of equation (4.1).

However, once the spatial curvature is included in the filtering procedure and the full non-linear relation between overdensity and curvature is used, filtering the overdensity or the curvature fields is not equivalent any more (*cf.* equation (4.2)). Although we do not report

[10] Here we report a practical example of the linear limit. In the case of a Top-Hat filter function in physical coordinates we have $w_S(|\mathbf{Y}|) = \Theta(1-|\mathbf{Y}|/S)$, where Θ is the Heaviside function. The physical volume reads as $V_w^{\text{phys.}} = 4\pi S^3/3 = a^3 e^{-3\zeta(\mathbf{s})}4\pi s^3/3 \to a^3 V_w^{\text{com.}}$ when $\zeta \ll 1$. In the same limit the unnormalized filter function reads as $w_S(|\mathbf{Y}|) = \Theta(1-ye^{-\zeta(\mathbf{y})}/se^{-\zeta(\mathbf{s})}) \to \Theta(1-y/s) = w_s(|\mathbf{y}|)$.

the full calculation, it can be easily shown that

$$\begin{aligned}\delta_s(\mathbf{x}) &= \int d^3y \frac{a^3}{V_w^{\text{phys.}}} w_{S(s)}(|\mathbf{X}(\mathbf{x}) - \mathbf{Y}(\mathbf{y})|)\delta_{\text{new}}(\mathbf{y}) \\ &\neq \frac{4}{9}\left(\frac{1}{aH}\right)^2 e^{2\zeta_s(\mathbf{x})}\left[\nabla^2\zeta_s(\mathbf{y}) - \frac{1}{2}\nabla\zeta_s(\mathbf{y})\cdot\nabla\zeta_s(\mathbf{y})\right],\end{aligned} \tag{4.10}$$

using the same smoothing function w_s for both δ and ζ, where the second line of RHS corresponds to equation (3.7).

Notice also that the curvature enters in the argument of the window function $a^3 W_S$, hence the domain of integration in comoving coordinates will be different from a sphere centred at a given point $\mathbf{x}$. Large curvature fluctuations will produce large deformation in the domain, however we expect this effect to be negligible when estimating the statistical properties of the whole field since large fluctuations are extremely rare. Moreover, as explained in § 4.2, we are smoothing on scales much smaller than the scale of the peak, therefore we can neglect this curvature dependence when taking correlators of the smoothed overdensity of equation (4.8) and treat the window function as curvature-independent.

According to equation (4.10), in principle filtering ζ is not equivalent to filtering δ in the non-linear case. The effect of ignoring this subtlety in the filtering procedures cannot be established a priori, since it depends on the statistical properties of the curvature and density fields. However, given that the abundance of CPBHs depends on those statistical properties, it is important to assess which is the role of the filtering procedure in determining the statistics of the field at initial time (see also § 5.1). Given the general nature of this paper, we leave the quantitative estimation of this effect to a future work. In this paper we will apply the smoothing to the density field.

4.3 Impact of primordial non-Gaussianities

Non-Gaussianities can be separated into two categories: primordial non-Gaussianities, generated by some inflationary mechanism and imprinted into the "matter" fields at horizon re-entry, and non-Gaussianities generated dynamically, for instance by gravitational evolution. In this section we are interested only in the former.

The fact that non-linearities are so important in the context of CPBHs already suggests that non-Gaussianities, linked to non-linearities, could be important as well. In fact, primordial non-Gaussianities affect both CPBH formation and abundance and are generally expected to be produced in many of the proposed models for CPBHs generation, see e.g., Refs. [173–179]. While it has been tested that at cosmological scales initial conditions are very close to be Gaussian [148, 180–183], this has not been verified at very small scales, i.e., for the range of scales $k \gtrsim 10^5$ Mpc^{-1} relevant for CPBH formation.

Here we assess for the first time what is the contribution of primordial non-Gaussianities to the n-point function of the smoothed overdensity field including the non-linear effects of equation (3.7). The procedure is exact and can be applied to any n-point function, however in this work we concentrate only on the two-point function, i.e., the power spectrum, for reasons that will become clear in section 5.

For simplicity, we initially neglect filter and transfer functions and re-introduce them at the end. The full non-linear overdensity field in Fourier is computed from equation (4.9)

yielding:

$$\begin{aligned}\widehat{\delta}(\mathbf{k}) &= \frac{4}{9}\frac{1}{a^2H^2}\int d^3r\,[1-\mathbf{r}\cdot\nabla\zeta(\mathbf{r})]\left[\nabla^2\zeta(\mathbf{r})-\frac{1}{2}\nabla\zeta(\mathbf{r})\cdot\nabla\zeta(\mathbf{r})\right]e^{-\zeta(\mathbf{r})}e^{-i\mathbf{k}\cdot\mathbf{r}}\\ &= -\frac{4}{9}\frac{1}{a^2H^2}\sum_n\frac{(-1)^n}{n!}\int\frac{d^3q_1}{(2\pi)^3}\frac{d^3q_2}{(2\pi)^3}\frac{d^3q_3}{(2\pi)^3}\left[\widehat{\zeta}^0(\mathbf{q}_1)+3\widehat{\zeta}(\mathbf{q}_1)-\left.\frac{\partial\widehat{\zeta}(\mathbf{q}_1/\lambda)}{\partial\lambda}\right|_{\lambda=1}\right]\times\\ &\quad\times\mathbf{q}_2\cdot\mathbf{q}_3\left[\widehat{\zeta}(\mathbf{q}_2)\widehat{\zeta^0}(\mathbf{q}_3-\mathbf{q}_2)\widehat{\zeta^n}(\mathbf{k}-\mathbf{q}_{12})-\frac{1}{2}\widehat{\zeta}(\mathbf{q}_2)\widehat{\zeta}(\mathbf{q}_3)\widehat{\zeta^n}(\mathbf{k}-\mathbf{q}_{123})\right],\end{aligned} \tag{4.11}$$

where we have introduced an auxiliary parameter λ[11] and we have expanded the exponential $e^{-\zeta}$ in series, introducing the function $\widehat{\zeta^n}$, which is the Fourier transform of ζ^n. The function $\widehat{\zeta^n}$ can be computed at every order in n and it is given by

$$\begin{aligned}&\widehat{\zeta^0}(\mathbf{k}^\star) = (2\pi)^3\delta^D(\mathbf{k}^\star) && n=0,\\ &\widehat{\zeta^1}(\mathbf{k}^\star) = \widehat{\zeta}(\mathbf{k}^\star) && n=1,\\ &\widehat{\zeta^n}(\mathbf{k}^\star) = \int\prod_{j=1}^{n-1}\left[\frac{\mathrm{d}^3p_j}{(2\pi)^3}\widehat{\zeta}(\mathbf{p}_j)\right]\widehat{\zeta}\left(\mathbf{k}^\star-\sum_{j=1}^{n-1}\mathbf{p}_j\right) && n\geq 2.\end{aligned} \tag{4.12}$$

Because of non-linearities, even when the ζ-curvature field is Gaussian and has zero one-point correlator $\left(\langle\widehat{\zeta}(\mathbf{k})\rangle=0\right)$, the one-point correlator of the overdensity field is non-zero. Its exact value can be computed from equation (4.11) and it can be checked that it is non-zero only for the ultra-long mode $\mathbf{k}=0$ and it depends only on the statistical properties of the field:

$$\left\langle\widehat{\delta}(\mathbf{k})\right\rangle = (2\pi)^3\delta^D(\mathbf{k})\mathcal{G}(\sigma_j^2), \tag{4.13}$$

where the $\mathcal{G}(\sigma_j^2)$ is a function of the spectral moments of the ζ-curvature field (see section 5 for the definition of spectral moments).

Notice that in computing the two-point function $\left\langle\widehat{\delta}(\mathbf{k}_1)\widehat{\delta}(\mathbf{k}_2)\right\rangle$ of the overdensity field we should include also the disconnected component $\left\langle\widehat{\delta}(\mathbf{k}_1)\right\rangle\left\langle\widehat{\delta}(\mathbf{k}_2)\right\rangle$, however this contribution is zero for our range of scales of interest, i.e., when $\mathbf{k}\neq 0$. On the other hand, the connected

[11] Equation (4.11) has been obtained using

$$\begin{aligned}\int d^3r\mathbf{r}\cdot\nabla\zeta(\mathbf{r})e^{-i\mathbf{k}\cdot\mathbf{r}} &= \int d^3r\int\frac{d^3q}{(2\pi)^3}i\mathbf{r}\cdot\mathbf{q}\widehat{\zeta}(\mathbf{q})e^{i\mathbf{q}\cdot\mathbf{r}}e^{-i\mathbf{k}\cdot\mathbf{r}} = \int d^3r\int\frac{d^3q}{(2\pi)^3}\widehat{\zeta}(\mathbf{q})\left.\frac{\partial e^{i\lambda\mathbf{q}\cdot\mathbf{r}}}{\partial\lambda}\right|_{\lambda=1}e^{-i\mathbf{k}\cdot\mathbf{r}}\\ &= \frac{\partial}{\partial\lambda}\left[\int d^3r\zeta(\lambda\mathbf{r})e^{-i\mathbf{k}\cdot\mathbf{r}}\right]_{\lambda=1} = \frac{\partial}{\partial\lambda}\left[\lambda^{-3}\widehat{\zeta}(\mathbf{k}/\lambda)\right]_{\lambda=1} = -3\widehat{\zeta}(\mathbf{k})+\left.\frac{\partial\widehat{\zeta}(\mathbf{k}/\lambda)}{\partial\lambda}\right|_{\lambda=1}.\end{aligned}$$

component of the overdensity field power spectrum is given by

$$\left\langle \widehat{\delta}(\mathbf{k}_1)\widehat{\delta}(\mathbf{k}_2)\right\rangle_{\rm c} = \frac{16}{81}\left(\frac{1}{aH}\right)^4 \sum_{n,m}\frac{(-1)^{n+m}}{n!m!}\int \frac{d^3q_1}{(2\pi)^3}\frac{d^3q_2}{(2\pi)^3}\frac{d^3q_3}{(2\pi)^3}\frac{d^3q_4}{(2\pi)^3}\frac{d^3q_5}{(2\pi)^3}\frac{d^3q_6}{(2\pi)^3}(\mathbf{q}_2\cdot\mathbf{q}_3)(\mathbf{q}_5\cdot\mathbf{q}_6)\times$$
$$\times\left\langle\left[\widehat{\zeta}^0(\mathbf{q}_1)+3\widehat{\zeta}(\mathbf{q}_1)-\left.\frac{\partial\widehat{\zeta}(\mathbf{q}_1/\lambda)}{\partial\lambda}\right|_{\lambda=1}\right]\left[\widehat{\zeta}(\mathbf{q}_2)\widehat{\zeta^0}(\mathbf{q}_3-\mathbf{q}_2)\widehat{\zeta^n}(\mathbf{k}_1-\mathbf{q}_{12})-\frac{1}{2}\widehat{\zeta}(\mathbf{q}_2)\widehat{\zeta}(\mathbf{q}_3)\widehat{\zeta^n}(\mathbf{k}_1-\mathbf{q}_{123})\right]\right.$$
$$\left.\left[\widehat{\zeta}^0(\mathbf{q}_4)+3\widehat{\zeta}(\mathbf{q}_4)-\left.\frac{\partial\widehat{\zeta}(\mathbf{q}_4/\lambda)}{\partial\lambda}\right|_{\lambda=1}\right]\left[\widehat{\zeta}(\mathbf{q}_5)\widehat{\zeta^0}(\mathbf{q}_6-\mathbf{q}_5)\widehat{\zeta^m}(\mathbf{k}_2-\mathbf{q}_{45})-\frac{1}{2}\widehat{\zeta}(\mathbf{q}_5)\widehat{\zeta}(\mathbf{q}_6)\widehat{\zeta^m}(\mathbf{k}_2-\mathbf{q}_{456})\right]\right\rangle \tag{4.14}$$

First of all we stress that this result is exact, no approximation has been taken so far. Second, we see that the entire family of n-point function of the ζ-curvature contributes to the two-point function of the overdensity due to the $e^{-\zeta}$ factor. In this sense, non-linearities and primordial non-Gaussianities are very important in determining the full power-spectrum of the overdensity field. From the inflationary model-building side, it is therefore important not only to compute the primordial curvature power spectrum, but also the primordial bispectrum and higher-order correlations, and to assess the magnitude of their contribution, given by equation (4.14), to the overdensity two-point function.

As we will explain in section 5, we are interested in filtering only the overdensity field, hence filter functions can be introduced multiplying equation (4.14) by $\widehat{W'}_s(\mathbf{k}_1)\widehat{W'}_s(\mathbf{k}_1)$, where $\widehat{W'}_s$ is the Fourier transform of the filter function a^3W_S. As explained after equation (4.10), this procedure is not strictly correct, since the curvature perturbation appears also in the argument of the filter function, deforming the volume of the smoothing region. However, since we are performing the smoothing on scales much smaller than the scale of the perturbations, this effect is expected to be sub-leading. The other (physical) smoothing is the one introduced by the sound horizon and described by the transfer function. The transfer function, by definition describes the evolution of the curvature perturbation on sub-horizon modes, hence in equations (4.12) and (4.14), every curvature perturbation $\widehat{\zeta}$ should be substituted with $\widehat{\mathcal{T}}_{\rm NL}\widehat{\zeta}$, where $\widehat{\mathcal{T}}_{\rm NL}$ is the fully non-linear transfer function.

Finally, we provide a practical example of how equation (4.14) can be used to compute the leading bispectrum B_ζ contribution to the two-point function of the smoothed overdensity field:

$$P_s(\tau,k) = \frac{16}{81}\frac{k^4}{a^4H^4}\widehat{W'}_s^2(k)\widehat{\mathcal{T}}^2_{\rm NL}(\tau,k)\left[P_\zeta(k)\ +\frac{1}{k^2\widehat{\mathcal{T}}_{\rm NL}(\tau,k)}\times\right.$$
$$\left.\int\frac{d^3q}{(2\pi)^3}\widehat{\mathcal{T}}_{\rm NL}(\tau,q)\widehat{\mathcal{T}}_{\rm NL}(\tau,|\mathbf{k}+\mathbf{q}|)\left[6|\mathbf{k}+\mathbf{q}|^2-2q^2+\mathbf{q}\cdot(\mathbf{k}+\mathbf{q})\right]B_\zeta(k,q,|\mathbf{k}+\mathbf{q}|)+\cdots\right]. \tag{4.15}$$

The dots in the second line represent sub-leading Gaussian and mixed Gaussian/non-Gaussian corrections, generated for instance by terms proportionals to $\langle\zeta\zeta\zeta\zeta\rangle \propto P_\zeta P_\zeta$ and $\langle\zeta\zeta\zeta\zeta\zeta\rangle \propto P_\zeta B_\zeta$, respectively[12]. Similar terms appear also in the analysis of clustering properties of halos, see e.g., Ref. [184], and they appear to be a general prediction of non-linear overdensity fields.

[12]The fact that these extra Gaussian terms are subleading can be easily seen by noticing that they contain four transfer functions instead of just two, as in the leading term, hence they will be highly suppressed compared to the first line of equation (4.15). The same reasoning applies also to mixed terms, where there will be even more transfer functions.

Equation (4.15) reduces to the well-known form of equation (4.6) (but with a different window function) in case of Gaussian initial conditions, i.e., $B_\zeta \equiv 0$, and neglecting sub-leading contributions. This equation also shows that the relation between the power spectrum of δ and that of ζ is not univocal: in this example, the same smoothed overdensity power spectrum can be generated by a non-Gaussian ζ with power spectrum P_ζ and bispectrum B_ζ or by a Gaussian ζ' with power spectrum $P_{\zeta'}$ equal to the argument of the square bracket in the RHS of equation (4.15). We conclude that particular care is needed when trying to reconstruct the primordial curvature power spectrum from the overdensity two-point function (see section 6).

5 Peak theory applied to Primordial Black Holes

Since CPBHs form from peaks in the overdensity field, we resort to peak theory [166] to calculate PBH abundance at formation time, starting from the statistical distribution of the local maxima. In order to define a maxima, we need a smooth and differentiable random field, obtained by using the prescription given in § 4.2. In principle the field can be either Gaussian or non-Gaussian, however we work with a smoothed Gaussian random overdensity field, whose statistical properties are completely specified by its power spectrum P_s or, alternatively, by its Fourier transform, the correlation function $\xi_s(|\mathbf{x}_1 - \mathbf{x}_2|) = \langle \delta_s(\mathbf{x}_1)\delta_s(\mathbf{x}_2)\rangle$. To be accurate, the Gaussian assumption might be too strict for the PBHs scenario, in fact we already saw in § 4.3 that non-linearities induce departures from the Gaussian statistics in the overdensity field. However peak theory has not been fully developed for non-Gaussian fields, hence we will consider only the Gaussian case.

The original framework considers the statistics of a smoothed random field deep in the matter-dominated era and it connects the initial statistics to the formation of large-scale structure. The original framework was designed for matter-domination, where pressure effects are negligible, hence we need to slightly upgrade it to employ it also during radiation-domination. In fact, pressure effects on sub-horizon scales naturally wash out perturbations, changing the statistical properties of the random field.

5.1 Primordial Black Holes abundance

The statistical properties of the field are encoded in the spectral moments

$$\sigma_j^2(\tau) = \int \frac{d^3k}{(2\pi)^3} k^{2j} P_s(k,\tau), \tag{5.1}$$

where the smoothed power spectrum is given in equation (4.15) after imposing Gaussian initial conditions ($B_\zeta \equiv 0$).

The statistical properties must be evaluated for the entire field at once, therefore in this case we are not filtering out ultra-long scales (*cf.* § 4.2). In section 3 we considered each perturbation separately; in reality the Universe is filled by a superposition of perturbations, with a distribution of shapes (or, equivalently, of shape parameter α) and typical scales. If PBHs form from rare events drawn from the tail of the probability distribution of peaks, at any given time the distribution of α and typical scales for PBH "seeds" is likely to be fairly narrow. In particular, the typical scale is of the order of the horizon and the higher the peak, the narrower the distribution of α (see also § 5.2).

As anticipated in § 4.2, the smoothing of the field on small scales should be done on a scale $r_{\rm hor}(\tau_{\rm ini})$, where $\tau_{\rm ini}$ is some initial time, much smaller than all the typical scales of the

entire set of perturbations that will be relevant for PBH formation. The exact value of $\tau_{\rm ini}$ is not relevant, as long as the condition is satisfied. The smoothing procedure should also guarantee that the three spectral moments σ_0, σ_1 and σ_2 are finite at initial time. This extra requirement ensures that spectral moments remain finite at every time and that statistical properties are well-defined. Any result of peak theory cannot be used unless this preliminary requisite is satisfied. Note that if statistical properties are evaluated incorrectly because of a wrong filtering procedure, one could reach incorrect conclusions and thus incorrect inference of cosmology.

Once spectral moments are well defined, we can construct the spectral parameters

$$\gamma(\tau) = \frac{\sigma_1^2(\tau)}{\sigma_2(\tau)\sigma_0(\tau)}, \qquad R_\star(\tau) = \sqrt{3}\frac{\sigma_1(\tau)}{\sigma_2(\tau)}, \tag{5.2}$$

which completely determine the comoving density of peaks. In fact, by defining the relative peak height as $\nu = \delta_{\rm peak,0}/\sigma_0$, the differential comoving peak density reads [166]

$$\frac{dn_{\rm peak}^{\rm com.}(\tau,\nu)}{d\nu} = \frac{1}{(2\pi)^2 R_\star^3(\tau)} e^{-\nu^2/2} G\left(\gamma(\tau), \gamma(\tau)\nu\right), \tag{5.3}$$

where the function $G(\gamma, \gamma\nu)$ can be approximated by [166]

$$G(\gamma,\omega) \approx \frac{\omega^3 - 3\gamma^2\omega + [B(\gamma)\omega^2 + C_1(\gamma)]e^{-A(\gamma)\omega^2}}{1 + C_2(\gamma)e^{-C_3(\gamma)\omega}} \tag{5.4}$$

for $0.3 < \gamma < 0.7$ and for $-1 < \omega < +\infty$, keeping the difference between the numerical result and the analytic estimation below 1%[13].

During matter-dominated era, at linear order, the overdensity field grows self-similarly on every scale, hence all the spectral moments share the same time dependencies and the spectral parameters of equation (5.2) are time-independent. Therefore, in the large-scale structure framework, the comoving density of peaks does not depend on the time at which it is computed. This is not the case during radiation-domination where the magnitude of the spectral moments diminishes with time because of the suppression of perturbations with high wave modes k due to pressure effects (see equation (4.4)). Therefore, evaluating equation (5.3) at different times yield different number densities because the random field itself is different.

The evolution of the field is uniquely determined by the cosmic expansion and pressure effects, therefore it is possible to compute consistently the comoving peak density at any time by accounting for these two effects. For convenience we choose to evaluate the differential physical number density of peaks at horizon crossing (conformal) time (see Sec 3.2), τ_m:

$$\frac{dn_{\rm peak}^{\rm phys.}(\nu,\tau_m)}{d\nu} = a_m^{-3}\frac{dn_{\rm peak}^{\rm com.}(\nu,\tau_m)}{d\nu}. \tag{5.5}$$

This is the number density of regions that will collapse and form a PBH at formation time $\tau_f \gtrsim \tau_m$. Notice that, since CPBH formation is not instantaneous, the differential

[13] The coefficients of equation (5.4) are given by [166]

$$A(\gamma) = \frac{5/2}{9-5\gamma^2}, \qquad B(\gamma) = \frac{432}{(10\pi)^{1/2}\left(9-5\gamma^2\right)^{5/2}},$$
$$C_1(\gamma) = 1.84 + 1.13\left(1-\gamma^2\right)^{5.72}, \quad C_2(\gamma) = 8.91 + 1.27e^{6.51\gamma^2}, \quad C_3(\gamma) = 2.58e^{1.05\gamma^2}.$$

physical number density of CPBHs has to be rescaled by a factor a_f^{-3}/a_m^{-3}, where $a_f = a(\tau_f)$. Numerical simulations show that the the cosmic time of formation $t_f/t_m \simeq 10$ [137], where t_m is the horizon crossing time defined in § 3.2, and therefore $\tau_f/\tau_m = a_f/a_m \simeq 3$. The exact relation between horizon crossing and formation time is not important, since this factor cancels out when computing the PBHs abundance today (see section 6, equation (6.4)).

We have already discussed in section 3 that not all the peaks correspond to sites where a CPBH forms and that we need a threshold criterion to assess which peaks collapse and which do not. As seen in equations (3.12) and (3.13), in this case the criterion to start gravitational collapse reads as $\delta_{\rm peak,0}(\tau_m) > \delta_{\rm peak,0,c}(\alpha)$, where $\delta_{\rm peak,0,c}(\alpha)$ depends on the shape of the perturbation. Since CPBHs are non-relativistic compact objects, their differential energy density is expected to be written as $d\rho_{\rm PBH}/d\nu \propto M_{\rm PBH}(\nu) dn_{\rm peak}/d\nu$. Here there are two subtleties that enter in $M_{\rm PBH}(\nu)$: the time evolution of $\delta_{\rm peak,0}(\tau_m)$ and the shape dependence of the threshold.

Two considerations are in order. First, the amplitude of the peak, $\delta_{\rm peak,0}$, has been computed considering only cosmic expansion and not pressure effects. Thus the argument of $M_{\rm PBH}$ should be ν' instead of ν, because it refers to the relative amplitude of a field that has been evolved in time in a different way. On the other hand, if we evaluate the effects of pressure, i.e., the contribution due the linear transfer function, on scales close to the typical scale of the perturbation, i.e., for $k\tau \simeq 1$, we find that $\widehat{\mathcal{T}}_{\rm LIN} \simeq 0.9$. However the required transfer function in our case is the non-linear one $\widehat{\mathcal{T}}_{\rm NL}$. It is not possible to estimate the non-linear transfer function from the linear one reported in equation (4.4). It has been shown for instance in Refs. [185–187], that the transfer function at second order in perturbation theory is not simply the square of the linear transfer function, as one would have naïvely expected. We leave the derivation of the non-linear transfer function for future work [188], however here we give a first estimate of these effects. By comparing the profiles obtained assuming linear theory, i.e., using the linear transfer function, and profiles obtained from our numerical simulations, we estimate the relative difference between the non-linear and linear transfer function as the average difference between the density profiles for scales smaller than the typical scale of the perturbation:

$$\frac{\left[\left(\widehat{\mathcal{T}}_{\rm NL} - \widehat{\mathcal{T}}_{\rm LIN}\right)^2\right]^{1/2}}{\widehat{\mathcal{T}}_{\rm LIN}} \sim \frac{\left[\left(\bar{\delta}^{\rm NL}_{\rm peak} - \bar{\delta}^{\rm LIN}_{\rm peak}\right)^2\right]^{1/2}}{\bar{\delta}^{\rm LIN}_{\rm peak}}, \tag{5.6}$$

where the profiles $\bar{\delta}^{\rm NL}_{\rm peak}$ have been obtained using numerical simulations. Even if the estimation is crude, we find that $\widehat{\mathcal{T}}_{\rm NL}/\widehat{\mathcal{T}}_{\rm LIN} \simeq 1.8,\ 1.5,\ 1.2$ for profiles characterised by $\alpha = 0.15,\ 1.0,\ 30.0$, respectively. In conclusion we find that at horizon crossing, pressure effects are inefficient at smoothing inhomogeneities on horizon scales at horizon re-entry time simply because such region was not in causal contact before and effects due to the non-linear growth of the perturbation have not produce significant deviations from the linear theory. Therefore, in what follows, we will assume $\nu' \simeq \nu$ for simplicity.

We also find that the position of the maximum of the compaction function changes by a factor $10 - 15\%$ towards larger values with respect to the position estimated using initial conditions (*cf.* section 3). Therefore the true horizon crossing happens later than what predicted by initial conditions criteria, even when considering non-linearities (see the updated version of Ref. [137] for more details). This difference in horizon crossing scales generates a 20% difference in the horizon crossing time and in the mass contained inside the

horizon, however these differences will not affect significantly our conclusions because what really determines the CPBH mass is how much above the critical threshold the perturbation is.

Second, the threshold is shape-dependent, therefore the approach to get the correct energy density would be to integrate

$$\frac{d^{10}\rho_{\rm PBH}}{d\nu d^3\mathcal{J} d^6\mathcal{H}} \propto M_{\rm PBH}(\nu, \boldsymbol{\mathcal{J}}, \boldsymbol{\mathcal{H}}) \frac{d^{10}n_{\rm peak}}{d\nu d^3\mathcal{J} d^6\mathcal{H}}, \tag{5.7}$$

where $\boldsymbol{\mathcal{J}}$ is a three-dimensional vector containing information on first derivatives (η_j, with $j \in \{1,2,3\}$ in the notation of Ref. [166]) and $\boldsymbol{\mathcal{H}}$ is a six-dimensional vector containing information on second derivatives (ζ_{ij}, with $ij \in \{11,22,33,12,13,23\}$ in Ref. [166]). Since the estimation of this integral for a population of different perturbations with different shapes goes beyond the purpose of this paper, in the following we assume that all the peaks share the same shape, i.e., $M_{\rm PBH}(\nu, \boldsymbol{\mathcal{J}}, \boldsymbol{\mathcal{H}}) = M_{\rm PBH}(\nu)$, thus the same (time-dependent) critical threshold $\nu^{(\alpha)}_{c,m} = \delta_{{\rm peak},0,c}(\alpha)/\sigma_0(\tau_m)$.

Therefore, under these approximation and following Ref. [189], we define the relative energy density of CPBHs with respect to the energy density of radiation at formation time as

$$\begin{aligned}\beta(\tau_f) &= \frac{\rho_{\rm PBH}(\tau_f)}{\rho_{\rm rad}(\tau_f)} = \frac{1}{\rho_{\rm rad}(\tau_f)} \int_{\nu^{(\alpha)}_{c,m}}^{\infty} d\nu \frac{d\rho^{\rm phys.}_{\rm PBH}(\nu,\tau_f)}{d\nu} \\ &= \frac{1}{\rho_{\rm rad}(\tau_f)} \int_{\nu^{(\alpha)}_{c,m}}^{\infty} d\nu \left(\frac{a_f}{a_m}\right)^{-3} M_{\rm PBH}(\nu,\tau_m) \frac{dn^{\rm phys.}_{\rm peak}(\nu,\tau_m)}{d\nu}.\end{aligned} \tag{5.8}$$

Given that CPBHs effectively behave as dark matter, we can connect the abundance at initial time to the constrained abundance $f_{\rm PBH} = \rho_{\rm PBH}/\rho_{\rm dm}$, i.e., the fraction of dark matter in PBHs (assuming that they all form at the time τ_f), as [190, 191]

$$\beta(\tau_f) = \frac{\rho_{\rm PBH}(\tau_f)}{\rho_{\rm rad}(\tau_f)} = \frac{g_{\star,\rho}(\tau_0)}{g_{\star,\rho}(\tau_f)} \left(\frac{g_{\star,s}(\tau_f)}{g_{\star,s}(\tau_0)}\right)^{4/3} \frac{\Omega_{\rm dm,0}}{\Omega_{\rm rad,0}} f_{\rm PBH} a_f, \tag{5.9}$$

where τ_0 is the conformal time today, $\Omega_{\rm dm,0}$ and $\Omega_{\rm rad,0}$ are the present dark matter and radiation densities with respect to the critical density today ρ_{0c}, while $g_{\star,\rho}$ and $g_{\star,s}$ are the total number of effective degrees of freedom for the energy density and the entropy density [192]. Significantly different approximations of equation (5.9) have been used in the literature; we report here the correct result and we refer the reader to appendix B for its derivation, our choice of values for the effective degrees of freedom and further comments, especially on the role of neutrinos. Typical values of initial abundance are $\beta(\tau_f) \simeq 10^{-17}$ ($\beta(\tau_f) \simeq 10^{-6}$) for $M_{\rm hor} \simeq 10^{-18}\ M_\odot$ ($M_{\rm hor} \simeq 10^{4}\ M_\odot$) and $f_{\rm PBH} = 1$, explicitly showing that regions where overdensity perturbations are large enough to collapse are very rare (hence justifying also our treatment of windows functions in § 4.2 and § 4.3).

The definition in equation (5.8) is accurate only when all the CPBHs form at a given time (or, equivalently, at a given scale). However, in a realistic scenario, CPBHs form over some time interval, therefore equations (5.8) and (5.9) should be interpreted as $d\beta/d\tau_f$ and the total abundance of CPBHs would become

$$\beta^{\rm tot}_f = \int_{\tau_{\rm min}}^{\tau_{\rm max}} d\tau_f \frac{d\beta}{d\tau_f}, \tag{5.10}$$

with the condition $\tau_m = \tau_f/3$, $\tau_{\rm min} \gg \tau_{\rm ini}$ to avoid being biased by the filtering procedure, and $\tau_{\rm max} \lesssim \tau_{\rm eq}$ since we are interested only in PBHs forming during the radiation-dominated era.

In principle peak theory would suffer from the cloud-in-cloud problem or, in this case, the black-hole-in-black-hole problem. If CPBHs are generated by a localised peak in the primordial power spectrum, this problem is unimportant. For a very broad peak or a plateau, it may in principle be an issue but since CPBHs are exceedingly rare the black-hole-in-black-hole problem should be much reduced compared to the standard cloud-in-cloud one for dark matter haloes (see also e.g., Ref. [193]). In the context of large-scale structure this problem has already been cured in Ref. [194], introducing the so called Excursion Set Peaks formalism. We leave its implementation to future work.

5.2 The shape of the overdensity peak

Peak theory enables us to connect the average shape of the peaks to the statistical properties of the random field. Assuming that at $\mathbf{x} = 0$ there is a peak of height ν and averaging over all possible curvatures and orientations[14], the mean value of the overdensity at distance r from the peak, i.e., the average shape of the peak, can be written as [166]

$$\frac{\bar{\delta}_{\rm peak}(\tau, r)}{\sigma_0(\tau)} = \nu\psi(\tau, r) - \frac{\theta\left(\gamma(\tau), \gamma(\tau)\nu\right)}{\gamma(\tau)\left(1-\gamma^2(\tau)\right)}\left[\gamma^2(\tau)\psi(\tau, r) + \frac{\nabla^2\psi(\tau, r)}{3}\right], \tag{5.11}$$

where $\psi(\tau, r) = \xi_s(\tau, r)/\sigma_0^2(\tau)$ and the function $\theta(\gamma, \omega)$ is given by [166]

$$\theta(\gamma, \omega) = \frac{3(1-\gamma^2) + (1.216 - 0.9\gamma^4)e^{-2\gamma/\omega^2}}{\left[3(1-\gamma^2) + 0.45 + \frac{\omega^2}{4}\right]^{1/2} + \frac{\omega}{2}} \tag{5.12}$$

and it is accurate for $\gamma \in [0.4, 0.7]$ and $\omega \in [1, 3]$. This result is very similar to the average density profile around a point with the same height ν as the peak but which is not a peak, in fact in the latter case we have [164, 195]

$$\frac{\bar{\delta}_{\rm no-peak}(\tau, r)}{\sigma_0(\tau)} = \nu\psi(\tau, r), \tag{5.13}$$

where equations (5.11) and (5.13) coincide in the limit of high ν, since for high thresholds virtually all regions are peaks.

Not all peaks share the same shape, therefore we associate a variance of shapes $\sigma^2_{\rm peak}(\tau, r)$ and $\sigma^2_{\rm no-peak}(\tau, r)$ to the mean profiles of equations (5.11) and (5.13) (see Ref. [166] for the explicit form of the variance). For high peaks the variance is small, however far from the peak the variance grows and it becomes as large as the amplitude of the overdensity itself. Following Ref. [195], we call this distance the decoherence distance $r_{\rm dec}$, because at this point we cannot distinguish any more if we are "in a peak" or not. In the limit of zero shape variance ($\sigma^2_{\rm peak}, \sigma^2_{\rm no-peak} \equiv 0$) the decoherence distance corresponds to the zero-crossing distance r_0 defined in section 3 for the family of profiles under consideration. A more conservative choice

[14] In principle is not mandatory to average over curvatures and orientations, however deviations from spherical symmetry are suppressed by a factor $1/\nu$ [166], hence they are suppressed for high peaks, as in the cases of interest. Moreover the numerical simulations we use assume spherical symmetry, therefore our choice is natural.

of decoherence distance is given by r_m, however the difference between r_0 and r_m is of $\mathcal{O}(1)$ in our cases, therefore choosing one or the other does not significantly affect our results[15].

Since we consider high peaks (or alternatively, rare events), we can neglect the $\theta(\gamma, \gamma\nu)$ correction in equation (5.11) and use

$$\xi_s(\tau, r) = \sigma_0^2(\tau) \frac{\bar{\delta}_{\rm peak}(\tau, r)}{\bar{\delta}_{\rm peak}(\tau, 0)}, \tag{5.14}$$

which is valid for scales smaller than the decoherence radius. For distances greater than the decoherence length, the density fluctuations become "uncorrelated". In this regime, an estimate of the two-point correlation function $\Xi_s(\tau, r) = \xi_s(\tau, r > r_{\rm dec})$ can be obtained, for instance, by studying the effects of primordial clustering of PBHs [193, 196–201], however this goes beyond the scope of this article, hence we leave it for future work.

Equivalently, one can also work with the Fourier transform of equation (5.14), i.e., the smoothed power spectrum, which reads as

$$\begin{aligned} P_s(\tau, k) &= \int d^3 r \xi_s(\tau, r) e^{-i\mathbf{k}\cdot\mathbf{r}} \\ &= 4\pi \left[\sigma_0^2(\tau) \int_0^{r_{\rm dec}} dr\ r^2 \frac{\sin(kr)}{kr} \frac{\bar{\delta}_{\rm peak}(\tau, r)}{\bar{\delta}_{\rm peak}(\tau, 0)} + \int_{r_{\rm dec}}^{\infty} dr\ r^2 \frac{\sin(kr)}{kr} \Xi_s(\tau, r) \right]. \end{aligned} \tag{5.15}$$

Here we can neglect the second integral in the second line of equation (5.15) because of the $\sin(x)/x$ suppression factor, as long as we consider modes $k \gtrsim k_{\rm dec} = r_{\rm dec}^{-1}$, i.e., modes that play a role in the gravitational collapse. Moreover, all those scales are super-horizon at horizon crossing time, hence they should be filtered out using the second window function defined in § 4.2. Equation 5.15 makes evident how an incorrect estimate of the profile of the peak yields a mis-estimation of the statistical properties of the field. For this reason, in this work we have used a family of profiles which covers multiple possibilities. In section 6 we report the constraints on the power spectrum obtained from the entire family.

6 The reconstruction of primordial power spectrum amplitude and shape

We now combine the results from the previous sections, our three pillars, to reconstruct both the amplitude and the shape of the primordial curvature power spectrum, assuming Gaussian initial conditions.

By combining equation (4.15) (in the Gaussian limit, $B_\zeta \equiv 0$) and equation (5.15), and evaluating both at horizon crossing, we obtain

$$\widehat{W'}_s^2(k) \widehat{\mathcal{T}}^2_{\rm NL}(\tau_m, k) P_\zeta(k) = \frac{81}{16} \left(\frac{a_m H_m}{k} \right)^4 \times 4\pi \sigma_0^2(\tau_m) \int_0^{r_t} dr\ r^2 \frac{\sin(kr)}{kr} \frac{\bar{\delta}_{\rm peak}(\tau_m, r)}{\bar{\delta}_{\rm peak}(\tau_m, 0)}, \tag{6.1}$$

where we choose the typical scale of the perturbation as the decoherence radius, i.e., $r_{\rm dec} = r_t$. In the following we concentrate on wavemodes ranging from $k_t = r_t^{-1}$ to $5k_t$, which we expect to be the modes relevant for the collapse. Alternatively, we will also consider the "almost scale-invariant" power spectrum $\mathcal{P}_\zeta(k) = k^3 P_\zeta(k)/(2\pi^2)$, where P_ζ is obtained from equation (6.1).

[15] In general the ratio r_0/r_m varies from 1 to ∞, however it has been shown that shapes with a similar behaviour in the region $r \lesssim r_m$, but a different one in the outward region, have almost the same threshold. The variation is at most few percent even when r_0/r_m changing significantly [137].

Regarding the window functions, according to § 4.2, we will have a window function on super-horizon scales, implying that the second term on the RHS of equation (5.15) becomes negligible, and one, $\widehat{W'}_s$, on scales much smaller than the scales of the peak, which appear in the LHS of equation (6.1). In the range of wave modes of interest here $\widehat{W'}_s(k) \equiv 1$. We approximate the non-linear transfer function $\widehat{\mathcal{T}}_{\rm NL}$ as the linear transfer function corrected by the numerical factors found using numerical simulations and reported in § 5.1.

The statistical properties of the field that generates the collapsing peaks can be estimated given the assumed shape of the peaks. The spectral moments in equation (5.1) can be computed at any time as

$$\begin{aligned} \sigma_0^2(\tau) &= \int \frac{d^3k}{(2\pi)^3} P_s(k,\tau) e^{-i\mathbf{k}\cdot\mathbf{r}}\Big|_{\mathbf{r}=\mathbf{0}} = \xi_s(\tau,\mathbf{0}), \\ \sigma_1^2(\tau) = \cdots = -\nabla^2\xi_s(\tau,\mathbf{0}), &\qquad \sigma_2^2(\tau) = \cdots = \nabla^2\nabla^2\xi_s(\tau,\mathbf{0}), \end{aligned} \tag{6.2}$$

therefore, using equation (5.14), we can write the spectral parameters in equation (5.2) as

$$\gamma(\tau) = -\frac{\nabla^2\delta_{\rm peak}(\tau,\mathbf{0})}{\sqrt{\delta_{\rm peak}(\tau,\mathbf{0})\nabla^2\nabla^2\delta_{\rm peak}(\tau,\mathbf{0})}}, \qquad R_\star(\tau) = \sqrt{-3\frac{\nabla^2\delta_{\rm peak}(\tau,\mathbf{0})}{\nabla^2\nabla^2\delta_{\rm peak}(\tau,\mathbf{0})}}. \tag{6.3}$$

Finally, for every peak profile, we can derive the variance of the overdensity field at horizon crossing $\sigma_0(\tau_m)$ generating a given fraction of dark matter in PBHs by using equations (5.8) and (5.9):

$$\begin{aligned} f_{\rm PBH}\rho_{0c}\Omega_{\rm dm,0} = \frac{\mathcal{K}'(\alpha) M_{\rm hor}(\tau_m)\left[\sigma_0(\tau_m)\right]^{\gamma_{\rm crit}}}{4\pi^2 R_\star^3(\tau_m)} \times \\ \times \int_{\nu_{c,m}^{(\alpha)}}^{\infty} d\nu \left(\nu - \nu_{c,m}^{(\alpha)}\right)^{\gamma_{\rm crit}} G\left(\gamma(\tau_m), \gamma(\tau_m)\nu\right) e^{-\nu^2/2}, \end{aligned} \tag{6.4}$$

where the variance $\sigma_0(\tau_m)$ appears also in the expression for the critical threshold $\nu_{c,m}^{(\alpha)}$, computed using the peak height obtained in numerical simulations. Notice that the $g_\star$ factors simplifies when combining equations (5.8) and (5.9). The variance σ_0 obtained from the equation (6.4) is consistently $10-30\%$ smaller than the typical Press-Schechter-like estimate $\sigma_0^{\rm PS} = \delta_{{\rm peak},0,c}/\left(\sqrt{2}{\rm Erfc}^{-1}(\beta_f)\right)$, where ${\rm Erfc}^{-1}$ is the inverse of the complementary error function, for all the profiles and masses of interest. Therefore, using Press-Schechter overestimates the true amplitude of the curvature power spectrum by a factor $20-70\%$ with respect to the prediction from Peak Theory.

In this work we consider CPBHs with masses between $10^{-17}\ M_\odot$ and $10^3\ M_\odot$, even if our method applies also to different mass ranges. This mass range includes all the PBHs which have not evaporated by the present-day and for which we have observational constraints. We assume that all the CPBHs share the same formation time, hence that the primordial curvature power spectrum has a localised feature such as a spike. To connect typical scales and the compact object mass, we assume that all the CPBHs exceeded the critical threshold for formation by the same amount, which we choose to be $(\delta_I - \delta_{I,c}) = 0.01$, generating CPBHs with masses $M_{\rm PBH} = M_{\rm hor}(\tau_m)$, leaving the estimate of the CPBH initial mass function for future work. Following our conventions, the CPBHs mass is given by

$$M_{\rm PBH} = M_{\rm hor}(\tau_m) = \frac{a_{\rm eq}^2}{4t_{\rm eq}} k_t^{-2}, \tag{6.5}$$

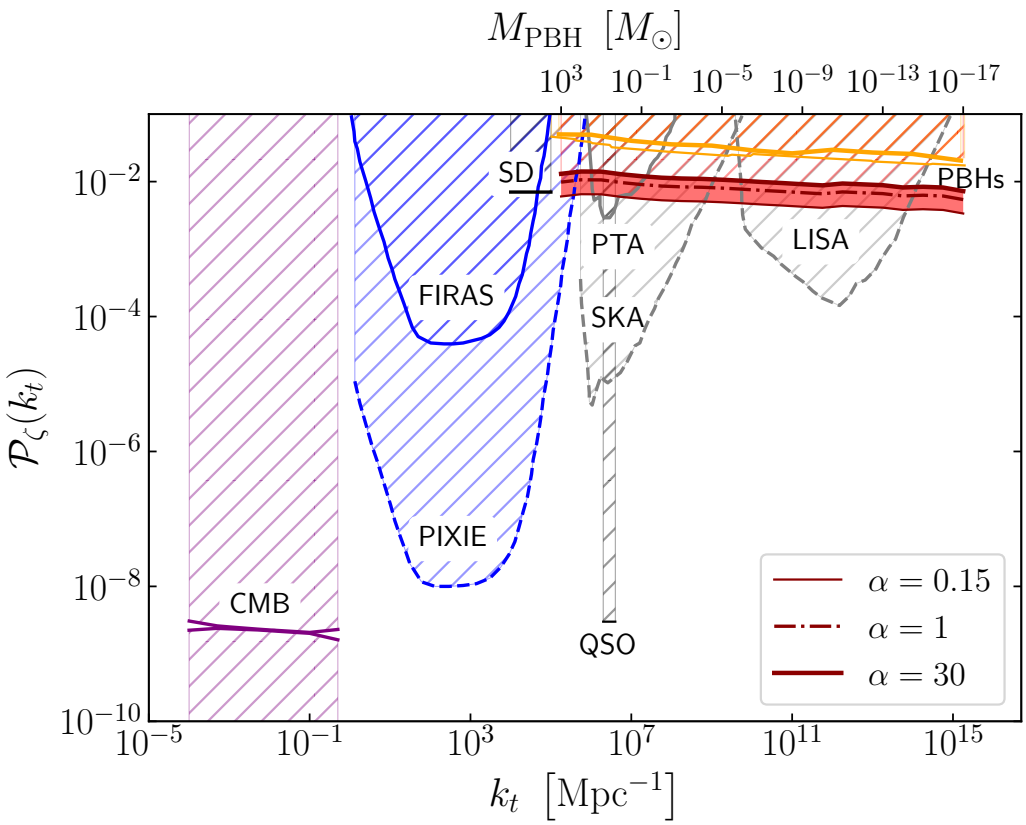

Figure 6: Maximum allowed amplitude of the primordial curvature power spectrum. Current (solid lines) and forecasted (dashed lines) constraints from the cosmic microwave background (CMB, 1σ CL) [183], spectral distortions (FIRAS and PIXIE) [98], gravitational waves (PTA, SKA and LISA) [108], Silk damping (SD) [99], quasar light curves (QSO) [102] and PBHs (the thin and thick orange lines correspond to Ref. [121] and [126], respectively). The red shaded region is the result of this work. It shows upper limits from PBH abundance for the range of profiles with shape parameter $\alpha \in [0.15, 30.0]$, considering the most recent constraints on the maximum allowed fraction of PBHs. We report our constraint for PBHs masses ranging from $M_{\rm PBH} = 10^{-17}\ M_\odot$ ($k_t \simeq 10^{15}$ Mpc^{-1}) to $M_{\rm PBH} = 10^{3}\ M_\odot$ ($k_t \simeq 10^{5}$ Mpc^{-1}).

where $a_{\rm eq}$ and $t_{\rm eq}$ are the scale factor and cosmic time at matter-radiation equality, respectively, and k_t is related to the typical scale of the collapsing perturbation (see § 4.2). Notice that relaxing this assumption does not have any impact on the constraint itself, in fact different choices of $(\delta_I - \delta_{I,c})$ induce a rescaling in the relation linking the CPBH mass to the characteristic scale of the perturbation that generate it. Notice that a factor 10 of difference in $(\delta_I - \delta_{I,c})$ generates a factor 3 of difference in $M_{\rm PBH}$, therefore the connection between typical scales of the perturbation and the CPBHS masses is not extremely sensitive to changes in the value of the critical threshold.

In the following we will explicitly consider two extreme and one intermediate cases,

$\alpha = 0.15$, $\alpha = 1$ and $\alpha = 30$, corresponding to very steep, a so-called "Mexican-hat" shape and very flat peaks, respectively. In figure 6 we show the maximum amplitude of the primordial curvature power spectrum computed using equation (6.1) along with the previous upper bound obtained using an approximated version of this procedure [121, 126] and current and future upper bounds coming from different observables[16]. This should be interpreted as the upper envelope of a family of spikes in the primordial curvature power spectrum each of which generates CPBHs of a given (monochromatic) mass falling in the range $10^{-17}\ M_\odot < M_{\rm PBH} < 10^3\ M_\odot$.

Compared to previous analyses, our more accurate procedure, which reduces the number of assumptions, gives stronger constraints on the maximum amplitude of the power spectrum. The improvement is approximately one order of magnitude on the scales of interest, from 10^5 Mpc^{-1} to 10^{15} Mpc^{-1}, with tighter constraints for steeper profiles. In figure 6 the red band includes all the peaks profiles considered here, for the maximum fraction of dark matter in PBHs $f_{\rm PBH}^{\rm max}$ allowed by observations (see e.g., figure 1 of Ref. [105]).

Even if the observational limits on $f_{\rm PBH}(M_{\rm PBH})$ are very irregular and vary of several orders of magnitude between different masses, these differences are almost erased in figure 6 because at leading order $\sigma_0 \propto (-\log f_{\rm PBH})^{-1/2}$, as can be estimated using the Press-Schechter result. Therefore the improvements on the modelling are much more important than improvements on the observational constraints. Moreover, given that abundance constraints for PBHs with extended mass distributions are typically of the same order of magnitude of those for monochromatic ones [60–62], the use of the former will not shift significantly our predictions.

Figure 6 also shows that the range of power spectrum amplitudes needed to generate PBHs as (a component of) the dark matter, can be probed by future experiments, as SKA and LISA. This enables interesting synergies between these different experiments and probes. For example, in case of PBHs detection, of, say, $\sim 1\ M_\odot$ by LIGO, if these are to be CPBHs then SKA should see the signature of the corresponding stochastic background of gravitational waves generated by large curvature fluctuations. A non-detection of this signal on the other hand would indicate a different origin for PBHs, such as generation by topological defects.

On the other hand, the weak sensitivity to the abundance fraction $f_{\rm PBH}$ already suggests that the existence of one single CPBH in our Universe is not compatible with a scale-invariant curvature power spectrum. The fraction of dark matter made of a single PBH can be written as

$$f_{\rm PBH}^{\rm single} = \frac{\rho_{\rm PBH,0}}{\rho_{\rm dm,0}} = \frac{n_{\rm PBH} M_{\rm PBH}}{\rho_{\rm dm,0}} = \frac{M_{\rm PBH}/V_U}{\rho_{\rm dm,0}}, \tag{6.6}$$

where V_U is the proper volume of the Universe[17]. Typical values of $f_{\rm PBH}^{\rm single}$ ranges form $f_{\rm PBH}^{\rm single} = 3.2 \times 10^{-39}$ for $M_{\rm PBH} = 10^{-17}\ M_\odot$ to $f_{\rm PBH}^{\rm single} = 3.2 \times 10^{-19}$ for $M_{\rm PBH} = 10^3\ M_\odot$. In figure 7 we show the minimum amplitude of the primordial power spectrum necessary for generating

[16] To compute certain constraints, for instance those coming from spectral distortions and GWs, it is necessary to assume a shape of the primordial curvature power spectrum. We refer the interested reader to Ref. [108], where the change in the constraints assuming different power spectra shapes is shown. Since many of these constraints are forecast and the specifics of the instruments are unknown, in this work we use the curves found in Ref. [108], obtained assuming a curvature power spectrum that grows as $\mathcal{P}_\zeta(k) \propto k^4$.

[17] The proper volume of the Universe is given by $V_U = 4\pi \int_0^\infty dz \frac{\chi^2(z)}{(1+z)^3 H(z)} \simeq 10^{11}$ Mpc^3, where χ is the comoving distance, and it is approximately 100 times smaller than the comoving volume of the Universe $V_c = 4\pi\chi^3(\infty)/3 \simeq 10^{13}$ Mpc^3.

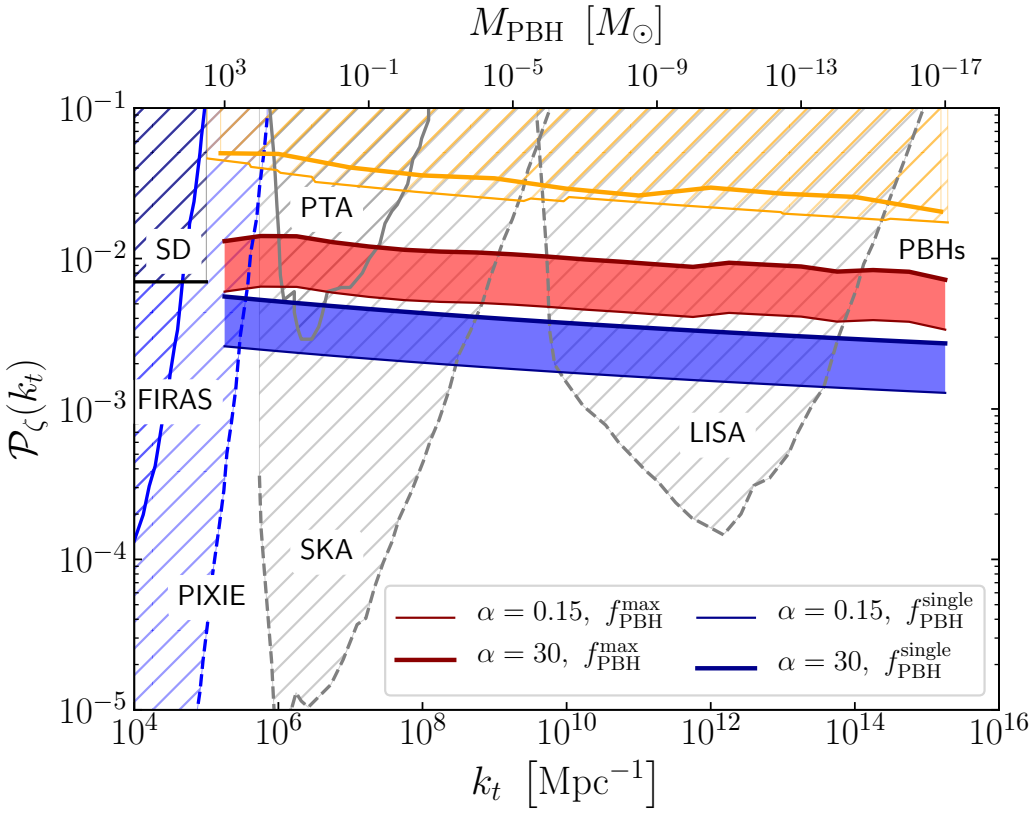

Figure 7: Same constraints of figure 6. Constraints from PBH abundance obtained using our methodology are indicated by the red shaded region and they assume the maximum abundance allowed by observations ($f_{\rm PBH} = f_{\rm PBH}^{\rm max}$), while the blue shaded region represents the constraints for the case where there is only one PBH in our Universe, i.e., $f_{\rm PBH} = f_{\rm PBH}^{\rm single}$.

a single PBH in the whole Universe, also in this case assuming a spike in the primordial curvature power spectrum.

Thus, even the existence of one single CPBH in the whole Universe is strongly incompatible, by orders of magnitude, with a simple scale invariant power spectrum at the level predicted by CMB observations (and extrapolated to these small scales). Therefore the detection of one single CPBH will reveal a completely different regime in the inflationary dynamic: it will indicate that the power spectrum has to rise from $\mathcal{P}_\zeta \simeq 10^{-9}$ to $\mathcal{P}_\zeta \simeq 10^{-3} - 10^{-2}$, almost independently from the abundance of these objects, if they exist at all. Conversely, a null result by future experiments (SKA or LISA) in their target region of Fig. 6 will rule out the possibility that PBHs might have formed via the collapse of primordial fluctuations.

Moreover, by using equation (6.1), we can also compute the shape of the spike for modes $k \gtrsim k_t$ comparable to or slightly larger than the typical mode k_t. As we show in figure 8, the power spectrum to the right of the spike becomes increasingly steeper when α increases, i.e., when the profile becomes flatter. Determining the shape of the power spectrum allow us to determine the shape parameter α, which together with the peak amplitude $\mathcal{P}_\zeta(k_t)$

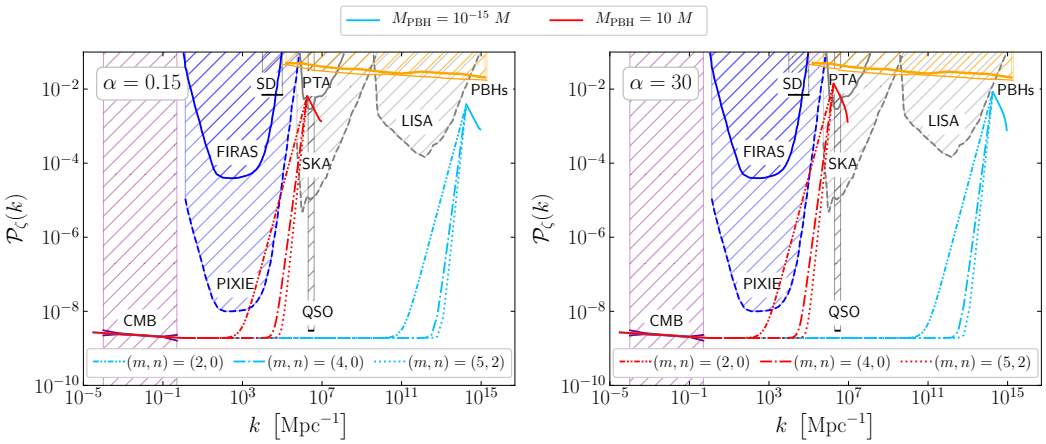

Figure 8: Shape of the reconstructed primordial curvature power spectra for steep (*left panel*) and flat profiles (*right panel*). In both cases we report the profile for $M_{\rm PBH} = 10^{-15}\ M_\odot$ (light blue line) and $M_{\rm PBH} = 10\ M_\odot$ (red line). To the right of the peak, the profile is reconstructed using equation (6.1), and to the left is computed assuming different model for the growth of the power spectrum (see text for details).

fix σ_0, thus the abundance $f_{\rm PBH}$ of CPBHs produced by the spike in the primordial curvature power spectrum. Therefore, without knowing the shape of the spike, it is not possible to uniquely determine if CPBHs form a relevant fraction of dark matter.

In figure 8 we show possible shapes of the curvature power spectrum profile from cosmological scales up to the scale of the peak. At cosmological scales ($k \lesssim 1\ \mathrm{Mpc}^{-1}$) the primordial curvature power spectrum is very well constrained to be almost scale invariant, namely $\mathcal{P}_\zeta(k) = A_s\,(k/k_{\rm pivot})^{n_s-1}$, where A_s is the scalar perturbations amplitude, n_s is the scalar tilt and $k_{\rm pivot}$ is the pivot scale[18]. At intermediate scales ($1\ \mathrm{Mpc}^{-1} \lesssim k \lesssim k_t$), the primordial curvature power spectrum determines the clustering properties of CPBHs [193, 196–201]. Since a full modelling of this goes beyond the scope of this paper, we phenomenologically parametrise the power spectrum in this range of scales using the formula $\mathcal{P}_\zeta^{(m,n)}(k) = Bk^m \log^n(k) + C$, where B and C are fitting parameters. Ref. [108] claimed that the choice $(m,n) = (4,0)$ represents the steepest rise of the primordial power spectrum in the context of single-field inflation, however it was later shown that an even steeper rise, characterized by the parameters $(m,n) = (5,2)$, is also possible [203]. We show in figure 8 both options, along with a third one, characterized by a milder rise $(m,n) = (2,0)$. These different curves effectively change the clustering properties of CPBHs which can in principle be determined observationally. As stated previously, to compute some of these constraints we need to assume a shape of the curvature power spectrum. The constraints reported in the figure are obtained in Ref. [108] for the $(4,0)$ case. While we expect that in the $(5,2)$ case the constraints do not change significantly, the amount of change in the shallower growth case $(2,0)$ might be larger.

In conclusion, we summarize here the relevant steps to follow to reconstruct both amplitude and shape of the primordial curvature power spectrum:

[18] According to the latest Planck collaboration results [202], we have $\log(10^{10} A_s) = 3.047 \pm 0.014$ and $n_s = 0.9665 \pm 0.0038$, measured with $k_{\rm pivot} = 0.05\ \mathrm{Mpc}^{-1}$.

1. choose an overdensity peak profile. In principle this should not be an arbitrary choice but in the absence of a complete prediction for the peak profile we advocate using one from the family of equation (3.5);

2. use peak theory's result in equation (5.14) to connect the overdensity peak profile and the two-point correlation function, thus the power spectrum combining equations (4.15) and (5.15);

3. in absence of a exact prediction of the non-linear transfer function $\widehat{\mathcal{T}}_{\rm NL}$, correct the linear one using the numerical factors calibrated on the numerical simulations. For the family of profiles we adopted, these values reads as $\widehat{\mathcal{T}}_{\rm NL}/\widehat{\mathcal{T}}_{\rm LIN} \simeq 1.8,\ 1.5,\ 1.2$ for profiles characterised by $\alpha = 0.15,\ 1.0,\ 30.0$;

4. after estimating the spectral parameters $\gamma(\tau_m)$ and $R_\star(\tau_m)$ from the profile shape, compute the variance at horizon crossing $\sigma_0(\tau_m)$ by solving equation (6.4). The amplitude of the peak (in the ν variable) has to be computed using numerical simulations. The PBHs abundance value $f_{\rm PBH}$ has to be set for the mass of the corresponding compact object which is related to the horizon crossing time via, for instance, equation (6.5);

5. finally, the peak maximum amplitude of figures 6 and 7 is obtained evaluating equation (6.1) at the wavemode $k_t = r_t^{-1}$;

6. the peak shape (e.g., red and cyan lines in figure 8) is obtained by evaluating equation (6.1) at wavemodes $k_t \leq k \leq 5k_t$ for scales smaller than the typical scale of the perturbation. For scales greater than the typical scale of the perturbation, match the $\mathcal{P}_\zeta$ at maximum to one of our $\mathcal{P}_\zeta^{(m,n)}$ models.

7 Conclusions

In the model where Primordial Black Holes (PBHs) form from large primordial curvature perturbations, CPBHs, PBH abundance can be used to set limits on the amplitude of the primordial power spectrum of perturbations on scales that are not easily accessible by other probes. However, making this connection requires a detailed modelling of PBHs collapse and formation in a cosmological context. We improve upon previous literature by eliminating a series of approximations used so far. It turns out that the accuracy in the modelling is (much) more important than the precision on the constraints on the PBH abundance, further motivating our effort.

In this work we set the connection between primordial power spectrum and PBH abundance on solid theoretical grounds. To achieve this goal we have, for the first time, combined three key inputs to the problem: *(i)* the numerical relativistic simulations, to assess the conditions under which CPBHs of a given mass form; *(ii)* the cosmology connection, to link the properties of individual overdensity peaks able to create CPBHs to the statistics of the underlying cosmological random field; and *(iii)* Peak theory, to interpret PBH abundance in terms of a primordial amplitude of the power spectrum of a cosmological density field.

Our major results can be summarised as follows. The first four results are methodological, the last two are new constraints.

1. Full non-linear results for the evolution of a curvature perturbation must be used, for which numerical simulations are crucial. Even if at initial time the ζ-curvature perturbation (eventually giving rise to a CPBH) and its gradients are small (and therefore

the equations can be linearised), at horizon crossing this is not the case any more. In fact, using a linear approximation underestimates the real size of the perturbation (and hence the mass enclosed in the horizon) by a relatively large factor (up to ~ 6), depending on the shape of the perturbation: steeper perturbation profiles are most dramatically affected (see § 3).

2. There are three scales involved in the problem to be compared to the horizon crossing scale of the perturbation. Two of which are physical, one is a mathematical requirement. One (small) scale is the one necessary to define a smoothing scale to make the underlying overdensity field at least differentiable and to define in it peaks and troughs. This scale is also necessary to define finite spectral moments of the field. One larger scale is the size of the sound horizon, below which pressure gradients smooth out perturbations. Finally scales well above the horizon at all times during the collapse should not influence the dynamics. The first scale is not physical, it is a mathematical operation and we have some freedom to decide what "smoothing" should be used. We argue that it should be smaller than the typical scale of the perturbation of interest in such a way that its specific choice should not influence the description of the dynamical evolution of a perturbation. The second scale is instead physical: pressure effects damp perturbations on scales smaller than the sound horizon. At horizon crossing this is comparable to the size of the perturbation itself. In our approach this is accounted for as the evolution of the collapse is modelled numerically (see appendix A for details). Finally, scales that are well above the horizon at all times during formation do not influence sub-horizon dynamics. The collapse is not instantaneous so perturbations of scales above but comparable to the horizon at a given time might influence the collapse at a later time. Nevertheless, ultra-long scale perturbations associated to modes well above the horizon throughout the CPBH formation and collapse must appear as a constant background, hence should not play any role in determining whether a CPBH forms or not.

3. Non-linearities are important also in the process of smoothing. In this work we recommend to perform the smoothing in physical coordinates, to correctly include the fact the curvature might be not negligible. In this sense, there is an ambiguity on which field should be smoothed, since smoothing the curvature or the overdensity field is not equivalent, as it is in linear theory. Moreover, the importance of non-linearities suggests that also non-Gaussianities might be important, in fact we proved in § 4.3 that the two-point function of the overdensity field receives contributions from all the n-point functions of the ζ-curvature field because of the non-linear relation between overdensity and curvature.

4. While numerical simulations can follow one perturbation at the time, the Universe is filled by a superposition of perturbations. Peak theory connects the statistics of a smoothed (Gaussian) random field defined by its power spectrum to the statistical distribution of its local maxima (above a given threshold). By identifying these local maxima with peaks of initial overdensity perturbations, the results from numerical simulations (especially the conditions on the peak height for collapse to a BH) can be used to derive the abundance of collapsed objects. Not all the peaks correspond to sites where a CPBH form; numerical simulations are key in defining a threshold criterion to assess which peaks collapse and which do not. This criterion depends

also on the shape of the initial perturbation. Peak theory then enables us to connect the average shape of the peaks and its variance to the statistical properties of the random field and thus make a statistical connection to the numerical simulation results. Future improvements in Peak theory, e.g., accounting for the "black-hole-in-black-hole" problem for models characterised by a very flat power spectrum, will certainly provide an even more accurate estimate of CPBHs abundance. Inclusion of non-Gaussianities will also contribute to increase the accuracy.

5. We show in figure 6 that the modelling done in the previous steps is fundamental in determining the correct constraint on the maximum amplitude of the primordial curvature perturbations power spectrum. In particular, our more accurate approach, which resorts to less approximations, for instance in the estimation of the variance or of the window and transfer functions, yields constraints are one order of magnitude tighter than what was previously estimated, for the entire range of modes or, equivalently, for a wide range of CPBHs masses.

6. The existence of CPBHs generated from primordial perturbations, we confirm, is incompatible with a scale-invariant power spectrum as measured at cosmological scales (see figure 7). Moreover we show that the detection of one single CPBHs would signal a significant departure from the standard slow-roll inflationary scenario.

7. The method presented in this work provides also an alternative way to probe the formation mechanism of PBHs. If PBHs are detected and no boost in the primordial curvature power spectrum is found by SKA or LISA, for instance by detecting a gravitational waves background generated by the same large scalar perturbation that created the PBHs, then an alternative PBH formation mechanism must be at play, e.g., cosmic topological defects. In this context it is crucial to find new ways to probe the origin (end-point of stellar evolution or primordial) of BHs detected by current and future gravitational waves observatories, for instance cross-correlating galaxy and gravitational waves maps [204–206], measuring BHs binaries eccentricity [207], the BH mass function [208, 209] and the BHs merger rate [44, 46], or using fast radio burst [210].

8. While here we have concentrated on scales comparable to the typical peak size, in principle our method can be extended to constrain larger scales, in the intermediate regime between standard cosmological scales and typical peaks size, via primordial clustering of PBHs [193, 196–201]. We have illustrated this in figure 8 and will be presented elsewhere.

This paper highlights that the details of the connection between the limits on the PBHs abundance, $f_{\rm PBH}$, and the primordial curvature power spectrum are much more important than the limits on the abundance themselves. Nevertheless many of the results presented in this work can be applied to estimate the CPBHs abundance from a given primordial curvature power spectrum, i.e., the way back. In particular, our work covers some key aspects up to the time of CPBHs formation. However there are many others subtleties involved in that estimation, for instance the modelling of processes involving the CPBHs from the time of formation to today, e.g., the modelling of CPBHs accretion or CPBHs clustering, that are not addressed. For this reason the way back is a very delicate issue. Even if our work does not treat those aspects, we believe it is of value as it still provides the first key steps to obtain the correct CPBHs abundance today.

To conclude, the results presented in this work represent a remarkable example of how both the existence and the non-existence of one of the most popular dark matter candidates can be used in cosmology. In particular, PBHs have the potential to probe 10 order of magnitude in terms of scales or, alternatively, 20 extra e-folds, shedding new light on the inflationary paradigm [211].

Acknowledgments

We thank Yashar Akrami, Christian Byrnes, Bernard Carr, Philippa Sarah Cole, Cristiano Germani, Anne Green and Sam Young for useful comments on the draft. Funding for this work was partially provided by the Spanish MINECO under projects AYA2014-58747-P AEI/FEDER, UE, and MDM-2014-0369 of ICCUB (Unidad de Excelencia María de Maeztu). AK was supported by Erasmus+Trainership scholaship and by MDM-2014-0369 of ICCUB (Unidad de Excelencia María de Maeztu). AK also acknowledges the Netherlands Organisation for Scientific Research (NWO) for support in the latest stages of the work. NBe is supported by the Spanish MINECO under grant BES-2015-073372. AR has received funding from the People Programme (Marie Curie Actions) of the European Union H2020 Programme under REA grant agreement number 706896 (COSMOFLAGS). NBa, DB and SM acknowledge partial financial support by ASI Grant No. 2016-24-H.0. IM has been supported by FPA2016-76005-C2-2-P,MDM-2014-0369 of ICCUB (Unidad de Excelencia Maria deMaeztu), AGAUR 2014-SGR-1474. LV acknowledges support by European Union's Horizon 2020 research and innovation programme ERC (BePreSySe, grant agreement 725327).

A Numerical simulations

The results for the threshold of PBH formation used in this paper to reconstruct the shape of the power spectrum, which allows PBHs to account for the whole dark matter, have been obtained with numerical simulation of gravitational collapse, stating from the initial conditions described in § 3.1. The numerical code used is the same of Refs. [133–137], which has been fully described previously and therefore we give only a brief outline of it here.

It is an explicit Lagrangian hydrodynamics code with the grid designed for calculations in an expanding cosmological background. The basic grid uses logarithmic spacing in a mass-type comoving coordinate, allowing it to reach out to very large radii while giving finer resolution at small radii necessary to have a good resolution of the initial perturbation. The initial conditions – initial data obtained as numerical solutions – are specified on a space-like slice at constant initial cosmic time $t_{\rm ini}$ defined as $a_{\rm ini}H_{\rm ini}\tilde{r}_m = 10$ while the outer edge of the grid has been placed at $90R_m$ (where $\tilde{r}_m$ and R_m have been defined in § 3.2), to ensure that there is no causal contact between it and the perturbed region during the time of the calculations. The initial data are evolved using the Misner-Sharp-Hernandez equations so as to generate a second set of initial data on an initial null slice which are then evolved using the Hernandez-Misner equations. During the evolution, the grid is modified with an adaptive mesh refinement scheme (AMR), built on top of the initial logarithmic grid, to provide sufficient resolution to follow black hole formation down to extremely small values of $(\delta_I - \delta_{I,c})$.

The critical threshold $\delta_{I,c}$ is found from the evolution of $2M/R$ as function of time, looking at the evolution of the peak of this ratio: when $\delta_I > \delta_{I,c}$, the peak is increasing during the collapse, reaching the condition for the apparent horizon $R(r,t) = 2M(r,t)$ identifying

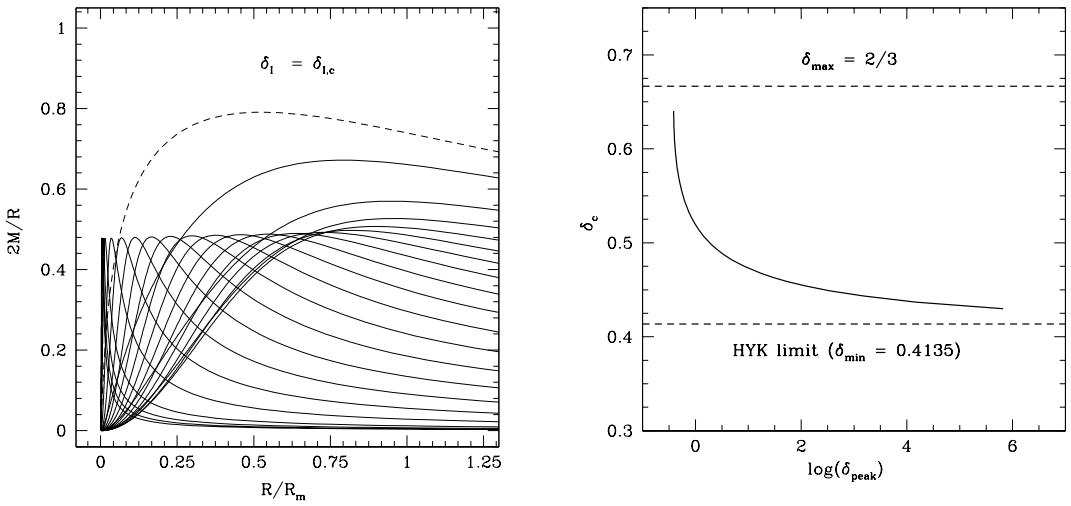

Figure 9: *Left panel:* dynamical behaviour of $2M/R$ against R/R_m plotted at different time-slice for the critical solution of a zero mass black hole when $\delta_I = \delta_{I,c}$ obtained from equation (3.12) when $\alpha = 1$ (Mexican-Hat shape). The dashed line corresponds to the initial time-slice, and the peak of $2M/R$ is initially decreasing when the perturbation is still expanding, reaching afterwards nearly equilibrium state moving inward when the perturbation is collapsing. Figure taken from Ref. [135]. *Right panel:* numerical behaviour of the critical threshold $\delta_{I,c}$ against the corresponding behaviour of the critical peak amplitude $\delta_{\rm peak,0}$ for different shapes ($0.15 \leq \alpha \leq 30$). Figure taken from Ref. [137].

the formation of a BH (see e.g., Ref. [140, 141]), while when $\delta_I < \delta_{I,c}$, the peak is decreasing, no apparent horizon forms and the collapsing overdensity bounces into the expanding Friedmann-Robertson-Walker Universe. In the left panel of figure 9 we show the behaviour of $2M/R$ when $\delta_I \simeq \delta_{I,c}$, where the dashed line is the time slice of the initial conditions. During the first stage of the evolution the perturbation is still expanding and the peak is decreasing, as can be seen from the following time slices, while when the perturbation starts to collapse, the peak of $2M/R$ is in equilibrium, moving towards the centre with an almost constant value, because of the very close equilibrium between gravity and pressure one has at the threshold ($\delta_I \simeq \delta_{I,c}$). During this nearly equilibrium phase, matter is spread outward from a relativistic wind, keeping the shrinking region with an almost constant compactness (see Ref. [135] for more details).

As we have seen in § 3.2, $\delta_I(r_m, t_m) \simeq (2M/R)_{\rm peak}$ and one can calculate the amplitude of $\delta_{I,c}$ looking for this equilibrium solution characterized by self-similar behaviour. This explains also the nature of the critical collapse characterizing PBH formation when $\delta_I \simeq \delta_{I,c}$, with the mass spectrum given by the scaling law of equation (3.12) (see Ref. [136] for more details).

In the right panel of figure 9 we can see the numerical relation between the threshold $\delta_{I,c}$ and the corresponding critical value of the peak amplitude $\delta_{\rm peak}$ for cosmological perturbations with the energy density profile obtained from equation (3.5), for the profile steepness parameter varying between $\alpha = 0.15$ (high $\delta_{\rm peak,0}$, low $\delta_{I,c}$), and $\alpha = 30$ (low $\delta_{\rm peak,0}$, high $\delta_{I,c}$)

corresponding to the lowest and the largest value of α for the simulated profiles, respectively.

Because we are considering here only shapes characterized by one parameter, each value of $\delta_{I,c}$ is associated to a different value of the peak amplitude $\delta_{\rm peak,0}$. The inverse behaviour between the two quantities is a key feature of the effect of the pressure gradients on the collapse, measuring the steepness of the profile, which can be simply measured by the ratio $(\tilde{r}_0/\tilde{r}_m) = (3/2)^{1/2\alpha}$ (if the profile is characterized by more than one parameter the measure of the steepness is more complicated). In general, when the profile of the compaction function is steeper, which corresponds to a broad profile of the density contrast ($\alpha \gg 1$), as one can see from figures 1 and 2, the pressure gradients modify significantly the shape during the non-linear evolution of the collapse after horizon crossing. This gives a larger value of the threshold $\delta_{I,c}$ which accounts for the additional excess of mass necessary to compensate the mass that will be lost during the collapse, up to the maximum value of $\delta_{I,c} = 2/3$ corresponding to a top-hat shape ($\tilde{r}_0/\tilde{r}_m = 1$). On the contrary, if the profile of the compaction function is not very steep ($\alpha \lesssim 1$), which corresponds to a steep profile of the density contrast, the pressure gradients do not modify substantially the shape during the collapse, with a smaller value of $\delta_{I,c}$, bounded by the numerical value $\delta_{I,c} \simeq 0.4135$ (Harada-Yoo-Kohri limit) found analytically in Ref. [212], where the role of the pressure gradients was neglected. The connection between the shape and the value of the threshold has been carefully analysed in Ref. [137].

B Counting the relativistic degrees of freedom

In this appendix we report the exact calculation of how the energy density of radiation scales from the Early Universe until today, since it is often presented in an approximated version. We review the main steps to derive equation (5.9), more details can be found in several classical books, see e.g., Ref. [213].

Consider a thermal bath of photons with temperature T_γ. Deep in radiation-dominated era there were other relativistic species in thermal equilibrium with photons (at least all or part of Standard Model particles, depending on the temperature), each characterised by g_j internal degrees of freedom. In principle the existence of other relativistic particles decoupled from photons is possible, hence in the following we account also for them, assuming that they have a thermal distribution with temperature $T_j \neq T_\gamma$. The energy density and entropy density of the entire fluid read as

$$\rho_{\rm rad}(T_\gamma) = \frac{\pi^2}{30}\frac{(k_B T_\gamma)^4}{(\hbar c)^3} g_{\star,\rho}(T_\gamma), \qquad s_{\rm rad}(T_\gamma) = \frac{2\pi^2}{45}\frac{k_B^4 T_\gamma^3}{(\hbar c)^3} g_{\star,s}(T_\gamma), \tag{B.1}$$

where k_B is the Boltzmann constant, $\hbar$ is the reduced Planck constant, c is the speed of light and the total number of effective degrees of freedom for energy and entropy densities are defined by

$$\begin{aligned} g_{\star,\rho}(T_\gamma) &= \sum_{\rm bosons} g_j \left(\frac{T_j}{T_\gamma}\right)^4 + \frac{7}{8}\sum_{\rm fermions} g_j \left(\frac{T_j}{T_\gamma}\right)^4, \\ g_{\star,s}(T_\gamma) &= \sum_{\rm bosons} g_j \left(\frac{T_j}{T_\gamma}\right)^3 + \frac{7}{8}\sum_{\rm fermions} g_j \left(\frac{T_j}{T_\gamma}\right)^3, \end{aligned} \tag{B.2}$$

where the sum runs over relativistic species only because their contribution dominates over that of non-relativistic ones.

Number of Relativistic Neutrinos Today	$g_{\star,\rho}(T_0)$	$g_{\star,s}^{4/3}(T_0)$
0	2.00	2.52
1	2.45	3.64
2	2.91	4.86
3	3.36	6.16

Table 1: Total number of effective degrees of freedom for energy density $g_{\star,\rho}(T_0)$ and entropy density $g_{\star,s}^{4/3}(T_0)$ today. Values are obtained using equation (B.2), neutrino temperature $T_\nu/T_\gamma = (4/11)^{1/3}$ and $g_\nu = 2$ for every neutrino family.

Using the conservation of entropy $g_{\star,s}a^3T^3 = const.$ we find the scaling of temperature in an expanding Universe. Therefore the energy density of radiation at any time can be consistently related to the radiation energy density today $\rho_{\rm rad}(T_0)$ writing equation (B.1) as

$$\rho_{\rm rad}(T_\gamma) = \rho_{\rm rad}(T_0)\left(\frac{T_\gamma}{T_0}\right)^4 \frac{g_{\star,\rho}(T_\gamma)}{g_{\star,\rho}(T_0)} = \rho_{\rm rad}(T_0)\frac{g_{\star,\rho}(T_\gamma)}{g_{\star,\rho}(T_0)}\left(\frac{g_{\star,s}(T_0)}{g_{\star,s}(T_\gamma)}\right)^{4/3}\left(\frac{a_0}{a_\gamma}\right)^4, \tag{B.3}$$

where T_0 is the photon temperature today, a_0 and a_γ are the scale factors today and of when photons had temperature T_γ, respectively. This relation is then used to obtain equation (5.9). Notice that the approximation $g_{\star,\rho} \sim g_{\star,s}$ has often been taken in the literature.

Now we want to consider the neutrino contribution to equations (B.3) and (5.9). Even if we have not measured neutrino masses yet, we know from neutrino oscillation that at least two of them are massive and we measured the mass gap between different mass eigenstates [214]:

$$m_2^2 - m_1^2 = 75\ (\text{meV})^2, \qquad |m_3^2 - m_l^2| = 2519\ (\text{meV})^2, \tag{B.4}$$

where $m_l = m_1$ in the normal hierarchy scenario ($m_1 < m_2 < m_3$) while $m_l = m_2$ in the inverted hierarchy scenario ($m_3 < m_1 < m_2$). Massive neutrinos become non-relativistic around redshift $1 + z_{\rm nr} \simeq 2 \times [m_\nu/(1\ \text{meV})]$ [215], therefore in the past at least two neutrinos became non-relativistic, even when the lightest mass eigenstate is massless, i.e., when $m_1 = 0$ and $m_3 = 0$ for normal and inverted hierarchies, respectively.

In the following we assume that all the neutrinos became non-relativistic, since this happens even for reasonably low values of the lightest state, e.g., $m_\nu \simeq 1$ meV. Therefore, when considering the energy density in radiation today, we have to include only photons, corresponding to $g_{\star,\rho}(T_0) = 2$.

On the other hand, when estimating the degrees of freedom for the entropy we have to be more careful, in fact the entropy conservation argument $g_{\star,s}(T_\gamma)a_\gamma^3T_\gamma^3 = g_{\star,s}(T_{\rm nr})a_{\rm nr}^3T_{\rm nr}^3$ can be used until when neutrinos were relativistic, the temperature of the photon bath was $T_{\rm nr}$ and the scale factor $a_{\rm nr}$. Afterwards they will not contribute to the entropy, however they "disappear" without warming the photons, as it happens with particles annihilation. Therefore after the non-relativistic transition of neutrinos, photon temperature evolves as $a_{\rm nr}^3T_{\rm nr}^3 = a_0^3T_0^3$. For this reason, it is more accurate to report $g_{\star,s}(T_{\rm nr})$ in equation (B.3) or, alternatively, to compute $g_{\star,s}(T_0)$ considering neutrino as relativistic particles, i.e., $g_{\star,s}(T_0) = 3.909$.

We report in table 1 the total number of effective degrees of freedom for energy and entropy density. As it can be seen, the relative difference in assuming 0 or 1 relativistic neutrinos today is 23% and 44% for $g_{\star,\rho}$ and $g_{\star,s}^{4/3}$, respectively. On the other hand, the relative

difference we have assuming 3 relativistic neutrino becomes 68% and 144% for $g_{\star,\rho}$ and $g_{\star,s}^{4/3}$, respectively, compared to the case of no relativistic neutrinos today. In our calculation we use $g_{\star,s}(T_0) = 3.909$ and $g_{\star,\rho}(T_0) = 2.0$.

References

[1] The **LIGO Scientific Collaboration and Virgo Collaboration**, B. P. Abbott *et al.*, "Observation of Gravitational Waves from a Binary Black Hole Merger", *Phys. Rev. Lett.* **116** (Feb, 2016) 061102, arXiv:1602.03837.

[2] The **LIGO Scientific Collaboration and Virgo Collaboration**, B. P. Abbott *et al.*, "GW151226: Observation of Gravitational Waves from a 22-Solar-Mass Binary Black Hole Coalescence", *Phys. Rev. Lett.* **116** (Jun, 2016) 241103, arXiv:1606.04855.

[3] The **LIGO Scientific Collaboration and Virgo Collaboration**, B. P. Abbott *et al.*, "GW170104: Observation of a 50-Solar-Mass Binary Black Hole Coalescence at Redshift 0.2", *Phys. Rev. Lett.* **118** (Jun, 2017) 221101, arXiv:1706.01812.

[4] The **LIGO Scientific Collaboration and Virgo Collaboration**, B. P. Abbott *et al.*, "GW170608: Observation of a 19 Solar-mass Binary Black Hole Coalescence", *The Astrophysical Journal Letters* **851** no. 2, (2017) L35, arXiv:arXiv:1711.05578.

[5] The **LIGO Scientific Collaboration and Virgo Collaboration**, B. P. Abbott *et al.*, "GW170814: A Three-Detector Observation of Gravitational Waves from a Binary Black Hole Coalescence", *Phys. Rev. Lett.* **119** (Oct, 2017) 141101, arXiv:1709.09660.

[6] The **LIGO Scientific Collaboration and Virgo Collaboration**, B. P. Abbott *et al.*, "GWTC-1: A Gravitational-Wave Transient Catalog of Compact Binary Mergers Observed by LIGO and Virgo during the First and Second Observing Runs", *Phys. Rev. X* **9** (Sep, 2019) 031040, arXiv:1811.12907.

[7] T. Venumadhav, B. Zackay, J. Roulet, L. Dai, and M. Zaldarriaga, "New Binary Black Hole Mergers in the Second Observing Run of Advanced LIGO and Advanced Virgo", arXiv:1904.07214.

[8] K. Belczynski, M. Dominik, T. Bulik, R. O'Shaughnessy, C. Fryer, and D. E. Holz, "The Effect of Metallicity on the Detection Prospects for Gravitational Waves", *The Astrophysical Journal Letters* **715** no. 2, (2010) L138, arXiv:1004.0386.

[9] M. Dominik, K. Belczynski, C. Fryer, D. E. Holz, E. Berti, T. Bulik, I. Mandel, and R. O'Shaughnessy, "Double Compact Objects. I. The Significance of the Common Envelope on Merger Rates", *The Astrophysical Journal* **759** no. 1, (2012) 52, arXiv:1202.4901.

[10] M. Dominik, K. Belczynski, C. Fryer, D. E. Holz, E. Berti, T. Bulik, I. Mandel, and R. O'Shaughnessy, "Double Compact Objects. II. Cosmological Merger Rates", *The Astrophysical Journal* **779** no. 1, (2013) 72, arXiv:1308.1546.

[11] M. Dominik, E. Berti, R. O'Shaughnessy, I. Mandel, K. Belczynski, C. Fryer, D. E. Holz, T. Bulik, and F. Pannarale, "Double Compact Objects III: Gravitational-wave Detection Rates", *The Astrophysical Journal* **806** no. 2, (2015) 263, arXiv:1405.7016.

[12] K. Belczynski, D. E. Holz, T. Bulik, and R. O'Shaughnessy, "The first gravitational-wave source from the isolated evolution of two stars in the 40-100 solar mass range", *Nature* **534** (2016) 512, arXiv:1602.04531.

[13] K. Belczynski, T. Bulik, C. L. Fryer, A. Ruiter, F. Valsecchi, J. S. Vink, and J. R. Hurley, "On the Maximum Mass of Stellar Black Holes", *The Astrophysical Journal* **714** no. 2, (2010) 1217, arXiv:0904.2784.

[14] K. Belczynski, A. Heger, W. Gladysz, A. J. Ruiter, S. Woosley, G. Wiktorowicz, H.-Y. Chen, T. Bulik, R. O'Shaughnessy, D. E. Holz, C. L. Fryer, and E. Berti, "The effect of pair-instability mass loss on black-hole mergers", *A&A* **594** (2016) A97, arXiv:1607.03116.

[15] S. Bird, I. Cholis, J. B. Muñoz, Y. Ali-Haïmoud, M. Kamionkowski, E. D. Kovetz, A. Raccanelli, and A. G. Riess, "Did LIGO Detect Dark Matter?", *Phys. Rev. Lett.* **116** (May, 2016) 201301, arXiv:1603.00464.

[16] S. Clesse and J. García-Bellido, "The clustering of massive Primordial Black Holes as Dark Matter: Measuring their mass distribution with advanced LIGO", *Physics of the Dark Universe* **15** no. Supplement C, (2017) 142 – 147, arXiv:1603.05234.

[17] M. Sasaki, T. Suyama, T. Tanaka, and S. Yokoyama, "Primordial Black Hole Scenario for the Gravitational-Wave Event GW150914", *Phys. Rev. Lett.* **117** (Aug, 2016) 061101, arXiv:1603.08338.

[18] T. Chiba and S. Yokoyama, "Spin distribution of primordial black holes", *Progress of Theoretical and Experimental Physics* **2017** no. 8, (08, 2017) , arXiv:1704.06573.

[19] M. Mirbabayi, A. Gruzinov, and J. Noreña, "Spin of Primordial Black Holes", arXiv:1901.05963.

[20] V. De Luca, V. Desjacques, G. Franciolini, A. Malhotra, and A. Riotto, "The Initial Spin Probability Distribution of Primordial Black Holes", *Journal of Cosmology and Astroparticle Physics* **2019** no. 05, (May, 2019) 018, arXiv:1903.01179.

[21] G. Fragione and B. Kocsis, "Black Hole Mergers from an Evolving Population of Globular Clusters", *Phys. Rev. Lett.* **121** (Oct, 2018) 161103, arXiv:1806.02351.

[22] M. Volonteri, "Formation of supermassive black holes", *The Astronomy and Astrophysics Review* **18** no. 3, (Jul, 2010) 279–315, arXiv:1003.4404.

[23] M. A. Latif and A. Ferrara, "Formation of Supermassive Black Hole Seeds", *Publications of the Astronomical Society of Australia* **33** (2016) e051, arXiv:1605.07391.

[24] X. Fan, V. K. Narayanan, R. H. Lupton, M. A. Strauss, G. R. Knapp, R. H. Becker, R. L. White, L. Pentericci, S. K. Leggett, Z. Haiman, J. E. Gunn, Z. Ivezic, D. P. Schneider, S. F. Anderson, J. Brinkmann, N. A. Bahcall, A. J. Connolly, I. Csabai, M. Doi, M. Fukugita, T. Geballe, E. K. Grebel, D. Harbeck, G. Hennessy, D. Q. Lamb, G. Miknaitis, J. A. Munn, R. Nichol, S. Okamura, J. R. Pier, F. Prada, G. T. Richards, A. Szalay, and D. G. York, "A Survey of $z > 5.8$ Quasars in the Sloan Digital Sky Survey. I. Discovery of Three New Quasars and the Spatial Density of Luminous Quasars at $z \sim 6$", *The Astronomical Journal* **122** no. 6, (Dec, 2001) 2833–2849, arXiv:astro-ph/0108063.

[25] D. J. Mortlock, S. J. Warren, B. P. Venemans, M. Patel, P. C. Hewett, R. G. McMahon, C. Simpson, T. Theuns, E. A. Gonzáles-Solares, A. Adamson, S. Dye, N. C. Hambly, P. Hirst, M. J. Irwin, E. Kuiper, A. Lawrence, and H. J. A. Rttgering, "A luminous quasar at a redshift of z = 7.085", *Nature* **474** (Jun, 2011) 616, arXiv:1106.6088.

[26] X.-B. Wu, F. Wang, X. Fan, W. Yi, W. Zuo, F. Bian, L. Jiang, I. D. McGreer, R. Wang, J. Yang, Q. Yang, D. Thompson, and Y. Beletsky, "An ultraluminous quasar with a twelve-billion-solar-mass black hole at redshift 6.30", *Nature* **518** (Feb, 2015) 512, arXiv:1502.07418.

[27] E. Baados, B. P. Venemans, C. Mazzucchelli, E. P. Farina, F. Walter, F. Wang, R. Decarli, D. Stern, X. Fan, F. B. Davies, J. F. Hennawi, R. A. Simcoe, M. L. Turner, H.-W. Rix, J. Yang, D. D. Kelson, G. C. Rudie, and J. M. Winters, "An 800-million-solar-mass black hole in a significantly neutral Universe at a redshift of 7.5", *Nature* **553** (Jan, 2018) 473, arXiv:1712.01860.

[28] A. Katz, J. Kopp, S. Sibiryakov, and W. Xue, "Femtolensing by dark matter revisited",

Journal of Cosmology and Astroparticle Physics **2018** no. 12, (Dec, 2018) 005, arXiv:1807.11495.

[29] K. Griest, A. M. Cieplak, and M. J. Lehner, "Experimental Limits on Primordial Black Hole Dark Matter from the First 2 yr of Kepler Data", *The Astrophysical Journal* **786** no. 2, (2014) 158, arXiv:1307.5798.

[30] H. Niikura, M. Takada, N. Yasuda, R. H. Lupton, T. Sumi, S. More, A. More, M. Oguri, and M. Chiba, "Microlensing constraints on primordial black holes with Subaru/HSC Andromeda observations", *Nature Astronomy* **3** (Jun, 2019) 524–534, arXiv:1701.02151.

[31] The **EROS-2 Collaboration**, P. Tisserand *et al.*, "Limits on the Macho content of the Galactic Halo from the EROS-2 Survey of the Magellanic Clouds", *A&A* **469** no. 2, (2007) 387–404, arXiv:astro-ph/0607207.

[32] S. Calchi Novati, S. Mirzoyan, P. Jetzer, and G. Scarpetta, "Microlensing towards the SMC: a new analysis of OGLE and EROS results", *Monthly Notices of the Royal Astronomical Society* **435** no. 2, (2013) 1582–1597, arXiv:1308.4281.

[33] The **MACHO Collaboration**, C. Alcock *et al.*, "MACHO Project Limits on Black Hole Dark Matter in the 1-30 $M_{\odot}$ Range", *The Astrophysical Journal Letters* **550** no. 2, (2001) L169, arXiv:astro-ph/0011506.

[34] E. Mediavilla, J. A. Munoz, E. Falco, V. Motta, E. Guerras, H. Canovas, C. Jean, A. Oscoz, and A. M. Mosquera, "Microlensing-based Estimate of the Mass Fraction in Compact Objects in Lens Galaxies", *The Astrophysical Journal* **706** no. 2, (2009) 1451, arXiv:0910.3645.

[35] P. N. Wilkinson, D. R. Henstock, I. W. A. Browne, A. G. Polatidis, P. Augusto, A. C. S. Readhead, T. J. Pearson, W. Xu, G. B. Taylor, and R. C. Vermeulen, "Limits on the Cosmological Abundance of Supermassive Compact Objects from a Search for Multiple Imaging in Compact Radio Sources", *Phys. Rev. Lett.* **86** (Jan, 2001) 584–587, arXiv:astro-ph/0101328.

[36] M. Zumalacárregui and U. Seljak, "Limits on Stellar-Mass Compact Objects as Dark Matter from Gravitational Lensing of Type Ia Supernovae", *Phys. Rev. Lett.* **121** (Oct, 2018) 141101, arXiv:1712.02240.

[37] B. J. Carr, K. Kohri, Y. Sendouda, and J. Yokoyama, "New cosmological constraints on primordial black holes", *Phys. Rev. D* **81** (May, 2010) 104019, arXiv:0912.5297.

[38] A. Raccanelli, F. Vidotto, and L. Verde, "Effects of primordial black holes quantum gravity decay on galaxy clustering", *Journal of Cosmology and Astroparticle Physics* **2018** no. 08, (Aug, 2018) 003, arXiv:1708.02588.

[39] G. Ballesteros, J. Coronado-Blázquez, and D. Gaggero, "X-ray and gamma-ray limits on the primordial black hole abundance from Hawking radiation", arXiv:1906.10113.

[40] H. Poulter, Y. Ali-Haïmoud, J. H. M. White, and A. G. Williams, "CMB constraints on ultra-light primordial black holes with extended mass distributions", arXiv:1907.06485.

[41] P. W. Graham, S. Rajendran, and J. Varela, "Dark matter triggers of supernovae", *Phys. Rev. D* **92** (Sep, 2015) 063007, arXiv:1505.04444.

[42] D. P. Quinn, M. I. Wilkinson, M. J. Irwin, J. Marshall, A. Koch, and V. Belokurov, "On the reported death of the MACHO era", *Monthly Notices of the Royal Astronomical Society: Letters* **396** no. 1, (2009) L11–L15, arXiv:0903.1644.

[43] T. D. Brandt, "Constraints on MACHO Dark Matter from Compact Stellar Systems in Ultra-faint Dwarf Galaxies", *The Astrophysical Journal Letters* **824** no. 2, (2016) L31, arXiv:1605.03665.

[44] T. Nakamura, M. Sasaki, T. Tanaka, and K. S. Thorne, "Gravitational Waves from Coalescing Black Hole MACHO Binaries", *The Astrophysical Journal Letters* **487** no. 2, (1997) L139, arXiv:astro-ph/9708060.

[45] M. Raidal, V. Vaskonen, and H. Veermäe, "Gravitational waves from primordial black hole mergers", *Journal of Cosmology and Astroparticle Physics* **2017** no. 09, (2017) 037, arXiv:1707.01480.

[46] Y. Ali-Haïmoud, E. D. Kovetz, and M. Kamionkowski, "Merger rate of primordial black-hole binaries", *Phys. Rev. D* **96** (Dec, 2017) 123523, arXiv:1709.06576.

[47] R. Magee, A.-S. Deutsch, P. McClincy, C. Hanna, C. Horst, D. Meacher, C. Messick, S. Shandera, and M. Wade, "Methods for the detection of gravitational waves from subsolar mass ultracompact binaries", *Phys. Rev. D* **98** (Nov, 2018) 103024, arXiv:1808.04772.

[48] M. Raidal, C. Spethmann, V. Vaskonen, and H. Veermäe, "Formation and evolution of primordial black hole binaries in the early universe", *Journal of Cosmology and Astroparticle Physics* **2019** no. 02, (Feb, 2019) 018, arXiv:1812.01930.

[49] M. Ricotti, J. P. Ostriker, and K. J. Mack, "Effect of Primordial Black Holes on the Cosmic Microwave Background and Cosmological Parameter Estimates", *The Astrophysical Journal* **680** no. 2, (2008) 829, arXiv:0709.0524.

[50] D. Gaggero, G. Bertone, F. Calore, R. M. T. Connors, M. Lovell, S. Markoff, and E. Storm, "Searching for Primordial Black Holes in the radio and X-ray sky", *Phys. Rev. Lett.* **118** no. 24, (2017) 241101, arXiv:1612.00457.

[51] Y. Ali-Haïmoud and M. Kamionkowski, "Cosmic microwave background limits on accreting primordial black holes", *Phys. Rev. D* **95** (Feb, 2017) 043534, arXiv:1612.05644.

[52] V. Poulin, P. D. Serpico, F. Calore, S. Clesse, and K. Kohri, "CMB bounds on disk-accreting massive primordial black holes", *Phys. Rev. D* **96** (Oct, 2017) 083524, arXiv:1707.04206.

[53] J. L. Bernal, N. Bellomo, A. Raccanelli, and L. Verde, "Cosmological Implications of Primordial Black Holes", *Journal of Cosmology and Astroparticle Physics* **2017** no. 10, (2017) 052, arXiv:1709.07465.

[54] T. Nakama, B. Carr, and J. Silk, "Limits on primordial black holes from μ distortions in cosmic microwave background", *Phys. Rev. D* **97** (Feb, 2018) 043525, arXiv:1710.06945.

[55] A. Hektor, G. Hütsi, L. Marzola, M. Raidal, V. Vaskonen, and H. Veermäe, "Constraining primordial black holes with the EDGES 21-cm absorption signal", *Phys. Rev. D* **98** (Jul, 2018) 023503, arXiv:1803.09697.

[56] J. Manshanden, D. Gaggero, G. Bertone, R. M. T. Connors, and M. Ricotti, "Multi-wavelength astronomical searches for primordial black holes", *Journal of Cosmology and Astroparticle Physics* **2019** no. 06, (Jun, 2019) 026, arXiv:1812.07967.

[57] G. Hütsi, M. Raidal, and H. Veermäe, "Small-scale structure of primordial black hole dark matter and its implications for accretion", arXiv:1907.06533.

[58] N. Afshordi, P. McDonald, and D. N. Spergel, "Primordial Black Holes as Dark Matter: The Power Spectrum and Evaporation of Early Structures", *The Astrophysical Journal* **594** no. 2, (Aug, 2003) L71–L74, arXiv:astro-ph/0302035.

[59] R. Murgia, G. Scelfo, M. Viel, and A. Raccanelli, "Lyman-α Forest Constraints on Primordial Black Holes as Dark Matter", *Phys. Rev. Lett.* **123** (Aug, 2019) 071102, arXiv:1903.10509.

[60] N. Bellomo, J. L. Bernal, A. Raccanelli, and L. Verde, "Primordial black holes as dark matter: converting constraints from monochromatic to extended mass distributions", *Journal of Cosmology and Astroparticle Physics* **2018** no. 01, (2018) 004, arXiv:1709.07467.

[61] B. Carr, F. Kühnel, and M. Sandstad, "Primordial black holes as dark matter", *Phys. Rev. D* **94** (Oct, 2016) 083504, arXiv:1607.06077.

[62] B. Carr, M. Raidal, T. Tenkanen, V. Vaskonen, and H. Veermäe, "Primordial black hole constraints for extended mass functions", *Phys. Rev. D* **96** (Jul, 2017) 023514, arXiv:1705.05567.

[63] Y. B. Zel'dovich and I. D. Novikov, "The Hypothesis of Cores Retarded during Expansion and the Hot Cosmological Model", *Soviet Astronomy* **10** (Feb, 1967) 602.

[64] S. Hawking, "Gravitationally Collapsed Objects of Very Low Mass", *Monthly Notices of the Royal Astronomical Society* **152** no. 1, (1971) 75–78.

[65] B. J. Carr and S. W. Hawking, "Black Holes in the Early Universe", *Monthly Notices of the Royal Astronomical Society* **168** no. 2, (Aug, 1974) 399–415.

[66] G. F. Chapline, "Cosmological effects of primordial black holes", *Nature* **253** (Jan, 1975) 251.

[67] S. W. Hawking, "Black holes from cosmic strings", *Physics Letters B* **231** (Nov, 1989) 237–239.

[68] J. Garriga and M. Sakellariadou, "Effects of friction on cosmic strings", *Phys. Rev. D* **48** (Sep, 1993) 2502–2515, arXiv:hep-th/9303024.

[69] R. R. Caldwell and P. Casper, "Formation of black holes from collapsed cosmic string loops", *Phys. Rev. D* **53** (Mar, 1996) 3002–3010, arXiv:gr-qc/9509012.

[70] T. Matsuda, "Primordial black holes from cosmic necklaces", *Journal of High Energy Physics* **2006** no. 04, (2006) 017, arXiv:hep-ph/0509062.

[71] M. Lake, S. Thomas, and J. Ward, "String necklaces and primordial black holes from type IIB strings", *Journal of High Energy Physics* **2009** no. 12, (2009) 033, arXiv:0906.3695.

[72] R. R. Caldwell, H. A. Chamblin, and G. W. Gibbons, "Pair creation of black holes by domain walls", *Phys. Rev. D* **53** (Jun, 1996) 7103–7114, arXiv:hep-th/9602126.

[73] S. W. Hawking, I. G. Moss, and J. M. Stewart, "Bubble collisions in the very early universe", *Phys. Rev. D* **26** (Nov, 1982) 2681–2693.

[74] M. Crawford and D. N. Schramm, "Spontaneous generation of density perturbations in the early Universe", *Nature* **298** (1982) 538–540.

[75] I. G. Moss, "Singularity formation from colliding bubbles", *Phys. Rev. D* **50** (Jul, 1994) 676–681.

[76] S. Shandera, D. Jeong, and H. S. G. Gebhardt, "Gravitational Waves from Binary Mergers of Subsolar Mass Dark Black Holes", *Phys. Rev. Lett.* **120** (Jun, 2018) 241102, arXiv:1802.08206.

[77] P. Ivanov, P. Naselsky, and I. Novikov, "Inflation and primordial black holes as dark matter", *Phys. Rev. D* **50** (Dec, 1994) 7173–7178.

[78] J. García-Bellido, A. Linde, and D. Wands, "Density perturbations and black hole formation in hybrid inflation", *Phys. Rev. D* **54** (Nov, 1996) 6040–6058, arXiv:astro-ph/9605094.

[79] P. Ivanov, "Nonlinear metric perturbations and production of primordial black holes", *Phys. Rev. D* **57** (Jun, 1998) 7145–7154, arXiv:astro-ph/9708224.

[80] S. M. Leach, I. J. Grivell, and A. R. Liddle, "Black hole constraints on the running-mass inflation model", *Phys. Rev. D* **62** (Jul, 2000) 043516, arXiv:astro-ph/0004296.

[81] M. Drees and E. Erfani, "Running-mass inflation model and primordial black holes", *Journal of Cosmology and Astroparticle Physics* **2011** no. 04, (2011) 005, arXiv:1102.2340.

[82] M. Drees and E. Erfani, "Running spectral index and formation of primordial black hole in single field inflation models", *Journal of Cosmology and Astroparticle Physics* **2012** no. 01, (Jan, 2012) 035, arXiv:1110.6052.

[83] M. Kawasaki, N. Kitajima, and T. T. Yanagida, "Primordial black hole formation from an axionlike curvaton model", *Phys. Rev. D* **87** (Mar, 2013) 063519, arXiv:1207.2550.

[84] K. Kohri, C.-M. Lin, and T. Matsuda, "Primordial black holes from the inflating curvaton", *Phys. Rev. D* **87** (May, 2013) 103527, arXiv:1211.2371.

[85] J. Garcia-Bellido and E. Ruiz Morales, "Primordial black holes from single field models of inflation", *Physics of the Dark Universe* **18** (2017) 47–54, arXiv:1702.03901.

[86] C. Germani and T. Prokopec, "On primordial black holes from an inflection point", *Physics of the Dark Universe* **18** (2017) 6–10, arXiv:1706.04226.

[87] K. Kannike, L. Marzola, M. Raidal, and H. Veermäe, "Single field double inflation and primordial black holes", *Journal of Cosmology and Astroparticle Physics* **2017** no. 09, (Sep, 2017) 020, arXiv:1705.06225.

[88] H. Motohashi and W. Hu, "Primordial black holes and slow-roll violation", *Phys. Rev. D* **96** (Sep, 2017) 063503, arXiv:1706.06784.

[89] G. Ballesteros and M. Taoso, "Primordial black hole dark matter from single field inflation", *Phys. Rev. D* **97** (Jan, 2018) 023501, arXiv:1709.05565.

[90] O. Özsoy, S. Parameswaran, G. Tasinato, and I. Zavala, "Mechanisms for primordial black hole production in string theory", *Journal of Cosmology and Astroparticle Physics* **2018** no. 07, (Jul, 2018) 005, arXiv:1803.07626.

[91] M. Cicoli, V. A. Diaz, and F. G. Pedro, "Primordial black holes from string inflation", *Journal of Cosmology and Astroparticle Physics* **2018** no. 06, (Jun, 2018) 034, arXiv:1803.02837.

[92] I. Dalianis, A. Kehagias, and G. Tringas, "Primordial black holes from α-attractors", *Journal of Cosmology and Astroparticle Physics* **2019** no. 01, (Jan, 2019) 037, arXiv:1805.09483.

[93] N. Bhaumik and R. K. Jain, "Primordial black holes dark matter from inflection point models of inflation and the effects of reheating", arXiv:1907.04125.

[94] A. Ravenni, L. Verde, and A. J. Cuesta, "Red, Straight, no bends: primordial power spectrum reconstruction from CMB and large-scale structure", *Journal of Cosmology and Astroparticle Physics* **2016** no. 08, (2016) 028, arXiv:1605.06637.

[95] D. N. Spergel *et al.*, "First-Year Wilkinson Microwave Anisotropy Probe (WMAP) Observations: Determination of Cosmological Parameters", *The Astrophysical Journal Supplement Series* **148** (Sep, 2003) 175–194, arXiv:astro-ph/0302209.

[96] The **Planck Collaboration**, P. A. R. Ade *et al.*, "Planck 2013 results. XVI. Cosmological parameters", *A&A* **571** (Nov, 2014) A16, arXiv:1303.5076.

[97] The **Planck Collaboration**, P. A. R. Ade *et al.*, "Planck 2013 results. XXII. Constraints on inflation", *A&A* **571** (2014) A22, arXiv:1303.5082.

[98] J. Chluba, A. L. Erickcek, and I. Ben-Dayan, "Probing the Inflaton: Small-scale Power Spectrum Constraints from Measurements of the Cosmic Microwave Background Energy Spectrum", *The Astrophysical Journal* **758** no. 2, (2012) 76, arXiv:1203.2681.

[99] D. Jeong, J. Pradler, J. Chluba, and M. Kamionkowski, "Silk Damping at a Redshift of a Billion: New Limit on Small-Scale Adiabatic Perturbations", *Phys. Rev. Lett.* **113** (Aug, 2014) 061301, arXiv:1403.3697.

[100] A. S. Josan and A. M. Green, "Gamma rays from ultracompact minihalos: Potential constraints on the primordial curvature perturbation", *Phys. Rev. D* **82** (Oct, 2010) 083527, arXiv:1006.4970.

[101] T. Bringmann, P. Scott, and Y. Akrami, "Improved constraints on the primordial power spectrum at small scales from ultracompact minihalos", *Phys. Rev. D* **85** (Jun, 2012) 125027, arXiv:1110.2484.

[102] M. Karami, N. Afshordi, and J. Zavala, "Forward modelling of quasar light curves and the cosmological matter power spectrum on milliparsec scales", arXiv:1805.06984.

[103] J. García-Bellido, M. Peloso, and C. Unal, "Gravitational wave signatures of inflationary models from Primordial Black Hole dark matter", *Journal of Cosmology and Astroparticle Physics* **2017** no. 09, (Sep, 2017) 013, arXiv:1707.02441.

[104] R.-G. Cai, S. Pi, and M. Sasaki, "Gravitational Waves Induced by Non-Gaussian Scalar Perturbations", *Phys. Rev. Lett.* **122** (May, 2019) 201101, arXiv:1810.11000.

[105] N. Bartolo, V. De Luca, G. Franciolini, A. Lewis, M. Peloso, and A. Riotto, "Primordial Black Hole Dark Matter: LISA Serendipity", *Phys. Rev. Lett.* **122** (May, 2019) 211301, arXiv:1810.12218.

[106] N. Bartolo, V. De Luca, G. Franciolini, M. Peloso, D. Racco, and A. Riotto, "Testing primordial black holes as dark matter with LISA", *Phys. Rev. D* **99** (May, 2019) 103521, arXiv:1810.12224.

[107] C. Ünal, "Imprints of primordial non-Gaussianity on gravitational wave spectrum", *Phys. Rev. D* **99** (Feb, 2019) 041301, arXiv:1811.09151.

[108] C. T. Byrnes, P. S. Cole, and S. P. Patil, "Steepest growth of the power spectrum and primordial black holes", *Journal of Cosmology and Astroparticle Physics* **2019** no. 06, (Jun, 2018) 028, arXiv:1811.11158.

[109] K. Inomata and T. Nakama, "Gravitational waves induced by scalar perturbations as probes of the small-scale primordial spectrum", *Phys. Rev. D* **99** (Feb, 2019) 043511, arXiv:1812.00674.

[110] C. Yuan, Z.-C. Chen, and Q.-G. Huang, "Probing Primordial-Black-Hole Dark Matter with Scalar Induced Gravitational Waves", arXiv:1906.11549.

[111] R.-G. Cai, S. Pi, S.-J. Wang, and X.-Y. Yang, "Pulsar Timing Array Constraints on the Induced Gravitational Waves", arXiv:1907.06372.

[112] L. Lentati *et al.*, "European Pulsar Timing Array limits on an isotropic stochastic gravitational-wave background", *Monthly Notices of the Royal Astronomical Society* **453** no. 3, (08, 2015) 2576–2598, arXiv:1504.03692.

[113] Z. Arzoumanian *et al.*, "The NANOGrav Nine-year Data Set: Limits on the Isotropic Stochastic Gravitational Wave Background", *The Astrophysical Journal* **821** no. 1, (Apr, 2016) 13, arXiv:1508.03024.

[114] R. M. Shannon *et al.*, "Gravitational waves from binary supermassive black holes missing in pulsar observations", *Science* **349** no. 6255, (2015) 1522–1525, arXiv:1509.07320.

[115] C. J. Moore, R. H. Cole, and C. P. L. Berry, "Gravitational-wave sensitivity curves", *Classical and Quantum Gravity* **32** no. 1, (Dec, 2014) 015014, arXiv:1408.0740.

[116] G. H. Janssen, G. Hobbs, M. McLaughlin, C. G. Bassa, A. T. Deller, M. Kramer, K. J. Lee, C. M. F. Mingarelli, P. A. Rosado, S. Sanidas, A. Sesana, L. Shao, I. H. Stairs, B. W. Stappers, and J. P. W. Verbiest, "Gravitational wave astronomy with the SKA", *Proceedings of Science* **AASKA14** (2015) 037, arXiv:1501.00127.

[117] P. Amaro-Seoane *et al.*, "Laser Interferometer Space Antenna", arXiv:1702.00786.

[118] B. J. Carr, "The primordial black hole mass spectrum", *The Astrophysical Journal* **201** (Oct, 1975) 1–19.

[119] B. J. Carr and J. E. Lidsey, "Primordial black holes and generalized constraints on chaotic inflation", *Phys. Rev. D* **48** (Jul, 1993) 543–553.

[120] B. J. Carr, J. H. Gilbert, and J. E. Lidsey, "Black hole relics and inflation: Limits on blue perturbation spectra", *Phys. Rev. D* **50** (Oct, 1994) 4853–4867, arXiv:astro-ph/9405027.

[121] A. S. Josan, A. M. Green, and K. A. Malik, "Generalized constraints on the curvature perturbation from primordial black holes", *Phys. Rev. D* **79** (May, 2009) 103520, arXiv:0903.3184.

[122] P. S. Cole and C. T. Byrnes, "Extreme scenarios: the tightest possible constraints on the power spectrum due to primordial black holes", *Journal of Cosmology and Astroparticle Physics* **2018** no. 02, (2018) 019, arXiv:1706.10288.

[123] B. Carr, T. Tenkanen, and V. Vaskonen, "Primordial black holes from inflaton and spectator field perturbations in a matter-dominated era", *Phys. Rev. D* **96** (Sep, 2017) 063507, arXiv:1706.03746.

[124] I. Dalianis, "Constraints on the curvature power spectrum from primordial black hole evaporation", *Journal of Cosmology and Astroparticle Physics* **2019** no. 08, (Aug, 2019) 032, arXiv:1812.09807.

[125] J. Mifsud and C. van de Bruck, "Complementary probes of inflationary cosmology", arXiv:1904.09590.

[126] G. Sato-Polito, E. D. Kovetz, and M. Kamionkowski, "Constraints on the primordial curvature power spectrum from primordial black holes", arXiv:1904.10971.

[127] Y. Akrami, F. Kuhnel, and M. Sandstad, "Uncertainties in primordial black-hole constraints on the primordial power spectrum", *Physics of the Dark Universe* **19** (2018) 124 – 128, arXiv:1611.10069.

[128] D. K. Nadezhin, I. D. Novikov, and A. G. Polnarev, "The hydrodynamics of primordial black hole formation", *Sov. Astron.* **22** (Apr, 1978) 129–138.

[129] G. V. Bicknell and R. N. Henriksen, "Formation of primordial black holes", *Astrophysical Journal* **232** (Sep, 1979) 670–682.

[130] I. D. Novikov and A. G. Polnarev, "The Hydrodynamics of Primordial Black Hole Formation - Dependence on the Equation of State", *Sov. Astron.* **24** (Apr, 1980) 147–151.

[131] J. C. Niemeyer and K. Jedamzik, "Dynamics of primordial black hole formation", *Phys. Rev. D* **59** (May, 1999) 124013, arXiv:astro-ph/9901292.

[132] M. Shibata and M. Sasaki, "Black hole formation in the Friedmann universe: Formulation and computation in numerical relativity", *Phys. Rev. D* **60** (Sep, 1999) 084002, arXiv:gr-qc/9905064.

[133] I. Musco, J. C. Miller, and L. Rezzolla, "Computations of primordial black hole formation", *Classical and Quantum Gravity* **22** (2005) 1405–1424, arXiv:gr-qc/0412063.

[134] A. G. Polnarev and I. Musco, "Curvature profiles as initial conditions for primordial black hole formation", *Classical and Quantum Gravity* **24** (2007) 1405–1432, arXiv:gr-qc/0605122.

[135] I. Musco, J. C. Miller, and A. G. Polnarev, "Primordial black hole formation in the radiative era: investigation of the critical nature of the collapse", *Classical and Quantum Gravity* **26** no. 23, (2009) 235001, arXiv:0811.1452.

[136] I. Musco and J. C. Miller, "Primordial black hole formation in the early universe: critical behaviour and self-similarity", *Classical and Quantum Gravity* **30** (2013) 145009, arXiv:1201.2379.

[137] I. Musco, "The threshold for primordial black holes: dependence on the shape of the cosmological perturbations", arXiv:1809.02127.

[138] A. Escrivà, "Simulation of primordial black hole formation using pseudo-spectral methods", arXiv:1907.13065.

[139] A. Escrivà, C. Germani, and R. K. Sheth, "A universal threshold for primordial black hole formation", arXiv:1907.13311.

[140] A. Helou, I. Musco, and J. C. Miller, "Causal Nature and Dynamics of Trapping Horizons in Black Hole Collapse", *Classical and Quantum Gravity* **34** no. 13, (2017) 135012, arXiv:1601.05109.

[141] V. Faraoni, G. F. R. Ellis, J. T. Firouzjaee, A. Helou, and I. Musco, "Foliation dependence of black hole apparent horizons in spherical symmetry", *Phys. Rev. D* **95** (Jan, 2017) 024008, arXiv:1610.05822.

[142] D. S. Salopek and J. R. Bond, "Nonlinear evolution of long wavelength metric fluctuations in inflationary models", *Phys. Rev. D* **42** (Dec, 1990) 3936–3962.

[143] D. H. Lyth, K. A. Malik, and M. Sasaki, "A general proof of the conservation of the curvature perturbation", *Journal of Cosmology and Astroparticle Physics* **2005** no. 05, (2005) 004, arXiv:astro-ph/0411220.

[144] J. E. Lidsey, A. R. Liddle, E. W. Kolb, E. J. Copeland, T. Barreiro, and M. Abney, "Reconstructing the inflaton potential – an overview", *Rev. Mod. Phys.* **69** (Apr, 1997) 373–410, arXiv:astro-ph/9508078.

[145] D. H. Lyth and A. Riotto, "Particle physics models of inflation and the cosmological density perturbation", *Physics Reports* **314** no. 1, (1999) 1 – 146, arXiv:hep-ph/9807278.

[146] K. A. Malik and D. Wands, "Cosmological perturbations", *Physics Reports* **475** no. 1, (2009) 1 – 51, arXiv:0809.4944.

[147] E. Komatsu, K. M. Smith, J. Dunkley, C. L. Bennett, B. Gold, G. Hinshaw, N. Jarosik, D. Larson, M. R. Nolta, L. Page, D. N. Spergel, M. Halpern, R. S. Hill, A. Kogut, M. Limon, S. S. Meyer, N. Odegard, G. S. Tucker, J. L. Weiland, E. Wollack, and E. L. Wright, "Seven-Year Wilkinson Microwave Anisotropy Probe (WMAP) Observations: Cosmological Interpretation", *The Astrophysical Journal Supplement Series* **192** no. 2, (Jan, 2011) 18, arXiv:1001.4538.

[148] The **Planck Collaboration**, P. A. R. Ade *et al.*, "Planck 2013 results. XXIV. Constraints on primordial non-Gaussianity", *A&A* **571** (2014) A24, arXiv:1303.5084.

[149] T. Harada, C.-M. Yoo, T. Nakama, and Y. Koga, "Cosmological long-wavelength solutions and primordial black hole formation", *Phys. Rev. D* **91** (Apr, 2015) 084057, arXiv:1503.03934.

[150] A. Komar, "Covariant Conservation Laws in General Relativity", *Phys. Rev.* **113** (Feb, 1959) 934–936.

[151] H. Kodama, "Conserved Energy Flux for the Spherically Symmetric System and the Backreaction Problem in the Black Hole Evaporation", *Progress of Theoretical Physics* **63** no. 4, (04, 1980) 1217–1228.

[152] C. W. Misner and D. H. Sharp, "Relativistic Equations for Adiabatic, Spherically Symmetric Gravitational Collapse", *Phys. Rev.* **136** (Oct, 1964) B571–B576.

[153] J. C. Niemeyer and K. Jedamzik, "Near-Critical Gravitational Collapse and the Initial Mass Function of Primordial Black Holes", *Phys. Rev. Lett.* **80** (Jun, 1998) 5481–5484, arXiv:astro-ph/9709072.

[154] M. W. Choptuik, "Universality and scaling in gravitational collapse of a massless scalar field", *Phys. Rev. Lett.* **70** (Jan, 1993) 9–12.

[155] K. Jedamzik, "Primordial black hole formation during the QCD epoch", *Phys. Rev. D* **55** (May, 1997) R5871–R5875, arXiv:astro-ph/9605152.

[156] K. Jedamzik and J. C. Niemeyer, "Primordial black hole formation during first-order phase transitions", *Phys. Rev. D* **59** (May, 1999) 124014, arXiv:astro-ph/9901293.

[157] C. T. Byrnes, M. Hindmarsh, S. Young, and M. R. S. Hawkins, "Primordial black holes with an accurate QCD equation of state", *Journal of Cosmology and Astroparticle Physics* **2018** no. 08, (Aug, 2018) 041, arXiv:1801.06138.

[158] B. Carr, S. Clesse, J. García-Bellido, and F. Kuhnel, "Cosmic Conundra Explained by Thermal History and Primordial Black Holes", arXiv:1906.08217.

[159] D. W. Neilsen and M. W. Choptuik, "Critical phenomena in perfect fluids", *Classical and Quantum Gravity* **17** no. 4, (2000) 761, arXiv:gr-qc/9812053.

[160] M. Kawasaki and H. Nakatsuka, "Effect of nonlinearity between density and curvature perturbations on the primordial black hole formation", *Phys. Rev. D* **99** (Jun, 2019) 123501, arXiv:1903.02994.

[161] V. De Luca, G. Franciolini, A. Kehagias, M. Peloso, A. Riotto, and C. Ünal, "The Ineludible non-Gaussianity of the Primordial Black Hole Abundance", *Journal of Cosmology and Astroparticle Physics* **2019** no. 07, (Jul, 2019) 048, arXiv:1904.00970.

[162] S. Young, I. Musco, and C. T. Byrnes, "Primordial black hole formation and abundance: contribution from the non-linear relation between the density and curvature perturbation", arXiv:1904.00984.

[163] W. H. Press and P. Schechter, "Formation of Galaxies and Clusters of Galaxies by Self-Similar Gravitational Condensation", *The Astrophysical Journal* **187** (Feb, 1974) 425–438.

[164] S. O. Rice, "Mathematical Analysis of Random Noise", *Bell System Technical Journal* **23** no. 3, (1944) 282–332.

[165] R. J. Adler, *The Geometry of Random Fields*. 1981.

[166] J. M. Bardeen, J. R. Bond, N. Kaiser, and A. S. Szalay, "The statistics of peaks of Gaussian random fields", *The Astrophysical Journal* **304** (May, 1986) 15.

[167] K. Ando, K. Inomata, and M. Kawasaki, "Primordial black holes and uncertainties in the choice of the window function", *Phys. Rev. D* **97** (May, 2018) 103528, arXiv:1802.06393.

[168] S. Young, "The primordial black hole formation criterion re-examined: parameterisation, timing, and the choice of window function", arXiv:1905.01230.

[169] L. Verde, R. Jimenez, F. Simpson, L. Alvarez-Gaume, A. Heavens, and S. Matarrese, "The bias of weighted dark matter haloes from peak theory", *Monthly Notices of the Royal Astronomical Society* **443** no. 1, (2014) 122–137, arXiv:1404.2241.

[170] S. Dodelson, *Modern Cosmology*. 2003.

[171] D. Blais, T. Bringmann, C. Kiefer, and D. Polarski, "Accurate results for primordial black holes from spectra with a distinguished scale", *Phys. Rev. D* **67** (Jan, 2003) 024024, arXiv:astro-ph/0206262.

[172] C.-M. Yoo, T. Harada, J. Garriga, and K. Kohri, "Primordial black hole abundance from random Gaussian curvature perturbations and a local density threshold", *Progress of Theoretical and Experimental Physics* **2018** no. 12, (Dec, 2018) , arXiv:1805.03946.

[173] S. Young and C. T. Byrnes, "Long-short wavelength mode coupling tightens primordial black hole constraints", *Phys. Rev. D* **91** (Apr, 2015) 083521, arXiv:1411.4620.

[174] S. Young and C. T. Byrnes, "Signatures of non-gaussianity in the isocurvature modes of primordial black hole dark matter", *Journal of Cosmology and Astroparticle Physics* **2015** no. 04, (Apr, 2015) 034, arXiv:1503.01505.

[175] S. Young, D. Regan, and C. T. Byrnes, "Influence of large local and non-local bispectra on primordial black hole abundance", *Journal of Cosmology and Astroparticle Physics* **2016** no. 02, (Feb, 2016) 029, arXiv:1512.07224.

[176] G. Franciolini, A. Kehagias, S. Matarrese, and A. Riotto, "Primordial black holes from inflation and non-Gaussianity", *Journal of Cosmology and Astroparticle Physics* **2018** no. 03, (2018) 016, arXiv:1801.09415.

[177] V. Atal and C. Germani, "The role of non-gaussianities in Primordial Black Hole formation", *Physics of the Dark Universe* **24** (2019) 100275, arXiv:1811.07857.

[178] S. Passaglia, W. Hu, and H. Motohashi, "Primordial black holes and local non-Gaussianity in canonical inflation", *Phys. Rev. D* **99** (Feb, 2019) 043536, arXiv:1812.08243.

[179] A. Kehagias, I. Musco, and A. Riotto, "Non-Gaussian Formation of Primordial Black Holes: Effects on the Threshold", arXiv:1906.07135.

[180] H. V. Peiris *et al.*, "First-Year Wilkinson Microwave Anisotropy Probe (WMAP) Observations: Implications For Inflation", *The Astrophysical Journal Supplement Series* **148** (Sep, 2003) 213–231, arXiv:astro-ph/0302225.

[181] E. Komatsu *et al.*, "First-Year Wilkinson Microwave Anisotropy Probe (WMAP) Observations: Tests of Gaussianity", *The Astrophysical Journal Supplement Series* **148** (Sep, 2003) 119–134, arXiv:astro-ph/0302223.

[182] The **Planck Collaboration**, P. A. R. Ade *et al.*, "Planck 2015 results. XVII. Constraints on primordial non-Gaussianity", *A&A* **594** (Sept., 2016) A17, arXiv:1502.01592.

[183] The **Planck Collaboration**, Y. Akrami *et al.*, "Planck 2018 results. X. Constraints on inflation", arXiv:1807.06211.

[184] N. Bellomo, N. Bartolo, R. Jimenez, S. Matarrese, and L. Verde, "Measuring the energy scale of inflation with large scale structures", *Journal of Cosmology and Astroparticle Physics* **2018** no. 11, (Nov, 2018) 043, arXiv:1809.07113.

[185] N. Bartolo, S. Matarrese, and A. Riotto, "The full second-order radiation transfer function for large-scale CMB anisotropies", *Journal of Cosmology and Astroparticle Physics* **2006** no. 05, (May, 2006) 010, arXiv:astro-ph/0512481.

[186] N. Bartolo, S. Matarrese, and A. Riotto, "CMB anisotropies at second-order II: analytical approach", *Journal of Cosmology and Astroparticle Physics* **2007** no. 01, (Jan, 2007) 019, arXiv:astro-ph/0610110.

[187] N. Bartolo, S. Matarrese, O. Pantano, and A. Riotto, "Second-order matter perturbations in a ΛCDM cosmology and non-Gaussianity", *Classical and Quantum Gravity* **27** no. 12, (May, 2010) 124009, arXiv:1002.3759.

[188] C. Byrnes, I. Musco, S. Young, and N. Bellomo, "Non-linear transfer function", arXiv:ToAppear.

[189] C. Germani and I. Musco, "Abundance of Primordial Black Holes Depends on the Shape of the Inflationary Power Spectrum", *Phys. Rev. Lett.* **122** (Apr, 2019) 141302, arXiv:1805.04087.

[190] T. Nakama, J. Silk, and M. Kamionkowski, "Stochastic gravitational waves associated with the formation of primordial black holes", *Phys. Rev. D* **95** (Feb, 2017) 043511, arXiv:1612.06264.

[191] T. Nakama and Y. Wang, "Do we need fine-tuning to create primordial black holes?", *Phys. Rev. D* **99** (Jan, 2019) 023504, arXiv:1811.01126.

[192] L. Husdal, "On Effective Degrees of Freedom in the Early Universe", *Galaxies* **4** no. 4, (2016) , arXiv:1609.04979.

[193] A. Moradinezhad Dizgah, G. Franciolini, and A. Riotto, "Primordial Black Holes from Broad Spectra: Abundance and Clustering", arXiv:1906.08978.

[194] A. Paranjape and R. K. Sheth, "Peaks theory and the excursion set approach", *Monthly Notices of the Royal Astronomical Society* **426** no. 4, (11, 2012) 2789–2796, arXiv:1206.3506.

[195] A. Dekel, "Imprints of the Damping of Adiabatic Perturbations", *A&A* **101** (Aug, 1981) 79.

[196] J. R. Chisholm, "Clustering of primordial black holes: Basic results", *Phys. Rev. D* **73** (Apr, 2006) 083504, arXiv:astro-ph/0509141.

[197] J. R. Chisholm, "Clustering of primordial black holes. II. Evolution of bound systems", *Phys. Rev. D* **84** (Dec, 2011) 124031, arXiv:1110.4402.

[198] Y. Ali-Haïmoud, "Correlation Function of High-Threshold Regions and Application to the Initial Small-Scale Clustering of Primordial Black Holes", *Phys. Rev. Lett.* **121** (Aug, 2018) 081304, arXiv:1805.05912.

[199] V. Desjacques and A. Riotto, "Spatial clustering of primordial black holes", *Phys. Rev. D* **98** (Dec, 2018) 123533, arXiv:1806.10414.

[200] G. Ballesteros, P. D. Serpico, and M. Taoso, "On the merger rate of primordial black holes: effects of nearest neighbours distribution and clustering", *Journal of Cosmology and Astroparticle Physics* **2018** no. 10, (2018) 043, arXiv:1807.02084.

[201] J. Garriga and N. Triantafyllou, "Enhanced cosmological perturbations and the merger rate of PBH binaries", arXiv:1907.01455.

[202] The **Planck Collaboration**, N. Aghanim *et al.*, "Planck 2018 results. VI. Cosmological parameters", arXiv:1807.06209.

[203] P. Carrilho, K. A. Malik, and D. J. Mulryne, "Dissecting the growth of the power spectrum for primordial black holes", arXiv:1907.05237.

[204] A. Raccanelli, E. D. Kovetz, S. Bird, I. Cholis, and J. B. Muñoz, "Determining the progenitors of merging black-hole binaries", *Phys. Rev. D* **94** (Jul, 2016) 023516, arXiv:1605.01405.

[205] A. Raccanelli, "Gravitational wave astronomy with radio galaxy surveys", *Monthly Notices of the Royal Astronomical Society* **469** no. 1, (2017) 656–670, arXiv:1609.09377.

[206] G. Scelfo, N. Bellomo, A. Raccanelli, S. Matarrese, and L. Verde, "GW×LSS: chasing the progenitors of merging binary black holes", *Journal of Cosmology and Astroparticle Physics* **2018** no. 09, (Sep, 2018) 039, arXiv:1809.03528.

[207] I. Cholis, E. D. Kovetz, Y. Ali-Haïmoud, S. Bird, M. Kamionkowski, J. B. Muñoz, and A. Raccanelli, "Orbital eccentricities in primordial black hole binaries", *Physical Review D* **94** no. 8, (2016) 084013, arXiv:1606.07437.

[208] E. D. Kovetz, I. Cholis, P. C. Breysse, and M. Kamionkowski, "Black hole mass function from gravitational wave measurements", *Phys. Rev. D* **95** (May, 2017) 103010, arXiv:1611.01157.

[209] E. D. Kovetz, "Probing Primordial Black Hole Dark Matter with Gravitational Waves", *Phys. Rev. Lett.* **119** (Sep, 2017) 131301, arXiv:1705.09182.

[210] J. B. Muñoz, E. D. Kovetz, L. Dai, and M. Kamionkowski, "Lensing of Fast Radio Bursts as a Probe of Compact Dark Matter", *Phys. Rev. Lett.* **117** no. 9, (2016) 091301, arXiv:1605.00008.

[211] N. Bellomo, A. Raccanelli, and R. Brustein arXiv:ToAppear.

[212] T. Harada, C.-M. Yoo, and K. Kohri, "Threshold of primordial black hole formation", *Phys. Rev. D* **88** (Oct, 2013) 084051, arXiv:1309.4201.

[213] E. W. Kolb and M. S. Turner, *The Early Universe*. 1990.

[214] M. C. Gonzalez-Garcia, M. Maltoni, and T. Schwetz, "Updated fit to three neutrino mixing: status of leptonic CP violation", *Journal of High Energy Physics* **2014** no. 11, (Nov, 2014) 52, arXiv:1409.5439.

[215] J. Lesgourgues and S. Pastor, "Massive neutrinos and cosmology", *Physics Reports* **429** no. 6, (2006) 307 – 379, arXiv:astro-ph/0603494.

Part IV

SUMMARY OF RESULTS, DISCUSSION AND CONCLUSIONS

5

SUMMARY OF RESULTS, DISCUSSIONS AND CONCLUSIONS

In this chapter I present a summary of results and discussions. I also summarize the conclusions we reached and I outline how these works can be extended in future works.

5.1 NEUTRINOS - MODIFIED GRAVITY DEGENERACY

In "Hiding neutrino mass in modified gravity cosmologies" [32] I investigate the potential degeneracy between the cosmological effects of neutrinos, which are guaranteed to exist since we have already detected them in laboratory experiments, and theories of modified gravity, which provide an interesting alternative to the standard ΛCDM.

Standard analyses of this degeneracy typically assume simple models of modified gravity, for instance $f(R)$ models, however in this work I focus on Horndeski theory of gravity, the most general minimally coupled scalar-tensor theory that propagates one extra scalar field whose equations of motion are of the second order. Horndeski theory include many specific models, as the $f(R)$ ones mentioned above, hence it allows us to explore the parameter space of different alternative theories of gravity at once.

Even if the theory is stated in terms of four free functions $\{K, G_3, G_4, G_5\}$ (*cf.* equation (2.2)), the effects on cosmological observables up to linear order in perturbation theory depends on combinations of these functions. Using the Effective Field Theory of dark energy, it was proved that in Horndeski gravity we have the freedom to set five functions of time and one constant [43]. In particular, to describe the expansion history of the Universe we need to fix the equation of state of the scalar field $w_\phi(t)$, while to describe perturbations we need four functions of time called kineticity $\alpha_K(t)$, braiding $\alpha_B(t)$, Planck mass running $\alpha_M(t)$, tensor speed excess $\alpha_T(t)$ and a constant that can be taken to be the fractional density of dark matter today Ω_{m0}.

The simplest modified gravity theory does not have enough freedom to produce a stage of accelerated expansion at low redshift ($z \lesssim 1$) and to affect large scale structure formation at high redshift ($z \sim \mathcal{O}(10)$) as done by massive neutrinos. However Horndeski gravity does have such freedom, hence I fix the equation of state to $w_\phi = -1$ (given that it cannot differ from this value more than 5% [44]), and I choose a parametrisation for the four $\alpha_I(t)$ functions such that they will be non-zero since when neutrinos became non-relativistic. I consider three quasi-degenerate neutrinos with normal mass ordering and total

mass $\sum m_\nu = 500$ meV (`M500` model) as neutrino model: even is these neutrino masses are already ruled out assuming ΛCDM, it is not the case for modified gravity models.

I investigate the impact of this model on temperature, polarization and deflection angle power spectra (and their cross-correlation) for a Planck-like CMB experiment and on the galaxy power spectrum for a Euclid-like galaxy survey. I find that even in the most optimistic case in which there are no theoretical uncertainties, a modified gravity model with `M500` neutrinos can mimic the clustering properties of matter produced by standard ΛCDM and massless neutrinos.

Neutrino mass is degenerate especially with one of the modified gravity functions, i.e., the braiding, which causes dark energy to cluster and enhances the matter power spectrum at small scales. This property is robust against changes in the details of the parametrisation of the α_J functions. Moreover, to have a cancellation between neutrinos and modified gravity effects, we need to match the relevant scales of the two sectors: the neutrino free-streaming scale $k_{\rm nr}$ and the braiding scale k_B in Horndeski theory. In particular we need to boost the growth of structure for modes larger than the neutrino free-streaming scale $k_{\rm nr}$ and to have $k_{\rm nr} \simeq k_B$. The latter requirement is in fact a constraint on the value of the kineticity: since $k_B \propto \alpha_K/\alpha_B^2$ and the value of α_B is fixed by the value of neutrino masses we have to compensate, we could find for the first time a constraint on this parameter.

Finally, I show that if we allow deviations from ΛCDM in the gravity sector, not even state-of-the-art CMB and next generation galaxy survey will be able to constraint the sum of neutrino masses better than $\sum m_\nu \lesssim \mathcal{O}(0.1\ \text{eV})$. Only through combinations with other probes, for instance with weak gravitational lensing surveys, or investigating the effects of neutrinos in different observables, for instance in galaxy bias, we might be able to lift this degeneracy.

The significance of this degeneracy has not changed, even after the neutron stars binary merger events, which allow to constraint the speed of tensors with respect to the speed of light. This event provided one of the strongest constraints on modified gravity, in fact requiring that $|\alpha_T| \lesssim 10^{-15}$ imposes constraints on the functional form of the G_j functions [45, 46]. This was in fact the first constrain we could put on the free functions of Horndeski Lagrangian. However, models with non-zero kineticity and braiding are still allowed and it is certainly interesting to repeat the work done in this article imposing the new constraints that emerged from this event.

Moreover, in recent years, several authors proposed the so called Swampland Conjecture [47]. According to this conjecture, the existence of a cosmological constant is disfavoured with respect to the scenario in which a scalar field drives this accelerated expansion stage. In other words, also by a theoretical perspective, simple models of modified gravity are not only motivated, but also favoured.

5.2 ABUNDANCE CONSTRAINTS FOR PRIMORDIAL BLACK HOLES

In the paper "Primordial black holes as dark matter: converting constraints from monochromatic to extended mass distributions" [39] I propose a novel way to compute abundance constraints for PBHs with an extended mass distribution (EMD).

Despite the fact that it is well established that PBHs cannot have a monochromatic mass distribution (MMD), the vast majority of the literature reports only abundance constraints for PBHs assuming they all have the same mass. Moreover, the naive idea of claiming that a mass distribution is allowed by current data only because it does not overlap with the constraints once the two are superimposed is know to be incorrect.

On the other hand, it is certainly useful to look for potential ways to convert MMD constraint into constraints for a given EMD: for example such procedure would allow to reinterpret CMB constraints very quickly without repeating a computationally intensive analysis. In this work we introduce the concept of equivalent mass $M_{\rm eq}$: given an EMD and an observable in which PBHs with different masses contributes independently (as in the vast majority of observables), it is always possible to find a MMD with mass $M_{\rm eq}$ which produces an equivalent observable effect, therefore, in both cases, the abundance constraint will be the same. This simple concept allows to interpret MMD constraint as EMD constraints, on the base of the observable effects of both distributions.

The same EMD will have multiple equivalent masses, one different from the other because the physics associated to each observable depends in different ways on the PBHs mass. The method is more robust than previous ones because it allows to take into account the effects of the tails of the EMD. We explicitly show that accounting for the effects of the tails is crucial to establish the robustness of the constraint: while for a MMD it is always clear whether assumptions taken in the theoretical modelling are satisfied, in the EMD case parts of your mass distribution may satisfied them while other parts might not. It is precisely in those case that some criteria is needed to assess whether you still trust the theoretical modelling or if you need a better one.

In this work I analyse the $\mathcal{O}(10\ M_\odot)$ window and those constraints that are more relevant for that range of masses, namely microlensing constraints, dynamical constraints coming from ultra-faint dwarf galaxies and CMB constraints. I show that for popular mass distributions (power-law and lognormal, motivated by different formation mechanisms) the constraints in that window become tighter with respect to those obtained for a MMD. Notice that this finding cannot be extended to all the possible mass distributions, in fact since the EMD

enters in the computation of the equivalent mass, it is possible to find weaker constraints for certain mass distributions.

The method have been tested successfully in multiple occasions. In Ref. [48] we showed that the approximations made in the computation of the equivalent mass are acceptable due to the size of current error bars in state-of-the-art CMB experiments. We run a full MCMC analysis and we also computed the equivalent mass and from there the abundance constraint: both methods gave us the same result. Moreover, also independent analysis, as the one done in Ref. [49] in the context of CMB constraints coming from radio and X-ray observations, explicitly showed that our method provides a remarkably good alternative to run computationally expensive numerical simulations.

The natural extension of this work would be to compute the equivalent mass for all the existing constraints in literature, at least for power-law and lognormal EMD. However, the most relevant issue is the robustness of the constraints themselves, as can be seen comparing those appearing in Ref. [50] in 2016 to those appearing in Ref. [51] in 2019. In many constraints, in fact, we make assumptions that are not justified, as in the case of femtolensing constraints [52], or that are at least debatable, as for CMB constraints, in which accretion on PBHs is assumed spherical since when the compact object formed.

5.3 PRIMORDIAL BLACK HOLES ORIGIN

In "GW$\times$LSS: chasing the progenitors of merging binary black holes" [40] I discuss how to establish whether the origin of resolved gravitational waves (GWs) events, detected by GWs present and future observatories, is stellar or primordial.

In the case where these events come from binaries with stellar progenitors, the resulting GWs map we would correlate with maps of the large scale structure (LSS) of the Universe, since we expect stellar BHs to come from massive halos which host galaxies that had an intense star formation history. On the other hand, if the origin of the progenitors is primordial, we expect the GWs to come from low mass halos, dominated by dark matter and where PBHs binaries are more likely to form due to a smaller relative velocity of the compact objects: since low mass halos live mainly in filaments, cross-correlating GWs and LSS maps will result in a smaller degree of correlation. Finally, if the binaries have primordial progenitors but they formed already during the radiation-dominated era, we expect them to trace the totality of the dark matter distribution.

Apart for the application to the PBHs scenario, this kind of multitracing technique can be used to characterise properties of astrophysical objects that emit GWs, hence it gives access to the environment in which these objects formed and lived. Moreover, the theoretical formalism is the same of galaxy number counts, hence I generalised the

`CLASSgal` creating a new code, called `Multi_CLASS`, able to compute angular power spectra for different tracers. The code will be made public along with another paper [53], however it has already been used in an other work [54] to constraint cosmological parameters using different tracers probed by the same survey.

While the properties of galaxies for different LSS survey are known quite well, some of the GWs properties are not. The GWs distribution in redshift was computed by calculating the merger rate for PBHs binaries, both for monochromatic and extend mass distributions, using state-of-the-art prescriptions. I defined and compute for the first time the magnification bias of GWs, which is crucial to describe GWs lensing properties. I found that the magnification bias will be very small, close to zero, both for existing and future GWs observatories, therefore eventual changes in the detection threshold would not impact significantly the number of objects we include in our maps.

Stellar and primordial scenarios are associated to different bias, which we aim to constraint. In the case of the stellar scenario, the bias of GWs and galaxies coincide, while in the primordial scenario the bias of GWs is the one of low-mass halos if the binary formed in the Late Universe or that of dark matter if the binary formed during the radiation-dominated era. I used two different Signal-to-Noise ratio to establish whether the constraining power of the cross-correlation depends on the statistical technique adopted. The first one was based on a Fisher matrix approach, the other on the full likelihood, both provided similar results.

Given the low resolution of GWs maps (due to the poor localisation of GWs events in the sky), we will be limited to investigate only the clustering properties at large scales. It is well known that at those scales we have to account for a series of different effects due to velocity, lensing and gravitational potentials, also to break possible degeneracies between cosmological parameters. I explicitly show that including all these general relativistic effects we are able to boost the Signal-to-Noise ratio from a factor few to a factor ten, also avoiding a possible source of systematic error.

Finally, I forecast the capability of present and next generation LSS surveys and GWs observatories to discriminate between the three different scenarios presented in this work. Even if we have to wait one-two decades to claim what the origin of these events really is, already in the next five years we could observe some hint or preference for one of these. Moreover I show that reducing the uncertainties in the theoretical modelling will be a crucial factor in selecting one of the scenario, much more important than improve the sky localization.

The most obvious extension of this work is represented by using this framework to constrain properties of standard astrophysical sources by cross-correlating the GWs maps with different galaxy catalogs. In

our analysis we neglect some details which should be implemented to increase the robustness of the result, as the effect of metallicity.

Moreover, the same technique can be extended to the case of unresolved GWs events to characterize the astrophysical stochastic GWs background (ASGWB). Despite the similarities of the two cases, the theoretical prediction for the ASGWB has been developed only recently in Ref. [55], where it was also presented for the first time the `CLASS_SGWB` code I developed.

5.4 ENERGY SCALE OF INFLATION

In "Measuring the energy scale of inflation using large scale structures" [41] I propose a novel way to measure the energy scale of inflation, which in the single-field slow-roll models is directly connected to the tensor-to-scalar ratio r parameter. There are different ways in which this parameter can be measured, from measuring B-modes of CMB polarization to the detection of the stochastic gravitational waves background produced by inflation, however this is the first proposal of using large scale structure data to measure r.

In particular, we aim to detect the signal left by a specific type of non-Gaussianity, called "graviton exchange". The existence of non-Gaussianities is guaranteed by the coupling of the scalar field to gravity, which is intrinsically non-linear. Of all the different types of non-Gaussianity that might exist, the one we are interested in exist in every inflationary models because it is generated by the exchange of a graviton between a pair of scalar fields.

Even if this non-Gaussianity is expected to be small, since it appears at the level of the four-point function of the curvature, it depends directly on the parameter r. Moreover, in certain configurations called "kite" and "folded kite", the contribution of the graviton exchange is boosted, increasing the probability of a detection. The boosting can be further increased by looking to the clustering properties, i.e., the n-point function of dark matter halos, especially at large scale and high redshift.

Instead of measuring directly the trispectrum of dark matter halos, I proposed to look to the four-point function contribution to the halo two- and three-point functions. I expanded the existing computation of these correlators, also finding and characterizing new mixed Gaussian/non-Gaussian terms never discussed before in the literature, to include the graviton exchange contribution. I found that at large scale this kind of non-Gaussianity is more relevant than other primordial ones, for instance those represented by the bispectrum contribution to the two-point function. Moreover, the scale dependence of this kind of non-Gaussianity is unique, both in the power spectrum and bispectrum cases. In the latter, the amplitude of the graviton exchange contribution is found to be at large scales of the

same order of magnitude of the Gaussian halo bispectrum for values of r compatible with the current upper bound.

There is a huge debate of whether non-Gaussianities can be detected in the Late Universe, in particular local non-Gaussianities. The general argument is that the parameter $f_{\rm NL}$, which describes the strength of the non-Gaussian correction, is suppressed by a small factor $(k_{\rm long}/k_{\rm short})^2$, where $k_{\rm long}$ and $k_{\rm short}$ are a long and short mode, respectively. While the controversy is still open, it is well established that modes still on super-horizon scales today appear as a flat background and cannot be probed. In this work we have eliminated all those kite configurations in which the sum of two momenta was smaller the smallest momentum that entered the horizon up to present-day, hence our predictions are not affected by any gauge consideration.

The road to the possible detection of this signal has not been fully explored yet. The present work can be improved first of all by computing some estimator of this type of non-Gaussianity that fully exploits the unique scale dependence of the graviton exchange contribution. Then, once we can compute a Signal-to-Noise ratio, we need to test the estimator on some mocks containing this kind of effect to test our capability to recover the signal. However, the most crucial point will certainly be implementing multitracing techniques in this framework: the scales we are interested in are exactly those dominated by cosmic variance, therefore we can easily predict that using multiple tracers of the underlying matter distribution will be the only possibility to ever detect this signal.

5.5 PRIMORDIAL CURVATURE POWER SPECTRUM

In "From primordial black hole abundance to primordial curvature power spectrum (and back)" I discuss the connection between the primordial curvature power spectrum and the present-day abundance of primordial black holes (PBHs), assuming they were formed by the collapse of large overdensity perturbations generated by curvature fluctuations. The idea was already explored in the literature, however the existing procedure included many assumptions that are not necessary any more due to advances both in theoretical understanding of PBHs physics and in numerical simulations of their formation. The connection was improved in three different ways.

First I used numerical simulations to establish a robust collapse criteria for different kind of overdensity perturbations, in fact it has been proved in numerous works that the critical threshold for the collapse depends significantly on the shape of the perturbation. Numerical simulations are mandatory at this stage, in fact I explicitly show that treating analytically the problem (by using linear theory predictions) bias all the relevant quantities of the problem: the typical scale of the

perturbation, the typical shape of the perturbation, thus its typical critical threshold, and the typical mass of the resulting PBH.

In a second step, I developed the connection between numerical simulations, which study the evolution of a single perturbation, and the cosmological framework, in which the Universe is filled by many of these perturbations. I proposed a solution to the long-standing problem of which is the correct field to filter, i.e., overdensity or curvature field, and which is the correct way to filter it without modifying the statistics of the field. Moreover I obtained for the first time the exact expression of the two-point function of the overdensity field in terms of all the n-points functions of the curvature field, which in turn encode the information on the inflationary dynamics.

Finally, I discussed how, in the context of Peak theory, the abundance of PBHs should be consistently computed from the statistics of the overdensity field at the horizon re-entry of perturbations and how the overdensity power spectrum and the typical shape of the peaks are connected.

These improvements were used to compute the new upper bound on the primordial curvature power spectrum. Given that PBHs can span a remarkably large range of masses, I was able to constraint around ten order of magnitude in terms of scales or, equivalently, around twenty inflationary e-folds. The upper bound I find is approximately one order of magnitude tighter than the previous ones, showing the importance of reducing the number of assumptions taken. I also show that the existence of a single PBH in the entire observable Universe is completely incompatible with an almost scale-invariant power spectrum, therefore the detection of just one PBH (for instance a BH with sub-solar mass) will immediately signal a deviation from the slow-roll dynamics.

Thanks to numerical simulation I also gave a proof of principle of how we can reconstruct not only the maximum amplitude, but also the shape of the curvature power spectrum, at least for scales smaller than the typical scale of the peak. For larger scales it is necessary to analyse the effects of PBHs primordial clustering, which are still an open issue. The shape of the primordial curvature power spectrum can be probed by future experiments as SKA or LISA through the detection of a stochastic gravitational waves background, confirming that PBHs were generated by large curvature fluctuations. However it is still possible to detect PBHs but no stochastic gravitational waves background, for instance in those cases where PBHs have an alternative formation mechanism, for instance due to phase transitions.

According to our analysis, the improvement that affected the most the constraint on the amplitude was using Peak theory instead of the Press-Schechter formalism. However Peak theory has been not fully developed for non-Gaussian field, therefore the next step we

must take to improve the current analysis is certainly the inclusion of non-Gaussianity in Peak theory.

BIBLIOGRAPHY

[1] Scott Dodelson. *Modern Cosmology*. 2003.

[2] Peter Coles and Francesco Lucchin. *Cosmology - The Origin and Evolution of Cosmic Structure*. 2008.

[3] Edward W. Kolb and Michael S. Turner. *The Early Universe*. 1990.

[4] Steven Weinberg. *Cosmology*. 2008.

[5] D. N. Spergel et al. "First-Year Wilkinson Microwave Anisotropy Probe (WMAP) Observations: Determination of Cosmological Parameters." In: *The Astrophysical Journal Supplement Series* 148 (2003), pp. 175–194. DOI: 10.1086/377226. arXiv: astro-ph/0302209.

[6] G. Hinshaw et al. "Nine-year Wilkinson Microwave Anisotropy Probe (WMAP) Observations: Cosmological Parameter Results." In: *The Astrophysical Journal Supplement Series* 208 (2013), p. 19. DOI: 10.1088/0067-0049/208/2/19. arXiv: 1212.5226.

[7] P. A. R. Ade et al. "Planck 2013 results. XVI. Cosmological parameters." In: *A&A* 571 (2014), A16. DOI: 10.1051/0004-6361/201321591. arXiv: 1303.5076.

[8] P. A. R. Ade et al. "Planck 2015 results. XIII. Cosmological parameters." In: *A&A* 594 (2016), A13. DOI: 10.1051/0004-6361/201525830. arXiv: 1502.01589.

[9] N. Aghanim et al. "Planck 2018 results. VI. Cosmological parameters." In: (2018). arXiv: 1807.06209.

[10] C. L. Bennett et al. "Seven-year Wilkinson Microwave Anisotropy Probe (WMAP) Observations: Are There Cosmic Microwave Background Anomalies?" In: *The Astrophysical Journal Supplement Series* 192.2 (2011), p. 17. DOI: 10.1088/0067-0049/192/2/17. arXiv: 1001.4758.

[11] P. A. R. Ade et al. "Planck 2013 results. XXIII. Isotropy and statistics of the CMB." In: *A&A* 571 (2014), A23. DOI: 10.1051/0004-6361/201321534. arXiv: 1303.5083.

[12] P. A. R. Ade et al. "Planck 2015 results - XVI. Isotropy and statistics of the CMB." In: *A&A* 594 (2016), A16. DOI: 10.1051/0004-6361/201526681. arXiv: 1506.07135.

[13] Raul Jimenez, Roy Maartens, Ali Rida Khalifeh, Robert R. Caldwell, Alan F. Heavens, and Licia Verde. "Measuring the homogeneity of the universe using polarization drift." In: *Journal of Cosmology and Astroparticle Physics* 2019.05 (2019), p. 048. DOI: 10.1088/1475-7516/2019/05/048. arXiv: 1902.11298.

[14] Nathalie Palanque-Delabrouille et al. "Neutrino masses and cosmology with Lyman-alpha forest power spectrum." In: *Journal of Cosmology and Astroparticle Physics* 2015.11 (2015), p. 011. DOI: 10.1088/1475-7516/2015/11/011. arXiv: 1506.05976.

[15] Antonio J. Cuesta, Viviana Niro, and Licia Verde. "Neutrino mass limits: Robust information from the power spectrum of galaxy surveys." In: *Physics of the Dark Universe* 13 (2016), pp. 77–86. DOI: 10.1016/j.dark.2016.04.005. arXiv: 1511.05983.

[16] Christophe Yèche, Nathalie Palanque-Delabrouille, Julien Baur, and Hélion du Mas des Bourboux. "Constraints on neutrino masses from Lyman-alpha forest power spectrum with BOSS and XQ-100." In: *Journal of Cosmology and Astroparticle Physics* 2017.06 (2017), p. 047. DOI: 10.1088/1475-7516/2017/06/047. arXiv: 1702.03314.

[17] Elena Giusarma, Sunny Vagnozzi, Shirley Ho, Simone Ferraro, Katherine Freese, Rocky Kamen-Rubio, and Kam-Biu Luk. "Scale-dependent galaxy bias, CMB lensing-galaxy cross-correlation, and neutrino masses." In: *Phys. Rev. D* 98 (2018), p. 123526. DOI: 10.1103/PhysRevD.98.123526. arXiv: 1802.08694.

[18] J. Angrik et al. "KATRIN design report 2004." In: (2005).

[19] M. Aker et al. "An improved upper limit on the neutrino mass from a direct kinematic method by KATRIN." In: (2019). arXiv: 1909.06048.

[20] Amir Aghamousa et al. "The DESI Experiment Part I: Science, Targeting, and Survey Design." In: (2016). arXiv: 1611.00036.

[21] Jérome Martin. "Everything you always wanted to know about the cosmological constant problem (but were afraid to ask)." In: *Comptes Rendus Physique* 13.6 (2012), pp. 566–665. DOI: 10.1016/j.crhy.2012.04.008. arXiv: 1205.3365.

[22] Alan H. Guth. "Inflationary universe: A possible solution to the horizon and flatness problems." In: *Phys. Rev. D* 23 (1981), pp. 347–356. DOI: 10.1103/PhysRevD.23.347.

[23] Paul J. Steinhardt and Neil Turok. "A Cyclic Model of the Universe." In: *Science* 296 (2002), pp. 1436–1439. DOI: 10.1126/science.1070462. arXiv: hep-th/0111030.

[24] Robert H. Brandenberger. "Alternatives to the Inflationary Paradigm of Structure Formation." In: *International Journal of Modern Physics Conference Series* 1 (2011), pp. 67–79. DOI: 10.1142/S2010194511000109. arXiv: 0902.4731.

[25] Julien Lesgourgues and Sergio Pastor. "Massive neutrinos and cosmology." In: *Physics Reports* 429.6 (2006), pp. 307–379. DOI: 10.1016/j.physrep.2006.04.001. arXiv: astro-ph/0603494.

[26] Gregory Walter Horndeski. "Second-order scalar-tensor field equations in a four-dimensional space." In: *International Journal of Theoretical Physics* 10.6 (1974), pp. 363–384. DOI: 10.1007/BF01807638.

[27] C. Deffayet, S. Deser, and G. Esposito-Farèse. "Generalized Galileons: All scalar models whose curved background extensions maintain second-order field equations and stress tensors." In: *Phys. Rev. D* 80 (2009), p. 064015. DOI: 10.1103/PhysRevD.80.064015. arXiv: 0906.1967.

[28] Bharat Ratra and P. J. E. Peebles. "Cosmological consequences of a rolling homogeneous scalar field." In: *Phys. Rev. D* 37 (1988), pp. 3406–3427. DOI: 10.1103/PhysRevD.37.3406.

[29] C. Wetterich. "Cosmology and the fate of dilatation symmetry." In: *Nuclear Physics B* 302.4 (1988), pp. 668 –696. DOI: 10.1016/0550-3213(88)90193-9.

[30] Sean M. Carroll, Vikram Duvvuri, Mark Trodden, and Michael S. Turner. "Is cosmic speed-up due to new gravitational physics?" In: *Phys. Rev. D* 70 (2004), p. 043528. DOI: 10.1103/PhysRevD.70.043528. arXiv: astro-ph/0306438.

[31] Alberto Nicolis, Riccardo Rattazzi, and Enrico Trincherini. "Galileon as a local modification of gravity." In: *Phys. Rev. D* 79 (2009), p. 064036. DOI: 10.1103/PhysRevD.79.064036. arXiv: 0811.2197.

[32] **Nicola Bellomo**, Emilio Bellini, Bin Hu, Raul Jimenez, Carlos Pena-Garay, and Licia Verde. "Hiding neutrino mass in modified gravity cosmologies." In: *Journal of Cosmology and Astroparticle Physics* 2017.2 (Feb. 2017), p. 043. DOI: 10.1088/1475-7516/2017/02/043. arXiv: 1612.02598.

[33] Gianfranco Bertone and Dan Hooper. "History of dark matter." In: *Rev. Mod. Phys.* 90.4 (2018), p. 045002. DOI: 10.1103/RevModPhys.90.045002. arXiv: 1605.04909.

[34] Gianfranco Bertone and Tim M. P. Tait. "A new era in the search for dark matter." In: *Nature* 562 (2018), pp. 51–56. DOI: 10.1038/s41586-018-0542-z. arXiv: 1810.01668.

[35] B. P. Abbott et al. "GWTC-1: A Gravitational-Wave Transient Catalog of Compact Binary Mergers Observed by LIGO and Virgo during the First and Second Observing Runs." In: *Phys. Rev. X* 9 (2019), p. 031040. DOI: 10.1103/PhysRevX.9.031040. arXiv: 1811.12907.

[36] Takeshi Chiba and Shuichiro Yokoyama. "Spin distribution of primordial black holes." In: *Progress of Theoretical and Experimental Physics* 2017.8 (2017). DOI: 10.1093/ptep/ptx087. arXiv: 1704.06573.

[37] Mehrdad Mirbabayi, Andrei Gruzinov, and Jorge Noreña. "Spin of Primordial Black Holes." In: (2019). arXiv: 1901.05963.

[38] V. De Luca, V. Desjacques, G. Franciolini, A. Malhotra, and A. Riotto. "The Initial Spin Probability Distribution of Primordial Black Holes." In: *Journal of Cosmology and Astroparticle Physics* 2019.05 (2019), p. 018. DOI: 10.1088/1475-7516/2019/05/018. arXiv: 1903.01179.

[39] **Nicola Bellomo**, José Luis Bernal, Alvise Raccanelli, and Licia Verde. "Primordial black holes as dark matter: converting constraints from monochromatic to extended mass distributions." In: *Journal of Cosmology and Astroparticle Physics* 2018.1 (Jan. 2018), p. 004. DOI: 10.1088/1475-7516/2018/01/004. arXiv: 1709.07467.

[40] Giulio Scelfo, **Nicola Bellomo**, Alvise Raccanelli, Sabino Matarrese, and Licia Verde. "GW×LSS: chasing the progenitors of merging binary black holes." In: *Journal of Cosmology and Astroparticle Physics* 2018.9 (Sept. 2018), p. 039. DOI: 10.1088/1475-7516/2018/09/039. arXiv: 1809.03528.

[41] **Nicola Bellomo**, Nicola Bartolo, Raul Jimenez, Sabino Matarrese, and Licia Verde. "Measuring the energy scale of inflation with large scale structures." In: *Journal of Cosmology and Astroparticle Physics* 2018.11 (Nov. 2018), p. 043. DOI: 10.1088/1475-7516/2018/11/043. arXiv: 1809.07113.

[42] Alba Kalaja, **Nicola Bellomo**, Nicola Bartolo, Daniele Bertacca, Sabino Matarrese, Ilia Musco, Alvise Raccanelli, and Licia Verde. "From Primordial Black Holes Abundance to Primordial Curvature Power Spectrum (and back)." In: (Aug. 2019). arXiv: 1908.03596.

[43] Emilio Bellini and Ignacy Sawicki. "Maximal freedom at minimum cost: linear large-scale structure in general modifications of gravity." In: *Journal of Cosmology and Astroparticle Physics* 2014.07 (2014), p. 050. DOI: 10.1088/1475-7516/2014/07/050. arXiv: 1404.3713.

[44] José Luis Bernal, Licia Verde, and Adam G. Riess. "The trouble with H_0." In: *Journal of Cosmology and Astroparticle Physics* 2016.10 (2016), p. 019. DOI: 10.1088/1475-7516/2016/10/019. arXiv: 1607.05617.

[45] Jose María Ezquiaga and Miguel Zumalacárregui. "Dark Energy After GW170817: Dead Ends and the Road Ahead." In: *Phys. Rev. Lett.* 119 (2017), p. 251304. DOI: 10.1103/PhysRevLett.119.251304. arXiv: 1710.05901.

[46] Paolo Creminelli and Filippo Vernizzi. "Dark Energy after GW170817 and GRB170817A." In: *Phys. Rev. Lett.* 119 (2017), p. 251302. DOI: 10.1103/PhysRevLett.119.251302. arXiv: 1710.05877.

[47] Georges Obied, Hirosi Ooguri, Lev Spodyneiko, and Cumrun Vafa. "De Sitter Space and the Swampland." In: (2018). arXiv: 1806.08362.

[48] José Luis Bernal, **Nicola Bellomo**, Alvise Raccanelli, and Licia Verde. "Cosmological implications of primordial black holes." In: *Journal of Cosmology and Astroparticle Physics* 2017.10 (Oct. 2017), p. 052. DOI: 10.1088/1475-7516/2017/10/052. arXiv: 1709.07465.

[49] Julien Manshanden, Daniele Gaggero, Gianfranco Bertone, Riley M. T. Connors, and Massimo Ricotti. "Multi-wavelength astronomical searches for primordial black holes." In: *Journal of Cosmology and Astroparticle Physics* 2019.06 (2019), p. 026. DOI: 10.1088/1475-7516/2019/06/026. arXiv: 1812.07967.

[50] Bernard Carr, Florian Kühnel, and Marit Sandstad. "Primordial black holes as dark matter." In: *Phys. Rev. D* 94 (2016), p. 083504. DOI: 10.1103/PhysRevD.94.083504. arXiv: 1607.06077.

[51] N. Bartolo, V. De Luca, G. Franciolini, A. Lewis, M. Peloso, and A. Riotto. "Primordial Black Hole Dark Matter: LISA Serendipity." In: *Phys. Rev. Lett.* 122 (2019), p. 211301. DOI: 10.1103/PhysRevLett.122.211301. arXiv: 1810.12218.

[52] Andrey Katz, Joachim Kopp, Sergey Sibiryakov, and Wei Xue. "Femtolensing by dark matter revisited." In: *Journal of Cosmology and Astroparticle Physics* 2018.12 (2018), p. 005. DOI: 10.1088/1475-7516/2018/12/005. arXiv: 1807.11495.

[53] Nicola Bellomo, José Luis Bernal, Giulio Scelfo, Alvise Raccanelli, and Licia Verde. "Beware of commonly used approximations when estimating errors." In: (2019). arXiv: ToAppear.

[54] José Luis Bernal, Alvise Raccanelli, Ely D. Kovetz, David Parkinson, Ray P. Norris, George Danforth, and Courtney Schmitt. "Probing ΛCDM cosmology with the Evolutionary Map of the Universe survey." In: *Journal of Cosmology and Astroparticle Physics* 2019.02 (2019), p. 030. DOI: 10.1088/1475-7516/2019/02/030. arXiv: 1810.06672.

[55] Daniele Bertacca, Angelo Ricciardone, **Nicola Bellomo**, Alexander C. Jenkins, Sabino Matarrese, Alvise Raccanelli, Tania Regimbau, and Mairi Sakellariadou. "Projection effects on the observed angular spectrum of the astrophysical stochastic gravitational wave background." In: (Sept. 2019). arXiv: 1909.11627.

The bibliography printed above refers to citations in the Introduction, in individual chapter introductions and in Summary of Results, Discussions and Conclusions. Citations in each individual publication can be found listed within the corresponding publication.

COLOPHON

This document was typeset using the typographical look-and-feel `classicthesis` developed by André Miede and Ivo Pletikosić. The style was inspired by Robert Bringhurst's seminal book on typography "*The Elements of Typographic Style*". `classicthesis` is available for both LaTeX and LyX:

https://bitbucket.org/amiede/classicthesis/

Happy users of `classicthesis` usually send a real postcard to the author, a collection of postcards received so far is featured here:

http://postcards.miede.de/

Thank you very much for your feedback and contribution.